School of Chemical, Environmental and Mining Engineering

NUMERICAL MODELLING OF TUNNEL FIRES AND WATER MIST SUPPRESSION

Robert Andrew Hart MEng

Thesis submitted to the University of Nottingham
for the degree of Doctor of Philosophy
December 2005

Abstract

Fires in mine tunnels and other underground space are a serious hazard, that can, if left unchecked, result in significant economic loss and human tragedy. In the UK, methods such as water deluge, foam application, and various types of hand-held extinguishers have been used, but statistics show no improvement in the incidence of fire. Water mist has the potential to be an effective fire suppression system for tunnel spaces. Typical water mist systems utilise small droplets of around 100 µm that have a low terminal velocity and a high surface to volume ratio. This leads to behaviour distinct from that of traditional sprinklers. Various mechanisms of action have been identified: removal of heat; oxygen depletion; fuel cooling; attenuation of radiation; and disruption of air flow. The relative importance of each is case dependent.

Current research has focussed almost exclusively on enclosures with minimal or no ventilation, and no data relevant to the application of mist in tunnels exists.

In this thesis, a series of Computational Fluid Dynamics (CFD) simulations, based on published experimental data, are used to indirectly validate a CFD model of a hypothetical water mist system applied to a real tunnel fire, and to improve the understanding of how water mist performs in a strongly ventilated space. The water mist is represented by a Lagrangian-based particle-tracking model. This model is fully coupled to the continuous phase, accounting for transfer of momentum, heat, and mass.

A 16 m^3 unventilated enclosure is used first to validate a pool fire model based on 0.3 m square pools of methanol (27 kW) and hexane (115 kW). The behaviour of a thermal plume in a tunnel with forced ventilation is then validated, initially using a fixed volumetric heat source of 7.5 kW in a small-scale tunnel, and then on a full-scale 3 m square cross-section tunnel with a 3 m diesel pool using the pool fire model.

The water mist model is validated with the enclosure fire, and a sensitivity study assesses the effect of droplet diameter, spray velocity and angle, and water flow rate on the performance of the system. Finally water mist is applied to the tunnel fire At low ventilation, oxygen depletion and air-flow disruption are significant, whereas at high ventilation the only effect of the mist is to remove heat and reduce temperature.

To Hannah

Acknowledgements

I would like to thank:

- my original supervisors, Dr Julian Edwards and Dr TX Ren, and my current supervisors Dr Ian Lowndes, and Dr Hervé Morvan.
- the ECSC for funding this project, and also the other project partners who provided valuable input, particularly at the start of this work: Dr Horst Hejny and Dr Werner Foit from DMT, Pedro Morillo from Aitemin, and Dr Bob Jozefowicz and others from MRSL.
- my fellow students and close friends Chanchala 'චංචල' Ariyaratne, Smeeta Fokeer, Tim Appleton, YiXiang Cai, Andrew Bachelor, and many others.
- my family and friends: Mum, Dad (especially for doing the proof reading), Liz, Matt (aka Nigel), James, Angela (aka Big Bird), Rebeca, Belinda, David, Hazel, various folk at THBC (particularly Kathryn), Naomi, Laura, and all the other people who've supported and encouraged me over the last few years.

This thesis was typeset with LaTeX running on Debian GNU/Linux. Graphics were produced with XFig, gnuplot, and The GIMP.

Contents

List of Figures

List of Tables

List of Animations

The animations below are on the accompanying CD-ROM. This will not be available on the eTheses version of this document.

Nomenclature

Constants	
g	gravitation acceleration ($9.81\,\mathrm{m/s^2}$)
R	Gas constant ($8.3143\,\mathrm{J/K/mol}$)
Variables	
c_p	Specific heat capacity (kJ/kgK)
D_{pq}	representative diameter (m)
	e.g:
D_{10}	Arithmetic Mean Diameter
D_{20}	Area Mean Diameter
D_{30}	Volume Mean Diameter
D_{32}	Sauter Mean Diameter
D_{43}	de Brouckere Mean Diameter
Da	Damköhler Number
Fr	Froude Number
ΔH_v	Enthalpy of Evaporation (kJ/mol)
Eo	Eötvös Number
E_r	Activation Energy (kJ/mol)
Gr	Grashof Number
$\bar{H}$	hydraulic diameter (m)
k	Nozzle k-factor ($\mathrm{m^{3.5}kg^{-0.5}}$, $\mathrm{lpm/bar^{0.5}}$, or $\mathrm{gpm/psi^{0.5}}$)
k	Reaction rate constant (units depend on reaction mechanism)
k	Thermal conductivity (W/mK)
k	Turbulent kinetic energy (J)
Nu	Nusselt Number
Oh	Ohnesorge Number
P, p	Pressure (Pa, bar)
Pe	Peclet Number
Pr	Prandtl Number
Q^*_D	Dimensionless fire power
q	Heat flux
Ra	Rayleigh Number

Re	Reynolds Number
Re_d	Droplet Reynolds Number
Sc	Schmidt Number
T	Temperature (K, °C)
T_∞, T_0	ambient temperature
u, v, w	components of velocity in x, y, & z directions (m/s)
We	Weber Number
x, y, z	position (m)
Y_i	Mixture fraction (dimensionless)

Greek Symbols

α	Under relaxation factor
β	Thermal expansion coefficient
ε	Turbulent dissipation rate ($\mathrm{m}^2/\mathrm{s}^3$)
κ	thermal diffusivity (???)
λ	Second viscosity coefficient (kg/m/s)
μ	dynamic viscosity (Pa s)
μ_t	turbulent viscosity (kg/ms)
ν	kinematic viscosity (m^2/s)
ρ	density (kg/m^3)
ρ_∞, ρ_0	ambient density ($\sim 1.2\,\mathrm{kg}/\mathrm{m}^3$)
σ	surface tension (N/m)
τ	shear stress (N/m^2)
τ	time scale (s)
ϕ	generic scalar quantity

Subscripts

$_d$	Droplet
$_r$	Reaction
$_r$	Radiative
$_t$	Turbulent
$_\infty$	Free Stream/Ambient
$_0$	Initial/Ambient

Glossary

Courant Number C – relationship between physical properties (wave speed, etc.) and numerical properties (grid and time step size).

$$C = \beta V \frac{\Delta t}{\Delta x}$$

$C \approx 1$ for convergence. Sometimes referred to as the CFL (Courant-Friedrichs-Lewy) condition.

CPU Central Processing Unit – component of a computer that performs calculations (e.g. Intel Pentium IV, or AMD Athlon). In **parallel processing** each individual CPU is referred to as a node.

Dimensionless fire power Q_D^* – A measure of the size of a fire.

$$Q_D^* = \frac{\dot{Q}}{\rho_\infty c_p T_\infty \sqrt{gD} D^2}$$

Damköhler Number D – ratio of a vapour's residence time in the reaction zone to the chemical reaction time.

$$\mathrm{D} = \frac{\tau_r}{\tau_{ch}}$$

There is a critical Damköhler number below which "blowout" occurs. Conversely high Damköhler numbers correspond to infinite rate chemistry and mixing controlled reactions.

DNS – Direct Numerical Simulation – form of CFD simulation where turbulence is directly simulated using a very fine grid and small time steps.

Droplet – isolated free-body of water, held together by surface tension, and often assumed to be spherical. In a numerical simulation, a single **tracking particle** represents many droplets.

Eötvös Number Eo – ratio of acceleration force to surface tension of a droplet. Used as a measure of droplet stability.

$$\mathrm{Eo} = \frac{\rho_D \frac{\mathrm{d}u}{\mathrm{d}t} D^2}{\sigma}$$

Similar in principle to the **Weber** number and **Ohnesorge** number.

FDS – Fire Dynamics Simulator – open source CFD code designed for fire driven flow. Includes mixture fraction combustion, radiation, and **LES** turbulence. Produced by NIST. http://fire.nist.gov/fds

Froude Number Fr – square root of ratio of kinetic energy to potential energy. For a buoyant plume, Fr $\simeq 1.5$.

$$\mathrm{Fr} = \frac{u}{\sqrt{gh}}$$

Grashof Number Gr – ratio of buoyancy forces to viscous forces

$$\mathrm{Gr} = \frac{g\alpha\Delta T L^3}{\nu^2}$$

Injection – the point at which liquid water is discharged into the air.

Knudsen Number Kn – ratio of molecule free path to the physical length scale.

$$\mathrm{Kn} = \frac{\lambda}{L}$$

At low Knudsen number a fluid can no longer be considered a continuum.

LES – Large Eddy Simulation – hybrid of **RANS** and **DNS**. Large-scale turbulent eddies are simulated, whilst small scale dissipation is modelled.

Lewis Number Le – ratio of mass diffusivity to thermal diffusivity. It is sometimes convenient to assume a Lewis number of unity.

$$\mathrm{Le} = \frac{D}{\kappa}$$

Nusselt Number Nu – ratio of temperature gradients (non-dimensionalised heat transfer coefficient). For high Nusselt number convection is dominant and at low Nusselt number, conduction dominates.

$$\mathrm{Nu} = \frac{hL}{k}$$

It is common to estimate Nu by expressions of the form $\mathrm{Nu} = a\mathrm{Re}^x\mathrm{Pr}^y$ where Re is the **Reynolds Number** and Pr the **Prandtl Number**.

Ohnesorge Number Oh – ratio between viscous forces and surface tension for

a stream of fluid. $\mathrm{Oh} = \frac{\sqrt{\mathrm{We}}}{\mathrm{Re}}$

$$\mathrm{Oh} = \frac{\mu}{\sqrt{\rho\sigma d}}$$

where d is the nozzle diameter, and μ, ρ and σ are fluid properties. Similar to **Weber** number and **Eötvös** number.

Particle (or Tracking Particle) – conceptual particle used to represent multiple droplets within a numerical simulation.

Parallel Processing – the utilisation of more than one physical CPU to carry out a task in order to reduce the total time taken. The CPUs may be located on a single computer, or spread out on several computers on a network.

Péclet Number Pe – ratio of convection to conduction.

$$\mathrm{Pe} \equiv \frac{\text{advection of heat}}{\text{conduction of heat}} = \frac{UL}{k}$$

In CFD, the use of Péclet numbers is not restricted to thermal transport and is extended to any convective-diffusive transport.

Prandtl Number Pr – ratio of momentum diffusivity and thermal diffusivity:

$$\mathrm{Pr} = \frac{\nu}{\kappa}$$

It is related to the **Nusselt Number**.

Products of Combustion POC – the various products of the combustion reaction. Typically carbon dioxide, carbon monoxide, water, and NO_x, etc.

Quenching Diameter D_Q – size below which heat loss will always prevent a flame from propagating. Conceptual the diameter of a pipe through which a flame front will not pass.

RANS – Reynolds Averaged Navier-Stokes equations – the governing equations of CFD in a form where the effects of turbulence are modelled by a separate turbulence model.

Rayleigh Number Ra – measure of strength of convective flow. $\mathrm{Ra} = |\mathrm{GrPr}|$

$$\mathrm{Ra} = \frac{g\beta\Delta T L^3 \rho}{\mu\kappa}$$

Reynolds Number Re – characteristic flow behaviour, typically used as an indicator of turbulence

$$\mathrm{Re} \equiv \frac{\rho u d}{\mu}$$

Richardson Number Ri – ratio of potential to kinetic energy, commonly used as a measure of the strength of buoyancy in a flow

$$\mathrm{Ri} = \frac{gh}{u^2}$$

Related to Froude number.

Sauter Mean Diameter SMD or D_{32} – mean droplet diameter representative of surface-to-volume ratio.

Schmidt Number Sc – ratio of momentum diffusivity to mass diffusivity.

$$\mathrm{Sc} \equiv \frac{\nu}{\kappa_C}$$

Stoichiometric ratio – ratio of fuel to air required so that all reactants are converted to products.

Viscosity *"resistance of a liquid to shear forces (and hence to flow)"*

Weber Number We – ratio of drag force to surface tension.

$$\mathrm{We} = \frac{\rho(u - u_D)^2 D}{\sigma}$$

Similar in principle to the **Eötvös** number and **Ohnesorge** number.

(Drysdale, 1998; Lefebvre, 1989; Wikipedia, 2004)

Chapter 1

Introduction

1.1 Motivation

There is a need for fire suppression systems in mine tunnels and other underground spaces.

Fires in mines can have a range of consequences: temporary withdrawal of workers; destruction of infrastructure; the permanent closure of a mine or section of a mine; but most seriously the substantial loss of human life.

Statistics for UK coal mines (MacMillan, 1997) show that the number of fires *per man shift* is increasing. These fires are attributed to a wide variety of sources including conveyor belts, mechanical plant, drilling rigs, vehicles and spontaneous combustion. Unless dealt with promptly, fires can grow to a size where they trap workers underground, and are unapproachable by fire fighters from either side.

Civil transportation tunnels are also at risk from fires, primarily due to vehicle collisions or breakdown, and can also lead to loss of life (e.g. the Mont Blanc Tunnel fire in 1999 caused 39 deaths), and substantial economic losses due to the closure of important trade routes.

Water mist has been identified as a potential fire suppression system that meets the requirements of mining operations:

flexible – a mine is a dynamic environments, and the fire hazard changes as the coal face moves relentlessly forward and as production moves from one area to another.

economic – mine workings can be very extensive, and the cost of fire protection per kilometre must be low to minimise the impact on profitability.

safe – it is important that activation of the fire suppression system does not represent a hazard to workers (such as intoxication or asphyxiation) or to the mine itself (such as flooding or equipment damage).

Water mist fire suppression systems (WMFSS) produce fine water droplets, typically with diameters of around 100 µm. Compared to traditional sprinklers and deluge systems, these have low terminal velocities and high surface to volume ratio. These have long residence time, are easily transported and dispersed by air currents, and are rapidly evaporated in a flame or fire plume. This has led to water mist being used as replacement for banned Halon systems, where the dispersion properties are similar to a total flooding agent, and in naval applications such as submarines or ship engine rooms, where low water usage is essential.

A variety of mechanisms for the action of water mist on a fire have been suggested in the academic literature, including gas phase cooling, oxygen dilution, fuel cooling, disruption to air flow, attenuation of radiation, and modification to the combustion reaction. The relative importance of these varies on a case-by-case basis, and to date research has concentrated on enclosed spaces with little or no ventilation. There is no published research concerning water mist in tunnels or strongly ventilated spaces.

This research was funded by the European Coal and Steel Community (ECSC), as part of project ECSC-PR/094, which was titled *"Fire Fighting Systems"*. The project was a collaboration between Deutsche Montan Technologie GmbH, Germany, AITEMIN, Spain, Mines Rescue Service Ltd. and the University of Nottingham, UK, and aimed to research a number of topics related to the use of water mist in coal mine tunnels, including: fire detection systems, remote and/or automatic activation, development of application guidelines, as well as the development and optimisation of water mist systems themselves (DMT et al., 2004b).

1.2 Aims and methodology

The aim of this thesis is to apply computational fluid dynamics (CFD) techniques to the modelling of water mist fire suppression of a tunnel fire, and to demonstrate whether the technique is appropriate and effective.

As little experimental data exist relating to water mist in tunnels, and there is no established empirical understanding concerning its behaviour, this thesis will utilise a series of related scenarios in order to build towards the ultimate goal. This is illustrated in Figure 1.1.

- Fire in an enclosure
- Thermally driven flow in a ventilated tunnel
- Fire in a tunnel
- Water mist suppression of a fire in an enclosure
- Water mist suppression of a fire in a tunnel

In each case a rigorous methodology will be applied in order to ensure, where possible:

- grid independence,
- reproducibility,
- sensitivity is established,

and

- results are backed by experimental validation.

Conceptually, these scenario can be split into two groups, those related to enclosures, and those related to tunnels. The enclosure scenarios are intended to inform and support the corresponding tunnel scenarios. Existing applications of water mist have been primarily in enclosures, and this is mirrored by the information available in published research.

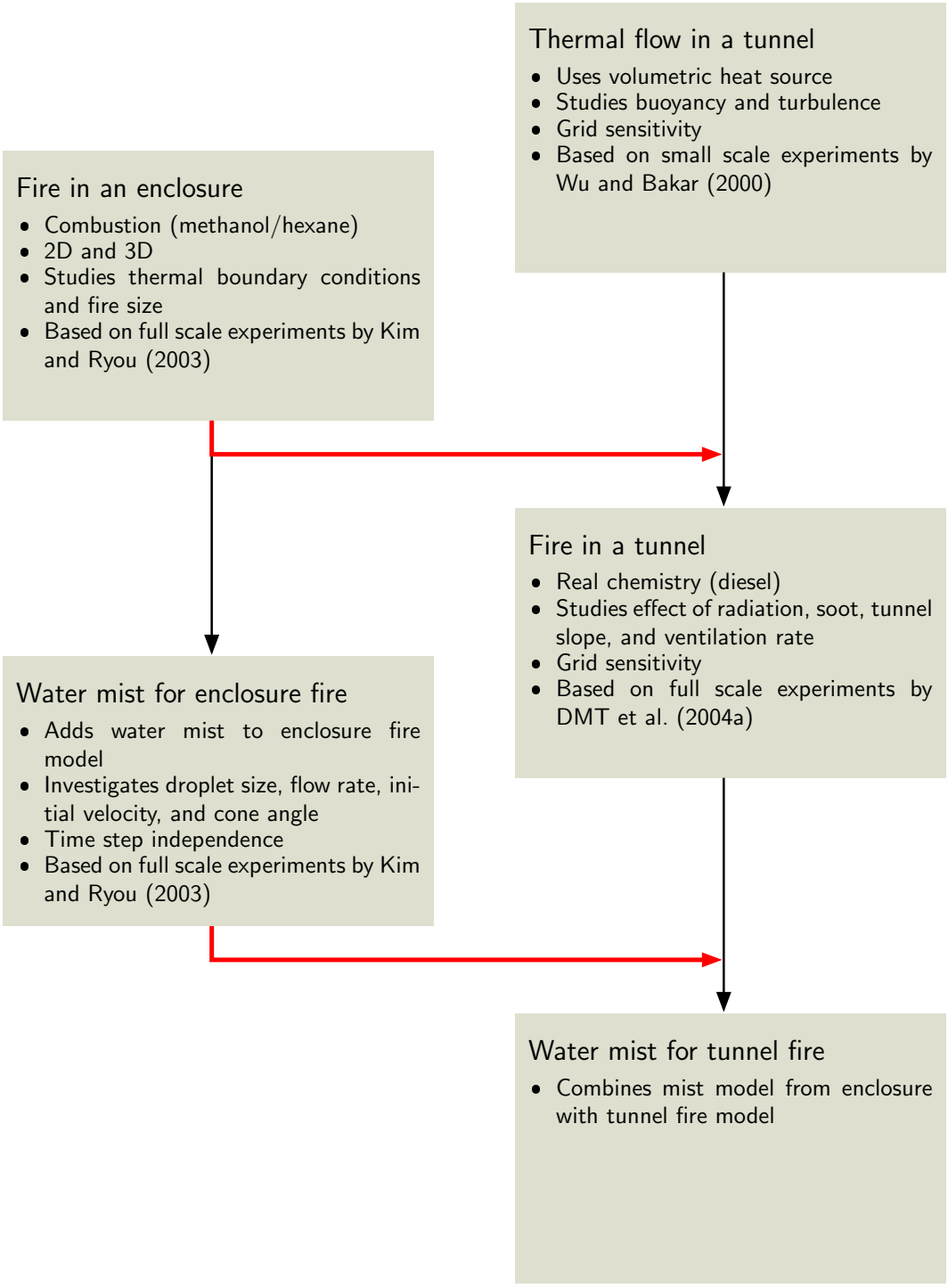

Figure 1.1: Overview of scenarios modelled for this thesis

Table 1.1: Summary of physics/models used in each scenario

Case	see	2D/3D	**Turbulence**	**Ventilation**	**Combustion**	EBU	Hybrid	**Radiation**	Soot	Multiband	**Discrete Phase**
Fire in an enclosure	§5	Both	k-ε		•	•	•	•			
Thermal flow in a tunnel	§6.1	3D	k-ε	•							
Fire in a tunnel	§6.2	3D	k-ε	•	•	•		•	•	•	
Water mist for enclosure fire	§7.1	Both	k-ε		•	•	•	•			•
Water mist for tunnel fire	§7.2	3D	k-ε	•	•		•	•	•		•

1.2.1 Physics

Table 1.1 summarises the physics and computational models tested in each of the five scenarios examined in this thesis.

1.3 Thesis structure

Chapter 2 provides an overview of existing knowledge related to fires and fire safety, particularly tunnel and mine fires, but also covering the fundamentals of fire and combustion processes. A summary of relevant experimental studies from the academic literature is presented.

Chapter 3 reviews existing firefighting practise – in particular the use of water mist as a fire suppression system – and presents a synopsis of relevant theoretical and numerical analyses, and experimental data available in the published literature.

Chapter 4 provides an overview of the *Computational Fluid Dynamics* (CFD) techniques that are used in subsequent chapters to model the physical processes involved in a tunnel fire and water mist suppression. Some of the details and models presented in Chapter 4 relate specifically to the *Fluent* CFD code, as

that is used for the majority of the subsequent work.

In Chapter 5, a CFD model for a pool fire in an enclosure is developed and tested. The sensitivity of the model to variation in key parameters such as time step size, mesh resolution and boundary conditions is explored. The model is based on experimental data published by Kim and Ryou (2003). The pool fire model is applied to a tunnel fire scenario in Chapter 6, and is extended to include water mist fire suppression for both the enclosure and the tunnel fire in Chapter 7.

In Chapter 6, a CFD model of a pool fire in a tunnel is developed and validated. Initially a simple heat source is used to represent the fire, and small scale experimental data from Wu and Bakar (2000) is used to validate the thermally driven flow regime. Subsequently, a true combustion model is used to model a full scale tunnel fire based on recent experimental data collected by DMT et al. as part of this project. The fire is approximately 10 MW and forced ventilation gives a net air flow.

In Chapter 7, a CFD model of a water mist fire suppression system is developed. The discrete phase model (DPM) of *Fluent* is used to represent the water mist. The model is applied to the enclosure and tunnel fire scenarios that were modelled in Chapters 5 and 6 respectively. For the enclosure, experimental data are available (Kim and Ryou, 2003), allowing the model to be validated. For the tunnel, the modelled system is hypothetical because no adequate source of experimental data is available. In both cases, the sensitivity of the water mist system to variation in key parameters – such as water flow rate, droplet diameter, spray angle and nozzle velocity – is explored.

Chapter 8 brings together the findings of this thesis and highlights the original contributions to knowledge. Some areas requiring further research are also identified.

Chapter 2

Fires

This chapter provides an overview of existing knowledge related to fires and fire safety, particularly tunnel and mine fires, but also covering the fundamentals of fire and combustion processes. A summary of relevant experimental studies from the academic literature is presented.

2.1 Fundamentals of fire

Fire is the chemical reaction (known as combustion) that occurs when a fuel and an oxidiser are bought together with sufficient energy to cause ignition. A simplistic representation of this is the *"fire triangle"* (see Figure 2.1) which shows the components required for fire to occur. Conversely if one or more components are missing, then fire will not occur.

Fire has been used throughout history as a source of heat and light for purposes such as cooking, forging metals and disposal of waste. This thesis, however, is concerned solely with undesirable fires that occur accidentally (or perhaps maliciously), and in particular in tunnel-like spaces.

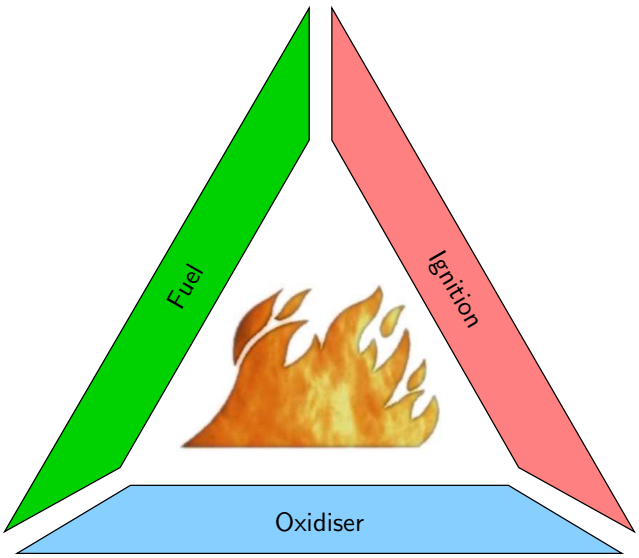

Figure 2.1: Combustion triangle

Gas	Chemical Composition	Molecular Mass g/mol	Percentage by volume	by mass
Nitrogen	N_2	28	$78 \cdot 094$	$75 \cdot 5$
Oxygen	O_2	32	$20 \cdot 947$	$23 \cdot 15$
Argon	Ar	40	$0 \cdot 935$	$1 \cdot 29$
Carbon Dioxide	CO_2	44	$0 \cdot 033$	$0 \cdot 05$

Table 2.1: Composition of atmosphere (Rogers and Mayhew, 1995)

2.1.1 Stoichiometry

For a given quantity of fuel, the minimum quantity of oxidiser required can be determined from the balanced chemical equation for the reaction. For example, for propane and oxygen, the chemical equation is:

$$C_3H_8 + 5O_2 \longrightarrow 4H_2O + 3CO_2 \tag{2.1}$$

giving an oxygen to fuel ratio of 5 mol/mol (or 3.63 kg/kg). This ratio is called the stoichiometric ratio.

In the common case of the oxidiser being atmospheric oxygen – which forms 20.9 % by volume of the atmosphere (see Table 2.1) – it is common to express the stoichiometric ratio as an air to fuel ratio. (e.g. for propane 15.7 kg_{Air}/kg_{fuel})

Note that the concept of stoichiometry is based on a simple overall reaction. In reality, the chemistry of the combustion process means that dozens of reaction steps exist even for simple fuels. The 'Leeds Mechanism' for the oxidation of methane contains 177 separate reaction steps. A further 67 steps can be added if atmospheric nitrogen is also considered. For example, carbon monoxide is converted to carbon dioxide in a temperature dependent reversible reaction:

$$\mathrm{CO} + \frac{1}{2}\mathrm{O_2} \overset{f(T)}{\rightleftharpoons} \mathrm{CO_2} \tag{2.2}$$

Fires where the air supply is *less* than stoichiometric are said to be *fuel rich* or *ventilation controlled*, and the overall rate of combustion is determined by the ventilation rate. The lack of oxygen means that some of the reaction steps will not complete, and the products of combustion will contain partly burnt fuel, and compounds such as carbon monoxide or NO_x (various nitrogen oxides).

Fires where the air supply is *greater* than stoichiometric are said to be *air rich* or *fuel controlled*. The rate of reaction is determined by the rate of fuel release.

2.1.2 Types of fuel

Fires can be classified according to the nature of the fuel involved. Although combustion itself is always a gaseous reaction, the source of the fuel is often a liquid or solid material. Feedback of heat from the flames allows further fuel to volatilise creating a self-sustaining reaction. The term 'volatilise' includes processes such as evaporation, sublimation, chemical decomposition, etc. In other cases fuel can be supplied by a leak from a vessel or pipeline.

In Section 2.1.3 below, a detailed description of the physics of a liquid pool fire is given. This case has been selected firstly because it is illustrative of many of the processes involved with fires in general, but secondly because it is a type of fire commonly used for research and experimentation. This is because:

- they have a well defined behaviour. A pure substance burned with a fixed surface area will give a near constant rate of heat release,
- they can be scaled over a large range of sizes, and

Figure 2.2: Example pool fires
a) 0.3 m aviation fuel fire (ICES, 2005) b) 6 m kerosene fire at AEA Technology (Sinai, 1999b)

- they are relatively common in nature.

2.1.3 Pool fires

The Health and Safety Executive (2002) define a pool fire as:

> a turbulent diffusion fire burning above a horizontal pool of vapourising hydrocarbon fuel where the fuel has zero or low initial momentum.

In particular, pool fires should be differentiated from 'spray fires', which can occur when a leak or rupture occurs in a high pressure pipeline or vessel.

Figure 2.2 shows two different sized pool fires at experimental facilities.

2.1.3.1 Fuel

Apte (1998) carried out tests on 1 m diameter pools for a range of fuels in a 12.96 m^2 cross-section tunnel. Pure alcohol fuels produce virtually no soot, and are therefore non-visible. Fuels containing a quantity of hydrocarbons (even if the fuel is predominantly alcohol) are visible. As the proportion of hydrocarbon

Table 2.2: Flame temperatures and radiation properties for different fuels (taken from Drysdale (1998), based on 0.3 m diameter pool fire)

	Flame temperature (°C)	Emission coefficient, K (/m)	Emissivity, ϵ	Principle chemical structure
Alcohol	1218	0.37	0.066	CH_3OH
Petrol	1026	2.0	0.36	C_8H_{18}
Kerosene	990	2.6	0.37	$C_{12}H_{26}$
Benzene	921	3.9	0.59	C_6H_6

increases, the amount of soot and carbon monoxide produced increases. Alcohol does however have a much higher flame temperature (see Table 2.2).

As the rate of burning of a pool fire is determined by the amount of heat transfered from the flame into the pool, the shape of the flame is affected by the mechanism of heat transfer. For alcohol, convection dominates, and the flame occurs in a zone close to the surface. For alkanes, radiation dominates, and there is a vapour region above the fuel surface (Drysdale, 1998).

The presence of an exposed lip (or rim) above the liquid surface can have a significant effect on the rate of combustion and on the flame characteristics, due to the separation of the flame from the fuel. Nakakuki (2002) demonstrates this by numerically calculating the heat balance for a 30 cm diameter pool with a 2 cm exposed lip. The balance involves 20 separate heat fluxes (conduction, radiation, evaporation, etc. between various combinations of fuel, flame, pan walls, etc.). Unfortunately only a single lip height is considered, so there are no broadly applicable conclusions.

Generally speaking, the temperature of the liquid varies exponentially with depth, and is close to (but below) the boiling point at the surface, and approaches ambient with depth (see Figure 2.3).

The rate of evaporation of fuel can be calculated from the *Clausius-Clapeyron* pressure:

$$P_{cc} = P_1 \exp\left(\frac{-\Delta H_v}{R}\left(\frac{1}{T_{cc}} - \frac{1}{T_1}\right)\right) \tag{2.3}$$

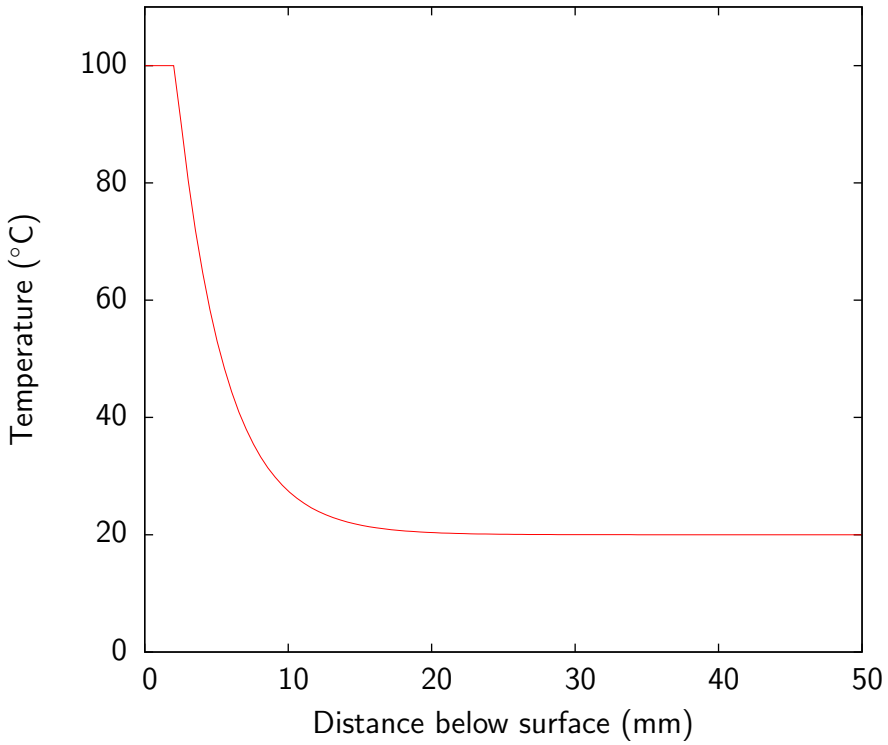

Figure 2.3: Temperature distribution below surface of n-butanol during steady burning
(adapted from Drysdale, 1998)

where

P_1 is the vapour pressure,

P_{cc} and T_{cc} are the temperature and partial pressure of the vapour at the fuel surface,

R is the gas constant (8.3144 J/mol/K), and

T_1 and ΔH_v are the boiling temperature and the heat of evaporation for the fuel ($T_1 = 337.8\,\mathrm{K}$ and $\Delta H_v = 1099\,\mathrm{kJ/kg}$ for methanol).

For methanol, this gives Figure 2.4.

Prasad et al. (1999) used this technique for numerical modelling of methanol pool fires in Fire Dynamics Simulator (*FDS*).

The burning of liquid mixtures, such as crude oil, is more complex due to the variability of the boiling-point. This can give rise to phenomena such as *boilover*, and *hot zone descent* (Drysdale, 1998).

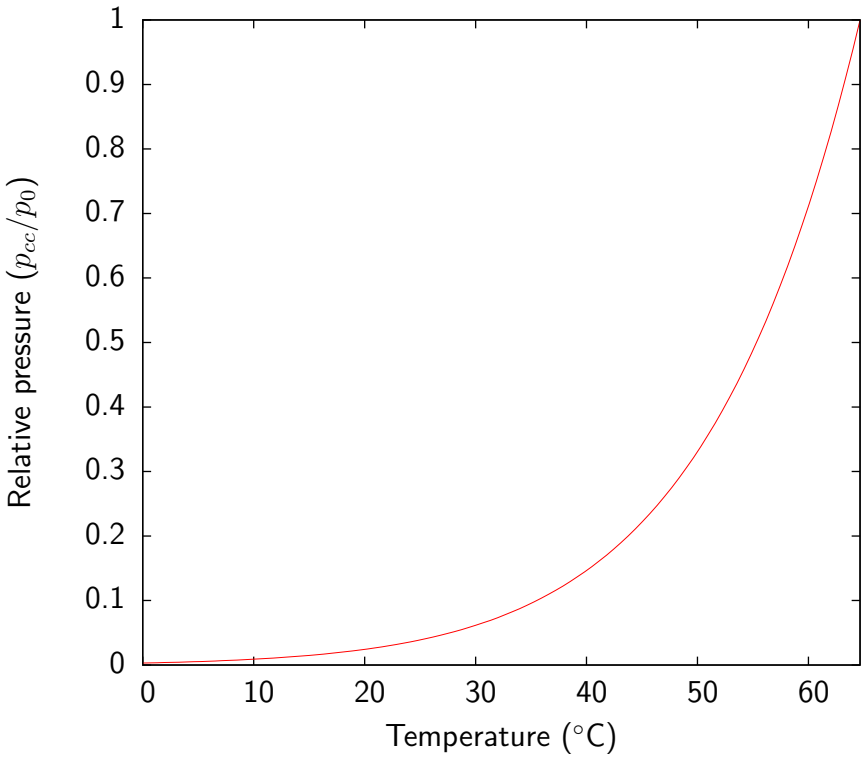

Figure 2.4: Clausius-Clapeyron pressure for methanol

2.1.3.2 Size

The properties of a pool fire depend on its size (Apte, 1998). Efficient combustion depends on good mixing of air into the fuel vapour, which is harder for larger diameter fires. Larger diameter fires therefore burn less efficiently and produce greater amounts of carbon monoxide and soot.

Larger diameter pools tend to give a greater unit heat release rate, and a greater unit burning rate, due to an increased efficiency of the *feedback of heat from the flame to the fuel* which is helped by both the geometry of the flame and the higher soot yields. This is particularly true for hydrocarbon fuels.

2.1.4 Buoyant plumes

For a fire with a solid or stationary liquid fuel source, the initial momentum of the fuel is low, but buoyancy forces are large due to the density difference between the hot combustion products and the ambient atmosphere. The *Froude number*

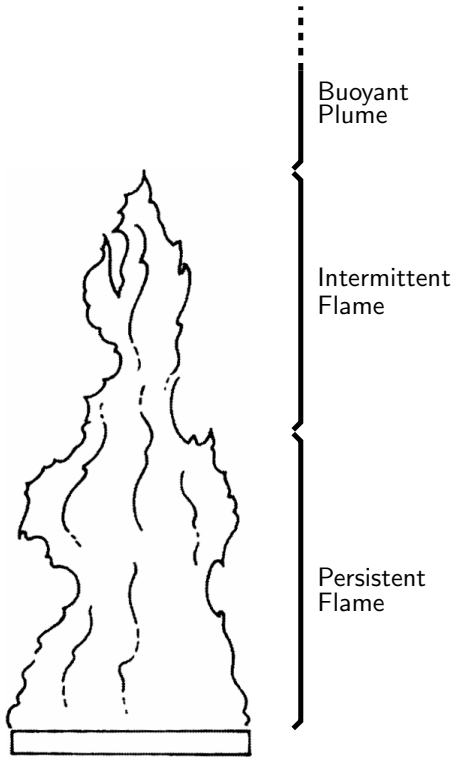

Figure 2.5: Plume structure (Drysdale, 1998)

is the ratio of kinetic forces to buoyancy forces and is approximately equal to 1.5 for this kind of fire.

For a typical fire of this kind, the region above the fire can be split into three zones (Drysdale, 1998). Immediately above the fuel source is a region of *persistent flame*, where vapourising fuel burns continuously. Above this is a region of *intermittent flame*, where partly burnt fuel may ignite sporadically when mixed with fresh oxygen. This is equivalent to the flickering of a candle flame. Finally above this is a region consisting of the hot products of combustion, which is termed a *buoyant plume* (see Figure 2.5).

The structure of the plume is determined by an interaction with the surrounding air. Viscous shear forces resist the relative movement, and cause air to be entrained into the plume (see Figure 2.6). The plume thus gets wider with height, and at the same time the temperature decreases, until the buoyancy force is entirely overcome by viscous drag.

An analytical solution to the conservation equations for an unconfined axisymmetric plume (mass, momentum, energy) is only possible with some simplifying

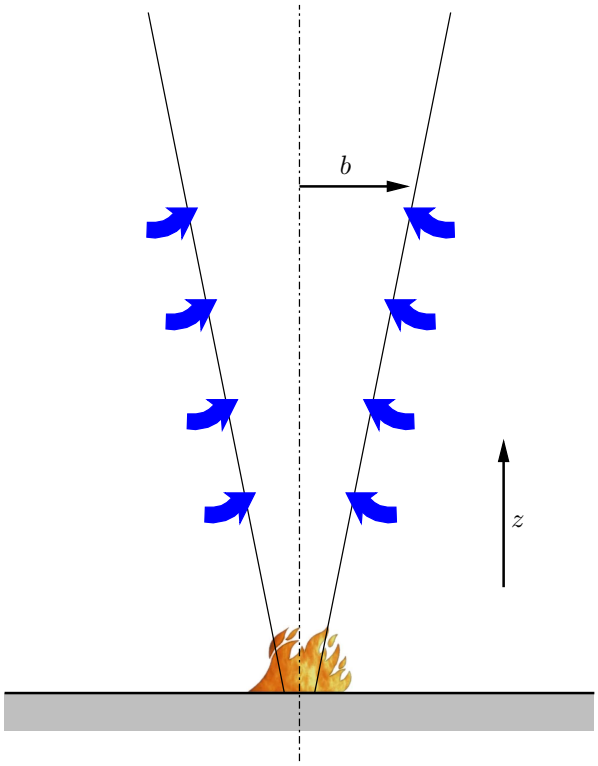

Figure 2.6: The unconfined buoyant plume (Drysdale, 1998)

assumptions, (typically assuming radial distributions of density, temperature, etc.) but leads to widely used relationships.

For example, the plume temperature (assuming $T_\infty = 293\,\mathrm{K}$) is:

$$\Delta T_0 = 26 \frac{\dot{Q}_{\mathrm{conv}}^{\frac{2}{3}}}{z^{\frac{5}{3}}} \tag{2.4}$$

where

z is the height above the fire source and

$\dot{Q}_{\mathrm{conv}}$ is the rate of energy release by convection.

For non point-source fires, a *virtual origin* can be defined as the location of an equivalent point-source fire (Heskestad, 2002a). For flat fire sources,

$$\frac{z_0}{D} = -1.02 + 0.083 \frac{\dot{Q}_{\mathrm{c}}^{\frac{2}{3}}}{D} \tag{2.5}$$

where

z_0 is the virtual origin position (usually negative) (m),

D is the fire diameter (or equivalent) (m) and

$\dot{Q}_c$ is the heat release due to combustion (kW).

Air currents, such as wind or ventilation, and the presence of walls, ceilings, or other obstructions has a significant effect on the behaviour and temperature of a plume. If a fire is close to a wall then there will be a reduction in the volume of air that is entrained, and therefore the plume will not cool so rapidly. It will also cause a deflection of the plume towards the surface, which could cause rapid growth in the fire if the surface is made of some kind of combustible material. If a ceiling is present, the rising plume will be deflected and form a *ceiling jet*, where the hot gases rapidly spread out radially. The rate of entrainment for the ceiling jet is low due to *temperature stratification*. The temperature is highest immediately below the ceiling, and decreases sharply to ambient.

There is a distinct difference between the case of a plume impinging on a ceiling, and the case of the flames themselves reaching the ceiling. In this case the highest temperature will occur close to the fresh air as the combustion continues. Flames spreading along a ceiling are much longer than the corresponding unconfined flame due to the reduced air entrainment.

Walls close to the point of impingement will confine the spread of the ceiling jet/flames. For a fire in the corner of a room, or in a corridor, the flame length can be 12 times longer than the unconfined flame height (Drysdale, 1998).

2.1.5 Ignition and extinction

According to Kanury (2002),

> *Ignition* is defined as the onset or initiation of combustion, usually flaming. As such, ignition is indicated by the oxidation reaction attaining a rapidly increasing rate. The rapidity often makes the ignition phenomenon an abrupt event. In practice, ignition is noted by the appearance of a flame, by a significant increase in oxidative energy release, or by a corresponding large rise in temperature.

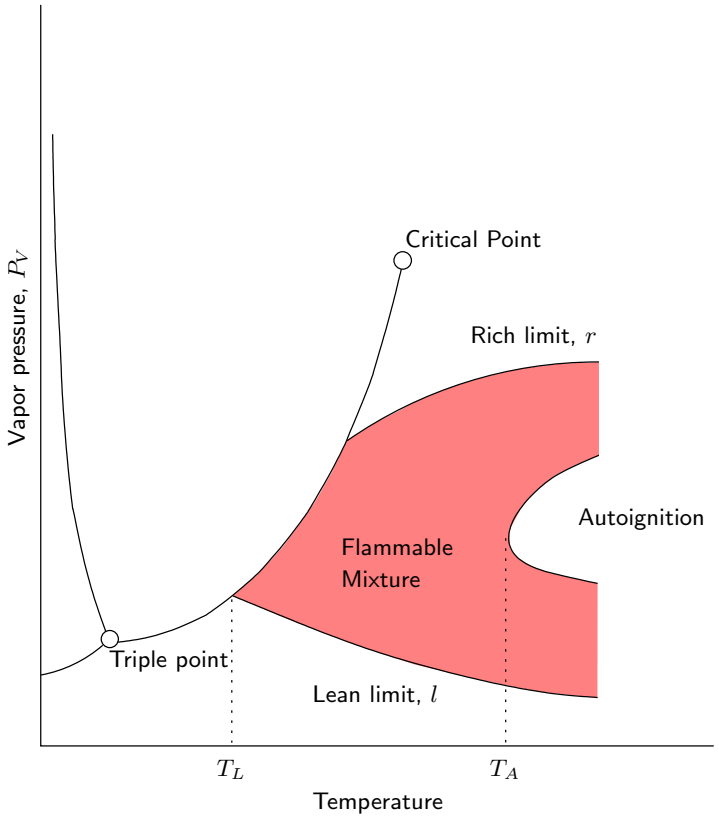

Figure 2.7: Phase-change diagram for a combustible liquid (Drysdale, 1998)

For liquid fuels to ignite, a sufficient quantity of fuel must vaporise, and then mix with the oxidiser (usually air). Finally the reaction must reach a self sustaining level.

Ignition can either be *spontaneous* or *piloted*. With piloted ignition, an external energy input is required to locally heat some of the fuel-air mixture up to the flame temperature. Spontaneous ignition will occur if the temperature exceeds the autoignition temperature (T_A) (see Figure 2.7).

The American National Fire Protection Association standard NFPA 750 (2003) defines extinguishment as "the complete suppression of a fire until there are no burning combustibles". Suppression is merely "the sharp reduction of the rate of heat release of a fire and the prevention of regrowth".

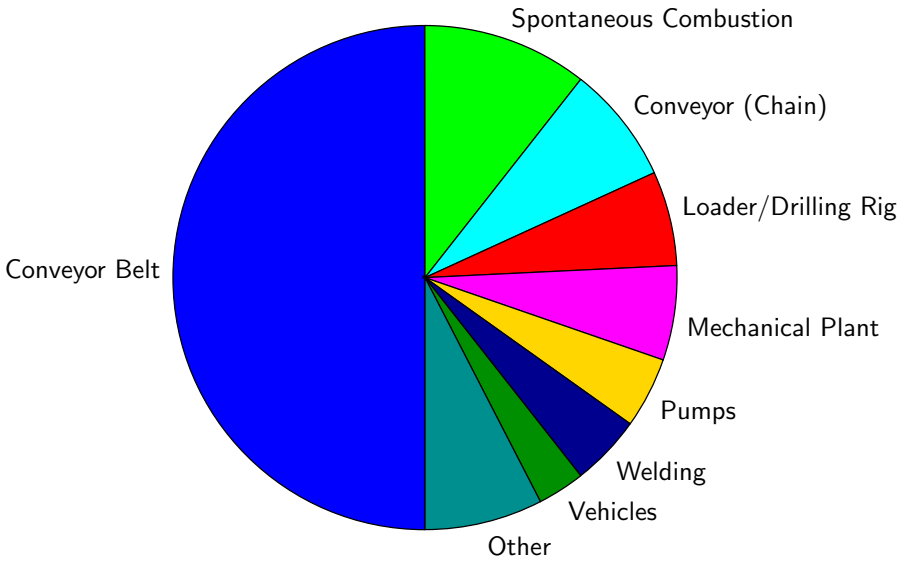

Figure 2.8: Sources of fires in mines for 1989/90 (Bottom and Denton, 1991)

2.2 Fire in tunnels

In this section an overview of tunnel fires is given, including specific hazards, fuel type and ignition-sources present in mining and transportation tunnels, and peculiarities of the behaviour of fires within a tunnel due to the confinement of the tunnel envelope and lateral ventilation.

2.2.1 Mining

The use of tunnels as part of mining operations began in the 18$^{\text{th}}$ century, when the adoption of the room and pillar method, and later other roof support systems, allowed a mine to extend a significant distance from its surface connection. Modern mechanised mining techniques have lead to incredibly extensive underground workings (Silvester, 2002). The former Selby mine complex in Yorkshire consisted of 120 miles (193 km) of underground roadways (Department of Trade and Industry, 2002b), and the Daw Mill Colliery in the Midlands currently has ventilation circuits of over 6 km (3.7 miles) which may increase in length if workings are extended in future (Department of Trade and Industry, 2002a).

Bottom and Denton (1991) presented an analysis of the incidents of fire in UK mines reported to HM Mines Inspector in the period 1950-1990 (See Figure 2.8). Over this period there have been many positive improvements, with certain

classes of fire being virtually eliminated. However, the overall frequency of fires did not decline, despite a sharp reduction in the number of operational mines.

The number of fires related to conveyor belt systems increased, and had reached 50% of all fires by 1990. This rise is primarily due to the high usage of conveyors in modern mines (estimated at 1040 km in 1990). MacMillan (1997) shows that conveyors have remained the dominant cause of mine fires, and despite a reduction in the total number of incidents, the number of incidents *per man shift* has increased.

Conveyor fires can result from friction at idlers (particularly if bearings have failed), friction at the belt-drive (if the belt stalls), or at any point where the belt rubs against a stationary object.

A variety of different fuels have been implicated in conveyor related fires: coal dust, oil, the conveyor belt, waste paper, etc. In many cases environmental monitoring failed to detect the fire.

MacMillan (1997) reports that in 73% of underground incidents, the fire was discovered by personnel rather than automatic monitors. Fires discovered within 15 minutes resulted in minimal damage to infrastructure, whereas those that developed often lead to abandonment of sections of a mine (DMT et al., 2004b). Many small fires were successfully extinguished using hand-held extinguishers.

Deployment of fire detection systems in a mining environment is challenging, due in part to the continuously advancing workings and the varying nature of the fire hazard, but also due to high levels of gases and other contaminants that would not normally be present in the atmosphere.

The most common types of detector are for smoke, carbon monoxide or POC (products of combustion). The suitability of these detectors depends on the type of fire hazard and the location within the ventilation route. Return air may already be contaminated with high or fluctuating levels of carbon monoxide as part of normal mining operations.

The development of new or improved fire detections systems is an area of active research. DMT et al. (2004b) reviews the current state-of-the-art in underground fire detection and emergent technology such as neural networks and cross-correlation of multiple sensor types. Cheng et al. (1999) proposes use of

CCD video cameras sensitive to infra-red radiation to detect flames. Although this would be less prone to variations in the environment, the system would not be well suited to narrow (cluttered) tunnels which would restrict the field of view of each camera.

Unlike civil transportation tunnels, mine tunnels usually form part of a large interconnected network of underground workings. The flow of air to and from a fire in any given tunnel can only be fully determined in the context of this network. Depending on the size and location of the fire, the network flow may be influenced by the fire. According to Wu and Li (1993) the *"resistance in a branch increases with flow temperature, hindering the flow movement. This phenomenon is called the* throttling effect*"*. Additionally any changes in temperature occurring in a *"slope or shaft ... will induce a potential energy change"* called a *fire pressure*. In some cases this could cause air flows to *"decrease rapidly or even reverse"*. As real fires have a heat output that varies significantly over time, this process is dynamic. A sudden unexpected flow-reversal could be catastrophic for any fire fighting personnel attempting to approach or fight a fire.

Example: Fire in UK coal mine, 15th November 2003 At the start of the working day at a small UK coal mine officials noticed that the fire detector in the return drift was in an alarm condition. They traced the source to a burnt out electro-hydraulic loading shovel that had been parked some 10 hours before at the end of the previous working day. They quickly extinguished the remnant fire. The motor cooling fan was heavily contaminated by fine coal soaked in oil emulsion and this appears to have been ignited by frictional heat that had built up by contact with the rotating impeller; any cooling effect being lost when the machine was switched off. The fire eventually spread to the electric cables, hydraulic hoses and three of the shovel's rubber tyres (Health and Safety Executive, 2005).

This kind of minor incident is fairly typical for UK coal mines.

Example: Explosion in Zasyadko mine, Ukraine, 19th August 2001 An explosion of coal dust and methane killed 37 people and hospitalised many more. Ten miners were trapped underground by a large fire triggered by the explosion. Rescue teams were unable to use water to douse the flames for fear of flooding the mine shaft, and any hopes of reaching the miners were eventually abandoned

(BBC News, 2001b).

Ukraine has suffered a spate of serious fires and explosions in recent years. This is attributed to the loss of government subsidies after the collapse of the Soviet Union, and the prioritisation of profit over safety. According to US Energy Information Adminstration (2005) there were 3,500 deaths in 700 separate fires between Ukraine's independence in 1991 and January 2005.

2.2.2 Transportation tunnels

Widespread usage of tunnels for transportation began over 150 years ago, as rail networks were laid out across Europe. The Great Western Railway, linking London to Bristol, was completed in 1841 with the construction of Box Tunnel (3 km) by Brunel. The London Underground Railway was begun not long after in 1863.

Following the success of London, underground railways (or metros) have been built in many other cities and metropolitan areas – Istanbul (1875), Chicago (1892), Budapest and Glasgow (1896), Boston (1897), Paris Métro (1900), and many more. Wikipedia (2004) lists over 150 metro systems in use (or under construction) around the world today.

The term *'metro'* originates from the Parisian *Chemin de Fer Métropolitain*, and is *not entirely synonymous* with the terms 'underground' or 'subway', as it includes ground level and elevated systems as well. In practice most metro systems, however they are named, include a mixture of both above and below ground track – for example, 40% of the New York subway is at (or above) ground level.

The earliest part of London Underground was constructed with 'cut and cover' tunnels immediately below the surface, but from the 1890s construction was switched to deep tunnels, due to the existence of a clay layer around 20 m below the surface. Clay is an ideal material for tunnelling, and switching to that depth allowed firstly for construction without any significant disruption at street level, and secondly for the crossing of the River Thames.

The deep tunnels can be as small as 3.5 m diameter (see Figure 2.9), and are of

Figure 2.9: Typical 'Tube' tunnel: Victoria line at Warren Street stations. Opened 1968

Table 2.3: Comparison of major metro systems (Wikipedia, 2004)

City	Opened	Annual passenger journeys	Number of stations	Length
Moscow	1935	**3.2 billion**	165	265 km
Tokyo	1927	2.7 billion	274	292 km
Seoul	1963	1.6 billion	263	287 km
Mexico City	1969	1.3 billion	175	208 km
New York City	1904	1.3 billion	**468**	368 km
Paris	1900	1.2 billion	369	213 km
London	**1863**	886 million	275	415 km
Munich	1971		229	**527 km**
Berlin	1902		254	473 km
Milan	1964		89	419 km

circular cross-section. This gives rise to the term *'Tube'* which is used colloquially for these sections of the Underground. Unlike the earlier tunnels which were designed for steam trains, the newer tunnels have much fewer ventilation shafts.

According to Transport for London (2005) the London Underground now has 408 km of track (although much of this is not actually underground) and is used for three million journeys every day. Table 2.3 shows a comparison of some of the world's largest metro systems.

Today tunnels are a key part of national and international transportation networks, particularly in mountainous regions – e.g. Lærdal, Norway (24.5 km, 2000) and St. Gotthard, Switzerland (17 km, 1980) – but also as river and sea crossings – e.g. Channel Tunnel (51 km, 1991), Dartford Tunnel (1.4 km, 1963) and Seikan Tunnel (54 km, 1988), although generally bridges are a more economic way of crossing moderate stretches of water.

More recently, tunnels are being proposed as alternatives to constructing roads in environmentally sensitive areas such as Stonehenge (Highways Agency, 1999).

The issue of fires in tunnels has become an important concern due to highly publicised fires in King's Cross Underground Station (1987, 31 deaths), Gotthard Tunnel (2001, 11 deaths), Tauern Tunnel (1999, 12 deaths), Mont Blanc Tunnel (1999, 39 deaths), and the Channel Tunnel (1996) (BBC News, 2000, 2001a; Leitner, 2001). In addition to the human cost of these tragedies, the economic cost of prolonged closures of such critical transport links is not insignificant.

Europe has an extensive network of transportation tunnels, and vehicle fires are not uncommon events (although generally less severe than those listed above). For example, the Gotthard Tunnel in Switzerland experiences an average of four fires per 100 million driven kilometres, whilst the Elbe Tunnel in Hamburg sees an incident virtually every month (Haack, 2002). These statistics are no worse than for the road network in general, and in fact may be slightly better, due to lower speed limits and more predictable driving conditions.

The rate of fires in transportation tunnels is only likely to increase. Both volumes of traffic – particularly the volume of dangerous goods transported – and the number of tunnels in the network is increasing.

Statistics show that for rail tunnels the probability of a fire is 20 to 25 times lower than for road tunnels. This is because many of the hazards of road tunnels – such as driver error, collision between vehicles, and vehicle breakdown – either do not apply to rail tunnels or are vastly reduced. Increasingly, automatic systems are being used to eliminate the 'human factor', and make collisions virtually impossible. For example, as a result of a derailment caused by a drunk driver falling asleep at the controls, and which killed five people, the New York Subway made the decision to convert to a fully automatic system. The transition began in 2005, but is expected to take up to 20 years to complete due to the size of the

network (Associated Press, 2005).

Case study – New York subway fire 7th April 2005 On 7th April, 2005, a fire broke out during routine maintenance of underground electrical equipment. Although there were no fatalities, a number of people were treated for burns and smoke inhalation, and 600 people were evacuated from stranded trains. Additionally, significant disruption was caused to the operation of the Subway system for several hours while the fire was brought under control and the cause investigated (Chan, 2005). Although the cause of the blaze has not been properly established, the New York system uses an aging 600 V DC electrical system that is not renowned for its reliability.

Case study – Mont Blanc fire 24th March 1999 The 11.6 km Mont Blanc tunnel is an important, and busy, arterial link between France and Italy. The single tunnel carries two-way traffic, and has seen a 17-fold increase in the number of goods vehicles since its opening in 1965 (Vuilleumier et al., 2002). On 24th March 1999, a refrigerated lorry carrying nine tons of margarine and 12 tons of flour caught fire. Although the fire was quickly detected by the tunnel authorities, their only effective response was the immediate closure of the tunnel to traffic (Minister of the Interior, 1999). The fire soon spread to involve 23 lorries and 10 cars (Haack, 2002). The fire burned for over two days and killed 39 people.

The initial report for the blaze (Minister of the Interior, 1999) makes harrowing reading. In particular:

- the lorry and its cargo were technically non-hazardous, but both the thermal insulation and the margarine made a significant contribution to the heat and toxicity of the fire.
- many of the tunnel systems, including emergency lighting, CCTV cameras, and communication equipment, failed at an early stage due to the intense heat and were, in any case, inadequate.
- there was a complete lack of communication between the French and Italian ends of the tunnel, who operated independently.
- ventilation was not sufficient to keep the tunnel free of smoke and there was no alternative escape route.

Figure 2.10: Photographs of the Mont Blanc tunnel fire (Minister of the Interior, 1999)

- temperatures reached 1800°C and caused damage to 1 km of the tunnel's physical structure.

This fire is unusual due to the spread of fire between vehicles. There had been 17 other non-catastrophic fires in the same tunnel since its opening, and in most cases portable fire extinguishers were sufficient to bring them under control.

A legal trial is currently in progress to determine responsibility for the disaster. The defendants include Belgian truck driver Gilbert Degrave, the truck manufacturer Volvo of Sweden, the Italian and French companies that manage the tunnel, safety regulators and Michel Charlet, mayor of the nearby town of Chamonix (BBC News, 2005).

Since the fire, a massive amount of money (€380 million) has been spent on upgrading the safety system, including the construction of a subterranean fire station at the middle of the tunnel, and a much greater number of emergency shelters, which are now linked to the under-road ventilation ducts to provide an escape route (see Figure 2.11).

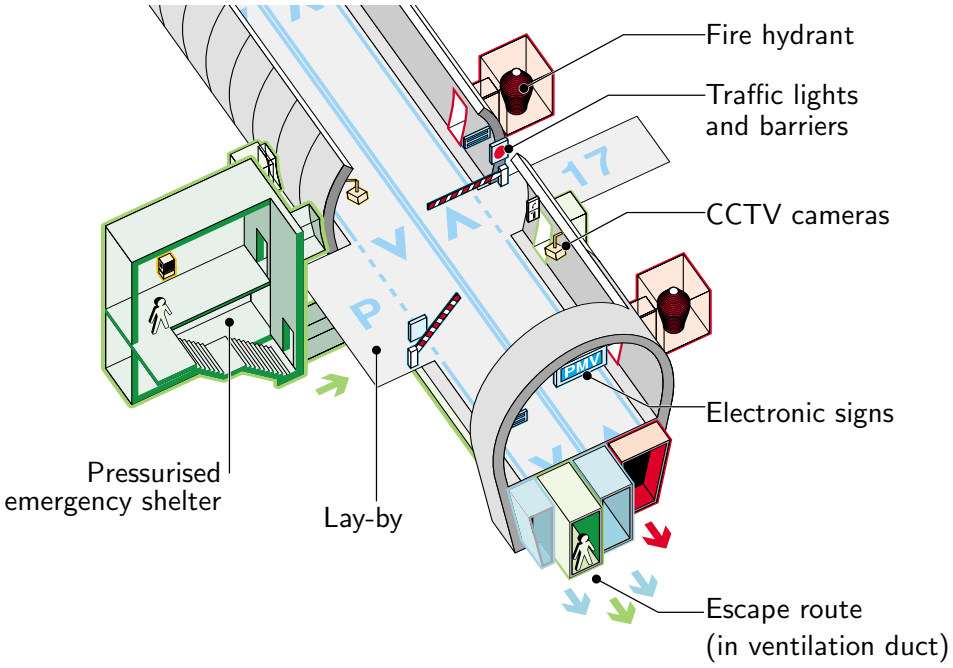

Figure 2.11: Improved safety features and escape route of reopened Mont Blanc tunnel
(adapted from Autoroutes et Tunnel du Mont Blanc, 2003)

2.2.3 Ventilation

The ventilation in a tunnel plays a significant role in the behaviour of a fire. Firstly it supplies the fire with the oxygen it needs to burn, and secondly it controls the movement, stratification and dilution of the smoke and the other hazardous products of combustion. A good understanding of the interaction between ventilation and a fire is therefore vital when developing a fire safety strategy.

Forced ventilation is commonly utilised during tunnel fires in order to control the movement of smoke in order to maintain safe escape routes for the tunnel's occupants and/or rescue personnel (Modic, 2003). This strategy is often prescribed by health and safety legislation, although tunnel operators (particularly when the tunnel is in use by the public) will consider human safety a high priority anyhow (Gabay, 2002). The movement of smoke against the direction of net ventilation is called back-layering, or reverse stratification. To avoid this, the ventilation rate needs to be large enough that no smoke is able to move upstream of the fire.

Wu and Bakar (2000) define the *critical velocity* as:

the minimum air velocity required to suppress the smoke spreading against the longitudinal ventilation flow during tunnel fire situations.

The critical velocity varies with the size of the fire, the size of the tunnel, and also with the shape of the cross-section and the slope of the tunnel. Experiments by Wu and Bakar (2000) have shown that for sufficiently large fires, the critical velocity is independent of the fire size. They propose the following relationship between non-dimensional fire size, Q'', and non-dimensional ventilation rate, V'':

$$\begin{aligned} V'' &= 0.4[0.2]^{-1/3}[Q'']^{1/3}\,, & Q'' \leq 0.2 \\ V'' &= 0.4\,, & Q'' > 0.2 \end{aligned} \tag{2.6}$$

where

$$\begin{aligned} Q'' &= \frac{Q}{\rho_0 C_p T_0 \sqrt{g\bar{H}^5}} \\ V'' &= \frac{V}{\sqrt{g\bar{H}}} \end{aligned}$$

and

- Q and V are the heat release rate and ventilation velocity
- $\bar{H}$ is the 'hydraulic tunnel height' (four times area divided by perimeter).
- ρ_0 and T_0 are the ambient density and temperature
- g is the acceleration due to gravity.
- C_p is the specific heat capacity of air.

This result is primarily obtained from small-scale (250 mm high tunnel) experiments, using a propane burner to represent a fire. They also show that data from other well known full-scale tests (e.g. Eureka, Memorial, etc.) is consistent with their result.

The difference between the two regimes is a result of the structure of a fire plume and its interaction with the tunnel boundary. The constant critical velocity corresponds to fire where the flames (either intermittent of persistent) reach the ceiling of the tunnel (see Figure 2.12 and compare with Figure 2.5)

Hwang and Edwards (2005) uses CFD techniques to further investigate the rela-

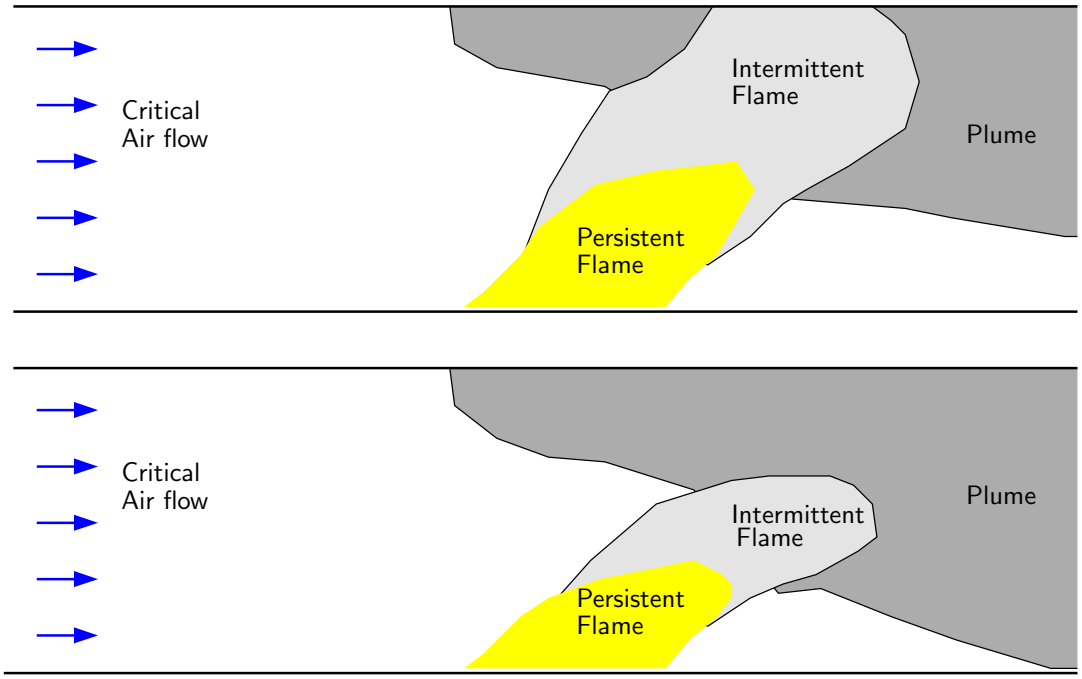

Figure 2.12: Plume geometry within tunnel
(Adapted from Wu and Bakar, 2000)

tionship of critical velocity and fire size. Their results broadly agree with Equation 2.6 but they prefer to explain the transition in terms of temperature stratification rather than the plume structure. It is not clear what the actual distinction is between the two explanations.

Carvel et al. (2001a,b) investigated the effect of forced ventilation on the rate of combustion and fire spread for different types of fire. The study highlights that for some fires, increased ventilation will provide a greater supply of oxygen and thus increase the rate of burning. For other fires, the ventilation will have a cooling effect which will reduce the severity of the fire, or perhaps put the fire out entirely. In the study, the factor k was defined to be the ratio of the heat release rate (HRR) in forced ventilation to the HRR of a similar fire in natural ventilation (see Figure 2.13).

Due to the lack of suitable experimental data (i.e. where the same test had been carried out in natural ventilation and over a range of forced ventilation rates) great lengths are taken to combine data from a range of sources. Froude number scaling, independent expert opinion, and *Bayesian* statistical analysis are all used to draw the maximum information out of the limited data available. There is a fair amount of estimation and assumption, and a reliance on data from significantly

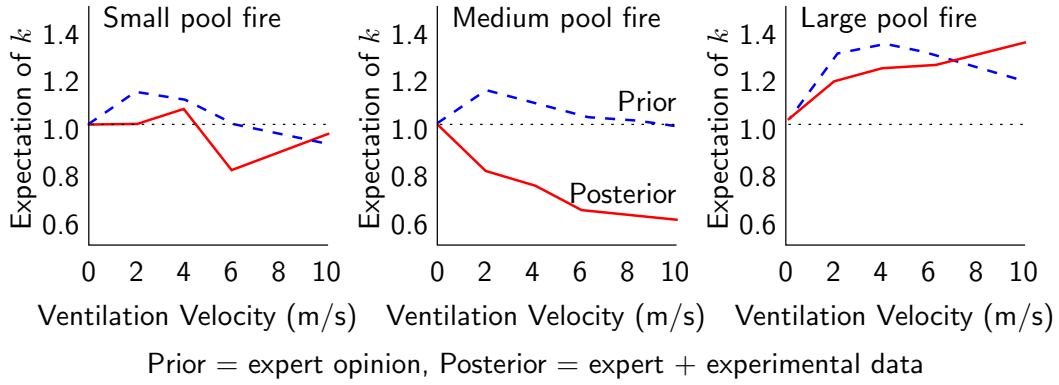

Prior = expert opinion, Posterior = expert + experimental data

Figure 2.13: Variation of fire heat release with ventilation velocity for pool fires (Carvel et al., 2001a)

different experiments. This mainly highlights the need for a systematic series of experimentation, and the inaccuracy of expert opinion.

Bettis et al. (1993) and Lea et al. (1997) investigated the extent of back flow from a fire on board a HGV being carried by a Channel Tunnel train using one-third scale experiments and CFD modelling.

There are some important difference between civil transportation tunnels and mine tunnels when it comes to using ventilation to control a fire.

Firstly, in a mine, the emphasis will be on isolating the fire from the unaffected area of the mine, rather then keeping escape routes clear. Mine personnel are well trained and equipped with breathing apparatus that can (to a limited extent) cope with smoke. Serious mine fires are often fuel-rich and therefore limiting the oxygen supply is essential if the fire is to remain controllable.

Secondly, the complexity of a mine ventilation network, and the generally limited information available about the size and location of the fire make decisions about ventilation strategy difficult to make.

Computer software such as MFS (Mine Fire Simulator) or MFIRE (Mine Fire) use 1D network models combined with simple fire models (typically taken as constant or heat release proportional to air-supply) to predict the air-flow and spread of POC within a mine. As these models are capable of running in less than real-time (Walla et al., 1995) they have the potential to be used during an actually incident, and certainly for planning and training purposes (Laage and Yang, 1995). Obviously to be useful during a live incident, an up-to-date survey

of the ventilation system is required along with environmental monitoring both inside and outside the mine.

2.2.3.1 Other considerations

The extent of back-layering observed in experiments is strongly influenced by the slope of a tunnel. In DMT et al. (2004a), tests carried out in sloping fire galleries showed very little back-layering with an upward slope (wrt. ventilation), but a much larger back-layering for downward slopes. This has a corresponding effect on the critical ventilation velocity.

2.3 Models

2.3.1 Zone models

Zone models take a vastly simplified representation of the geometry and physics of a particular scenario. They are popular with engineers because they provide instant results which are invaluable for iterative design. For this reason, the published models tend to deal with issues such as smoke filling (Delichatsios, 2003; Mowrer, 1999) for determining evacuation time and ceiling temperatures (Nam, 2004) for predicting sprinkler activation.

The degree of uncertainty inherent in the simplified physics or geometry can be compensated for by a large factor of safety.

Kunsch (2002) proposes a zone model of a fire plume in a ventilation tunnel. This yields an analytical formula for the critical ventilation velocity which is similar in form to that derived experimentally by Wu and Bakar (2000). Kurioka et al. (2003) derives a model for the shape of the plume from a square fire in a ventilated tunnel. This is limited to stratified air flows.

A variety of software packages for tunnel and tunnel network ventilation simulations exists and can be applied to fire safety problems: “Road Tunnel Ventilation and Fire Simulation Software” (Modic, 2003), MFIRE (Laage and Yang, 1995), and MFS (Mine Fire Simulator) (Walla et al., 1995). These are generally based

on a one-dimensional view of the fluid flow (i.e. a single value of pressure, temperature and velocity represents the entire flow at each cross-section) and as such cannot represent stratification, backflow or near field effects.

2.4 Field models

Field models attempt to represent the real geometry and physics of a particular scenario. Most field models are based on CFD techniques, which are outlined in Chapter 4. Examples of CFD models of fires, and in particular tunnel fires, from the published literature are given in Section 4.10.

2.5 Summary

There is nothing intrinsic about tunnels that makes the risk of a fire occurring any greater than anywhere else. The semi-enclosed nature of a tunnel results in a fire that behaves differently from either an enclosed or an open-space fire, and this must be taken into account in any fire-safety/fire-fighting strategy. Regrettably the nature of a tunnel means that the hazard represented by an uncontrolled fire is potentially quite large and this has led to a number of well publicised tragedies (as well as a number of not so well publicised near misses). Finally, the economic costs of closing a transportation tunnel or mine cannot be ignored, and any effective fire prevention or fire suppression scheme can be expected to pay for itself.

It goes without saying that any fire suppression system merely mitigates the effects of a fire, and fire *prevention* will also have a big impact on overall safety. This includes enforcing speed limits, maintaining equipment, particularly conveyors, restrictions on hazardous goods and materials, and so forth. Nevertheless, not all fires are preventable, so in the next chapter, methods of fire fighting are examined, particularly with respect to their applicability to tunnel fires.

Chapter 3

Firefighting

This chapter reviews existing firefighting practise – in particular the use of water mist as a fire suppression system – and presents a synopsis of relevant theoretical and numerical analyses, and experimental data available in the published literature.

3.1 Fire fighting methods

There are a wide variety of different methods in use to combat and suppress fires. Conceptually, most of these operate, either by removing one of the elements of the 'fire triangle' – fuel, oxidiser or heat (see Figure 2.1 in Section 2.1), or by disrupting the chemical reaction between the fuel and oxidiser.

The installation of fixed fire suppression systems in buildings and other spaces is often mandated by health and safety legislation, the local fire authority, insurers or other regulators. In other cases it may be installed simply out of prudence by the building operator. A summary of the various kinds of fire suppression system is provided below. Each system has unique advantages and disadvantages, particularly concerning the type of fires they are effective against. Many of the systems below are also in use in portable hand-held fire extinguishers.

Water sprinklers are one of the most commonly used fixed-installation fire suppression systems. The effectiveness of water as a suppression agent is primarily due to its high thermal capacity (see Figure 3.1). According to

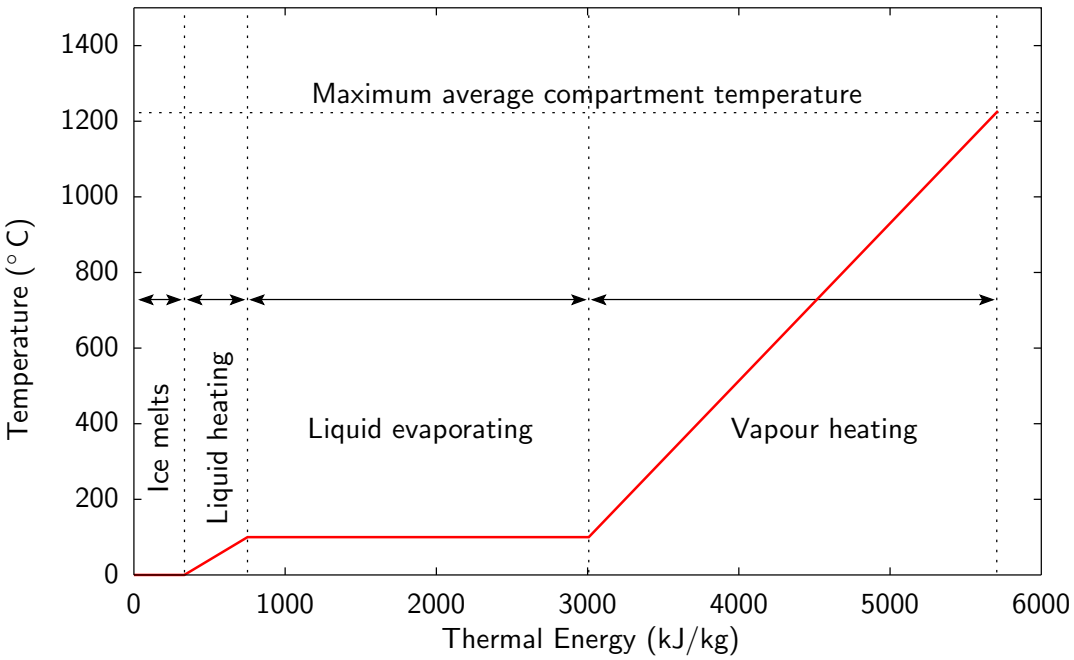

Figure 3.1: Thermal energy capacity of water with temperature (Grant et al., 2000)

Grant et al. (2000) the important suppression mechanisms are: cooling the fuel surface; cooling the flame zone; and volumetric displacement of the oxidant. In addition pre-wetting of adjacent combustible surfaces may help reduce the rate of growth of a fire.

Design standards such as BS 9251:2005 (2005) give detailed requirements for the design and installation of sprinkler systems for various different classes of building. For residential and commercial buildings, wet pipe systems are used (i.e. the supply pipework always contains water) with individually thermally activated sprinkler heads. These typically contain a glass bulb that shatters at elevated temperatures releasing water although other kinds of activation valve exist.

For a typical residential/domestic sprinkler system:

- activation is usually at 57 °C
- minimum flow rate of 60 l/min per sprinkler
- water supply capable of maintaining four active sprinklers for 30 minutes

Other types of building require a more detailed appraisal of the fire hazard, and the design of a sprinkler installation will depend on many factors such as

the amount of stored flammable materials, risk to human personnel and the presence of items such as hot oil baths, exposed electrical systems etc, which in combination with a sprinkler systems are hazardous (BS 5306-2:1990, 1990). In mines and industrial buildings a manually activated system may be preferred. This is known as a deluge system, because all sprinkler heads on the same water supply circuit activate simultaneously.

One of the main disadvantages of water sprinklers is the large quantity of water used. This can lead to extensive damage beyond that caused by the fire itself, and for mine tunnels could result in flooding.

Halon can be used either in hand-held fire extinguishers, or as a total flooding agent in enclosures, such as computer rooms, ship engine rooms, and submarines where a rapid quenching is desirable, or where other systems such as water are unsuitable.

Halogen compounds such as Halon-1301 ($CBrClF_2$) and Halon-1211 ($CBrF_3$) are very effective fire suppression agents because they inhibit the combustion reaction itself rather then attempting to cool the fire, or dilute the oxygen/fuel. This means halon can be effective at concentrations as low as 2.9%–7% by volume. They are generally non-toxic and can be used on many classes of fires, with the main exception being metal fires.

At high temperatures, the halons decompose into radicals that readily combine with the hydrogen radicals that are intermediates in the combustion mechanism (McCall et al., 1997).

Unfortunately it is the same property that has led to the banning of halons. In the upper-atmosphere, ultra-violet light causes the break-up of the halon to free-radicals that are able to react with ozone. Since the Montreal Protocol (United Nations Environment Programme, 2000), halon uses have been phased out, and atmospheric emissions should *not exceed zero* by 2010.

Carbon dioxide can also be used as a total flooding agent, but in comparison to Halon requires much higher concentrations (see Figure 3.2) to be effective, typically 34% by volume or higher (BS 5306-4:2001, 2001). At these levels it can cause death by respiratory paralysis (Wikipedia, 2004), and so is not suitable for occupied spaces. It is suitable for most liquid surface fires, electrical fires, and deep-seated 'smouldering' fires. Carbon dioxide is not suitable in areas that may contain an explosive atmosphere because it is known to produce electrostatic charges (BS 5306-4:2001, 2001).

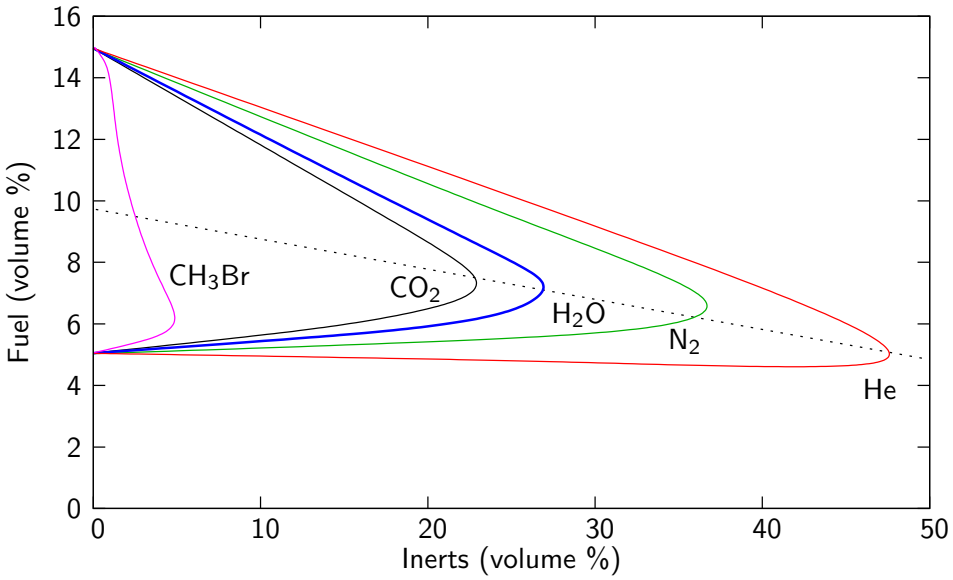

Figure 3.2: Flammability limits of various methane/air/inert gas mixtures at atmospheric pressure and 26°C (Drysdale, 1998)

Powder and Foam systems operate by coating the burning object in a blanket of the powder or foam and hence smothering the fire by preventing oxygen reaching the fuel. They are effective against liquid pools or large solids, and unlike halon or carbon dioxide do not require an enclosure to be effective (BS 5306-6:1988, 1988). They are often used in vehicle fires and are well known for their use by airport fire fighters. In mining, foam has the advantage that it can be applied through a temporary borehole sunk from the surface down to a tunnel that is no longer approachable due to the fire.

Fire dams, doors, stoppings or sluice gates can be used to isolate a section of tunnel and therefore sever the oxygen supply to a fire. This technique is sometimes used as a last resort for large uncontrollable mine fires. Tan (2002) suggests use of a similar technique in civilian transportation tunnels. This would require gates placed every 300 to 500 m along the tunnel, and the gates themselves would need to be heat proof and failsafe. No indication is given of how effective the technique might be.

Inert gas generation According to Dziurzyński et al. (1997) a device based on a turbo-jet engine has been successfully used to fight mine fires in Czechoslovakia, Poland and South Africa. The principle is simple: a burner is placed on the intake side of the tunnel network containing the fire. Water is fed into the jet exhaust. This produces a large volume of 'air' containing virtually no oxygen (See Figure 3.3 and Table 3.1). The system may need to be

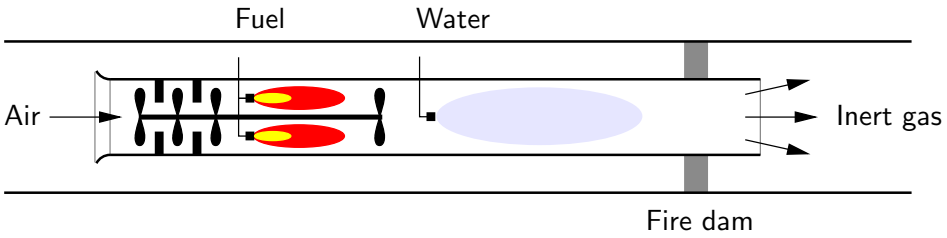

Figure 3.3: Schematics of GAG-3A inert gas generator

Flow rate	100,000 m^3/h
Water consumption	65 m^3/h
Fuel consumption	3 m^3/h
Gas composition	
- Nitrogen	44.93 %
- Carbon Dioxide	5.42 %
- Oxygen	0.82 %
- Carbon Monoxide	0.17 %
- Water vapour	44.82 %

Table 3.1: Inert gas produced by GAG-3A generator

applied for several hours in order for the temperatures to reduce sufficiently to prevent reignition and requires huge quantities of fuel and water. It is therefore only practical for large fires and in situations where it is possible to swamp the air supply to the fire location by use of the turbo-jet.

3.2 Mist

The interest in water mist as a fire fighting technology has been driven by its potential as a replacement for environmentally harmful halon-based systems which have now been banned.

Much of the research that has been carried out over the last decade concentrates on nautical applications (e.g Back III et al. (2000); Bill et al. (1997)). This is due to a strong interest from the US Navy and US Army (on the military side) and the International Maritime Organisation (IMO) and the US Coastguard (on the civilian side), and in particular for engine rooms and on submarines where minimal water usage is essential.

There are other areas of interest include aircraft engine nacelles (Disimile et al.,

2005), Chinese restaurants (Liu et al., 2004), and historic buildings and museums (Log and Cannon-Brookes, 1995).

A general design method is not yet recognized for water mist protection systems (BS ISO/TR 13387-7:1999, 1999), and any formal guidelines, such as NFPA 750 (2003), tend to refer designers to *'manufacturers' information'*.

A related application of water mist is for the mitigation of methane explosions in mine workings (Parra et al., 2004). In this usage, the mist is applied continuously, in order to prevent any deflagration or detonation wave from propagating.

3.2.1 Definition of water mist

Water mist has either been defined as a water spray where:

- 99% of the volume is droplets with a diameter below 1000 µm (Dvorjetski and Greenberg, 2004; Heskestad, 2003; NFPA 750, 2003).
- the mean diameter is 80–200 µm and 99% of the volume is below 500 µm diameter (Grant et al., 2000).

or

- the median droplet size is below 100 µm (Lentati and Chelliah, 1998).

The first definition is mainly intended to distinguish water mist systems from traditional sprinklers, whereas the other definitions are based on the droplet sizes required for an effective system.

3.2.2 Mechanism of extinction

The effectiveness of water mist as a fire fighting agent is easily demonstrated however there seems to be little consensus over the mechanism by which extinction is achieved. A number of different processes have been highlighted by researchers in the field. It seems the dominant mechanism depends on the type of fire (e.g. fuel type, fire size, degree of enclosure, etc.) and nature of the mist system (e.g.

droplet size, pressure, etc.) For example, Parra et al. (2004) concludes that oxygen dilution is most significant for deflagration mitigation, and gas-phase cooling for detonation mitigation.

Oxygen Dilution - The kinetics of the combustion reaction means that there is a *limiting oxygen concentration* (or LOC) below which the reaction is inviable. (The LOC is around 13% for most fuels) (Back III et al., 2000).

Oxygen dilution can occur on either a global or local manner. Local oxygen dilution occurs when water droplets are entrained into the reaction volume, where the evaporation of the droplet produces a volume of water vapour several orders of magnitude greater than the liquid droplet. This disrupts the entrainment of oxygen into the flame.

In other cases, typically for enclosures, the evaporation of the mist may have a significant effect on the oxygen concentration reaching the fire. In the absence of an enclosure, or where the enclosure is large compared to the size of the fire, the effectiveness of water mist is reduced (Bill et al., 1997). Global oxygen dilution is limited by the mean compartment temperature due to saturation (see Figure 3.4), so is more effective against large (relative to the enclosure volume) fires (Back III et al., 2000).

Gas phase cooling - Liquid water has a large latent heat (2270 kJ/kg) and water vapour has a higher specific heat than other atmospheric gases. The evaporation of mist will significantly reduce air temperatures. Even if this occurs outside the combustion region it can have a significant effect on the dynamics of a fire. For solid fuel and liquid pool fires, it is the feedback of heat from the fire that causes volatilization of the fuel. Significant cooling of the fuel can occur even when there is minimal penetration of the mist into the fire plume (Downie et al., 1995).

As a secondary effect, the production of soot is lessened by the reduction in temperature. This is important as radiation from hot soot particles is a significant form of heat feedback.

Fuel cooling - For solid fuels, water droplets reaching the solid surface will cool the fuel. This can reduce the rate of fuel volatilization and/or prevent the spread of the fire. Note, the droplet diameter has a significant impact on the ability of mist to reach the seat of a fire – small droplets evaporate faster, and have lower terminal velocities, so will generally not penetrate as far as larger droplets.

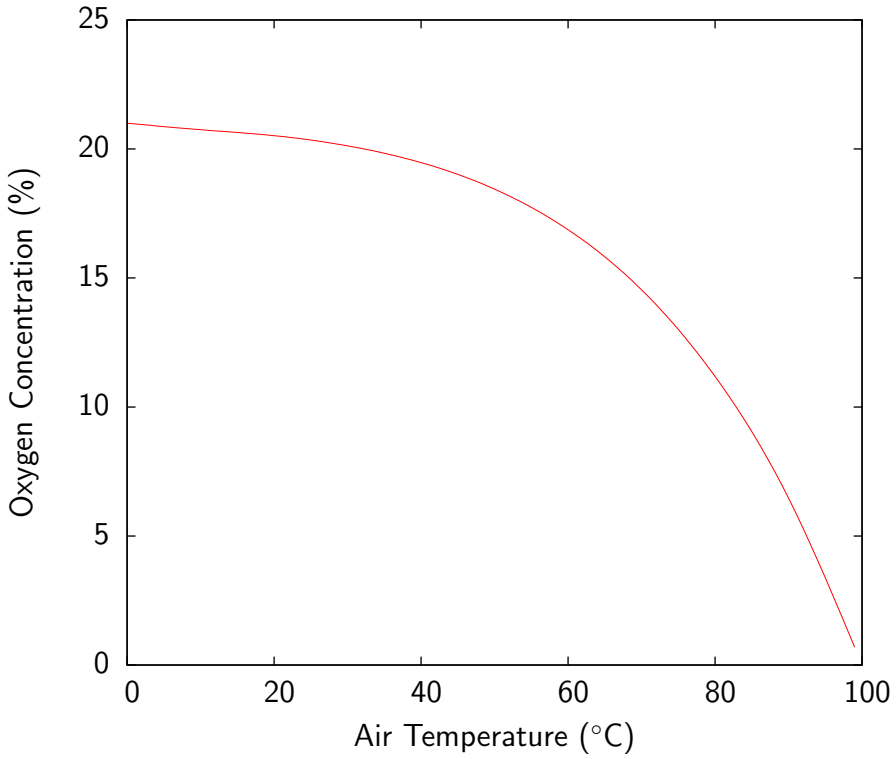

Figure 3.4: Oxygen concentration in air saturated with water vapour (Back III et al., 2000)

In certain circumstances, it may be undesirable for mist to reach the fire source. For example, splashing of liquid fuels can enhance combustion (Qin et al., 2004), and for operating electrical equipment or hot engines/turbines exposure to water and rapid cooling can have other dangerous consequences.

Attenuation of radiation - To sustain the supply of fuel, a fire is reliant on feedback of heat from the flame. The phenomenon of *flashover* occurs when the radiant intensity is sufficient to cause ignition of fuel remote from the initial fire.

It is plausible therefore to suggest that the attenuation and scattering of radiation by water droplets may inhibit the growth and spread of fire. According to Jiang et al. (2004), this method is rarely sufficient to extinguish a fire, and as water absorbs radiation only at particular wavelengths *"most of the black-body energy is not accessible for absorption"* (Yang et al., 2004).

In other cases however, the radiative heating of the droplets may cause them to fully evaporate *before entering the flame*, and hence make the mist much less effective Yang et al. (2004).

Disruption of air flow - the injection of water mist into a volume of air can

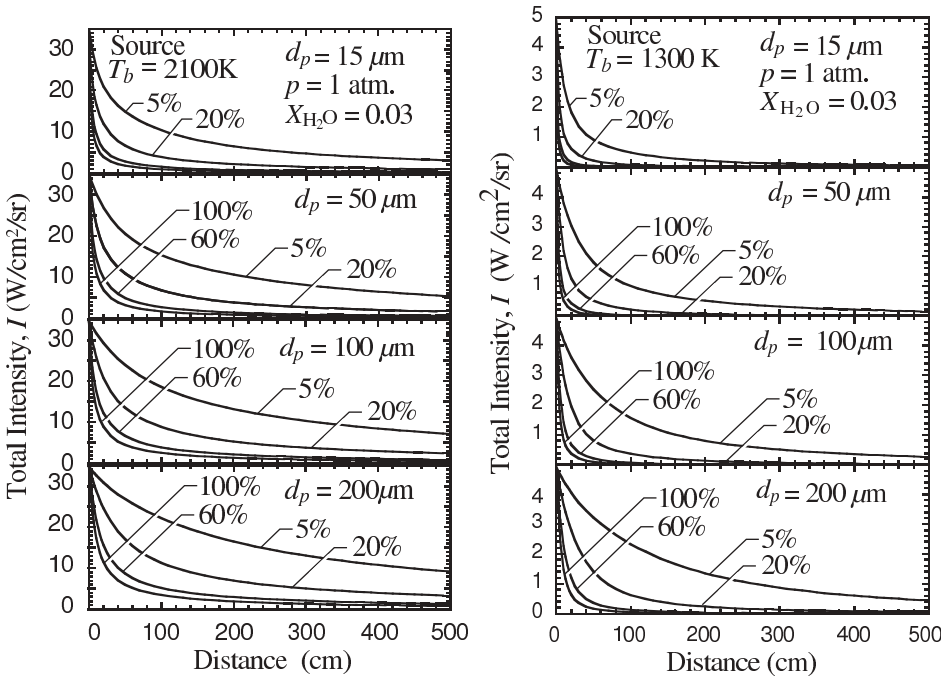

Figure 3.5: The attenuation of radiation from a black-body source of 2100 K and 1300 K as it passes through a slab of mist of various droplet sizes and liquid water loadings (Yang et al., 2004)
A water loading of 100% means equal masses of liquid and air. In all cases $T = 300$ K and $p = 1$ atm with 3% water vapour.

have two effects on the air flow. Firstly the momentum of the droplets can be transfered to the air (i.e. air is entrained into the mist) and secondly, the mist can cool the air altering the buoyant flow. In cases where the fire is ventilation controlled (fuel rich) this could have a knock-on effect on the rate of combustion. Experiments by Qin et al. (2004) showed an initial increase in rate of reaction after activation of water mist before extinction.

Modification to combustion mechanism - there is some evidence to suggest that the presence of water vapour in the reaction zone provides an additional source of hydroxyl radicals. This *may* lead to a reduction in soot production and hence heat feedback (Richard et al., 2003b).

3.2.3 Mechanism of transport

An important aspect of the behaviour of water mist unrelated to the mechanisms of extinction listed above is its ability to be transported and dispersed by air. For small diameter droplets, the magnitude of aerodynamic drag is large relative

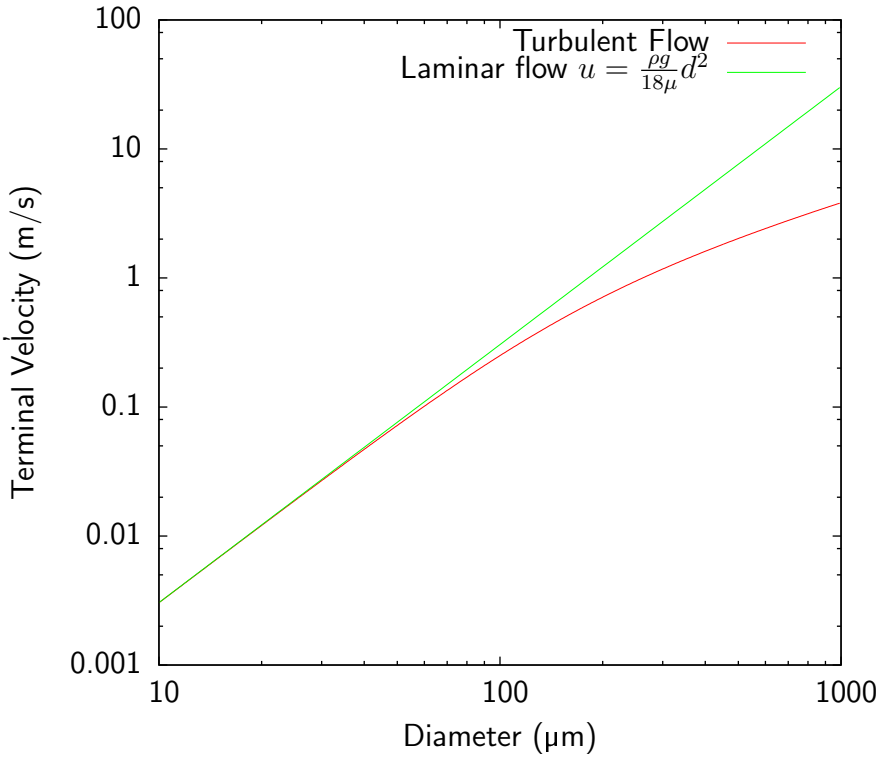

Figure 3.6: Terminal velocity for isolated spherical particles in stationary air at STP

to gravity and inertia. For example, the terminal velocity of a water droplet is roughly proportional to diameter squared (see Figure 3.6) and hence is much lower for mist droplets ($d \approx 100\,\mu m$) than for sprinkler droplets ($d \approx 1000\,\mu m$). This allows mist to remain airborne for long periods of time.

Furthermore the influence of the air flow is much more pronounced for small droplets. This allows convection currents to carry droplets towards a fire, and for turbulence in the air to disperse them throughout a volume.

3.2.4 Effect of enclosure

Water mist has successfully been tested on enclosure fires (Adiga, 2004; Back III et al., 2000; Kim and Ryou, 2003) and effectively unenclosed fires (Xishi et al., 2002). For enclosed spaces, the *degree of enclosure* – both in terms of the ventilation rate and the total enclosed volume – is significant to the performance of a WMFSS.

Back III et al. (2000) carried out tests in enclosures with various ventilation conditions including air-tight, naturally ventilated and with forced ventilation rates up to 15 air changes per hour. They used enclosures ranging in size from $100\,m^3$ to $1000\,m^3$. They conclude that increasing the rate of ventilation decreases the effectiveness of the oxygen depletion mechanism, and therefore increases the reliance on gas-phase cooling. This results in very poor performance on small and/or obstructed fires where little mist reaches the combustion volume. The maximum ventilation rate they investigate (15 air changes per hour in a $1000\,m^3$ enclosure) corresponds to a volumetric air flow rate of $4.17\,m^3/s$, which is significantly less than even a modest ventilation flow in a tunnel.

This would suggest that, in a tunnel, gas phase cooling will be the dominant effect of water mist. However, in the uniaxial ventilation regime of a tunnel the possibility of the air flow, and therefore the water mist, bypassing a fire is much reduced. The difficulty in reaching small fires is likely to be less severe than for a ventilated enclosures.

3.2.5 Nozzles and injection systems

Nozzles (or atomisers) are used to break-up a continuous flow of liquid into a spray of droplets. Nozzles are used in a variety of applications such as: fuel injection in diesel engines, gas turbines and rockets; crop spraying; drug delivery by inhalation; and evaporative cooling, as well as many others. Simple nozzles are also found in the home in the form of shower heads, garden sprinklers and cans of hair spray.

The basic functions of a nozzle are:

1. Control of liquid flow
2. Atomisation of liquid into droplets
3. Dispersal of droplets in a specific pattern
4. Generation of hydraulic momentum

(Delavan, 2005)

The wide range of application and function have given rise to many different designs for commercially available nozzles. In applications such as spray painting, uniformity of coverage is paramount, whereas in agricultural crop spraying small droplets are to be avoided because they can drift too far downwind. In other cases a nozzle must be able to produce a good quality spray over a large range of flow rates.

Most nozzles operate either on a single fluid – where the fluid's own kinetic energy is harnessed to break it up – or use a secondary fluid (typically compressed air) to accelerate and break-up the first (see Figure 3.7). In the latter case, the fluids can either be mixed internally, as in Figure 3.7 or can be injected concentrically.

Generally the break-up of the fluid occurs *after* leaving the nozzle as a result of aerodynamic drag or hydrodynamic instability. Lefebvre (1989, Chapter 2) provides a detailed discussion of these break-up processes. The role of the nozzle is simply to produce a jet of fluid with the necessary turbulence and velocity profile to achieve break-up in the desired manner.

The characteristics of a spray produced by a particular nozzle vary with the operating pressure. Flow rate is proportional to the square-root of pressure, and (as a rule of thumb) droplet size is inversely proportional to pressure to the power 0.3 (Grant et al., 2000).

$$Q = k\sqrt{p_1} \tag{3.1}$$

$$\frac{D_{30_1}}{D_{30_2}} = \left(\frac{p_2}{p_1}\right)^{0.3} \tag{3.2}$$

where

Q is the volumetric water flow rate (m^3/s),

p_i is the operating pressure of the nozzle (Pa),

D_{30_i} is the mean droplet diameter[1] corresponding to p_i (m), and

k is a property of the nozzle referred to as the k-factor. Values of k are often given in trade catalogues (and even academic literature) without stating units, which can lead to confu-

[1] see Section 3.2.7.1 and Equation 3.8 for an explanation of the various mean diameters

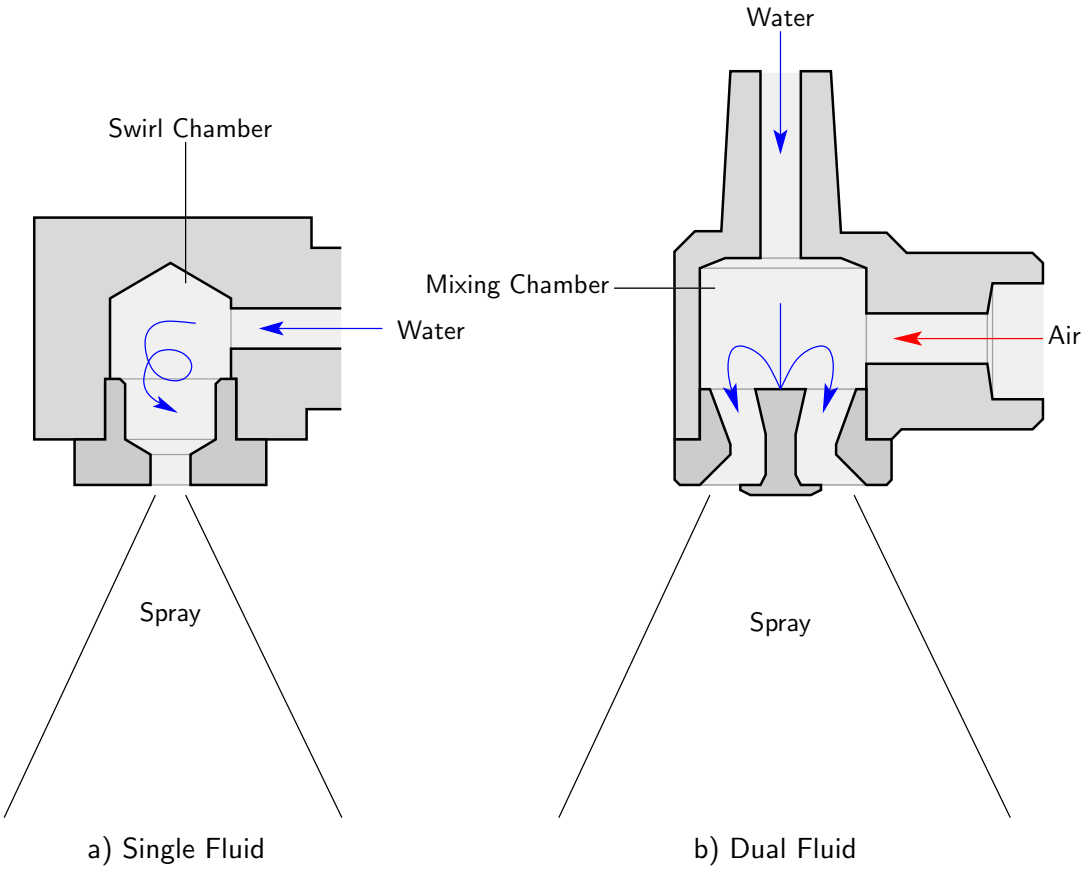

Figure 3.7: Basic nozzle types
(adapted from Delavan, 2005)

sion. In SI, the units of k are:

$$k = \frac{[\mathrm{m}^3/\mathrm{s}]}{\sqrt{[\mathrm{kg}/\mathrm{ms}^2]}} = [\mathrm{m}^{3.5}\mathrm{kg}^{-0.5}]$$

but it is often given in $[\mathrm{gallon}/\mathrm{min}/\sqrt{\mathrm{psi}}]$ or $[\mathrm{l}/\mathrm{min}/\sqrt{\mathrm{bar}}]$.

At high pressures, the relationship between droplet size and pressure is more complex than the rule of thumb given in Equation 3.2 – typically there is a much less significant decrease in diameter by further increasing pressure (Delavan, 2005; Husted et al., 2004).

Invariably when multiple design criteria are in place, there is a trade-off between how well each can be achieved. For example, solid-cone nozzles use an additional axial jet to 'fill the gap' in a hollow-cone. Whilst providing a more uniform angular distribution, it tends to lead to a bimodal size distribution with large droplets in the centre of the spray. Similarly ultrasonic and electrostatic nozzles

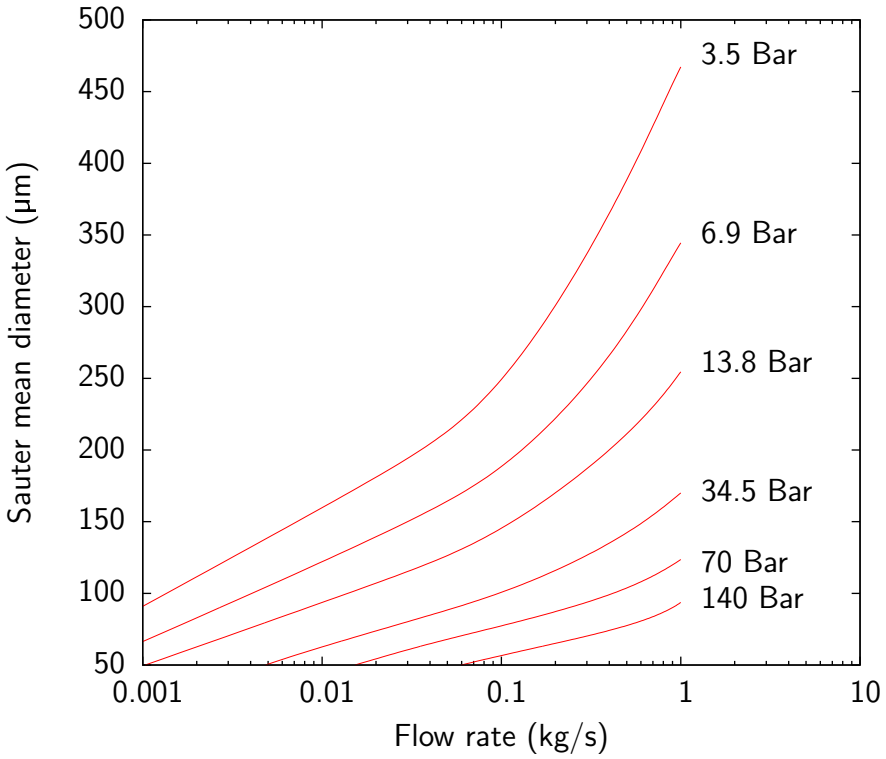

Figure 3.8: Typical droplet sizes for 80° hollow cone atomizer at different pressures and flow rate. (Delavan, 2005)

can produce very fine droplets but only at limited flow rates.

For water mist fire suppression systems, reliability and serviceability are clearly paramount, and whilst the flow rate will remain constant, the nozzles should remain functional over a range of temperatures. Nozzles containing moving parts, such as pressure valves (e.g. duplex nozzles) or rotating discs are to be avoided.

3.2.6 Droplet sizes

The purpose of the nozzles in a water mist system is to convert a continuous flow of water into discrete fragments or droplets (see Section 3.2.5). The physical processes involved are (partly) non-deterministic, and will therefore lead to droplets with a random distribution of sizes and velocities.

There is a *finite maximum* and *non-zero minimum* limit to the sizes produced – large droplets tend to be broken up by aerodynamic forces, whilst small droplets are relatively stable due to surface tension (Babinsky and Sojka, 2002).

There are two main modes of break-up: *bag break-up* and *stripping break-up*. In *bag break-up*, a single droplet splits into two or more droplets of comparable size. In *stripping break-up* small droplets break away from the surface of a large droplet. Parra et al. (2004) define break-up criterion in terms of the Weber number and the Eötvös number:

$$\text{Weber} = \frac{\text{drag force}}{\text{surface tension}} = \frac{\rho(u-u_d)^2 D}{\sigma} \tag{3.3}$$

$$\text{Eötvös} = \frac{\text{acceleration force}}{\text{surface tension}} = \frac{\rho_d \frac{\mathrm{d}u}{\mathrm{d}t} D^2}{\sigma} \tag{3.4}$$

where

ρ and ρ_d are the air and droplet densities,

σ and D are the surface tension and diameter of the droplet and

$(u - u_d)$ is the relative velocity of the droplet.

Bag break-up occurs for Weber number greater than 12, or Eötvös number greater than 16 and stripping break-up for $\frac{\text{We}}{\text{Re}^{\frac{1}{2}}} > 0.5$ and $\text{Eo} > 100$.

Husted et al. (2004) defines four separate droplet break-up regimes (see Figure 3.9) with the type of break-up being determined by the Reynolds number and Ohnesorge number of the nozzle:

Rayleigh break-up – droplets form far away from nozzle, and are bigger than the diameter of the nozzle (Figure 3.9a)

First wind-induced break-up – droplets form several nozzle diameters downstream and have diameters similar to the nozzle (Figure 3.9b)

Second wind-induced break-up – break-up begins a short distance downstream, and droplets are smaller than nozzle (Figure 3.9c)

Atomisation – Droplet formation takes place at the exit from the nozzle. The diameters are *much* smaller than the hole in the nozzle. (Figure 3.9d)

The Ohnesorge number is the ratio of viscous forces to surface tension for a stream of fluid:

$$\text{Ohnesorge} = \frac{\text{viscous forces}}{\text{surface tension}} = \frac{\mu}{\sqrt{\rho\sigma D}} \tag{3.5}$$

The break-up process will be influenced by changes in temperature, which could vary quite significantly in a fire scenario. Surface tension tends to decrease as temperature increases leading to smaller droplets (Lefebvre, 1989). The viscosity of water also reduces significantly (Rogers and Mayhew, 1995). This reduces the effect of turbulence leading to larger drops, but also affects the way water flows through the nozzle, the effect of which depends on the nozzle type – typically altering the cone angle, or in extreme cases causes the cone to collapse into a stream of large droplets.

For single fluid nozzles, the ambient air conditions, particularly the air density, which influences drag will have an effect. This is less significant for dual fluid nozzles.

For the purpose of analysis, a mist may be considered to be *monodisperse* (where all the droplets are the same size) or *polydisperse*.

3.2.7 Droplet size distributions

It is sometimes useful to describe the distribution of droplet sizes in a spray in terms of an idealised droplet size distribution. This could facilitate comparison between different sprays; theoretical analyses; algebraic manipulation; and interpolation/extrapolation of data.

A variety of model droplet size distributions are in common use, and are either *empirical* (e.g. Rosin-Rammler, log-normal, root-normal, etc.) or *analytical* (e.g. Maximum Entropy, and Discrete Probability Function). Analytical approaches are based on conservation of mass, momentum, surface energy, kinetic energy. Detailed descriptions of these distributions are available in text books and the literature (Babinsky and Sojka, 2002; Crowe et al., 1998).

The empirical methods are most flexible as they can be fitted to virtually any dataset. It can however be difficult to determine the values for the model parameters, particularly for the more complex distributions which tend to suffer from numerical instability.

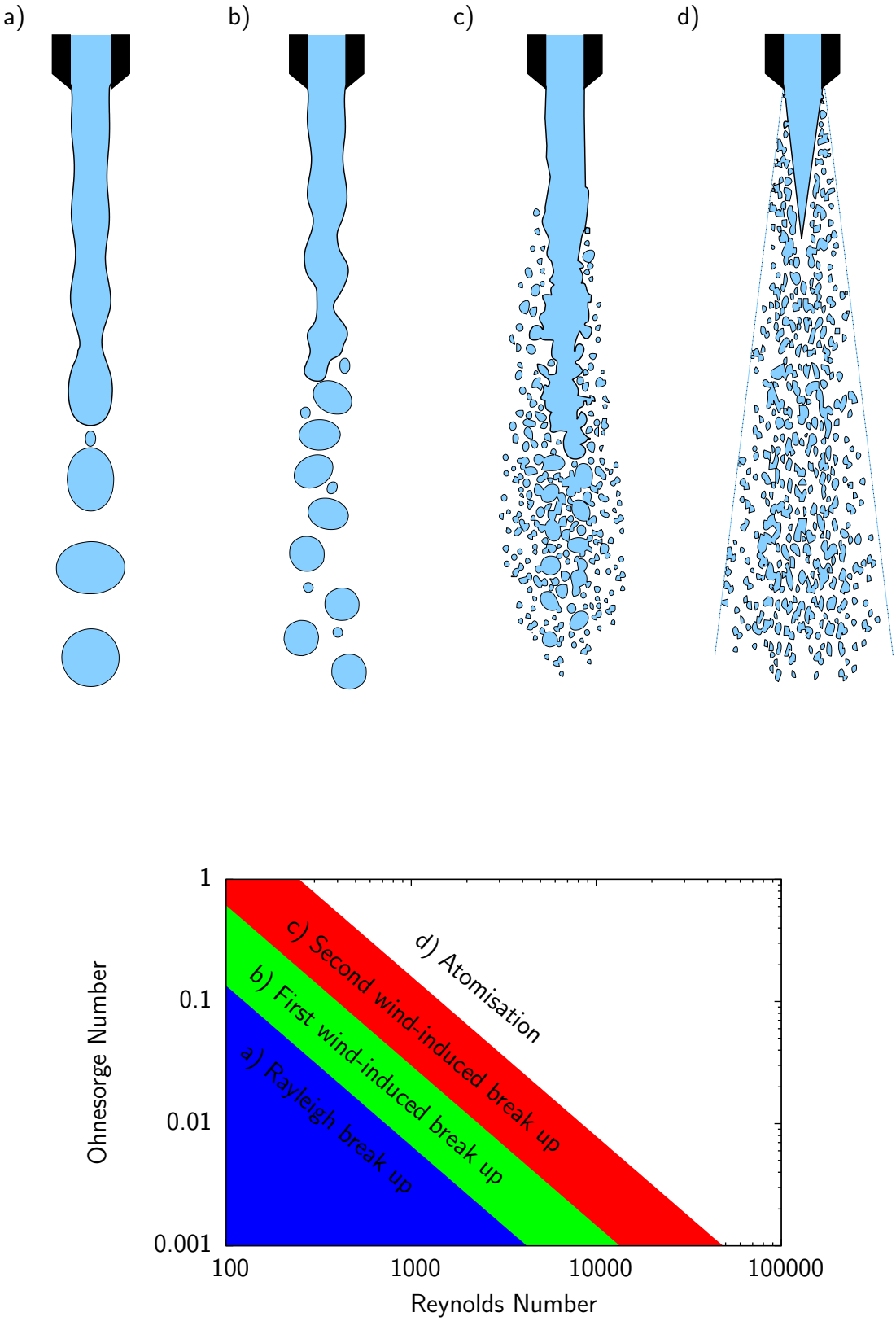

Figure 3.9: Fluid break-up regimes (Husted et al., 2004; Lefebvre, 1989)

The analytical methods are of benefit where no detailed data are available, however their use is not simple, and the have not yet seen widespread adoption or acceptance in the literature.

A particular distribution is often chosen for its ease of use rather than its ability to represent the real droplet size distribution.

One of the most widespread model distributions is the Rosin-Rammler distribution (Crowe et al., 1998; Fluent, 2002; Lefebvre, 1989):

$$Y(d) = 1 - e^{-(\frac{d}{\bar{d}})^n} \tag{3.6}$$

where

$Y(d)$ is the cumulative volume of drops with diameter less than d,

$\bar{d}$ is an 'average' diameter (by definition, 63.2% of the spray volume is droplets smaller than $\bar{d}$, as $Y(d = \bar{d}) = 1 - e^{-1}$) and

n is a measure of the spread of drop sizes. For most sprays n lies between 1.5 and 4 (Lefebvre, 1989).

A droplet size distribution can be expressed in terms of volume, surface area, or number (i.e. count). When fitting a dataset to a distribution, it is therefore important to choose a form appropriate to the source of the data, and the intended application of the model distribution. Figure 3.10 shows a measured droplet distribution and two Rosin-Rammler distributions. In the first case the fit is carried out on the derived cumulative volume, whereas in the second the fit is carried out directly on the droplet counts. Crowe et al. (1998) uses the gradient of a log-log plot of the cumulative mass distribution to obtain n, and then $\bar{d}$ can be found from

$$\bar{d} = \frac{D_{mM}}{0.693^{\frac{1}{n}}} \tag{3.7}$$

where D_{mM} is the mass median diameter.

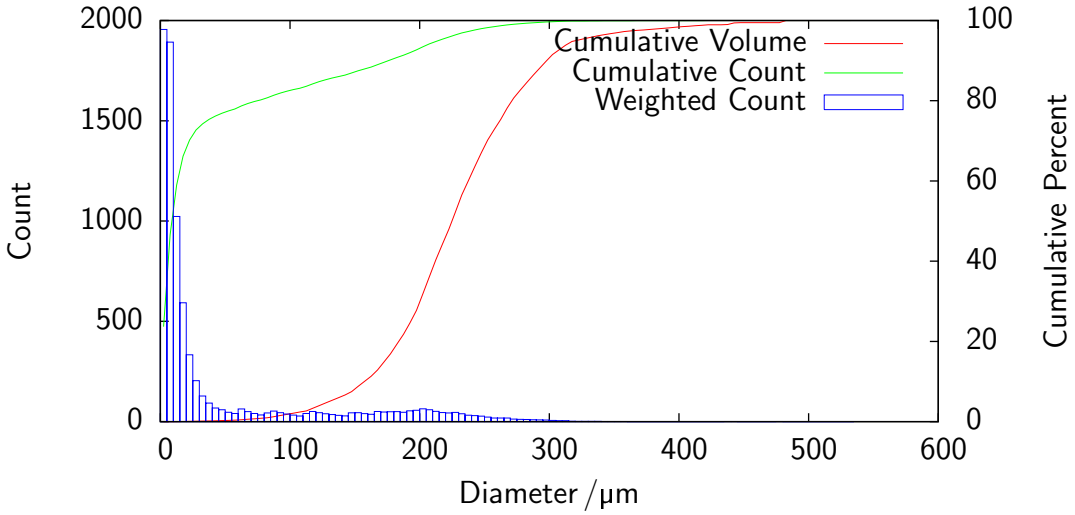

a) Real nozzle – Tyco AM4 *AquaMist*® Open Nozzle (Tyco, 2005)

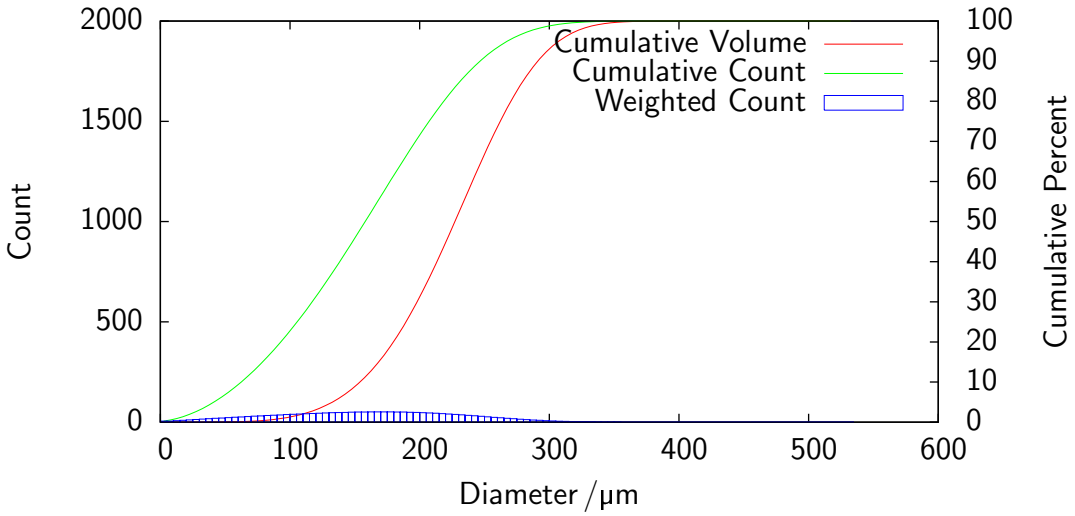

b) Rosin-Rammler fitted to cumulative volume ($\bar{d} = 245\,\mu m$, $n = 4.843$)

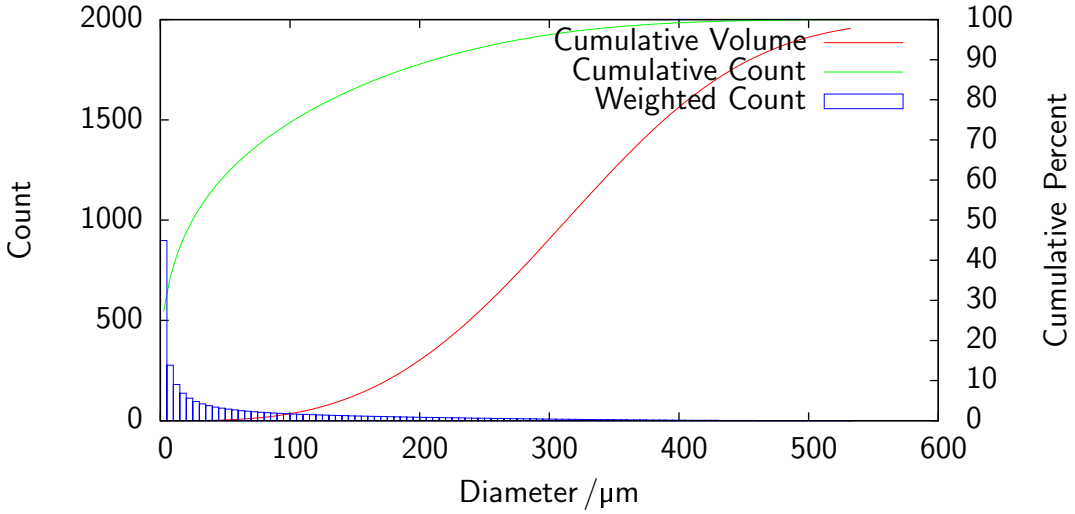

c) Rosin-Rammler fitted to count ($\bar{d} = 351\,\mu m$, $n = 3.219$)

Figure 3.10: Typical droplet size distribution

3.2.7.1 Representative diameters

Given a distribution of droplet sizes, $f(D)$, it is possible to calculate various *representative diameters* using Equation 3.8 (Babinsky and Sojka, 2002).

$$D_{pq} = \left[\frac{\int_0^\infty D^p f(D)\mathrm{d}D}{\int_0^\infty D^q f(D)\mathrm{d}D}\right]^{\frac{1}{(p-q)}} \tag{3.8}$$

where p and q are typically positive integers. There are a number of commonly used means:

D_{10}	Arithmetic Mean Diameter
D_{20}	Area Mean Diameter
D_{30}	Volume Mean Diameter
D_{32}	Sauter Mean Diameter
D_{43}	de Brouckere Mean Diameter

The Sauter Mean Diameter (SMD) is the diameter that corresponds to the mean surface-to-volume ratio (i.e. the total surface area of a volume of mist can be calculated directly from the SMD). This is relevant for heat transfer applications.

The de Brouckere Mean Diameter, or Mass Moment Diameter is relevant for chemical equilibrium or combustion applications.

3.2.8 Effect of initial droplet size distribution

Dvorjetski and Greenberg (2004) consider the hypothetical scenario of water spray extinction of laminar opposed flow diffusion flames. A flow of fuel from one direction meets a flow of oxidiser from the opposite direction. There is a stagnation point where the two streams meet, and combustion occurs on the oxidiser side of this, at a point determined by the stoichiometry of the reaction under consideration. The water droplets form part of the oxidiser stream, and begin to evaporate at an (unknown) point upstream of the flame front (See Figure 3.11).

The simplicity of the scenario (one-dimensional, absence of turbulence and gravi-

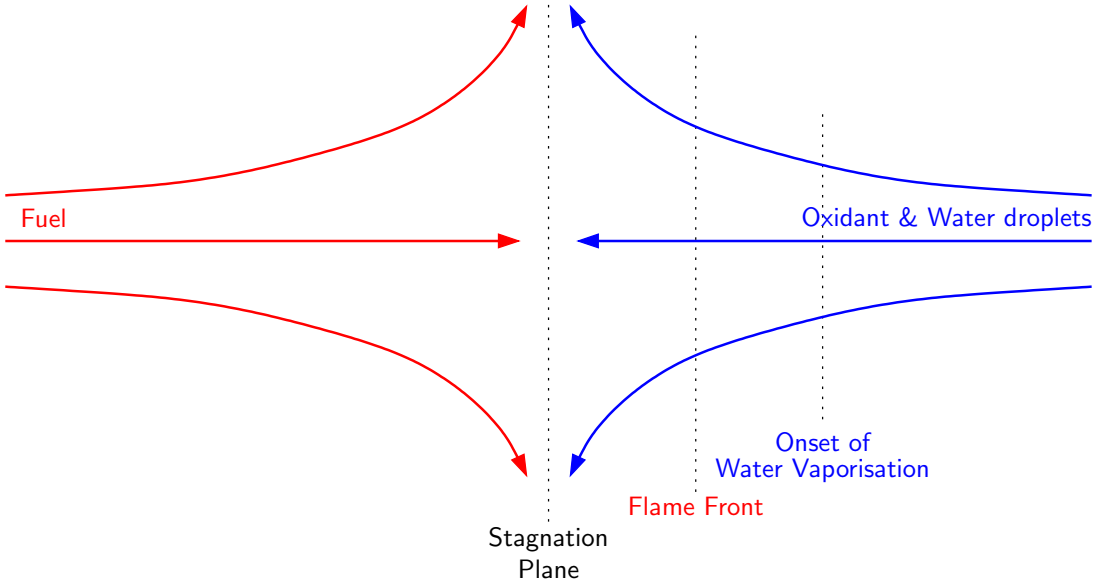

Figure 3.11: Laminar opposed flow combustion (Dvorjetski and Greenberg, 2004)

tation, single-step Arrhenius reaction, constant fluid properties, etc.) means that an analytical solution is possible (but not by any means simple).

The domain of the problem is split into four regions, $\mathfrak{R}_1$ (from $-\infty$ to the stagnation point), $\mathfrak{R}_2$ (from the stagnation point to the flame front), $\mathfrak{R}_3$ (from the flame to the point of onset of evaporation) and $\mathfrak{R}_4$ (from onset of evaporation to $+\infty$). Appropriate differential equations, boundary conditions and matching conditions are setup and solved.

The water mist is represented by splitting the droplet size distribution into N_s sections. During evaporation a droplet is progressively demoted through the various classes. This approach allows the mist to be represented in an Eulerian formulation, without the need to "track" individual droplets.

The analytical solution is then applied to six different initial droplet size distributions. The first three all have a Sauter Mean Diameter (D_{32}) of 44.8 µm, and the remaining three have the same area mean diameter (D_{20}) of 34.4 µm. Each set contains a monodisperse, bimodal, and full-polydisperse distributions.

Their results show that the monodisperse mist is more effective at reducing temperatures or causing extinction. The maximum variation in their results is around 18%, although generally the variation is much lower.

It is not clear, from this hypothetical case, how significant the choice of initial droplet size distribution would be when considering real-world scenarios. On the one hand, given the level of uncertainty and variation inherent in more complex scenarios, the small variations caused by the droplet size distribution are probably insignificant. On the other hand, given that droplet size has a significant effect on trajectory (which is irrelevant in the hypothetical scenario), the effect *could be* much stronger.

3.2.9 Cycling application

Liu et al. (1999) compared the performance of a continuous application of water mist with a cycling system, where the mist was activated for 50 s and then deactivated for 20 s.

They found for small easily extinguishable fires, there was little difference in performance between the two systems, although the cycling system used less water. For larger shielded fires, which were problematic for the continuous system, extinction times were significantly reduced. (e.g. from 300 s to 115 s for a 0.3 m heptane pool fire.)

Jozefowicz (2004) also reported that a 'pulsed' application seemed to give enhanced performance, and was able to extinguish fires more reliably, or from a greater distance than with continuous application.

3.3 Experimental data

Table 3.2 and Table 3.3 summarise the experimental water mist studies available in the literature. Experimental studies can be loosely divided into full-scale and small-scale tests. Generally speaking small-scale tests are designed to investigate the mechanisms of water mist action (such as effect of water vapour on the combustion reaction, penetration of mist into a flame, etc.) and are not intended to be realistic fire scenarios. Full-scale tests on the other hand, are generally based on real world scenarios (such as engine rooms, turbine halls, offices, hospital wards, and other room-like enclosures).

Reference	Fire	Enclosure	Ventilation	Nozzles	Mist	
Back III et al. (2000)	Hydrocarbon	100-750 m^3	4 m^2			
Bill et al. (1997)	6 MW Diesel spray/ 1 MW 'Shielded' Diesel spray/ 2 m^2 wood crib + kerosene	2800 m^2×18 m 188 m^2×5 m	4 m^2	90× 12 lpm or 5.3 lpm	300 µm 90 µm	[a]
Downie et al. (1995)	26.5, 40.0, & 53.0 kW Natural Gas	2 m × 2 m × 2 m	low	1× 0.78 lpm	260 µm	[b]
Heskestad (2003)	methane/heptane 1.1 kW-262 kW	n/a	n/a	1× 0.1-2.4 lpm	165-330 µm	[c]
Kim and Ryou (2003)	Methanol/Hexane	4 × 4 × 2.3 m	none	5 × 6 lpm	121µm	[d]

Table 3.2: Summary of full-scale experimental data

[a] Mock-up engine room - Extinction only in smaller enclosure
[b] Not designed to cause extinction.
[c] Open-space, 3 scales.
[d] See Section 7.1

Reference	Fire	Geometry	Ventilation	Nozzles	Mist	
Jiang et al. (2004)	PMMA	–	low/high	Water vapour		[a]
Ndubizu et al. (1998)	Methane	2D diffusion	coflow	Devalan@5 bar	50 µm	
Qin et al. (2004)	100mm^2 Peanut oil	0.6 m × 0.6 m × 0.7 m		6 bar	100 µm	–
Loomis and McPherson (1995)	coal	0.3 m × 0.3 m × 9 m	–[b]	2.22 lpm		

Table 3.3: Summary of small-scale experimental data

[a] Detailed analysis of combustion products to assess effect of water vapour on reaction mechanism
[b] Mist applied well upstream of fire source

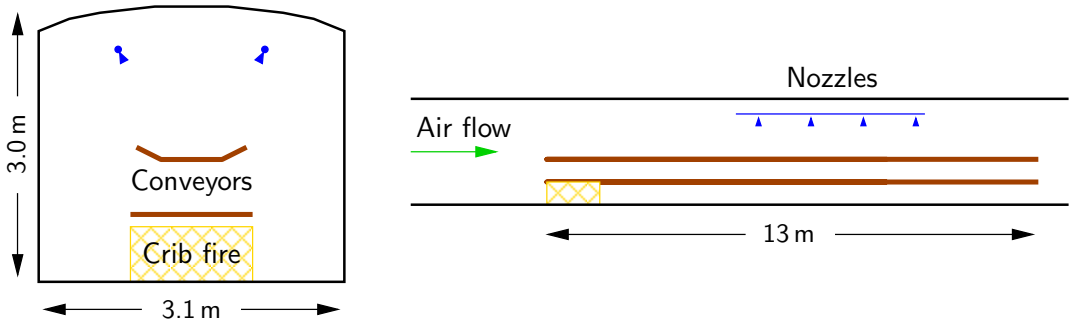

Figure 3.12: Schematic of DMT tunnel water mist tests (DMT et al., 2004b)

The experimental study by Kim and Ryou (2003) is used in Chapter 5 and Section 7.1 as the basis for a CFD model of an enclosure fire. This study was selected for a number of reasons. Firstly it is comparatively well controlled – for example, by using a contained pool fire, zero ventilation, and a regular and uncluttered enclosure. Secondly, the study was performed at full scale, and hence avoids any of the issues associated with scaling of results. Finally, the published paper concisely provides most of the details needed to create a representative CFD model.

3.3.1 Use of mist in tunnels

The only known experimental testing of water mist in tunnels was carried out in Germany by DMT as part of the same European Coal and Steel Community (ECSC) project that funded this PhD research. The results of this study are reported in DMT et al. (2004b). The tests used a pair of conveyor belts arranged one above the other (this is typical in German mines) as the fire source. Ignition was achieved by a 150 kg wooden crib located at one end of the conveyors (see Figure 3.12). Water mist was supplied by two rows of four nozzles located 2.5 m above the tunnel floor (1.2 m above the upper belt) and approximately 1.5 m apart. Typically each nozzle had a flow rate of 10 lpm (0.17 kg/s), although 6 lpm and 20 lpm nozzles were also tested.

Tests were performed with ventilation at 1.2 m/s and 2.4 m/s, and a variety of nozzle orientations. Results indicated that extinction was harder to achieve at higher ventilation rates. The upper conveyor shielded the lower from the mist, however with careful adjustment of the nozzle angle, it was possibly to increase the amount of mist reaching the lower belt and achieve suppression even at the

higher velocities and/or lower water flow rates.

Unfortunately the only data recorded for each test is whether suppression was achieved, and no information is available regarding the time for extinction or other details of the suppression behaviour.

3.3.2 Scaling

It is not possible to *rigorously* apply a scientific scaling procedure in order to carry out fire experiments at small scales, as there are two many non-dimensional quantities that should be preserved – Froude Number, Reynolds Number, Non-dimensional fire size, Rayleigh Number, and so on. In fact, according to Williams (2003) when considering combustion phenomena there are *30 [potential dimensionless] groups, and scaling keeping all of theses groups constant is manifestly impossible.*

A more limited scaling procedure may be carried out if the dominant groups can be identified by a consideration of the controlling mechanisms (e.g. by assuming convection is the important heat transfer mechanism).

This can be used to compare experimental results carried out on similar (but not identical) scales. For example HSE used a $\frac{1}{3}$ scale model of the escalator fire at King's Cross (Simcox et al., 1992).

For water mist extinction of pool fires, the scaling factors shown in Table 3.4 have been used by Heskestad (2003). These are difficult to achieve in practice, particularly the combination of drop diameter, drop velocity and water flux.

3.4 Models

3.4.1 Zone models

Zone models take a vastly simplified representation of the geometry and physics of a particular scenario.

Table 3.4: Experimental scaling factors (Heskestad, 2003)

Parameter	Scaling Factor
Length	$L_2/L_1 = S^1$
Heat release rate	$Q_2/Q_1 = S^{5/2}$
Temperature	$\Delta T_2/\Delta T_1 = S^0$
Gas concentration	$C_{i2}/C_{i1} = S^0$
Ventilation rate	$\dot{V}_2/\dot{V}_1 = S^{5/2}$
Time	$t_2/t_1 = S^{1/2}$
Water flow rate	$Q_{w2}/Q_{w1} = S^{5/2}$
Drop diameter	$d_2/d_1 = S^{1/2}$
Initial drop velocity	$u_{p_2}/u_{p_1} = S^{1/2}$
Water flux	$F_2/F_1 = S^{1/2}$
Volumetric water concentration	$C_{w2}/C_{w1} = S^0$

Back III et al. (2000), develops a model of the water mist suppression of a compartment fire. It is assumed that the mechanism of extinction is due to *global oxygen depletion/dilution*, and that the compartment is *well mixed* – i.e. at uniform temperature and humidity. These assumptions are based on results from a range of IMO (International Maritime Organisation) standard tests, where it was observed that the worst case scenario was an "obstructed" fire. In many other cases, the water mist was much more effective than the model predicts.

3.5 Field models

Field models attempt to represent the real geometry and physics of a particular scenario. Most field models are based on CFD techniques, which are outlined in Chapter 4. Examples of CFD models of water mist fire suppression for the published literature are given in Section 4.10.

3.6 Summary

There are several different fire suppression systems in current usage, which is not surprising given the variety that exists in the nature of fire and the environments in which fires must be tackled. The emergence of water mist as a replacement for environmentally damaging (and now outlawed) Halon systems has also created a

potential technology to improve safety.

Unfortunately there is a limited understanding of how such a system would behave, and there are obvious difficulties associated with developing and testing a prototype system on real fires. In Chapter 4 computational techniques that could be utilised to establish the effectiveness of water mist in a ventilated tunnel, and to determine the operational parameters of such a system are described.

Chapter 4

Basis of CFD techniques

This chapter provides an overview of the *Computational Fluid Dynamics* (CFD) techniques that are used in subsequent chapters to model the physical processes involved in a tunnel fire and water mist suppression. Some of the details and models presented in this chapter relate specifically to the *Fluent* CFD code, as that is used for the majority of the subsequent work.

The equations of fluid dynamics, and the numerical algorithms required to solve them, have been well known for centuries. However it was not until the development of the digital computer several decades ago that it became feasible to model the behaviour of fluids.

As the power of computers has continuously increased (Moore, 1965) and the understanding of fluid dynamics, and computational algorithms has improved, the range of applications that can be modelled has also increased. The application of CFD to fire safety problems began in the 1980s, most notably in the UK with the analysis of the King's Cross fire of 1987 (Simcox et al., 1992), but has become both more sophisticated and, with the rise of the personal computer, more common and accessible in industry.

4.1 Advantages of CFD

CFD has a number of advantages over other scientific methods, particularly when compared to physical experimentation. These include:

Reproducibility – As there are no variables outside the control of the experiment, the model will produce the same results every time it is run.

Parameterisation – Once a model has been set up, it is a trivial task to alter an input value and re-run. Many CFD codes have a *batch* mode to allow many cases to be queued up and run without user intervention. This can be used, for example, to obtain results over a range of ventilation rates, or to 'optimise' the value of certain parameters

Economics – A numerical study requires very little in the way of equipment, space and man-hours. Although the modelling process itself is less than real-time for most flows, the ability to run experiments back to back 24x7, means that the overall time for a study is reduced, typically leading to economic advantages. (e.g. reduced time to market, etc.)

In a similar way, physical experiments can have a 'cost' in terms of environmental impact and health and safety considerations, which would not apply to a numerical simulation.

Flexibility – A CFD model allows for independent variation of all model parameters, with very few limitations. Physical experimentation tends to be much more limited. For example, the slope of a real tunnel is fixed, however in a CFD model the gravity vector can take any value.

Full Scale – CFD techniques do not require any kind of artificial scaling, which is often a limitation of physical experiments.

Analysis – Physical experimentation requires instrumentation (thermocouples, velocity probes, pressure transducers, infra-red (IR) imaging, etc.) in order to produce quantitative data. This instrumentation will always be limited, and is often the major constraint on an experimental procedure. By contrast, a CFD model intrinsically contains all the data (and more) that could ever be required.

CFD should not, however, be considered as a replacement for physical experimentation or for theoretical analysis. Results from a CFD model are meaningless without *validation against experimental data.*

4.2 Verification and validation

In the context of CFD modelling, verification is defined as:

> the process of determining that a model implementation accurately represents the developer's conceptual description of the model and the solution to the model.

whereas validation is:

> the process of determining the degree to which a model is an accurate representation of the real world from the perspective of the intended uses of the model.
>
> (Grace and Taghipour, 2004)

Verification is perhaps the easier of these two, particularly when using well-established codes, such as *CFX* or *Fluent*, that are routinely tested as part of their development. Nevertheless, the verification process must include the implementation decisions made by the user, notably meshing, but also time step size, discretisation scheme, under-relaxation factors, convergence criteria, choice of sub-models, and so forth, on a case by case basis.

It is important not to be complacent in relying on the reputation of a particular code, as it is common, particularly when using new (or heavily modified) features, to come across obvious bugs and programming errors. It is entirely possible, therefore, that more subtle bugs exist and have remained undiscovered despite a large user base. In this sense, 100% verification is *not possible.*

Free and Open-Source Software (FOSS), such as *FDS* (Fire Dynamics Simulator), has a potential advantage with respect to verification, as any user has access to

the source code and is able to examine the way in which models have been implemented.

Validation, on the other hand, is the process of showing that the results from the model match what would be found in the *real world*, and is most simply achieved by directly comparing experimental results with model results. Validation may also be carried out against analytical results, or in the absence of directly applicable results, a *secondary* validation (where the validation is performed on a different, but related, scenario) could be considered. The data used in validation should be appropriate for the intended use of the model. For example, if temperature data from some thermocouples can be used to validate results from a model, it does *not* necessarily follow that velocities in the model will also be correct. In this sense, 100% validation is also *not possible*.

4.3 Governing equations

It is possible to derive a small number of fundamental equations that describe the physics of a fluid flow. These are referred to as *governing equations* or, more specifically:

- the continuity equation
- the momentum equation, and
- the energy equation

There is some variation of the form of these equations between different sources – such as textbooks (e.g. Versteeg and Malalasekera 1995, Shaw 1992, and Pozrikidis 1997) and code documentation (e.g. Fluent 2002 and McGrattan 2005) – due to different notations and conventions, however the basic principles presented here remain valid.

Each of these equations can be derived by considering an elemental volume within a fluid (see Figure 4.1). Note that the volume remains fixed in space whilst the fluid moves through it – this is referred to as an *Eulerian* system. (The alternative approach, where the volume tracks the motion of the fluid is termed *Lagrangian*)

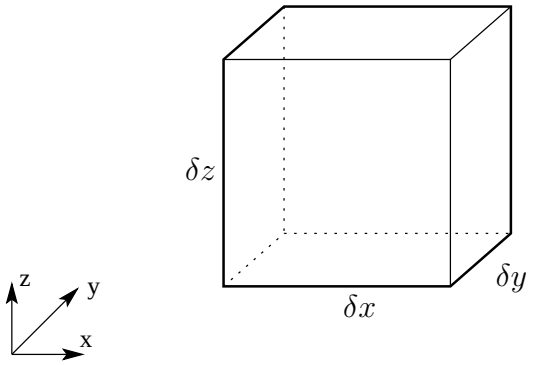

Figure 4.1: Elemental volume of fluid

4.3.1 Continuity equation

The continuity equation is based on the principle of *conservation of mass*. In order for mass to be conserved, the *rate of flow into a volume must be equal to the rate of change of mass within the volume.*

The flow into the volume is found by summing the product of the area, density, and normal velocity for each face of the volume (see Figure 4.2).

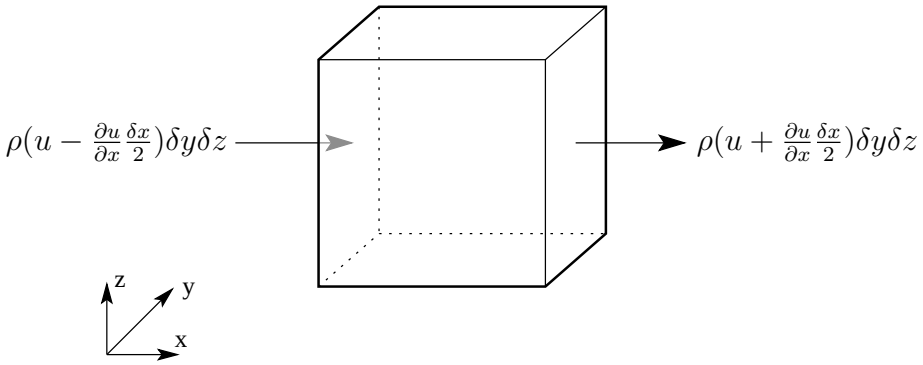

Figure 4.2: Flow into elemental volume

This leads to:

$$\frac{\partial \rho}{\partial t} + \frac{\partial(\rho u)}{\partial x} + \frac{\partial(\rho v)}{\partial y} + \frac{\partial(\rho w)}{\partial z} = 0 \tag{4.1}$$

or, in vector form:

$$\frac{\partial \rho}{\partial t} + \nabla \cdot \rho \boldsymbol{u} = 0 \tag{4.2}$$

Where ρ is the density, and $\boldsymbol{u}$ is the velocity vector.

For an incompressible fluid, density is constant, leaving simply:

$$\frac{\partial u}{\partial x} + \frac{\partial v}{\partial y} + \frac{\partial w}{\partial z} = 0 \tag{4.3}$$

or, in vector form:

$$\nabla \cdot \boldsymbol{u} = 0 \tag{4.4}$$

4.3.2 Momentum equation

Newton's second law of motion states that the rate of change in momentum of the fluid in the volume is equal to the sum of forces acting on it.

$$\rho \left(\frac{\partial \boldsymbol{u}}{\partial t} + (\boldsymbol{u} \cdot \nabla)\boldsymbol{u} \right) + \nabla p = \rho \boldsymbol{g} + \boldsymbol{S} + \nabla \cdot \boldsymbol{\tau} \tag{4.5}$$

Where

- ρ is the density,
- $\boldsymbol{u}$ is the velocity vector,
- p is the pressure,
- $\boldsymbol{g}$ is the gravitational vector,
- $\boldsymbol{S}$ is all other external forces (e.g. electrostatic, Coriolis, momentum transfer from sprinklers etc.), and
- $\boldsymbol{\tau}$ is the stress tensor.

The momentum equation can be considered to be three independent equations in the three principle directions.

4.3.3 Energy equation

The last of the governing equations is the energy equation, which is derived from the *first law of thermodynamics*. It states that the rate of change of energy of the elemental volume of fluid is equal to the rate of heat addition to the fluid plus the rate of work done on the fluid.

The energy equation is only of interest when the fluid is compressible, or there is a variation of temperature.

$$\frac{\partial}{\partial t}(\rho h) + \nabla \cdot \rho h \boldsymbol{u} = \frac{Dp}{Dt} - \nabla \cdot \boldsymbol{q}_r + \nabla \cdot k \nabla T + \sum_l \nabla \cdot h_l \rho D_l \nabla Y_l \qquad (4.6)$$

Where

h is the enthalpy of the fluid,

$\frac{Dp}{Dt}$ is the material derivative of p,

q_r is the radiative heat flux (see Section 4.8),

k is the thermal conductivity, and

T is the temperature.

The final term relates to the diffusion of the separate species in a multiphase flow.

4.3.4 Equation of state

The equation of state for a fluid is used to relate the variable material properties to each other. This reduces the number of unknowns that must be solved to a minimum.

By assuming thermodynamic equilibrium, it can be assumed that pressure and internal energy are functions of density and temperature:

$$p = p(\rho, T) \qquad \text{and} \qquad i = i(\rho, T) \qquad (4.7)$$

For a *perfect gas*, for example, $p = \rho RT$ and $i = C_v T$, where R is the gas constant and C_v is the specific heat capacity of the gas.

4.3.5 Viscous stress tensor

The momentum equations include the components of the viscous stress tensor τ_{ij}. If the fluid is assumed to be *isotropic* (which is generally the case unless the fluid contains long chain-like molecules), then the stress tensor can be found from the viscosity and rate of deformation of the fluid.

$$\tau_{ij} = \begin{cases} 2\mu \frac{\partial u_i}{\partial x_i} + \lambda \nabla \cdot \boldsymbol{u} & i = j, \\ \mu \left(\frac{\partial u_i}{\partial x_j} + \frac{\partial u_j}{\partial x_i} \right) & i \neq j. \end{cases} \tag{4.8}$$

Where

$\boldsymbol{\tau}$ is the viscous stress tensor,

$\boldsymbol{u}$ is the velocity vector,

μ is the dynamic viscosity, and

λ is the *second viscosity*

Note, $\boldsymbol{\tau}$ is symmetric, so $\tau_{ij} = \tau_{ji}$, and the second viscosity term can be ignored for incompressible flows.

4.3.6 Generic transport equation

The governing equations, and the equations for the transport of other scalars, can all be expressed in the form:

$$\frac{\partial(\rho\phi)}{\partial t} + \nabla \cdot (\rho\phi \boldsymbol{u}) = \nabla \cdot (\Gamma \nabla \phi) + S_\phi \tag{4.9}$$

or in words:

Figure 4.3: Turbulent fluid flow (Durbin and Reif, 2001)

Rate of increase of ϕ of fluid element	+	Net rate of flow of ϕ out of fluid element	=	Rate of increase of ϕ due to diffusion	+	Rate of increase of ϕ due to sources	(4.10)

The use of a generic form greatly simplifies the discussion, development, and implementation of algorithms to numerically solve the equations.

4.4 Turbulence models

Taylor and von Kármán defined turbulence as:

> an irregular motion which in general makes its appearance in fluids, gaseous or liquid, when the flow past solid surfaces or even when neighboring streams of the same fluid flow past or over one another.
>
> (Wilcox, 1994)

In practice, turbulence is both time-dependent and fully three-dimensional, and consists of rotational vortices, or *eddies*, superimposed over the net flow (see Figure 4.3). These eddies occur over a continuous spectrum of sizes, from very

large to very small, and persist for relatively long periods of time. This means that the level of turbulence at a point cannot be determined simply from the local strain-rate, but depends on the history of the fluid.

Virtually all interesting flows are turbulent, and turbulence has a significant impact on the diffusion of energy, mass and momentum in a fluid.

A large number of different turbulence models have been developed for use with CFD techniques, however, there is no *universal* turbulence model that is suitable for all applications of CFD. Most general purpose CFD codes implement a range of models and leave the choice up to the user (*Fluent* has six basic types, with a number of variants of these).

According to Wilcox (1994):

> An ideal model should introduce the minimum amount of complexity while capturing the essence of the relevant physics.

If a model is too complex, then at best, the amount of effort required to solve the problem will be unnecessarily high, and at worst, it will result in unexpected numerical difficulties. On the other hand, if a model is too simple, then the solution may be incorrect or inaccurate.

In addition to its effect on the flow of a fluid, *turbulence is the dominant mechanism for the mixing of a fuel and oxidiser* in a combustion reaction. As it is the mixing process which ultimately *limits the rate of reaction*, the choice of turbulence model is significant.

4.4.1 Reynolds Averaged Navier Stokes equations (RANS)

Consider a property of a flow, such as the velocity at a certain point, to consist of *fluctuating* part (due to turbulence) and a *non-fluctuating* part (see Figure 4.4).

$$u = U + u' \text{ , or in general, } \phi = \Phi + \phi' \tag{4.11}$$

where

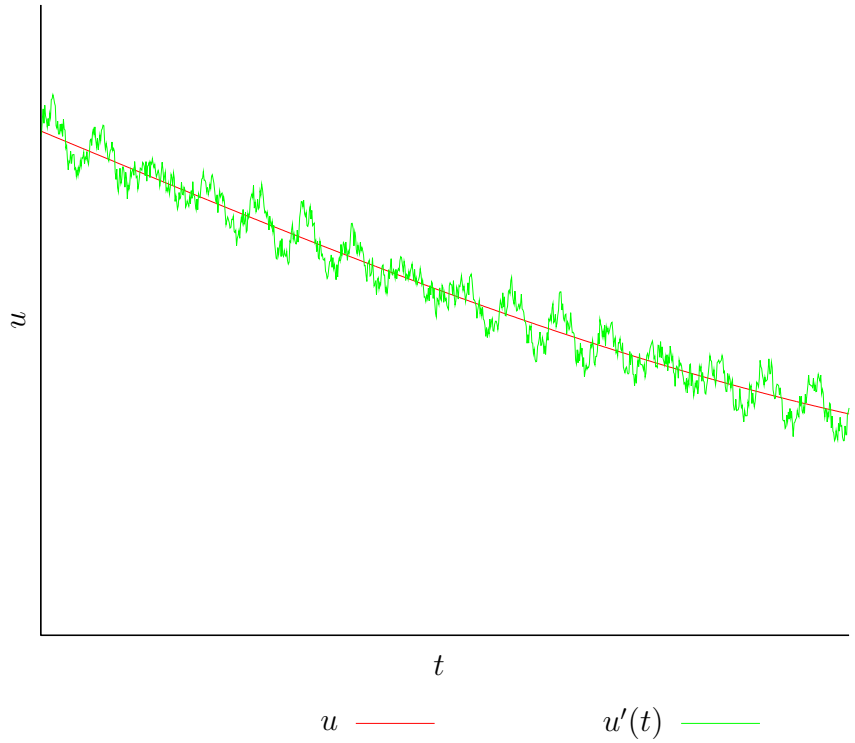

Figure 4.4: Random fluctuations superimposed onto net flow

Φ is the non-fluctuating part of a variable, and

ϕ' is the fluctuating part.

For a steady flow, the non-fluctuating part is equal to the time averaged value, but for an unsteady flow, the non-fluctuation part is taken to be the average instantaneous value of a large number of identical experiments, or the *ensemble average*. Note that the average of the fluctuating part is zero by definition:

$$\phi = \Phi + \phi' \tag{4.12}$$

$$\overline{\phi'} \equiv 0 \tag{4.13}$$

$$\overline{\phi} = \overline{\Phi + \phi'} = \overline{\Phi} + 0 \equiv \Phi \tag{4.14}$$

similarly

$$\overline{\frac{\partial \phi}{\partial s}} \equiv \frac{\partial \Phi}{\partial s} \tag{4.15}$$

etc., however:

$$\overline{\phi'^2} \not\equiv 0 \tag{4.16}$$

$$\overline{\phi'\psi'} \not\equiv 0 \tag{4.17}$$

where ψ' is the fluctuating part of some other variable ψ.

If the governing equations in Section 4.3 are re-derived using this technique, the *Reynolds Averaged Navier–Stokes* equations are produced. These contain additional stress terms than the standard Navier–Stokes equations. The extra stresses are called *Reynolds stresses* or *turbulent stresses*.

$$\tau_{ij} = -\rho\overline{u_i' u_j'} \tag{4.18}$$

As a result of the extra terms, the RANS equations contain too many unknowns to be solved directly. A *turbulence model* is needed to provide additional equations linking the flow variables to the Reynolds stresses.

Where the fluctuations in ϕ cause variations in density, a density weighted average, or *Favre average* is sometimes used (Veynante and Vervisch, 2002).

$$\widetilde{\Phi} \equiv \frac{\overline{\rho\Phi}}{\overline{\rho}} \tag{4.19}$$

$$\phi = \widetilde{\Phi} + \phi'' \tag{4.20}$$

Favre averaged Navier–Stokes equations can be derived, however they are more complex than the Reynolds averaged form.

4.4.2 The k-ε model

k-ε is one of the most widely used turbulence models. It was proposed by Launder and Spalding (1974), and is part of a class of *two-equation* models. Two-equation models assume isotropic turbulence, and therefore only need two additional equations to be mathematically complete.

The rationale behind k-ε and other similar models is that turbulence causes an increase in the effective viscosity of a fluid. This additional viscosity, or *eddy*

viscosity, can be calculated as follows from the turbulent kinetic energy, k, and the rate of dissipation of turbulent kinetic energy, ε:

$$\nu_T = C_\mu \frac{k^2}{\varepsilon} \tag{4.21}$$

Where ν_T is the eddy viscosity, and C_μ is an empirical constant. k and ε are transported scalars, and empirical equations for their production, diffusion and dissipation have been developed and validated for a wide range of flows. These contain several model constants.

Despite being widely used, k-ε is not without its weaknesses. There may be problems with any cases outside the range of validity of the empirical constants. For example, k-ε was developed primarily for shear flow parallel to a boundary. Other kinds of flow may contain features, such as a stagnation point in front of a bluff body, that are not handled well by k-ε.

As k-ε assumes turbulence to be isotropic, it will inevitable be inaccurate for any flow where anisotropy is significant.

The buoyant plume from a fire is one such case. Various studies Hara and Kato (2004); Nam and Bill (1993) have shown that k-ε overpredicts the velocities and temperatures, and that the width of the plume is correspondingly underpredicted.

These weaknesses can be overcome either by careful tuning of the model constants, or by making modifications to the k-ε equations.

For a thermal plume in free space, an investigation of the accuracy of the standard (i.e. unmodified) k-ε model by Hara and Kato (2004) showed temperatures and velocities to be within about 10%. Modifications to the value of C_3 (the buoyancy production term) only had a marginal effect. Although the study considered a large number of cases, the majority had a fairly low grid resolution in the region of the heat source (typically one or two cells), and found (unsurprisingly) a strong grid dependence. In other studies, such as Xue et al. (2001), C_3 is granted a greater level of significance. There is no widely accepted value within the academic literature.

4.4.2.1 Reynolds stress model (RSM)

The main weakness with k-ε and all other two-equation models is the assumption that turbulence is isotropic. All real flows contain some level of anisotropy, although it may not always be significant.

The Reynolds stress model does not make an isotropic assumption, and instead works directly with a transport equation for the Reynolds stress tensor. The price paid is an increase in the number of equations that must be solved and in the intricacy of the equations themselves.

RSM has been used by Chen (1996) to model the natural convection from a domestic radiator. Although it is shown to be superior to k-ε the improvement is not considered to be significant.

There are few references to the use of this kind of model in the field of fire engineering, as presumably researchers who find k-ε lacking tend to jump directly to LES or DNS, which are outlined below.

Sinai (2003) directly compares the SSG (Speziale, Sarkar and Gatski) Reynolds stress model with the standard k-ε and the RNG (renormalisation group) k-ε model for a fire in an enclosure with a large opening. The RSM results are the closest fit to the experimental data, however all three models perform reasonably well, and the increase in accuracy may not be worth the increased computational cost.

4.4.3 Other approaches

4.4.3.1 Direct numerical simulation (DNS)

A direct numerical simulation (DNS) is the most complete method of modelling turbulence, and conceptually the simplest. Simply stated, DNS removes the requirement for any turbulence model by using grids and time steps that are small enough to capture the real physics of turbulent flow. This makes it *extremely* computationally expensive, and therefore can only be used for problems with small length- and time-scales and typically only two dimensions. In particular it

is only feasible to deal with low to moderate Reynolds numbers, as the number of cells required increases with Reynolds number. Boundary conditions can also be difficult to define.

Hawkes and Chen (2004) used DNS to examine the behaviour of hydrogen-enriched premixed methane flames. The need for DNS in this case is justified because of intricate coupling between turbulence and the chemical mechanism. Hydrogen has a higher laminar diffusivity than methane, and is known to stabilise the combustion in the laminar regime. However it was not known whether this effect would extend to turbulent combustion. They consider a 15-step reaction involving 19 chemical species with a grid resolution of 25 µm. Whilst the study produced reasonable results, the limited problem domain made it difficult to validate the numerical results due to the absence of large scale effects.

Even at the current rate of increase of computer speed (Moore, 1965) and capacity, it will be some time before DNS is a practical method for engineering type problems. Luo (2003) places this as "*in the next decade*" whilst Strelets (2003) tentatitevly suggests 2080 as the date DNS will become ready.

4.4.3.2 Large eddy simulations (LES)

Conceptually, large eddy simulation (LES) is situated somewhere between DNS and the RANS approach. Basically large eddies are resolved directly, whilst small eddies are modelled. The rationale behind LES can be summarized as follows:

- Momentum, mass, energy, and other passive scalars are transported mostly by large eddies.
- Large eddies are more problem-dependent. They are dictated by the geometries and boundary conditions of the flow involved.
- Small eddies are less dependent on the geometry, tend to be more isotropic, and are consequently more universal.
- The chance of finding a universal model is much higher when only small eddies are modelled.

(Fluent, 2002)

LES is still computationally expensive when compared with RANS, but it is a feasible option for some real problems. It is available as an option in many general purpose CFD codes, and in some specialist codes such as *FDS* it is the default turbulence model. Others, such as Strelets (2003) are less optimistic, conservatively suggesting another 30 years' development of computer hardware is required, and Luo (2003) who concludes that more fundamental work on sub-grid scale models and on basic guidelines for the application of LES to fire dynamics is required.

Zhang et al. (2002) compares LES predictions from *FDS* with experimental measurement of turbulent quantities from a thermal plume. Although they find a good agreement, they also show that as the size of the heat source increases the number of grid cells required also increases. Their maximum heat source of (only) 5.4 kW required a cell size of less than 3 cm.

4.4.3.3 Hybrids

A further possibility that deserves mention is hybrid approaches, such as Detached-Eddy Simulation (DES), that fall somewhere between classic RANS techniques and full LES Spalart (2000). Typically these use a RANS formulation for the near-wall region and LES further out Abe (2005); Temmerman et al. (2005). This allows coarser grids than a pure LES model, and hence permits the solution of cases that would otherwise be infeasible.

4.5 Numerical schemes

4.5.1 Discretisation

It is not possible to directly solve the governing equations (which form a set of simultaneous non-linear partial differential equations). Instead the equations are converted to a simple algebraic form which can be solved numerically. This process is called discretisation because continuous variables, such as ϕ, are reduced to a set of discrete values ϕ_i, and differentials and integrals are merely the

differences between, and the summation of, these discrete values.

$$\text{Conceptually :} \qquad \left(\frac{\partial \phi}{\partial x}\right)_i \Rightarrow \frac{\phi_{i+1} - \phi_{i-1}}{2\Delta x} \tag{4.22}$$

$$\int \phi dx \Rightarrow \sum_i \phi_i \Delta x \tag{4.23}$$

The discrete values are located at the cell centres (or nodes) in a mesh (see Section 4.5.5), and must be interpolated to face-centred values as required.

Various different discretisation schemes exist, and whilst a complete derivation of each of these is beyond the scope of this document, they are at the heart of any CFD implementation, and are the key to the performance and accuracy of the entire process. In general terms, discretisation schemes can be assessed in terms of their accuracy, stability, and efficiency.

accuracy is often considered in terms of the Taylor series truncation errors. Most schemes are first or second order schemes, however some codes implement higher order schemes and hybrid schemes (where the scheme varies from cell to cell based on flow properties such as the Péclet number). In addition to the Taylor series error, some schemes, such as upwind differencing, are prone to *false diffusion*.

stability of a scheme is its ability to produce a valid solution over a wide range of problems. In practice stability can be ensured if a scheme is:

- **conservative** – the calculated flux of ϕ across the common face between two cells must be independent of which cell is being considered. This ensures that the principle of conservation that was used to derive the governing equations is maintained.
- **bounded** – the value of ϕ at a node should normally (in the absence of source terms) lie between the value of ϕ at neighbouring nodes.
- **transportive** – that is the scheme respects the relative importance of convection and diffusion (i.e. the Péclet number) and the direction of flow.

efficiency is the amount of calculation required to reach a final solution, and is highly case dependent. For example, although higher order schemes require more calculation per cell, they are often able to produce a solution in less iterations or using a coarser mesh than a solution of corresponding accuracy produced by a first order solution.

4.5.2 Temporal discretisation

For unsteady solutions (i.e. where $\frac{\partial(\rho\phi)}{\partial t} \neq 0$) the temporal domain of a problem is split into discrete *time steps* of finite size. This process is similar to the spatial discretisation outlined in Section 4.5.1

If a value of ϕ at a time step is found only by reference to the solution at the previous time step, then the time stepping is said to be *explicit*. Alternatively, if a value for ϕ is determined with reference both to the previous time step and the current time step (and hence simultaneously with ϕ at neighbouring cells) then it is said to be *implicit*. Implicit schemes are stable no matter how large the time-step size, and for this reason are preferred for most applications despite the increased complexity. Explicit schemes are only stable if the cell Courant number is less than unity throughout the domain, but can be more accurate for certain kinds of flows such as shock waves.

Time stepping schemes can be first- or second-order accurate. The principle disadvantage of second-order schemes is the increased memory needed to store an additional solution.

$$\text{First order:} \quad \frac{d\phi}{dt} = \frac{\phi^{n+1} - \phi^n}{\Delta t} \tag{4.24}$$

$$\text{Second order:} \quad \frac{d\phi}{dt} = \frac{3\phi^{n+1} - 4\phi^n + \phi^{n-1}}{2\Delta t} \tag{4.25}$$

where

ϕ^n is the value of ϕ at t_n. i.e.

ϕ^{n+1} is the future value of ϕ

ϕ^n is the current value of ϕ

ϕ^{n-1} is the past value of ϕ

and

Δt is the time-step size.

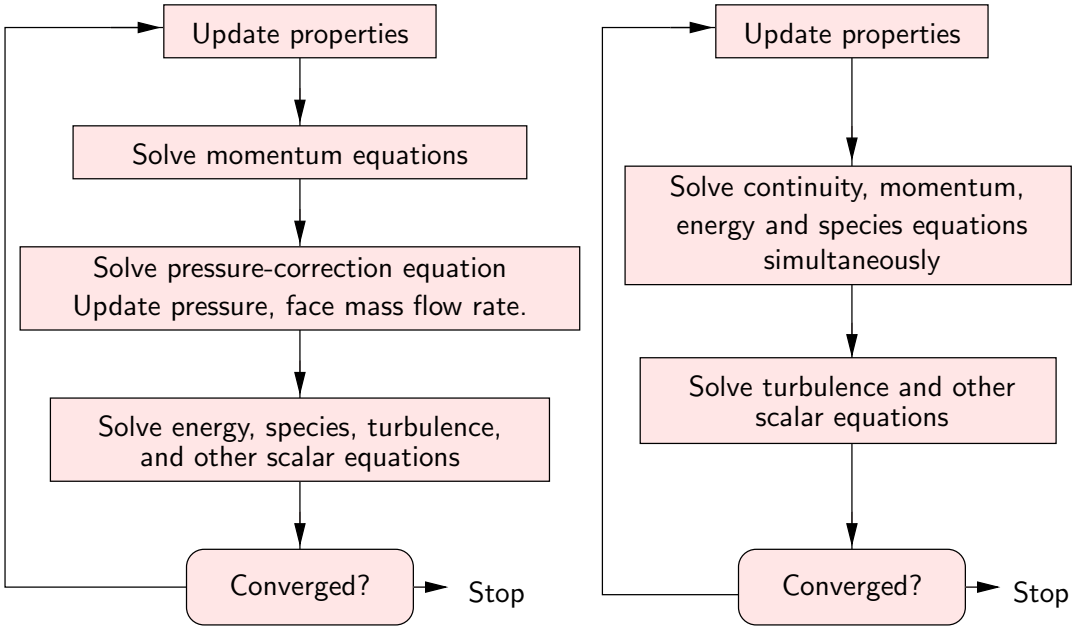

Figure 4.5: Overview of CFD solution algorithms a) segregated b) coupled

4.5.3 Solution algorithm

The set of simultaneous algebraic equations produced by the discretisation process must be solved in an efficient manner. The number of equations involves precludes a direct solution, and all CFD solvers use indirect iterative approaches. The algorithms in use by the various CFD packages can be either *segregated* or *coupled* depending on whether the continuity, momentum and energy equations are solved sequentially or simultaneously (see Figure 4.5). Although the distinction may seem subtle, the strong coupling between pressure and velocity (i.e. between continuity and momentum) means the extra effort required to solve them simultaneously can lead to a more rapidly converging solution.

4.5.4 Under relaxation

As the equations are both non-linear and simultaneous, it is most convenient to solve them iteratively. To ensure stability, an under-relaxation factor, α, is used:

$$\phi_{n+1} = \phi_n + \alpha\Delta\phi \tag{4.26}$$

Table 4.1: *Fluent*'s default under-relaxation values

Variable	Relaxation factor
Pressure	0.3
Density	1
Body Forces	1
Momentum	0.7
Turbulence Kinetic Energy	0.8
Turbulence Dissipation Rate	0.8
Turbulent Viscosity	1
Energy	1

where $\Delta\phi$ is the computed change in ϕ in a given iteration. The value of the under-relaxation factor needs to be small enough to ensure convergence of a solution without being overly conservative. The optimum value varies from case to case and between variables, being dependent on the solution scheme and the main driving force of the flow. For example, the default under-relaxation factors for *Fluent* (see Table 4.1) are based on a segregated solution scheme and a pressure driven flow. For a buoyancy driven flow it may be more efficient (or perhaps necessary) to reduce the factors for density and/or energy.

4.5.5 Meshing

In order to produce a discrete form of the governing equations, the physical domain must be subdivided into a mesh (or grid) of *cells* that defines the location of the *nodes* and the relationship between them.

The *density* of a grid determines the amount of memory and CPU required for a solution (with the total being roughly proportional to the number of nodes) and the accuracy of the final solution (due to the assumption that differentials can be represented as differences between values at adjacent nodes).

The quality of a mesh is not merely a trade-off between accuracy and computational resources. With some forethought, a mesh can be designed to have a higher density in regions where sharp gradients in flow variables will be present, such as at boundary layers or within a buoyant plume. This will give a better solution than a uniform mesh with the same number of nodes.

Historically, many CFD packages required *structured* meshes – consisting of a

single type of element in a regular arrangement – due to the simplicity and ease of optimisation. In recent years however, *unstructured* meshes have become the norm. These allow arbitrary arrangements of a mixture of hexahedral, tetrahedral, and prism elements. This gives a great deal of flexibility, allowing complex geometries and fairly arbitrary node spacing.

Despite this flexibility, structured meshes still retain some advantages. For example in the case of flow through a long narrow space (such as a tunnel or pipe), a regular hexahedral mesh would require less cells, as the acceptable range of cell aspect-ratio is high when the flow is known to be aligned with the mesh elements.

Some CFD packages provide a facility called *mesh adaption*, which allows the mesh to be refined during the calculation once an approximate solution has been reached. Typically a solution is begun with a relatively coarse mesh, and then later cells in areas of interest are repeatedly subdivided to produce a much finer mesh. This can be particularly beneficial for transient calculations where the requirements of the mesh may vary quite considerably over the time of the simulation. For example, in the development of a plume from stationary air, a high mesh density is initially only required close to the fire source due to strong gradients in temperature and density. As the plume forms, high velocity gradients are created at the edge of the plume, and wherever the plume impinges on a solid surface such as the ceiling.

Fluent (2002) recommends avoiding cells with aspect ratios greater than 5:1, avoiding highly skewed[1] cells, and large changes in size between adjacent cells, as this can lead to high truncation errors and numerical instability.

4.5.6 Convergence

In general, it is not possible to determine in advance how many iterations of a calculation will be required to reach a converged solution.

The *residual* of a variable is a measure of the level of convergence of a solution.

[1] skewness is a measure of how much a cell's shape deviates from an equilateral cell of the same volume

For example, the residual of the continuity equation is:

$$R^c = \sum_{\text{cells } P} |\text{rate of mass creation in cell P}| \tag{4.27}$$

which will tend to zero as a solution converges. Residuals for momentum, energy, and any other solver variables are defined in a similar way.

Even assuming a solution is stable, a residual of zero cannot be achieved due to the inherent errors and approximations used by practical solvers. It is common therefore to consider a reduction in residuals of three orders of magnitude to be sufficient for most applications.

In *Fluent* residuals are *scaled* by the maximum residual in the first five iterations:

$$\frac{R^c_{\text{iteration } N}}{R^c_{\text{iteration } 5}} \tag{4.28}$$

allowing convergence criteria to be defined and assessed on absolute values.

This technique has limitations, for example, for a flow dominated by natural convection, but with an initially uniform temperature field and zero velocity field, the velocity residuals will start low and then increase.

There are no universally applicable convergence criteria, and whilst residuals provide a simple measure of convergence for the whole of the flow domain, it is appropriate to monitor specific variables, such as rate of reaction, pressure drop or drag coefficient, on a case-by-case basis.

4.5.7 Discretisation error

The process of discretisation inherently introduces errors into the solution. These errors are hard to quantify directly (unless of course an exact solution is known), but will generally be reduced by refining the grid, using higher order schemes, and reducing the time step.

According to Freitas (2002) the only practical technique for estimating discretisation error is to perform the same calculation on three different grids of increasing density, preferably doubling each time. Freitas (2002) demonstrates how the solu-

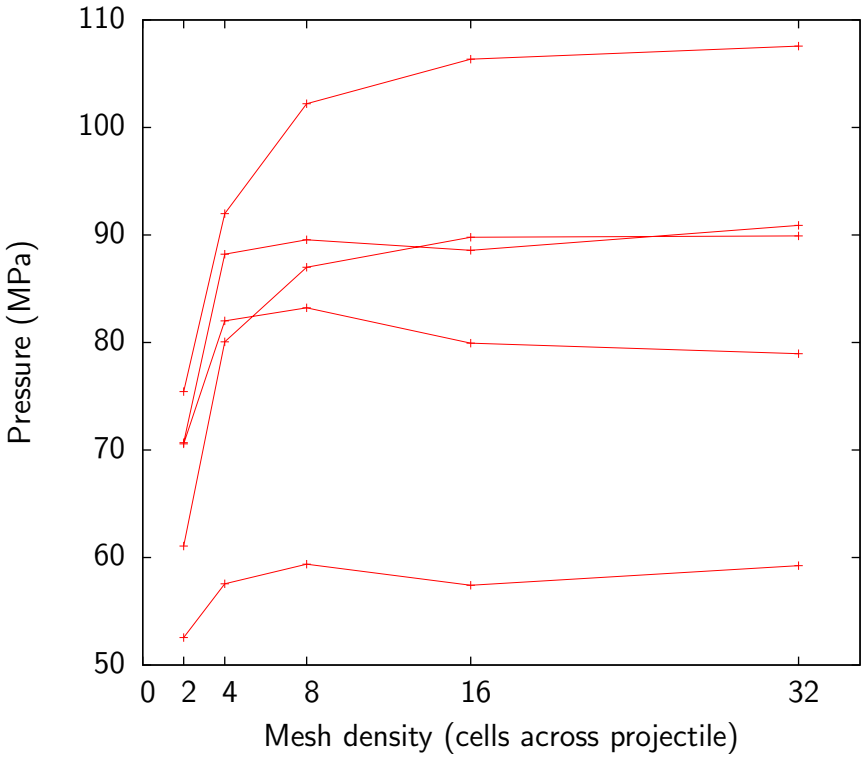

Figure 4.6: Effect of mesh density on pressure predictions at various points around a projectile (Freitas, 2002)

tion of a sample problem depends on grid resolution (see Figure 4.6). Two distinct regions are identified: at low mesh densities a rapid convergence with increasing density is observed; at higher mesh densities a slow asymptotic convergence is seen.

4.6 Combustion

The rate of combustion is determined by the *kinetics* of the chemical reaction between the fuel in question and oxygen. This rate is a function of the local temperature, the local concentrations of the reactants, and various constants that relate to the mechanism of the reaction.

However, for most interesting problems, CFD is not able to provide sufficient resolution of these variables at the length- and time-scales of the chemical processes. The mechanism of the reaction is often not known, or is too complex to be modelled practically.

As a consequence, a number of approaches to modelling fires and combustion have been developed that employ additional assumptions about the behaviour of the reaction in order to produce a practical model. Some of these approaches are described below. For the purposes of this thesis, a model is desired that is able to represent as many of the potential effects of water mist on the fire as possible (as identified in Section 3.2.2: oxygen dilution, gas phase cooling, fuel cooling, attenuation of radiation and disruption of air flow).

4.6.1 Volumetric heat source

Although not technically a combustion model, a fire can be represented by applying a heat source term over a predefined volume of the flow domain. The source term could either be a fixed value or could vary over time to fit the profile of an experimentally measured fire. Depending on the type of fire, a mass source and even a momentum source may also be required.

This technique is not particularly common in the academic literature, but its simplicity makes it an attractive choice for industrial applications.

The principle disadvantage of this approach is that it cannot be used in cases where the size or shape of the fire is not well known, for example in investigations of fire spread or fire suppression, for ventilation-dependent fires, or any scenario that is not directly backed by experimental data.

4.6.2 Non-premixed combustion

In practice combustion tends to take place in one of two regimes:

non-premixed – the fuel and air are initially separate. For a non-premixed flame (also known as a *diffusive* flame), combustion only occurs in the region where the fuel and air mix (Drysdale, 1998).

For example the combustion of propane is:

$$C_3H_8 + 5O_2 \xrightarrow{\text{Energy}} 3CO_2 + 4H_2O \tag{4.29}$$

This reaction can clearly only take place where both propane and oxygen are both present. If it also assumed that the temperature (in the burning region) is high enough for the rate of combustion to be nearly infinite, then propane and oxygen *cannot coexist*, and combustion may only take place at the point where they meet. In other words, the reaction is *mixing-controlled*. The non-dimensional *Damköhler* number is the ratio of the mixing time (or turbulence timescale) and reaction time (or chemical timescale). Mixing controlled reactions correspond to Damköhler numbers much greater than unity.

$$\mathrm{Da} = \frac{\tau_{\mathrm{turb}}}{\tau_{\mathrm{chem}}} >> 1 \tag{4.30}$$

where

τ_{turb} is the turbulent mixing timescale, and

τ_{chem} is the chemical reaction timescale

premixed – the fuel and air are intimately mixed before burning. As the reactants are initially cold they must be heated by the hot combustion products in order to reach a high enough temperature for a significant rate of reaction. The rate of reaction is therefore also *mixing controlled* but in this case it is mixing between reactants and products (rather then between different reactants).

Techniques for modelling non-premixed combustion are described below. As premixed combustion does not normally occur in accidental fires, it will not be considered in detail, but techniques similar to those used for non-premixed combustion can be used.

4.6.2.1 Eddy breakup model (EBU)

In the *Eddy breakup* model (also referred to as *Eddy-dissipation* model in the *Fluent* code), the rate of production of a species i due to a reaction r, $R_{i,r}$ is

given by the minimum of:

$$R_{i,r} = \nu'_{i,r} M_{w,i} A \rho \frac{\epsilon}{k} \min_{\mathcal{R}} \left(\frac{Y_{\mathcal{R}}}{\nu'_{\mathcal{R},r} M_{w,\mathcal{R}}} \right) \quad (4.31)$$

$$R_{i,r} = \nu'_{i,r} M_{w,i} A B \rho \frac{\epsilon}{k} \frac{\sum_P Y_P}{\sum_j^N \nu''_{j,r} M_{w,j}} \quad (4.32)$$

where

$\nu'_{i,r}$ and $\nu''_{i,r}$ are the stoichiometric coefficients of the reaction r,

$Y_{\mathcal{R}}$ is the mass fraction of reactant $\mathcal{R}$

$Y_{\mathcal{P}}$ is the mass fraction of product P,

M_w, i is the molecular weights of species i,

ρ is the total density, and,

A and B are constants taken as 4.0 and 0.5 (Fluent, 2002).

The model is based on the assumption that the rate of reaction is controlled by mixing processes, and that it is turbulence that causes this mixing. The rate is inversely proportional to the *large eddy mixing time-scale* ($\frac{k}{\epsilon}$), which is an approximation of the rate of mixing due to the unresolved turbulence fluctuations within a cell. Equation 4.31 determines the rate of reaction according to whichever of the reactants is in shortest supply. Equation 4.32 instead calculates a combustion rate in terms of the mass fraction of products.

The model does have a number of limitations:

- it does not contain a temperature term, and so is only valid where the temperature is high enough for the chemical timescale to be significantly shorter than the mixing timescale.
- it only works for single- or two-step reaction mechanisms.
- the model constants are not well understood, and according to Brizuela and Bilger (1996) 'A' varies over a range of 1.0 – 7.0 depending on the source.
- its dependence on the turbulent kinetic energy and dissipation rate means it inherits any weaknesses of the turbulence model.

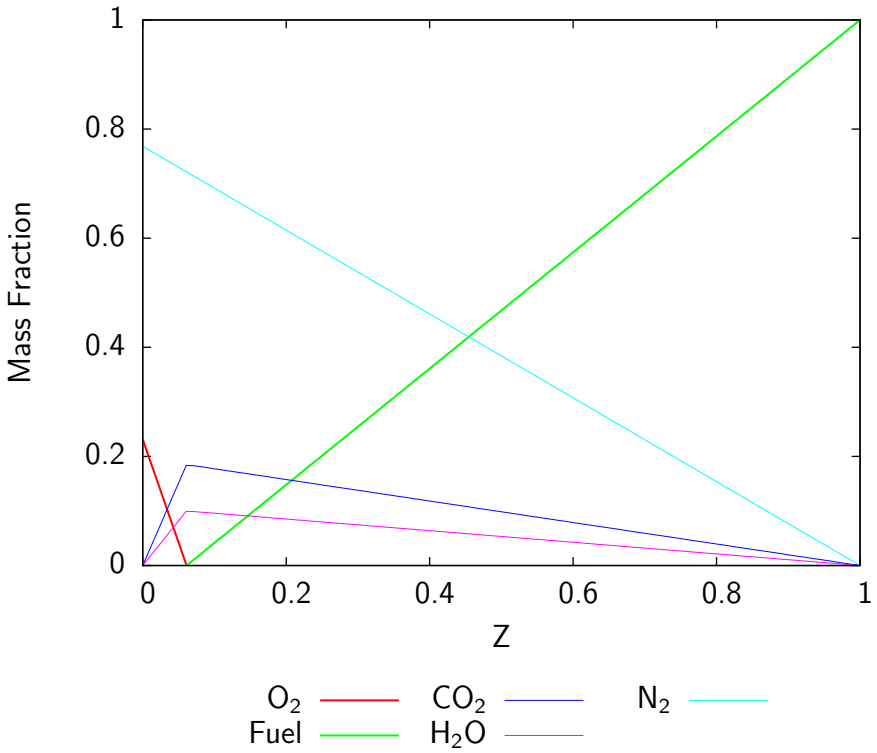

Figure 4.7: Relationship between mixture fraction and mass fractions (McGrattan, 2005)

4.6.2.2 Mixture fraction combustion model

An alternative approach, (used for example by *FDS*), is to define a mixture fraction, Z, which varies from $Z = 1$ for pure fuel, and $Z = 0$ for pure air. At intermediate values, the mixture contains products, and *either* unburnt fuel, *or* unburnt air. As unburnt fuel and unburnt oxygen cannot coexist, this uniquely defines the state of the system (see Figure 4.7). The mixture fraction is defined in such a way that it is a *conserved scalar*. It is implicitly assumed by this that each species has an equal diffusivity.

The actual combustion takes place at a surface, $Z = Z_f$, where neither fuel nor oxygen is present. The value of Z_f is determined by the stoichiometrics of the particular reaction, and is called the *stoichiometric surface*

The advantage of this approach is that it is only necessary to solve the transport equations for Z, and not for the mass fractions of five (or more) species. This saves computational time and memory usage.

The heat release from the reaction occurs only at the stoichiometric surface, and is proportional to the rate of consumption of oxygen. A numerical algorithm is used to locate the surface within the volume in order to determine the area of the surface in each cell.

This approach does not explicitly take turbulence into account. It is assumed in *FDS* that by using a *Large Eddy Simulation* (LES) for the flow field, that the significant effects of turbulence have been captured.

In practice, the gradient of Z can be high, to the point of being discontinuous, which means the solution can be susceptible to numerical diffusion. Various empirical relationships are suggested and implemented by McGrattan (2005) which ensure that the solution remains close to experimental data.

Whilst being computationally cheap, this method is limited to a single fuel, and cannot easily cope with additional source of species such as water vapour, that would be needed to represent evaporating mist droplets.

4.6.2.3 Presumed probability density function (PrePDF)

The presumed probability density function approach is based on a statistical treatment of the variables of interest. The mixture fraction concept, as described above, is extended to include a *mixture fraction variance* with a corresponding conservation equation. These two parameters are then used to determine values for properties such as temperature, density, and species mass fractions.

If a *secondary mixture fraction* is introduced, then the effects of an independent species (such as water vapour from evaporating water droplets) can be considered as well.

This technique has a number of advantages:

- By solving a transport equation for the mixture fraction variance, the effect of turbulent fluctuations on the chemistry can be modelled.
- By determining the mixture properties from the PDF function, the number of unknowns that have to be solved is minimised.

- As the PDF function depends on only a few variables, its values can be pre-calculated and tabulated in an efficient manner.

However, according to Veynante and Vervisch (2002) *this model lacks any prediction capacities when ignition, quenching or even small finite rate chemistry effects exist.* It therefore would not be capable of predicting the extinction of a fire, or the effects of a reasonably effective water mist system.

4.6.2.4 Hybrid Arrhenius/eddy breakup model

The assumption that the rate of reaction is mixing controlled is based on sustained high temperatures in the region of the reaction. For fire and particularly fire suppression applications this is not always true.

At low temperature, the rate of reaction is limited by temperature and can be calculated from the Arrhenius equation:

$$k = A_r T^{\beta_r} e^{\frac{-E_A}{RT}} \tag{4.33}$$

where k is the calculated rate constant, A_r, β_r and E_A are the pre-exponential factor, the exponential factor, and the activation energy of the reaction, and R and T the gas constant and absolute temperature.

As temperature increases, the Arrhenius rate increases until it reaches the limit imposed by the rate of turbulent mixing.

In the hybrid Arrhenius/EBU model, the *rate of reaction is the* minimum *of the Arrhenius and EBU rates of reaction.* The reaction may therefore be temperature controlled in some cells, whilst mixing controlled in others.

This model requires both rates of reaction to be calculated for each cell, and is therefore computationally expensive. As the Arrhenius rate for most combustion reactions is negligible at ambient temperatures, it is capable of modelling extinction.

4.6.3 Summary

Xue et al. (2001) compares the volumetric heat source, eddy-breakup and prePDF combustion models with experimental data from a number of model enclosure fires ranging from a room to a reduced-scale tunnel. All three models produce reasonable results in most cases, but none of them are consistently accurate over all cases considered. In general, velocity predictions were better than temperature predictions.

The volumetric heat source approach is clearly unsuitable for modelling water mist fire suppression, and the mixed-is-burned assumption of both prePDF and the plain EBU may have limitations close to the extinction point.

4.7 Mist models

The equations of CFD (as laid out above) model the behaviour of a single continuous fluid, or (with some extensions) simple mixtures of fluids. Colloidal systems, such as water mist, do not behave in this way – the water exists as *discrete* droplets dispersed within the air, and the interaction of these droplets with the air flow are complex. The term *discrete phase* is used to refer to the water, and *continuous phase* to the air.

There are two fundamentally different techniques for modelling a mist. *Lagrangian* models, where the frame of reference moves with the mist, or *Eulerian* models, where the reference frame remains fixed. In simple terms Lagrangian models track individual moving droplets, whereas Eulerian models keep a tally of the number of droplets in each of a number of fixed volumes (i.e. they use the same grid as the CFD model).

There are advantages of both schemes. Lagrangian models fit more naturally to the physics of a discrete phase, whereas Eulerian models integrate better with traditional CFD techniques, and may be more computationally efficient, particularly for long-running time dependent cases.

4.7.1 Lagrangian particle tracking

One common approach (Adiga, 2004; Lee and Ryou, 2000; Lentati and Chelliah, 1998; Nam, 1996; Yang and Kee, 2002) to modelling a mist system is a *Lagrangian particle tracking* algorithm. This is the basis for the discrete phase model (DPM) in *Fluent*. In this approach, the continuous phase is handled by standard CFD techniques, but the discrete phase is modelled using point-mass *tracking particles*. The trajectory of each particle is calculated using Newton's laws of motion, taking into account drag forces due to the relative motion of the two phases, and other forces, such as buoyancy and gravitation.

- The particles are assumed to take up a negligible volume in the continuous phase. In practice this limits the volume fraction of the discrete phase to around 10%. There is no limit on the mass fraction.
- Particle-particle interactions are ignored. In particular the collision and/or break-up of droplets, but additionally the empirical calculation of drag-force assumes isolated particles in uniform flow.
- The particle trajectories are calculated from mean continuous phase velocities. Although this is valid for an individual particle, it will produce unrealistic results when considering an ensemble of similar particles as, due to the butterfly effect, the turbulent element to the particle motion can be significant. "stochastic" term can be added to the trajectory calculations to account for turbulence, but these processes are not well understood, and the validity of this approach is unclear.

For many applications, including water mist, the number of tracking particles that can be modelled by a computer is substantially lower than the number of physical particles in the problem. The tracking particles (or super-particles) are therefore used to represent several (thousand) similar droplets. This is a form of discretisation similar to meshing, and there is trade off between computational cost and accuracy.

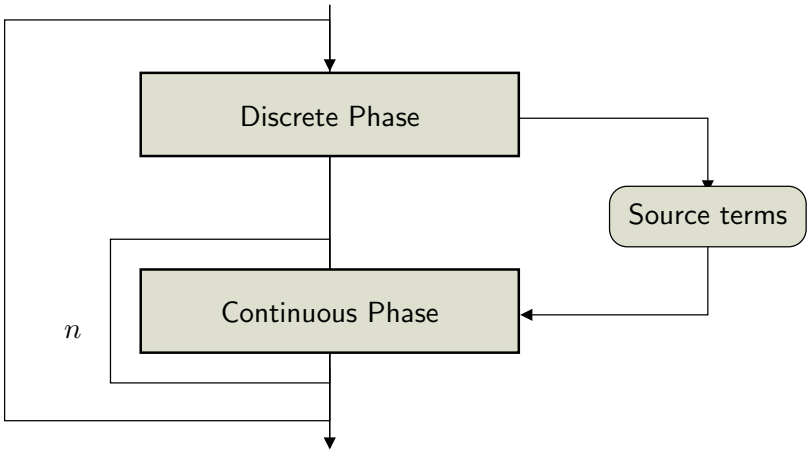

Figure 4.8: Coupling of DPM to continuous phase calculations

4.7.1.1 Coupling

The DPM is a general purpose model that can be used in both steady and unsteady simulations and for coupled and uncoupled flows.

The solution method employed by the DPM for coupled flows is to calculate a set of source terms for the continuous phase based on the discrete phase, taking into account the number of droplets represented by each tracking particle. The source terms are updates every n iterations of the continuous phase (see Figure 4.8).

4.7.1.2 Trajectory

The movement of a particle through a viscous medium (such as air) is determined largely from the action of two forces: gravity and aerodynamic drag:

$$\frac{du_p}{dt} = F_D(u - u_p) + \frac{g_x(\rho_p - \rho)}{\rho_p} + F_x \tag{4.34}$$

where

$\frac{du_p}{dt}$ is the particle acceleration (m/s^2)

$F_D = \frac{18\mu}{\rho_p d_p^2} \frac{C_D \mathrm{Re}}{24}$

u and u_p are the continuous phase (air) and particle velocities (m/s)

ρ and ρ_p are the continuous phase and particle densities (kg/m^3)

g_x is the gravity vector (m/s^2)

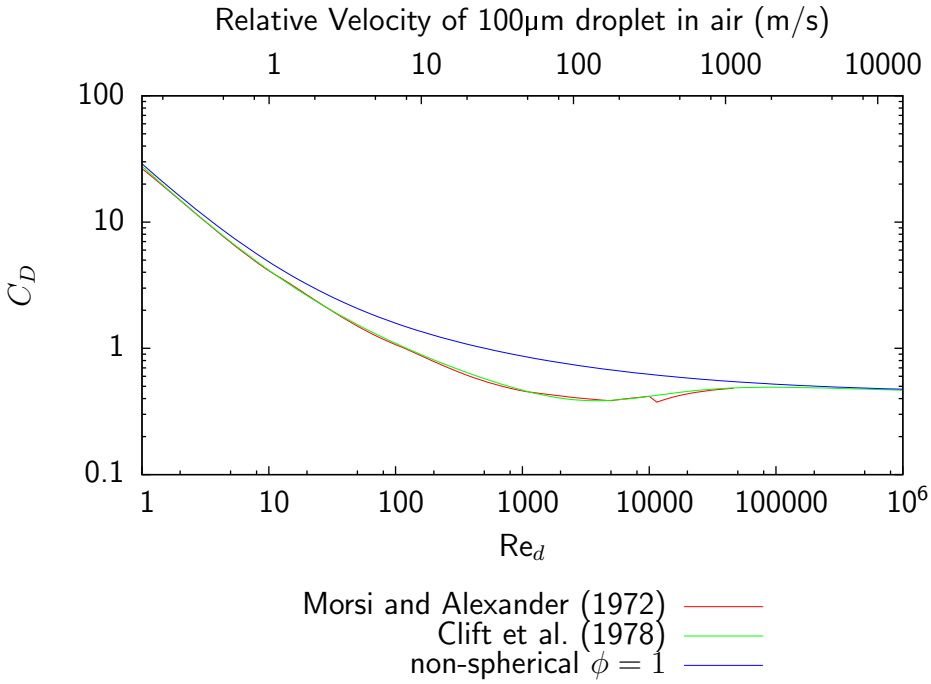

Figure 4.9: Drag coefficient for spherical particles

F_x is any additional forces ($\mathrm{m/s^2}$)

The calculation of gravitational force is trivial, however aerodynamic forces can only be calculated empirically from a drag coefficient (C_D).

For spherical particles, *Fluent* uses the piecewise quadratic fit of Morsi and Alexander (1972), which is valid for $\mathrm{Re}_d < 50,000$. This gives very similar values to those given by Clift et al. (1978), which uses a simple algebraic form (see Figure 4.9).

For non-spherical particles an alternative correlation is used based on a shape factor.

Note, for water mist, droplet Reynolds number is typically around 100 near the nozzle (when the relative velocity is highest) and around 20 elsewhere.

If the continuous phase is modelled using RANS, the continuous phase velocity u is an averaged quantity which does not contain turbulent fluctuations. Turbulence can have a substantial effect on particle motion, particularly for small particles. In the discrete random walk (DRW) algorithm, the particle is considered to be moving through a series of random eddies based on the k and ε values

(or equivalent) from the turbulence model.

The eddy velocity is:

$$u' = \zeta\sqrt{\frac{2k}{3}} \tag{4.35}$$

and the eddy lifetime is:

$$\tau_e = 2 \times 0.15\frac{k}{\varepsilon} \tag{4.36}$$

where ζ is a random variable from a Gaussian distribution.

These are empirical correlations of limited validity, and the DRW *may give non-physical results in strongly nonhomogeneous diffusion-dominated flows* Fluent (2002), and is only as accurate as the underlying turbulence model. It is however a substantial improvement over neglecting turbulence altogether.

4.7.1.3 Droplet evaporation

The evaporation of droplets into the continuous phase is governed by gradient diffusion from a vapour concentration $C_{i,s}$ at the droplet surface to $C_{i,\infty}$ in the continuous phase.

$$N_i = k_c(C_{i,s} - C_{i,\infty}) \tag{4.37}$$

where,

N_i molar flux of vapour (kgmol/m ^{2} -s)

k_c mass transfer coefficient (m/s)

$C_{i,s}$ vapour concentration at the droplet surface (kgmol/m^3)

$C_{i,\infty}$ vapour concentration in the bulk gas (kgmol/m^3)

The concentration of vapour in the bulk gas is known from the continuous phase calculations, and the concentration at the droplet surface is calculated by assuming the partial pressure of the vapour is equal to the saturated vapour pressure at the particle temperature:

$$C_{i,s} = \frac{p_{\text{sat}}(T_p)}{RT_p} \tag{4.38}$$

The mass transfer coefficient, k_c, is calculated from a Nusselt correlation (Fluent, 2002):

$$\mathrm{Nu}_{AB} = \frac{k_c d_p}{D_{i,m}} = 2.0 + 0.6\mathrm{Re}_d^{1/2}\mathrm{Sc}^{1/3} \tag{4.39}$$

Where Re_d is the droplet Reynolds number, and Sc the Schmidt number (ratio of momentum diffusivity to mass diffusivity).

The droplets are assumed to be effectively isolated, and the rate of evaporation is not affected by the proximity of other droplets (the spacing of droplets within a tracking particle is unknown, so this could not be calculated anyhow).

Devarakonda and Ray (2003) investigated the rate of evaporation of linear arrays of methanol droplets. For droplets spaced at six radii apart, the rate of evaporation falls to 50% of that of isolated droplets.

Equation 4.39 is based on experiments covering droplet Reynolds number in the range $2 < \mathrm{Re} < 200$ and temperatures up to 220°C. Smolík et al. (2001) suggests the following as an improvement, particularly at low Reynolds numbers.

$$\mathrm{Nu} = 1 + (1 + \mathrm{RePr})^{\frac{1}{3}} \max\left[1, \mathrm{Re}^{0.077}\right] \tag{4.40}$$

where Pr is the Prandtl number (ratio of momentum diffusivity to *thermal* diffusivity). They are concerned primarily with atmospheric applications, and only consider temperatures between 20 °C and 30 °C.

At high temperature, the *Leidenfrost effect* (where the evaporating water vapour reduces the heat-transfer coefficient for the droplet) can markedly reduce the rate of evaporation.

4.7.1.4 Boundary conditions

If the trajectory of a particle brings it to a boundary then an action appropriate for the type of boundary is taken. This can be:

escape the particle 'leaves' the flow domain and is no longer considered. This is appropriate for flow outlets, and may be appropriate at flow inlets.

reflect the particle bounces off the wall (i.e. the velocity component normal to

the boundary is reversed) and remains fully part of the simulation.

trap the trajectory of the particle is terminated and its mass is instantly released as vapour. This is consistent with a droplet reaching a hot surface, and would be appropriate for the surface of the burning object.

For wall boundaries, each of the above actions may be appropriate. Experimental studies (Disimile et al., 2005; Lee and Ryou, 2000) have shown behaviour equivalent to each of the above depending on droplet size, impact angle and surface/droplet temperature. Other more complex behaviours such as droplet break-up, surface film formation and non-elastic collision have also been observed (Lee and Ryou, 2000).

4.7.1.5 Stability

For uncoupled flows, the algorithms used by *Fluent*'s DPM are both robust and accurate. The situation is different for coupled calculations, and for strongly coupled flows care must be taken when setting up a model to ensure that both the continuous phase and discrete phase solutions will remain stable during the solution.

Stability problems can occur if either the source terms are large, or change significantly with each update of the discrete phase.

Large source terms occur if too many tracking particles are in (or pass through) the same continuous phase cell, or if the number of droplets represented by a particle is too large. These problems are exacerbated when the continuous phase cells are very small.

Significant changes in the source terms occur during the DPM update if the continuous flow field has changed sufficiently in the previous n iterations for a particle to end up in a different cell, or to a lesser extent for the magnitude of the source term to oscillate.

To a certain extent, this problem can be mitigated by reducing the under-relaxation factor for the DPM sources, or selecting either $n = 1$, to force a DPM update every iteration, or setting n to the total number of iterations per

time step, to only allow a DPM update at the start of each time step[2]. The latter approach is always stable, but may reduce the accuracy of the solution unless the time step is sufficiently small.

Alternatively, the number of droplets represented by each particle can be reduced, either by increasing the number of streams per injection, or by decreasing the time-step. Spreading the source over a larger number of particles will effectively spread the source over a larger number of cells, and reducing the time step will reduce the effect of the source in a given time step.

4.7.2 Eulerian multiphase

The alternative to Lagrangian particle tracking is an Eulerian sectional model, which has been use to successfully model water mist by Prasad et al. (2002). In this approach, also called a *two continuum* model, the water mist is treated as a continuum somewhat like a gaseous fluid. A set of conservation equations analogous to the Navier-Stokes equations can be derived in terms of particle number density and number flux, etc (see Crowe et al. (1998) for details). These are then solved on the same grid as the continuous phase (air) using the same solution methods. To account for variation in droplet size, the mist is split into a number of *'sections'* each corresponding to a range of diameters.

The two continua are coupled by source terms for momentum, species and heat in a similar way to the Lagrangian models, however because evaporation causes droplets to reduce in diameter, the 'sections' of the water mist phase are also coupled.

4.7.3 Contrast between Lagrangian and Eulerian models

The discrete phase model and the two continuum model clearly take very different approaches to solve the same problem, and both have been successfully used in past studies. The principle advantage of the continuum approach is that it makes use of the same solution techniques as a regular CFD solver. These solvers are well developed, fast, stable and scalable.

[2]Changing n to any other value seems to have little impact

In contrast, the advantages of the Lagrangian model are that it is conceptually closer to the physics of real droplets, and that it tracks the history of each particle. This means that it is more broadly applicable and can be used in cases where the continuum assumption is invalid, for example with large droplets (Novozhilov et al., 1997), where droplet-radiation coupling is important (Sinai and Stopford, 2001), or where particle residence time is of interest (Xia and Leung, 2001).

4.8 Radiation model

In general, the transfer of heat in a fluid is modelled by the energy equation (Equation 4.6). Heat transfer by convection and conduction is easily handled by this equation, as those modes of transfer are simple flow phenomena. According to Wen et al. (2001) radiative heat transfer can account for 30–40% of the heat output of a large fire.

Heat transfer by radiation occurs when thermal energy is transferred by the photons of electromagnetic radiation that are released by excited molecules. The amount of radiation given off by a substance is a function of its temperature. As photons can travel great distance through a vacuum or transparent media (such as air and water) it is not really a flow phenomenon, and so cannot be modelled as such. Instead, the effect of radiation is accounted for in the energy equation by use of a source term, which must be supplied by a separate radiation model.

A complete, generically applicable, radiation model is expensive as:

- radiation is transferred between every pair of cells with line of sight of each other. The cost of calculation is therefore proportional to the number of cells squared.
- emission and absorption of radiation varies with frequency. The electromagnetic spectrum must therefore be split into a number of discrete bands.
- radiation may be reflected, refracted, diffracted, scattered or absorbed.

In practice, there are a range of simplifying assumptions that may be appropriate for any given problem, and so a number of different radiation models have been developed and coded into common CFD packages.

For example, *Fluent* includes: P-1, Rosseland, discrete transfer radiation model (DTRM), Surface-to-Surface (S2S), and discrete ordinates (DO). Of these models, only P-1 and discrete ordinates are able to account for particles such as water droplets, and only DTRM, DO and S2S are suitable for optically thin[3]materials.

DO is therefore the only applicable model if the effects of water mist due to radiative heat-transfer and/or shielding are to be considered.

4.8.1 Discrete ordinates (DO) model

The discrete ordinates (DO) model as used by *Fluent* was proposed by Raithby and Chui (1990), and details of the model can be found in a variety of sources (Fluent, 2002).

In summary, the model uses the same spatial and temporal discretisation as the fluid domain, but with an additional angular discretisation (see Figure 4.10) and spectral discretisation.

The angular discretisation is necessary because the radiative energy flux is a tensor rather than a vector (like momentum) or scalar (like pressure). A further level of discretisation maybe necessary if a particular direction is not exclusively outgoing or exclusively incoming at a certain face.

The intensity of each ray increases due to emission within the cell, and inscattering from other directions, but decreases due to absorption and outscattering.

$$\frac{dI}{ds} = -(a + \sigma_s)I + (aI_b + \sigma_s \bar{I}) \tag{4.41}$$

Where

a is the absorption coefficient (m^{-1}),

σ_s is the scattering coefficient (m^{-1}),

[3] *Optical thickness* is the product of absorption coefficient (a) and a length scale (L) such as the diameter of the fire or height of a tunnel

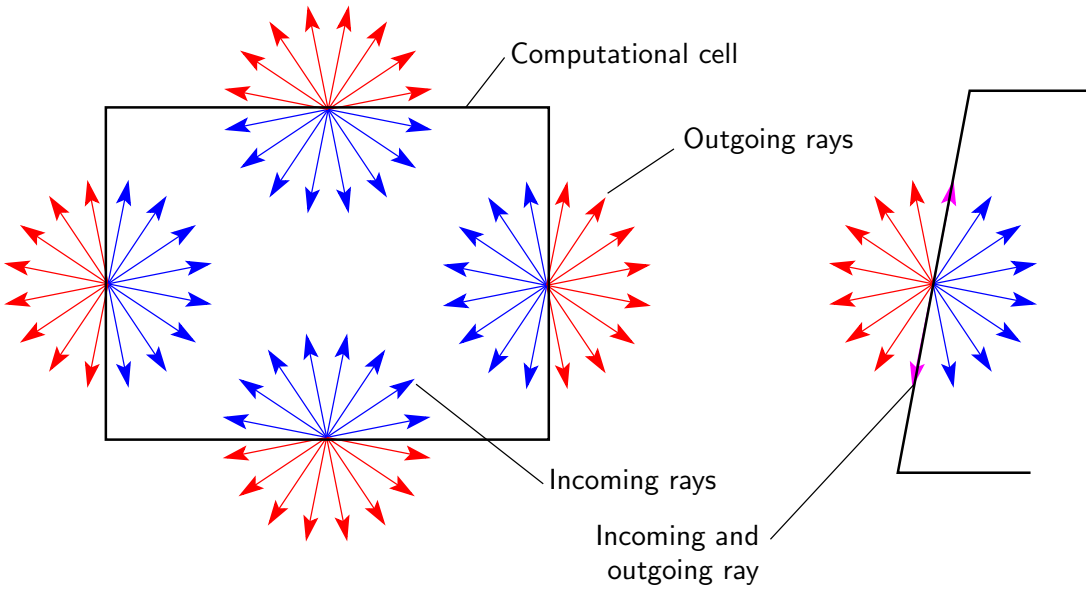

Figure 4.10: Angular discretisation for DO model

I is the radiation intensity (W/m^{2}sr),

I_b is the black body intensity,

$\bar{I}$ the scattered intensity, and

s is the path length (m).

The absorption coefficient is both composition and temperature dependent, and is calculated using the weighted sum of gray gases model (WSGGM). In cases where the composition of the mixture varies significantly there may also be a frequency dependency as the different components may absorb/emit at different frequencies.

McGrattan (2005) suggests that six bands is usually enough for most combustion problems, although as many as nine can be beneficial, particularly if the absorption of the fuel is known to be important (See Figure 4.11). In some studies involving water mist as many as 47 bands have been used (Yang et al., 2004), although this is almost certainly overkill for anything except studies primarily interested in radiation, given that the absorption of radiation by the mist is generally a minor effect.

It is also noted that in many large-scale fires the soot is the most important component for radiation, and as that has a continuous spectrum a single band can be used.

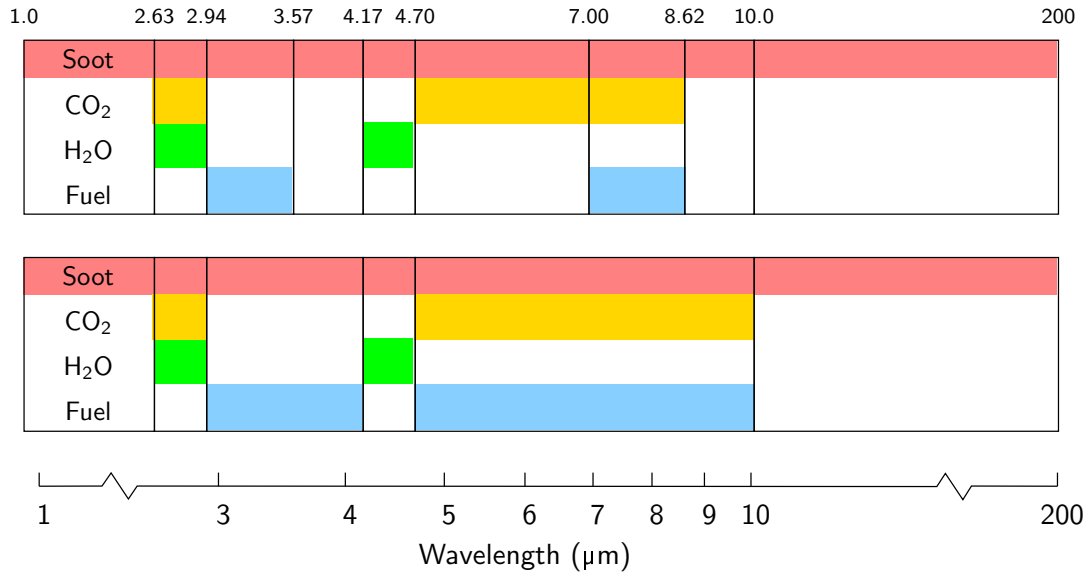

Figure 4.11: Discretisation of the spectrum into six and nine bands (adapted from McGrattan, 2005)

As there is often only a weak coupling between radiation and the Navier-Stokes equations, and as the radiation equation is expensive to solve (due to the high level of discretisation) it is sensible to solve it less frequently, say once every 10 iterations.

4.8.2 Weighted sum of gray gases model (WSGGM)

Any gaseous substance has an individual emission spectrum (and a corresponding absorption spectrum). A *gray gas* is a gas that emits and absorbs over a wide range of frequencies, whereas a *non-gray* gas has a stronger emission in certain areas of the spectrum than others, and possibly emits at quite specific frequencies.

> The weighted-sum-of-gray-gases model (WSGGM) is a reasonable compromise between an oversimplified gray gas model and a complete model which takes into account particular absorption bands.
>
> (Fluent, 2002)

WSGGM is used to calculate an absorption coefficient for a mixture of real gases but accounting for the possibility that gaps exist in the combined absorption

spectrum. The consequence of these gaps is that the total absorption is less than the sum of the individual absorptions from each species.

4.8.3 Interaction of thermal radiation and water mist

A full treatment of the effects of water mist on the radiation field is complex, and would be too computationally costly to include in a large scale CFD model. This is because:

1. the absorption characteristics of a droplet is a function of diameter and wavelength, with *"maximum attenuation ... when droplet radius is equal to the wavelength"* (Ravigururajan and Beltran, 1989)
2. the scattering of radiation by the droplets can be significant. This increases the potential for attenuation (as the mean path length is increased), and reduces the peak radiation intensity due to the more uniform distribution of the radiation energy. The scattering phenomenon is, again, diameter and wavelength dependent, but also anisotropic.

A more simplistic treatment of particle–radiation interaction is feasible, and is optionally implemented in *Fluent* as part of the particle heat transfer calculation:

$$m_p c_p \frac{dT_p}{dt} = hA_p(T_\infty - T_p) + \epsilon_p A_p \sigma(\theta_R^4 - T_p^4) \tag{4.42}$$

Where

m_p mass of the particle (kg)

c_p heat capacity of the particle (J/kg-K)

A_p surface area of the particle (m^2)

T_∞ local temperature of the continuous phase (K)

h convective heat transfer coefficient (W/m^2-K)

ϵ_p particle emissivity (dimensionless)

σ Stefan-Boltzmann constant (5.67 x 10 $^{-8}$ W/m^2-K^4)

θ_R radiation temperature, $(\frac{G}{4\sigma})^{1/4}$

The use of the droplet surface area (A_p) and the radiation temperature (θ_R) implies that radiation is assumed to be isotropic.

The particle emissivity (ϵ_p) could be supplied by a user defined function (UDF), and so could be diameter-dependent (assuming sufficient data were available), but not wavelength-dependent.

4.9 Choice of CFD code

The term 'CFD code' is used to refer to any computer software that implements the techniques described in this chapter. This can range from highly specialised programs, written by an individual for a single application, to large commercially-developed *general purpose* codes, such as *CFX* or *Fluent*. Olenick and Carpenter (2003) list 17 CFD codes with capabilities for modelling fire and/or smoke. Their paper is backed up by an invaluable web-site `http://www.firemodelsurvey.com/` which provides a more detailed comparison of the various codes than could be presented in their paper.

A number of factors affect the choice of CFD code for a given application:

Features Obviously to be any use a CFD code must include all the required modelling capabilities, but other features, such as import/export of other file formats, particular types of post-processing and so on, maybe significant.

Flexibility For particularly novel applications, (or in cases where a particular CFD code lacks a certain feature), it may be necessary for the user to modify or extend the code. Many codes allow for 'user defined functions', typically written in a common high-level language such as C, FORTRAN, or C++.

Ease of use 'Ease of use' is a wide ranging issue, that can mean very different things to different people, and so is hard to judge objectively. It includes quality of documentation, design of user interface, integration with the operating system, stability of software, and so on. Of particular importance is the user's (or the user's colleagues') existing experience.

Cost and performance All other things being equal, the code that completes the simulation first is best. However, there is a clear link between cost and performance, for example, it maybe be better to purchase multiple licenses of a cheaper code, or to spend more on the computer hardware and less on software.

Sections 4.9.1–4.9.3 give an overview of some of the common CFD packages in this field.

4.9.1 FDS

Fire Dynamics Simulator (FDS) is an open-source CFD code developed by the National Institute of Standards and Technology (NIST). It is designed specifically for fire applications, and as such falls somewhere between the general purpose CFD codes and highly specialised codes. Originally developed in the 1980s for in-house use, it was first publicly released in 2000, and as of July 2004 has reached version 4.0. Although it lacks many of the features of commercial CFD codes, it is well documented (McGrattan, 2005; McGrattan and Forney, 2005), simple to use, and (due to the availability of the source code) easily extended or modified. It is fairly popular within the field of fire engineering (DMT et al., 2004a,b; Kim and Ryou, 2003; Ma and Quintiere, 2003).

Based on LES turbulence and mixture fraction combustion, it uses a form of the Navier-Stokes equations optimised for low-speed, buoyancy driven flows. It has been extended with optional DNS turbulence, finite-rate chemistry, and Lagrangian sprinkler models. The latest version supports parallel processing.

The solver uses finite differences on a regular rectilinear grid. Multiple grids and 'obstructions' can be used for creating simple geometries, however curved (or even sloping) geometries are difficult. The user interface is based on text input and output files. A separate post-processor, *smokeview* is used to provide basic visualisation facilities.

Ma and Quintiere (2003) validated *FDS* (version 2.0) for unconfined fire plumes by using well established correlations between the non-dimensional fire power and properties of the plume, such as Froude number, flame temperature, flame height, and entrainment number. They showed temperatures near the burner to

be over-predicted, but temperatures and velocities outside the combustion region were predicted well.

4.9.2 Fluent

Fluent is the leading commercial CFD code. Originally released in 1983 as an *"easy-to-use interactive CFD software code for engineers"*, it is now in use in a diverse range of applications from aerospace and automotive to biomedical and food & drink (Fluent, 2005).

Its finite volume solver allows unstructured meshes with a variety of element types. Mesh adaption can be used to refine the mesh during a solution. A wide range of turbulence and combustion/chemistry models are available, as well as a generic Lagrangian particle model, which can be used to model a discrete phase such as water droplets.

Although the source code is not available, it is possible to modify the behaviour of the solver using user defined functions (UDFs) written in C. The code is controlled either using a graphical user interface, or via text commands either entered interactively, or read from an input file.

4.9.3 CFX

CFX is the main competitor to *Fluent*. Originally developed by the Atomic Energy Authority (AEA) in the UK, it has changed hands a number of times, and is now part of a collection of engineering software tools from ANSYS. It includes most of the features of *Fluent*, and (to an inexperienced user) a user interface that seems more consistent and logically arranged.

At the time this work was started *CFX* was in the process of transitioning from a structured-grid solver to an unstructured solver. There were therefore two separate versions on the market simultaneously, with many features only being available in one or the other.

4.9.4 Summary

At the time this work was commenced, *Fluent* represented the best choice of CFD code. It is widely used and supported within the University, and also provides a comprehensive list of features. In particular it had the best support for the Lagrangian particle model, which was only in an early stage of development in other codes.

In some cases, *FDS* was also tested. As it was designed from scratch for fire scenarios, it was simple to set up, and given the absence of license restrictions it could be used to run many cases simultaneously. However some of the models and features, showed a lack of maturity, or were overly simplistic, and it was therefore difficult to achieve confidence in the simulation results.

4.10 Example CFD studies

CFD is frequently used to perform simulations of the behaviour of fire, examples of which can be found in almost any issue of journals such as the Fire Safety Journal, and Combustion and Flame.

In Sections 4.10.1 and 4.10.2 some examples of published studies that relate specifically to tunnel fires or the application of water mist have been described.

4.10.1 Tunnel fires

One of the most notable examples of CFD studies related to tunnel fires is the modelling of the King's Cross Underground fire by (Simcox et al., 1992). This is often cited as a demonstration of the predictive power of CFD, as the model showed unexpected behaviour (the *Coanda* effect) that was subsequently demonstrated experimentally. The modelling is particularly crude when compared to more recent studies, neglecting combustion and radiation, and using an incredibly coarse grid.

Woodburn and Britter (1996a,b) performed simulations of experiments carried out by HSE in a horizontal tunnel, using FLOW3D (now CFX). They used the

eddy breakup model with a fixed fuel release, and had a more reasonable grid than Simcox et al.. The simulations were able to capture a backflow similar to that seen in the experiments.

Lea et al. (1997) also performed simulations based on experiments carried out by HSE, again in a horizontal tunnel (possible the same as above), but containing a one-third scale model of a Channel Tunnel train and HGV carriage. Validation was performed against measured velocities and temperatures. The results were better than those from a previous CFD model by the same authors carried out on the same grid. The difference is attributed to use of buoyancy modification in k-ε model, second order discretisation, and a more stable radiation model (Discrete transfer method instead of Monte-Carlo method).

More recently there are various examples of tunnel fire simulations performed for the purpose of determining empirical relationships for critical ventilation velocity (Hwang and Edwards, 2005; Wu and Bakar, 2000). These generally include radiation modelling, but are otherwise similar to the earlier studies. Hwang and Edwards (2005) is notable as LES turbulence modelling is used as k-ε is seen as having too many drawbacks for fire applications:

- uses time-averaged approximations leading to overly 'smooth' results.
- assumes high Reynolds number.
- assumes isotropic turbulence.
- needs wall functions.

However, it could be argued that the mesh resolution they use is not really sufficient for an LES model.

Reference	Details	Code	Turbulence	Combustion	Mesh	Radiation	Validation
Simcox et al. (1992)	Inclined escalator tunnel	FLOW3D[a]	k-ε	–	10 cells over height	–	[b]
Woodburn and Britter (1996a,b)	40 m × 2.5 m × 2.5 m, 1 m^2 kerosine pool fire (2.3 MW). 1.72 m/s ventilation	FLOW3D	k-ε	EBU fixed fuel release	30 cells over height	–[c]	Bettis et al. (1993)
Lea et al. (1997)	47 m long × 2.4 m high concrete tunnel obstructed by train, 2 MW kerosene pool	CFX4	k-ε	EBU fixed fuel release	32 cells	yes	Velocity, temperature and back flow length
Wu and Bakar (2000)	0.25 m × 0.25 m × 8 m, 106 mm propane burner	*Fluent*	k-ε	prePDF	28 cells over height	–	LDA velocities
Hwang and Edwards (2005)	853 m × 8.6 m × 7.0 m heptane pool	*FDS*	LES	mixture fraction	30 cells over height	yes	

Table 4.2: Summary of some published CFD studies related to tunnel fires

[a]FLOW3D is now CFX
[b]based on real events, and subsequently validated against scale experiments performed by HSE
[c]In some runs, a 30% reduction in fuel release was made to compensate for lack of radiation losses

4.10.2 Water mist fire suppression

There are several published studies of water mist fire suppression using CFD techniques. These numerical studies tend to focus either on the fundamental behaviour of mist (i.e. geometrically simple (e.g. one dimensional, monodisperse droplets, etc.), but with detailed physical modelling (e.g. LES/DNS turbulence, multi-band radiation, multi-step combustion, etc.) or are application-driven (i.e. intended to replicate a real fire suppression scenario).

Many of the early studies related to water mist are, strictly speaking concerned with traditional sprinkler systems (Nam, 1996; Novozhilov et al., 1997). For example, Novozhilov et al. (1997), simulates the extinction of a wood fires by a spray with a SMD of 410 µm. The fire consists of a number of wooden slats on a vertical frame in a tunnel ventilated at 0.7 m/s. The spray is represented by a Lagrangian model, with drag force and evaporation calculated as in Section 4.7.1. The computational mesh has 55 cells over the tunnel height, with a coarser mesh for the radiation model. Droplets reaching the wood surface are assumed to vapourise instantly, however, as pointed out by Novozhilov et al. the true behaviour is much more complex. As solid-phase cooling is the dominant mechanism of extinction this is a significant issue.

Prasad et al. (1999) uses CFD techniques to simulate the water mist suppression of liquid methanol pool fires. A detailed model for the pool is proposed, which accounts for the energy transfers (conduction, convection, and radiation) to and from the pool, and calculates the rate of evaporation of methanol across the surface of the pool using the *Clausius-Clapeyron* pressure (see Equation 2.3).

Within the fuel, heat is transfered by conduction only, and is calculated using an unsteady Laplacian relationship.

The combustion process is modelled by a simplified single-step reaction mechanism. The rate of reaction is calculated using a *laminar flame model*.

The *Eulerian* form is used to represent the water-mist, where the 'droplet properties are treated as if they were continuous in the domain of the gaseous properties'. To simplify the equations, the continuous range of droplet sizes is split into a small number (five) of 'sections'. Each section is assumed to have a single droplet diameter, and uniform droplet properties. Transport equations for the

concentration n_i (drops/m^3) of each size are developed, which permit evaporation to the next section. Each section is solved independently, and is coupled to the gas phase through source terms.

Hua et al. (2002) applies CFD techniques to a similar problem, but uses a Lagrangian particle model similar to the *Fluent* DPM. A k-ε turbulence model and the EBU combustion model are used. The study does not consider radiation or ventilation.

Sinai and Stopford (2001) and Sinai (2003) use CFX-4 to simulate the extinction of a 30 cm heptane pool fire in a 96 m^2 enclosure. A Lagrangian particle model is used, which is coupled to the discrete transfer radiation model. Details of the water mist system is unclear, however the maximum droplet size would appear to be 525 µm. The simulation is performed on two different grids. On the first, with 9200 cells, the fire is extinguished, whereas on the second, with over 100,000 (i.e. more than double the number of cells in each direction), there is merely a drop in the overall heat release rate.

Kim and Ryou (2003) performed tests of water-mist extinction of pool fires in a room-like enclosure, and subsequently modelled the scenario using *FDS*, which includes a Lagrangian particle model.

There are also references to CFD modelling of mist in promotional material by WMFSS manufacturers and CFD code developers (e.g. Adiga, 2004) however these tend not to give minimal detail and are therefore not very illuminating.

Reference	Details	Code	Turbulence	Combustion	Radiation	Mist	Validation
Novozhilov et al. (1997)	Wooden slats	FIRE	mod. k-ε	EBU	discrete transfer	Lagrangian	Burning rate, Temperature
Prasad et al. (1999)	1 cm methanol pool	FCT-based	laminar?	finite rate	yes	Eulerian	
Prasad et al. (2002)	0.74 m^2 propane in 23 m^3 enclosure[a]	FCT-based	?	?	yes	Eulerian	none
Sinai (2003); Sinai and Stopford (2001)	0.3 m heptane 96 m^3 enclosure	CFX-4	mod. k-ε	EBU	Discrete Transfer	Lagrangian	–
Hua et al. (2002)	0.25 m methane burner in open environment	*Fluent*	finite rate	EBU	–	Lagrangian	–
Kim and Ryou (2003)	0.3 m methanol/hexane pool 32 m^3 enclosure	*FDS*	LES	mixture frac.	yes	Lagrangian	yes

Table 4.3: Summary of some published CFD studies related to WMFSS

[a]based on Uniform Building Code Standard fire test

4.11 Summary

Computational Fluid Dynamics (CFD), is a powerful technique that, when used correctly, can simulate a wide range of complex phenomena. When supported by relevant experimental data it has the potential to deliver a comprehensive picture of the behaviour and performance of fires and water mist suppression systems.

A realistic CFD model must represent all the phenomena involved, and given the need for various models to interact, the following sub-models were selected:

- k-ε turbulence,
- Lagrangian discrete phase model (DPM),
- discrete ordinance (DO) radiation model, and
- hybrid Arrhenius/eddy breakup combustion model.

A commercial CFD code, called *Fluent* was selected, the most recent version of which is 6.2.16, although some of this work was performed with versions 6.0 and 6.1.

In Chapters 5–7 CFD techniques are applied to the modelling of a range of scenarios leading up to a model of the water mist suppression of a large tunnel fire.

Chapter 5

CFD modelling of an enclosure fire

In this chapter, a CFD model for a pool fire in an enclosure is developed and tested. The sensitivity of the model to variation in key parameters such as time step size, mesh resolution and boundary conditions is explored. The model is based on experimental data published by Kim and Ryou (2003). The pool fire model is applied to a tunnel fire scenario in Chapter 6, and is extended to include water mist fire suppression for both the enclosure and the tunnel fire in Chapter 7.

The aims of this chapter are to demonstrate that a pool fire can be modelled; that appropriate sub-models exist to model the various physical processes of such a fire; and to develop an understanding of the various numerical parameters of the models, such as under-relaxation factors, time-step size, etc. This will give a firm basis for the later development of the model to include water mist fire suppression.

5.1 Background

Kim and Ryou (2003) investigated the extinction of methanol and n-hexane pool fires in an enclosure using water-mist. They compare their experimental data with a CFD model using the *FDS* (Fire Dynamics Simulator) code.

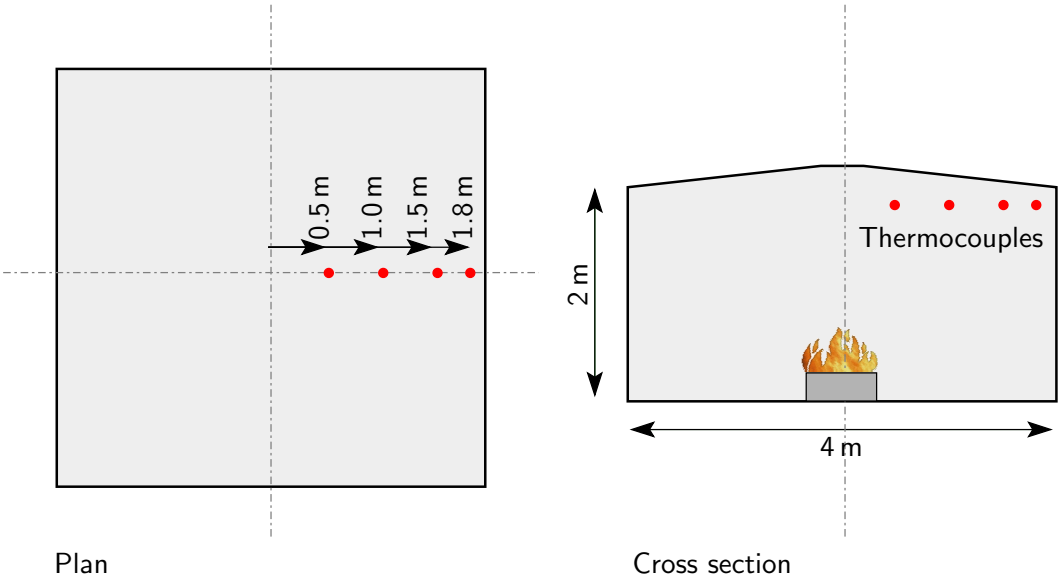

Figure 5.1: Schematic view of experimental setup (Kim and Ryou, 2003)

5.1.1 Enclosure

The experiment was carried out in a $4 \times 4 \times 2\,\text{m}$ steel walled enclosure (see Figure 5.1). During the experiment there was no ventilation to the enclosure (Ryou, 2004, private communication).

An array of K-type thermocouples was placed within the enclosure. In particular, the ceiling temperatures were measured by four thermocouples at a height of 1.8 m.

5.1.2 Fire

The series of experiments used methanol and *n*-hexane in 0.3 m and 0.4 m square pans, to give four different fire sizes. The average rate of combustion and heat release was calculated in terms of the mass of fuel consumed. (See Table 5.1). The pan is stated as being 5 cm deep, but it is not clear whether there was a 'lip' above the fuel surface. The presence of a lip can have a significant effect on the rate of combustion (see Section 2.1.3). The pan was located in the centre of the enclosure at an unspecified height above the floor (see Figure 5.1).

Table 5.1: Fire configurations used in experimental enclosure fire (Kim and Ryou, 2003)

Fuel	Pan Size (m)	Burning Rate (kg/m^2s)	Heat (kW)
Methanol	0.3	0.0148	26.64
Methanol	0.4	0.0155	49.60
n-Hexane	0.3	0.0284	114.51
n-Hexane	0.4	0.0270	193.10

5.2 CFD model

5.2.1 Meshing

For the initial studies outlined below, a 2D-axisymmetric mesh was created based on a circular enclosure (and burner) of equal floor area, fuel surface area, and therefore enclosed volume as the real enclosure. The area of the side walls is consequently overestimated by 13%.

For the later 3D simulations, symmetry was exploited to minimise the volume that needed to be modelled. The geometry of the enclosure has 3-fold symmetry, so potentially only one eighth of the volume needed to be modelled. For hexahedral meshes it is more practical however, to model one quarter of the enclosure, taking advantage only of the more natural symmetry planes aligned with the principle axes.

A boundary layer was used for the pool surface and the enclosure ceiling, due to anticipated high gradients due to the diffusion of fuel and the impinging plume (see Figure 5.2).

5.2.2 Fuel source

In order to produce a well grounded model of a pool fire, the various forms of heat and mass transfer between the pool and the enclosure need to be considered: heat transfer from flame to pool; heat lost from pool to surroundings; and evaporation of fuel (see Figure 5.3).

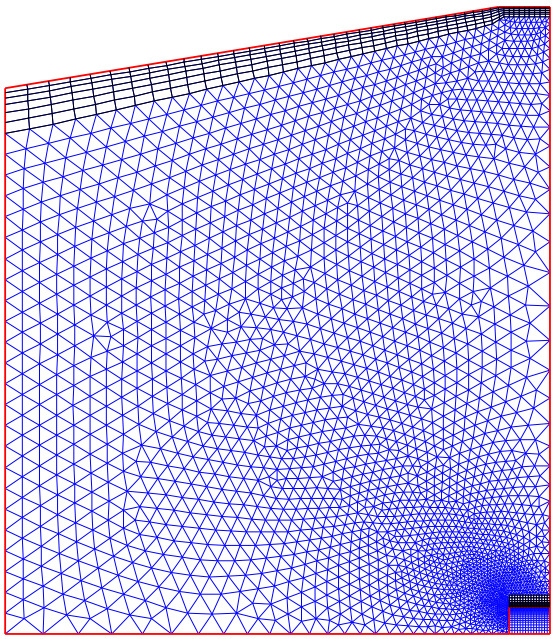

Figure 5.2: 2D mesh: $\sim$4000 cells. Boundary layer shown in black.

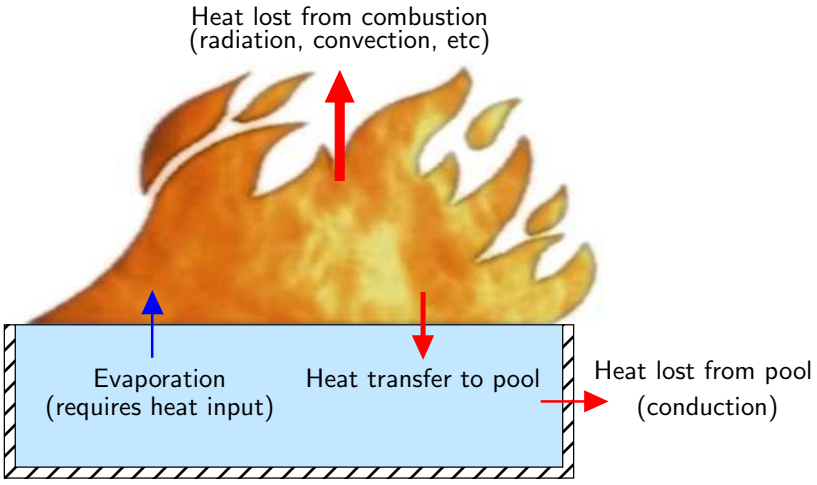

Figure 5.3: Heat transfer in pool fire

In this study, the pool is represented as a *solid* region within the computational domain, that is assigned the thermal properties (specific heat, thermal conductivity, etc.) of *liquid* methanol. The effect of the side walls were neglected (i.e. the wall is assumed to have zero thickness, and there is no lip above the fuel surface). The base of the pan is taken to be adiabatic. To model the release of fuel vapour, the air side of the upper boundary of the pan is assigned a fixed value for the mass fraction of fuel (by default all walls have a zero-diffusivity condition). As methanol has a low boiling point, the mass fraction was taken as 1.0, in order to saturate the air above the pool (see 5.2.4). At this stage the latent heat of evaporation was neglected. In principle a heat sink (i.e. negative source) term could be applied to the solid region, however no direct method could be determined to quantify the rate of evaporation.

5.2.3 Multi-phase and combustion

For the purposes of the CFD model, the life of the fire was considered to consist of three distinct phases: fire development; constant burning; and suppression.

In the fire development phase, combustion was modelled using the Eddy Break Up (EBU) model (see Section 4.6.2.1). This is based solely on the mixing of fuel with oxidiser, so there was no need to provide a source of ignition.

Early simulations showed an unrealistic 'fireball effect' due to the release of a large quantity of fuel into a zero airflow initial condition – leading to unrealistically high temperatures before the establishment of a buoyant plume. To avoid this effect, the release of fuel volatile was controlled by a user defined function (*UDF*) that increased the mixture fraction at the pool surface using a parabolic profile over a period of five seconds (see Figure 5.4 and Figure B.3). The mixture fraction was held constant at 1.0 for the remainder of the simulation.

Once the fire and plume were established (i.e. the steady burning phase had been reached), combustion was switched to the hybrid Arrhenius/eddy breakup model. This was adopted to allow fire suppression and extinction to be modelled, as the effect of reduced temperatures on reaction rate is taken into account (see Section 7.1). A slight drop in overall reaction rate was observed at the transition between combustion models. Parameters for the combustion chemistry where taken from the *Fluent* material library (see Table 5.2).

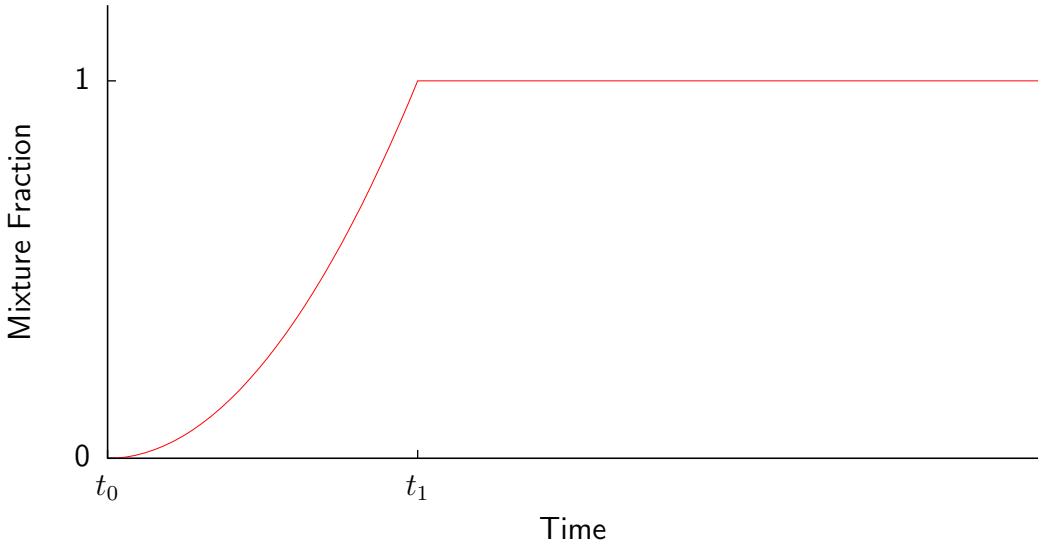

Figure 5.4: Time-dependent boundary condition for fuel surface

Table 5.2: Parameters used for EBU/Arrhenius combustion model

	Methanol	Hexane
Stoichiometric Coefficients		
Fuel	1	1
O_2	$1 \cdot 5$	$9 \cdot 5$
CO_2	6	6
H_2O	7	7
Rate Exponents		
Fuel	$0 \cdot 25$	$0 \cdot 25$
O_2	$1 \cdot 5$	$1 \cdot 5$
Arrhenius Parameters		
Pre-Exponential Factor	$1 \cdot 799 \times 10^{10}$	$3 \cdot 205 \times 10^{9}$
Activation Energy (J/kgmol)	$1 \cdot 256 \times 10^{8}$	$1 \cdot 256 \times 10^{8}$
Temperature Exponent	0	0
EBU Parameters		
A	4	4
B	$0 \cdot 5$	$0 \cdot 5$

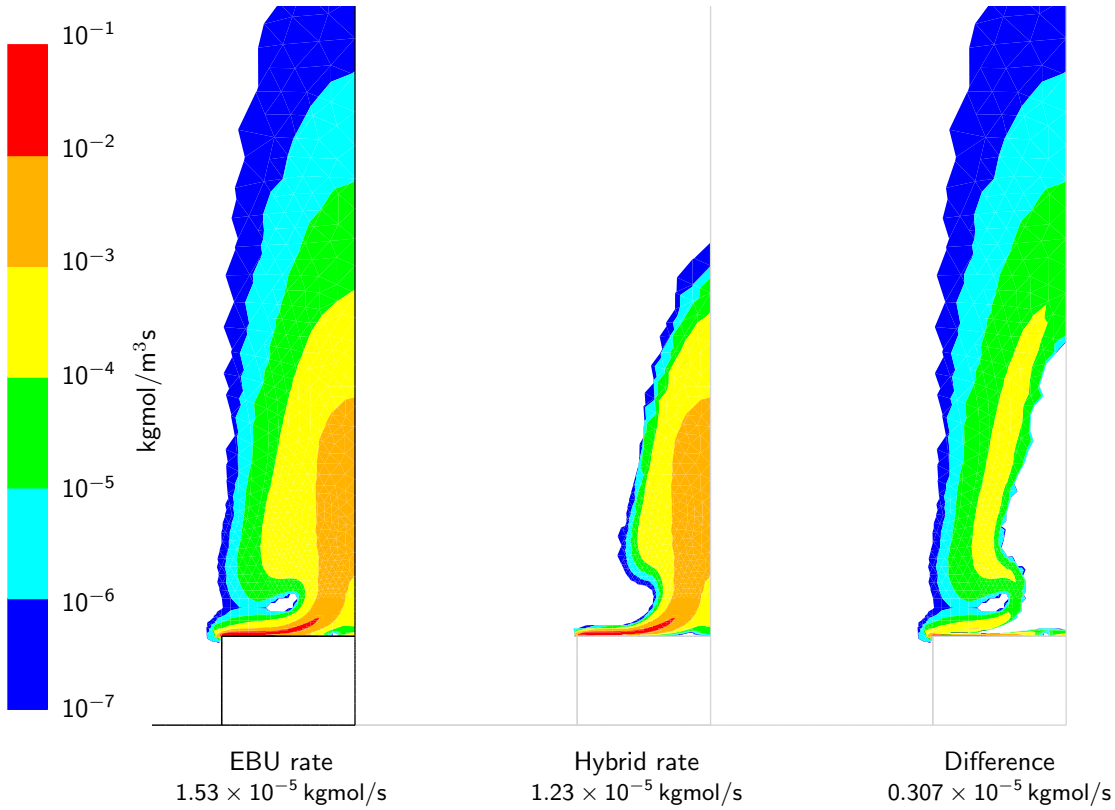

Figure 5.5: Difference between EBU reaction rate and hybrid reaction rate at transition between models (methanol fuel)

Figure 5.5 shows the difference between the EBU reaction rate and the hybrid rate of reaction (on a log scale) immediately after the hybrid model is activated (i.e. at $t = 300\,\mathrm{s}$). Although this difference seems significant, it can be shown that after a small number of time steps, the difference becomes a lot less significant, and the average rate of reaction remains unchanged (see Figure 5.6).

5.2.4 Volatilisation

In principle, the rate of evaporation of a substance from a liquid surface is dependent on both the temperature of the liquid and the vapour pressure immediately above the surface. In practice however, the temperature of the liquid is limited by its boiling point, which is relatively low for methanol.

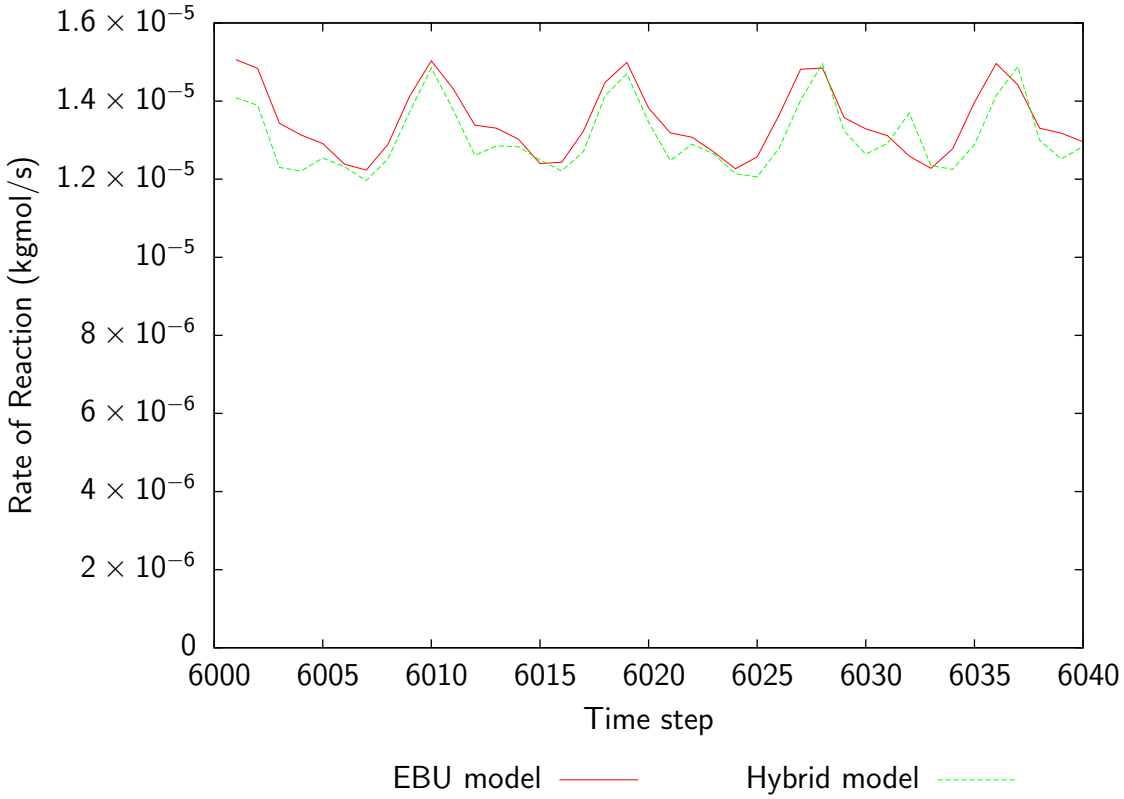

Figure 5.6: Difference between EBU and hybrid reaction rate (methanol fuel) over a number of time steps

5.2.4.1 Diffusion

The evaporation from the pool surface will (locally) saturate the gas layer immediately above it. The overall rate of evaporation will therefore depend on the rate at which fuel vapour is transported away from the pan. The pool surface is considered to be a wall, so there is a boundary layer, with zero velocity and turbulence. The fuel vapour is therefore assumed to be transported only by *laminar diffusion*.

The mass flux due to diffusion, J_i, is given by:

$$J_i = -(\rho D_{i,m} + \frac{\mu_t}{\mathrm{Sc}_t})\,\nabla Y_i - D_{T,i}\frac{\nabla T}{T} \tag{5.1}$$

where

Y_i is the mass fraction of species i,

$D_{i,m}$ is the (laminar) mass diffusion coefficient (m^2/s),

$D_{T,i}$ is the thermal diffusion coefficient (kg/ms),

ρ is the density (kg/m^3),

T is the temperature (K),

μ_t is the turbulent viscosity (kg/m-s), and

Sc_t is the turbulent Schmidt number.

In turbulent regions (i.e. the majority of the domain), the term $\frac{\mu_t}{Sc_t}$ dominates, and the contribution of $D_{i,m}$ and $D_{T,i}$ can be neglected. In a laminar region however, notably close to a surface the situation is reversed. By taking constant $D_{i,m}$, Equation 5.1 assumes that each species i is dilute in a carrier gas (i.e. $Y_i \ll 1$). In the more general case the diffusion coefficients will depend on the mixture composition (Fluent, 2002).

As there is such a steep gradient of mass fraction close to the surface, the rate of diffusion will be affected by the grid density close to the boundary. Figure 5.7 shows the steady state rate of reaction (which is equivalent to the rate of volatilisation) for different time steps, meshes and values of the diffusion coefficient.

5.2.5 Boundary conditions

The experiment consists of a enclosed room with a heat source. Equilibrium is reached because heat is lost due to conduction through the walls of the enclosure[1]. In order to model this heat loss an appropriate thermal boundary condition needs to be applied to the walls.

The two extreme cases are:

Adiabatic – zero heat loss. This implies that the wall surface temperature is the same as the local fluid temperature.

Isothermal – the wall surface temperature remains at the fixed 'ambient' temperature. This gives the maximum possible heat loss, which is determined by convection processes within the fluid.

[1]The term 'wall' will be used for the floor and ceiling of the room as well as the actual walls

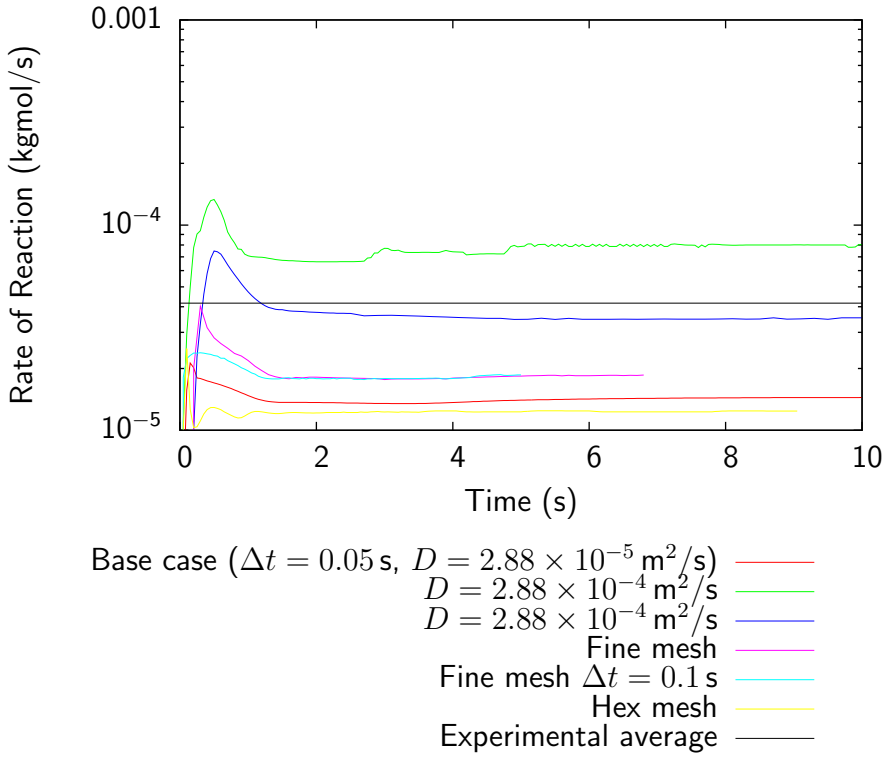

Figure 5.7: Dependence of reaction rate on diffusivity coefficient and grid

For a real wall, the surface temperature will lie somewhere between the external (or ambient) temperature, and the internal fluid temperature.

At equilibrium, and in the absence of radiation, the rate of heat loss is given by Fourier's Law:

$$Q = UA\Delta T \tag{5.2}$$

where A is the area of the wall, ΔT is the difference in temperature between 'inside' and 'outside', and U is the *conductance*. For a single layer, U is dependent on the thickness (Δx) and resistivity (K) of the material:

$$U = \frac{K}{\Delta x} \tag{5.3}$$

For multiple layers, it is the reciprocal sum of the U value for each layer.

$$\frac{1}{U} = \frac{1}{U_1} + \frac{1}{U_2} + \cdots + \frac{1}{U_n} \tag{5.4}$$

In some cases, particularly for thin walls made of highly conductive materials (such as steel plate), the layer of stationary fluid next to the wall surface can be significant (see Figure 5.8).

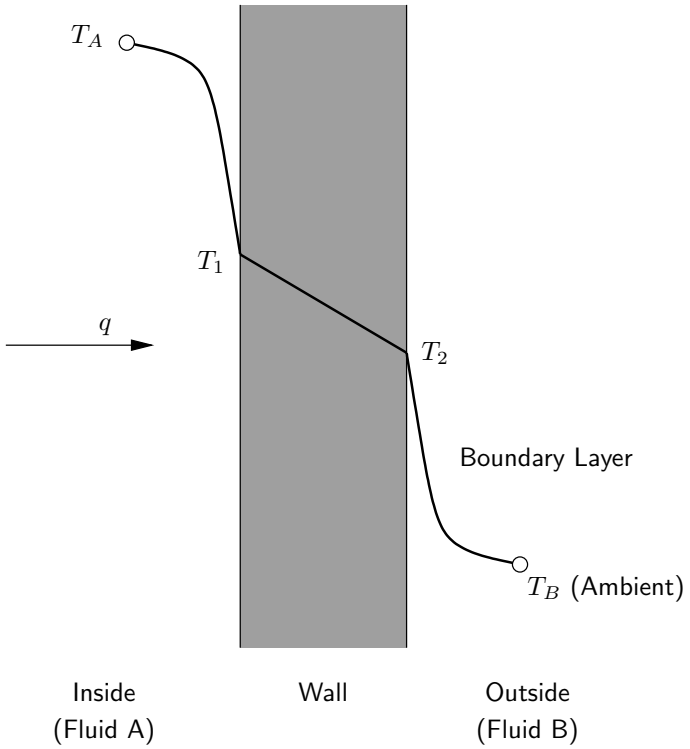

Figure 5.8: Heat transfer through a wall

In this case, the overall U value is:

$$\frac{1}{U} = \frac{1}{h_1} + \frac{\Delta x}{K} + \frac{1}{h_2} \tag{5.5}$$

Where h (W/m^2/K) is the heat transfer coefficient of the boundary layer. This gives:

$$Q = \frac{A\Delta T}{\frac{1}{h_1} + \frac{\Delta x}{K} + \frac{1}{h_2}} \tag{5.6}$$

For the case of steel walls (as used in the experiment) the boundary layers dominate the thermal resistance as the steel itself has such a high conductivity (typically around 30 W/mK depending on the specific alloy used) that it has a negligible impact on the overall resistance.

In the CFD model, the internal flow regime is known, and h_1 is computed as part of the boundary layer calculation. The external heat transfer coefficient h_2 is specified as part of the thermal boundary condition. Empirical correlations for h exist, but vary significantly with the geometry, orientation and material of the surface, as well as the external ventilation regime. The correlations are also only valid for limited temperature differences (Coulson and Richardson, 1996; Eckert

and Drake Jnr, 1972; Wolski, 1995).

When the internal temperature is unsteady, the *thermal inertia* of the wall becomes significant, because it determines how quickly the temperature profile across the wall will reach equilibrium. This will not be significant for this scenario.

Figure 5.9 shows the sensitivity of the CFD model to the thermal boundary condition. Although the adiabatic curve is a better numerical fit to the experimental values, it rises linearly with time and clearly does not follow the trend of the experimental data. The other curves (isothermal and $h = 3\,\mathrm{W/m^2/K}$ and $h = 30\,\mathrm{W/m^2/K}$) have an asymptotic shape that is more consistent with the experimental trend. The discrepancy in the temperature values could be due to radiative heating of the thermocouples, although Kim and Ryou (2003) describes them as *'sheathed'*. It should be noted that the CFD model does not utilise a radiation model.

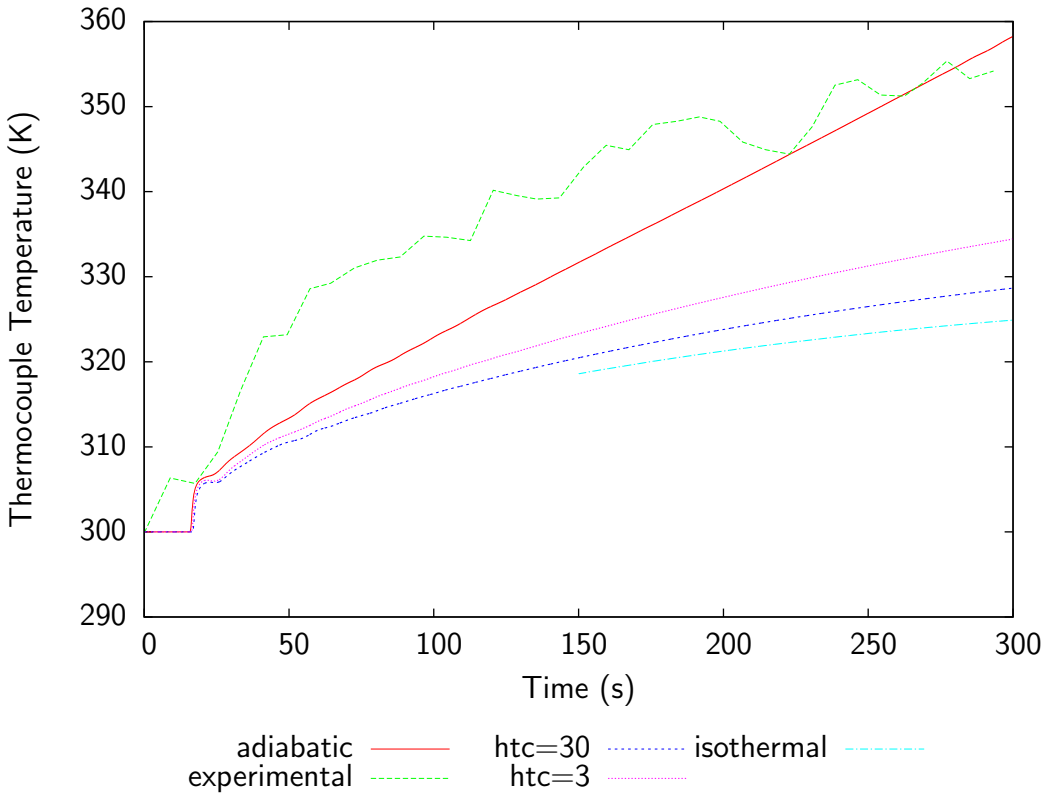

Figure 5.9: Temperature (at thermocouple $R = 0.5\,\mathrm{m}$) for different thermal boundary conditions

It is worth noting that no inflow or outflow boundaries are included in the model, and so the enclosure is completely sealed. This is not necessarily equivalent to the *no ventilation* described for the experimental facility, as there may well have

been some degree of leakage from drains, cable conduits, or closed extract ducts. However, as no information was available on their locations and magnitudes they could not be included. It has been reported by Sinai (1999a) that even small leaks can have subtle but important effects on fire behaviour.

5.2.6 Numerical scheme

In order to show that the solution to the above cases are independent of the discretisation scheme used, one of the cases was re-run with a range of time step sizes and numbers of iterations per time step. Time steps of 0.2, 0.1, 0.05 and 0.02 s were used, initially with a limit of 60 iterations per time step, and subsequently a limit of 120. Second order discretisation was used for all variables in both time and space.

These cases produced near-identical results for the monitored variables over the majority of the 300 s interval, except for the first 10 seconds and the last 50 seconds or so, where numerical instabilities led to poor convergence and random sharp spikes in rates of reaction, temperatures and air velocities (see Figure 5.10).

Further analysis of these instabilities showed that they were related to the turbulence model. By switching off the "Full Buoyancy Effect" option of the k-ε turbulence model[2] the cases ran without problem (see Figures 5.11 and 5.12), although with fractionally lower temperatures and plume velocities and a higher rate of reaction. This is not ideal, and the cause of this problem and a less drastic solution needs to be found.

At the smallest timestep (0.02 s) a small oscillation in the data was observed. It is not clear if this is a physical phenomenon or merely a numerical issue caused by a small timestep, however it does not appear to have any impact on the overall behaviour.

[2]With this option *Fluent* defines $C_{3\varepsilon} = \tanh \| \frac{u}{v} \|$. See sections 4.4.2 and 6.1.2.5.

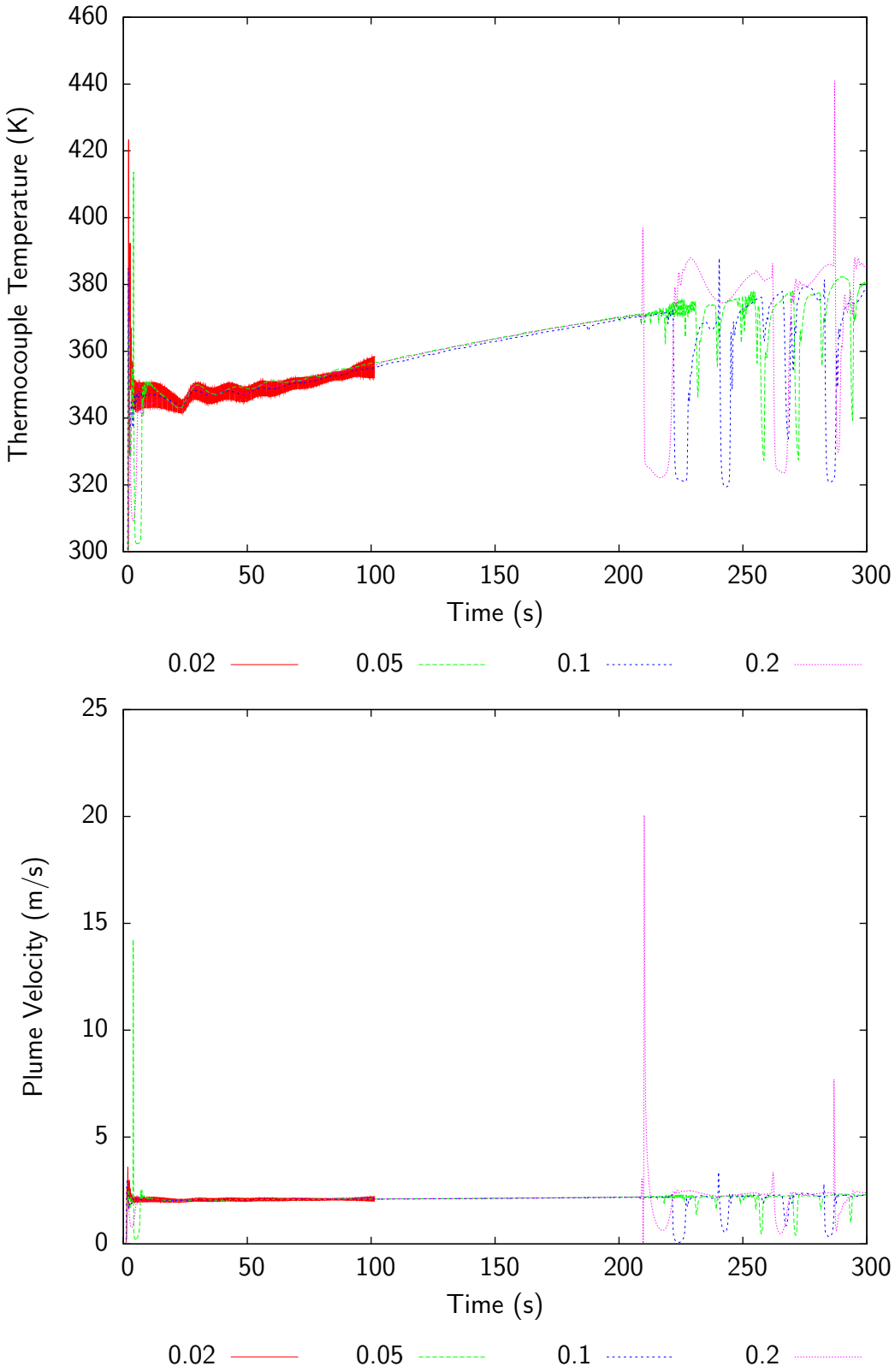

Figure 5.10: Temperature (at thermocouple $R = 0\,\mathrm{m}$) and plume velocity for different time steps with a 0.3 m diameter methanol pool fire

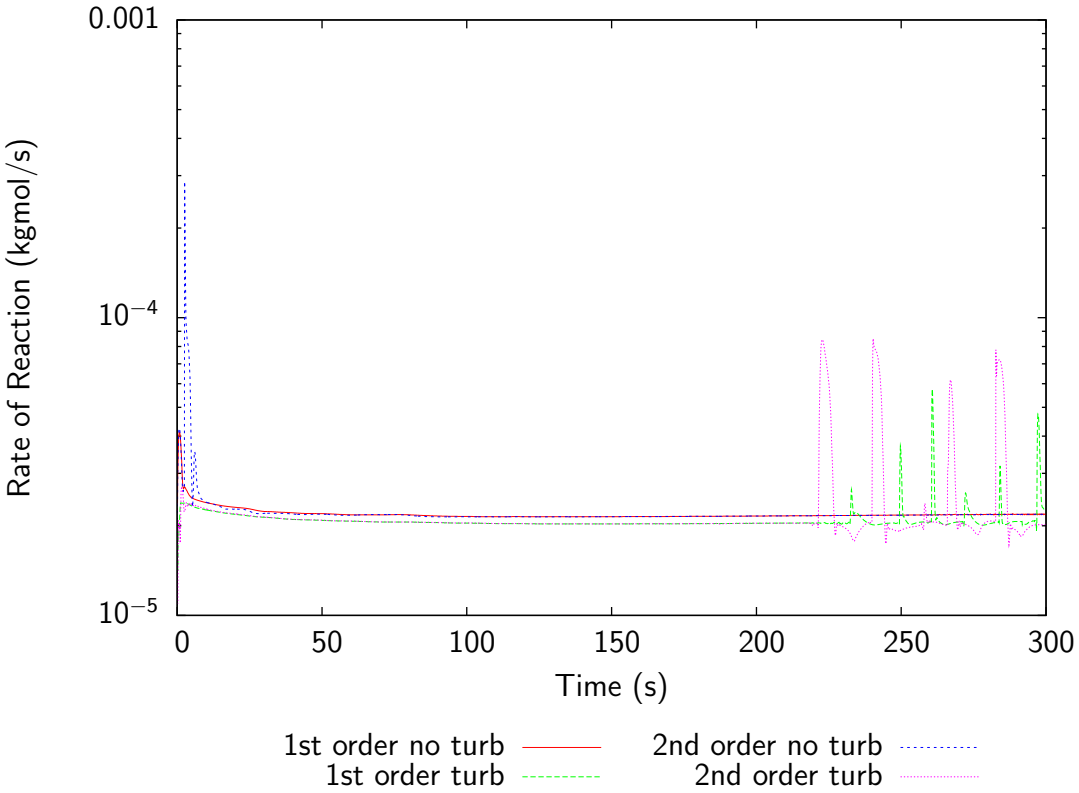

Figure 5.11: Total rate of reaction for 1st versus 2nd order discretisation and k-ε buoyancy modification for a 0.3 m diameter methanol pool fire

5.2.7 Convergence and residuals

It is standard practice to use the reduction in residuals as a measure of convergence during a calculation. Typically a reduction of 3–6 orders of magnitude is desired depending on the application. For this case however, with no inlets or outlets and an initial condition of zero velocity, the residual values for continuity are fairly low at the start of the calculation, so it is therefore okay to consider the solution converged at a lower reduction in residual than would normally be required.

On the other hand, the use of a fixed value for the mixture fraction for the fuel at the pan surface combined with the destruction of the fuel due to combustion leads to inevitably higher residual values for the fuel species. It was therefore necessary to reject the fuel residual as a convergence criterion.

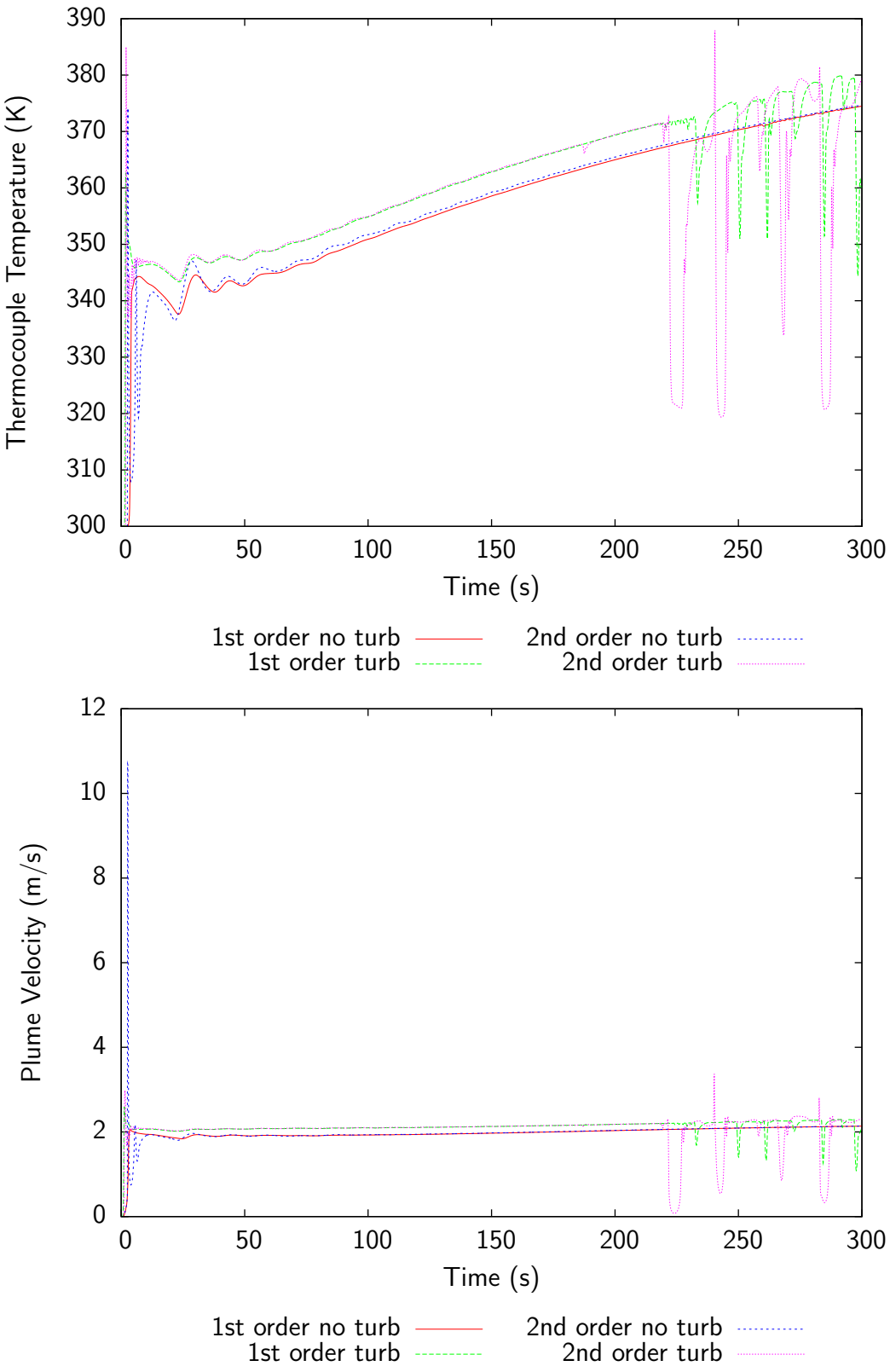

Figure 5.12: Temperature (at Thermocouple R=0 m) and plume velocity for 1st and 2nd order discretisation and k-ε buoyancy modification for a 0.3 m diameter methanol pool fire

5.3 Results

Figure 5.13 shows the temperatures predicted by the two dimensional model for the 0.3 m diameter methanol and *n*-hexane fires. The external heat transfer coefficient was 3 $W/m^2/K$, and results are shown after 300 s of elapsed time.

For both fires, the plume (i.e. the hot upward flowing region directly above the fire) is quickly established, with velocities and temperatures reaching a significant portion of their steady value within 20 s. The plume impinges on the ceiling and is deflected into the main part of the enclosure. The hot buoyant gases form a stable horizontal layer under the ceiling, which grows steadily downwards as more hot gas is supplied by the plume. The plume velocity rises gradually as the convection cell supplying the fire gains momentum. This causes a corresponding drop in flame temperature.

As the enclosure fills, the temperature at the walls and ceiling rises, the heat losses increase until they approach the heat input due to the fire and a pseudo-steady state is reached. Note that as the enclosure is sealed, the supply of oxygen in the space must eventually be consumed, at which point the fire would go out, and the enclosure would slowly cool back to ambient. Assuming perfect stratification and a constant rate of reaction, there is sufficient oxygen in the enclosure for the methanol fire to burn for 75 minutes, and the *n*-hexane to burn for 17 minutes.

5.3.1 Comparison of results with established theory

Figure 5.14 compares the temperatures predicted at the plume axis with the empirical plume temperature relationship (see Equation 2.4). The empirical form is based on a point-source, and hence will over predict the temperature in the flame region. It also does not account for the increased ambient temperature close to the ceiling, which accounts for the under prediction of temperature above 1.5 m for the hexane fire.

The CFD predicts a plume spread of 10°-15° which is consistent with the generally accepted value of around 15°.

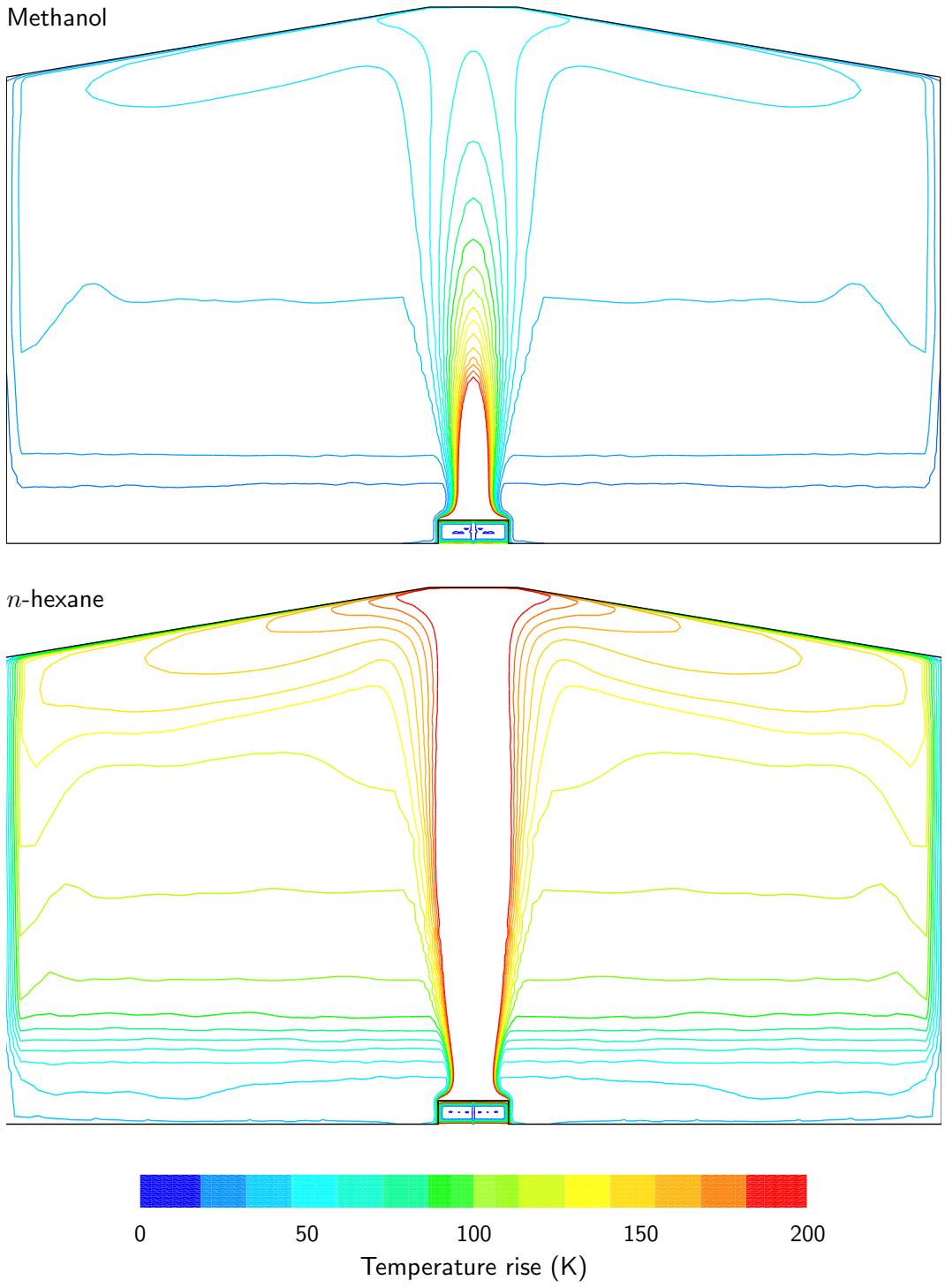

Figure 5.13: Temperature contours for 0.3 m diameter methanol and n-hexane fires at pseudo-steady state

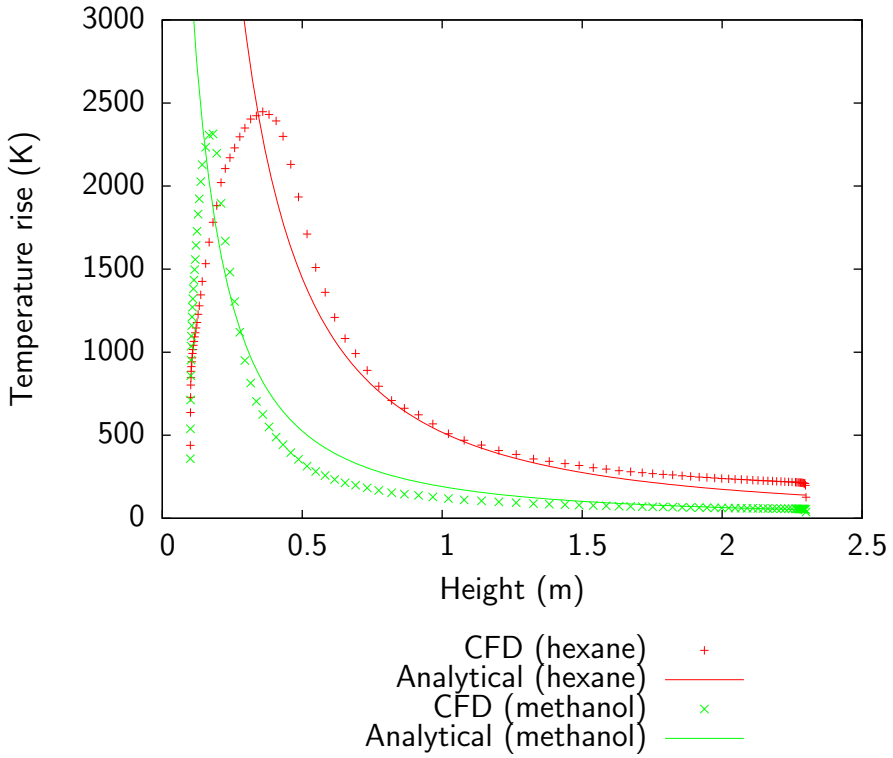

Figure 5.14: Comparison of CFD with empirical plume temperature relationship

5.3.2 Comparison of 2D and 3D cases

In order to assess whether 2D-axisymmetry is an acceptable approximation, a three dimensional version of the model was created, examined for asymmetric behaviour and compared quantitatively with the 2D case.

Table 5.3 shows the relative size and run time of the two models. Neither case required particularly large amounts of memory – a maximum of 200 MB for the 3D case.

For the 3–dimensional case, twofold symmetry was exploited to reduce the volume that needed to be modelled by a factor of four. For pragmatic reasons, the average cell size and the time step were increased by a factor of two relative to the 2D case.

Figure C.3 shows a comparison of the results of the two cases.

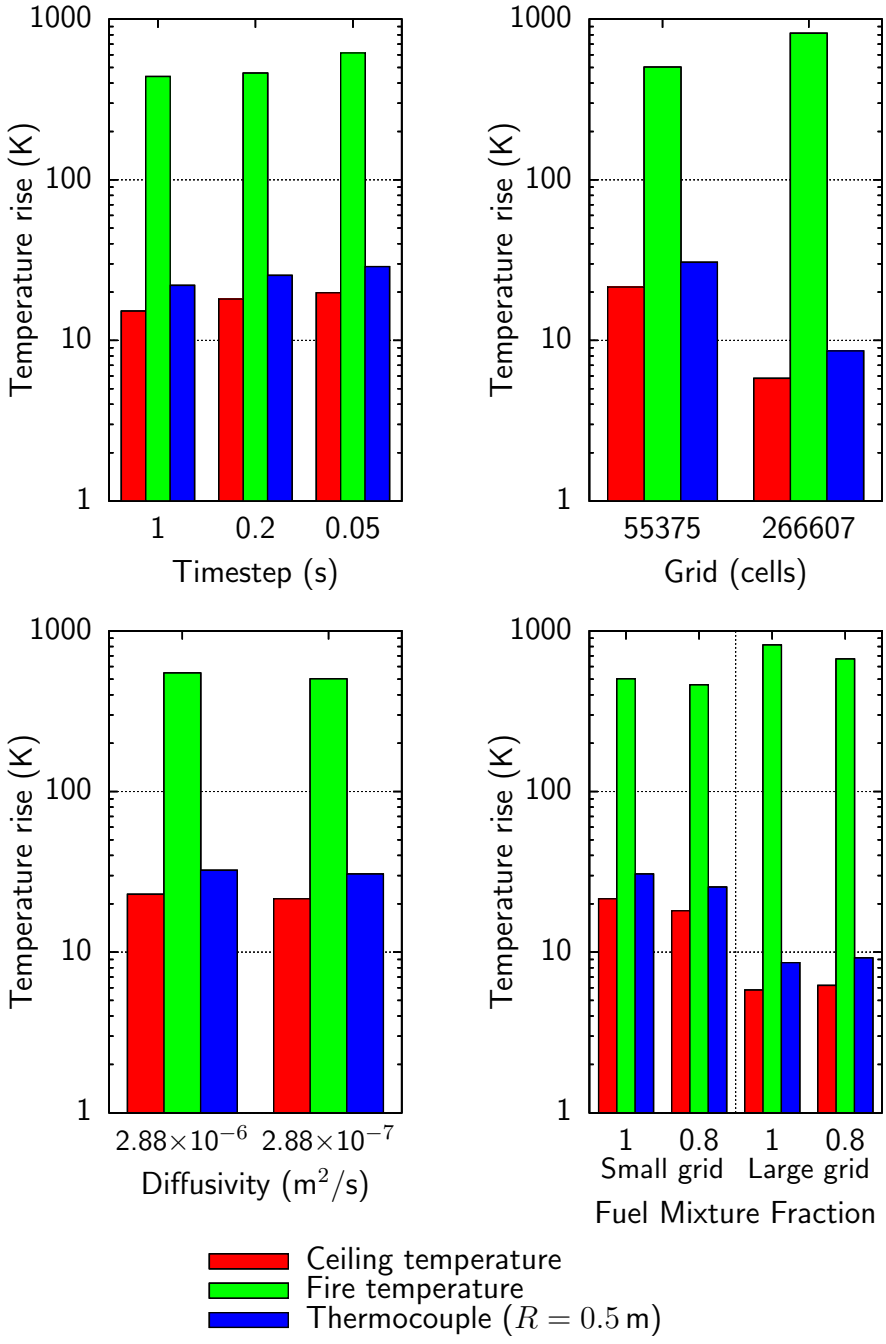

Figure 5.15: Grid and time step dependence of 3D case

Table 5.3: Parameters of 2D and 3D model

Parameter	2D	3D	3D (refined)
Number of cells	9,026	55,375	266,607
Symmetry	Axisymmetry		2-fold
Smallest cell[a](m)	0.00075	0.0027	0.00077
Average cell (m)	0.022	0.053	0.032
Largest cell (m)	0.068	0.12	0.12
Time step (s)	0.2	0.5	0.2
CPU time[b](h)	36	36	300

[a]cell size is square root of 2D cell area and cube root of 3D cell volume
[b]based on a 1.3 GHz AMD Athlon^{TM} CPU

5.4 Conclusions

- The temperature predictions of the CFD model are sensitive to the thermal boundary condition. In this scenario this does not have a significant impact on the flow field, but could be significant in more complex scenarios involving thermally driven or stratified flows.

- There are various issues associated with modelling a fully enclosed domain. It is unlikely that the enclosure was completely sealed and even small leakages can have significant effects (Sinai, 1999a) in certain cases. The lack of any external driver for the fluid flow may cause convergence difficulties or make the solution sensitive to numerical diffusion or truncation errors.

- For a low boiling point fuel in a quiescent environment, the fixed mass fraction approach to saturate the air with fuel vapour performs adequately. However, significant modification to the laminar diffusion constant was required in order to match the experimental value for the fuel release rate. This is possibly due to high temperatures, inaccurate turbulence modelling, or violation of the dilute mixture approximation.

  Other relationships for diffusion in the laminar region exist, but require detailed material properties that were not available.

- A time step of 0.2 s, and a grid with small cells in the fire plume (particularly where it impinges on the ceiling) and very small cells in the combustion region were required to achieve consistent convergence and mesh/time-step independent results. The cell dimension at the fuel surface was 0.00075 m, corresponding to 1/400th of the pool diameter.

In the next chapter, the CFD techniques used here will be extended to the case of a fire in a tunnel, particularly the behaviour of a buoyant plume in a strong ventilation flow.

Chapter 6

CFD modelling of a tunnel fire

In this chapter, a CFD model of a pool fire in a tunnel is developed and validated. Initially a simple heat source is used to represent the fire, and small scale experimental data from Wu and Bakar (2000) is used to validate the thermally driven flow regime. Subsequently, a true combustion model is used to model a full scale tunnel fire based on recent experimental data collected by DMT et al. as part of this project. The fire is approximately 10 MW and forced ventilation gives a net air flow.

The aims of this chapter are to demonstrate that a thermal plume in a ventilated tunnel can be modelled; that physical phenomena such as back flow and thermal stratification are represented by the model; and that the pool fire model developed for an enclosure fire in Chapter 5 can be applied to a tunnel fire scenario. This will form the basis of the fire suppression case that is the ultimate goal of this thesis.

6.1 Modelling of flow due to a heat source

In order to demonstrate that the CFD modelling technique is able to represent a thermally driven flow in a tunnel, it has been used to replicate part of an experimental study by Wu and Bakar (2000).

The experimental data are taken from tests carried out in small-scale tunnels for the purpose of determining an empirical relationship between heat release rate

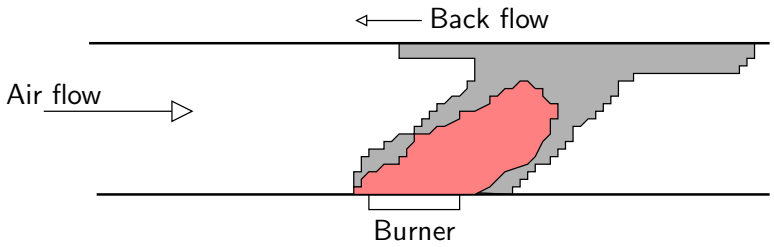

Figure 6.1: Schematic of experimental setup

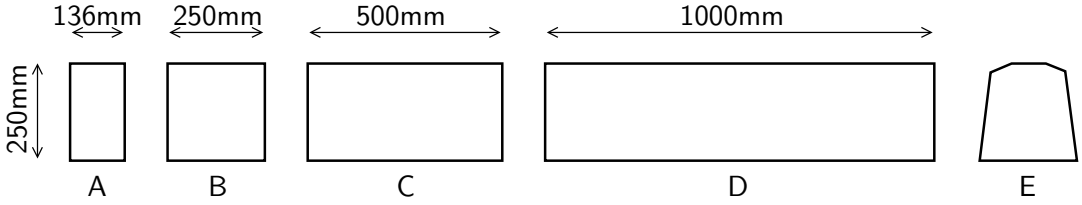

Figure 6.2: Tunnel cross sections

and the critical ventilation velocity.

Wu and Bakar compare this experimental data with a CFD model, and data from a variety of other data sources of full scale tunnel fires. Their CFD model used a much earlier version of *Fluent* than currently available, however the results were not unreasonable.

6.1.1 Experimental method

In each test carried out by Wu and Bakar, a heat source with a constant heat release rate was activated in a model wind tunnel. The ventilation rate was gradually increased until the length of the backflow (measured from the heat source) was zero.[1] Tests were carried out on five different cross-sections (see Figure 6.2), and at eight different heat release rates (1.5, 3, 7.5, 10.5, 12, 15, 22.5 and 30 kW). The heat source was a circular porous bed burner of 106 mm diameter (0.0088 m^2). The fuel used was propane.

The tunnels were constructed from a mixture of PMMA and steel plating. A water cooling system was applied to the outside of the tunnel if the temperatures were excessive.

[1] This does not mean that axial velocity is positive throughout the tunnel – and does in fact imply some reverse flow as the plume will be inclined and impinge on the tunnel roof some distance in front of the heat source.

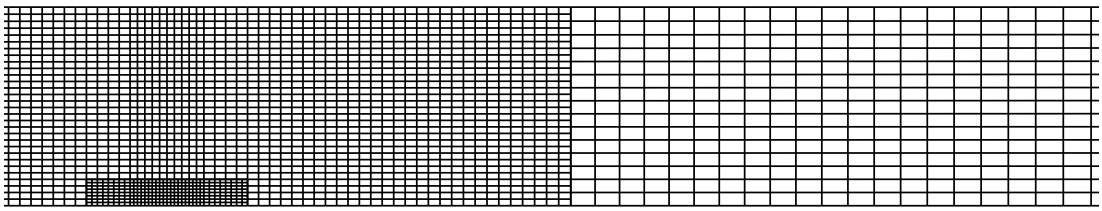

Figure 6.3: Slice of typical grid after refinement
Total number of cells = 181,920. See Table 6.1

For the purposes of verifying the CFD technique, there is no benefit in modelling such a large range of tests, so only the square cross-section (B) and a single heat-release rate (7.5 kW) were fully considered. According to Wu and Bakar, the critical velocity for this case is 0.56 m/s, and a range of other data, such as temperature contours, are available.

6.1.2 CFD model

6.1.2.1 Meshing

The geometry of the tunnel suggests that a structured hexahedral mesh is the most appropriate choice. As a relatively long length of tunnel is modelled, the size of the elements is varied along the length of the tunnel in order to increase the density of nodes in the region around the burner.

An 8m long section of tunnel was modelled, providing 16 diameters in either direction from the heat-source. This length was found to be sufficient in the modelling carried out by Wu and Bakar. In comparison the experimental study used 15 m of tunnel, with $25D$ upstream, and $35D$ downstream of the heat-source.

6.1.2.2 Mesh refinement

Fluent allows the mesh to be refined by splitting existing elements according to user specified conditions. The mesh was initially refined over the entire cross section of the tunnel from two tunnel heights downstream of the burner and eight tunnel heights upstream. An additional level of refinement was applied in the vicinity of the burner (see Figure 6.3).

Table 6.1: Grid densities used to determine mesh sensitivity

Grid	Number of cells
A	53,236
B	181,862
C	**422,920**
D	1,273,098

6.1.2.3 Mesh and discretisation scheme sensitivity

In order to be confident that the results of the study are independent of the grid used, the same model was run employing four different grid densities (see Table 6.1).

Initially first-order discretisation had been used, and to provide a comparison, Grids B and C were repeated with second-order schemes. These required a significant amount more CPU time than the corresponding first-order cases.

As a comparison of the results, the variation of axial velocity (i.e. the z component of velocity) with height, on the mid-plane of the tunnel, at a distance of 200 mm downstream of the heat source, was plotted for each grid (see Figure 6.4).

A clear progression can be seen between the first-order solutions carried out on Grids A, B, and C. The difference between Grid C and D is minimal with only a slight variation in the peak velocity. Grid C is therefore the minimum grid density that could be used to obtain reasonable results.

The time taken to run the case on Grid D was prohibitive; requiring two hours for a single time-step, and over 1 GB of memory whilst running.

The second-order solutions were better than the corresponding first-order solution, particularly for the coarser grid, where it was better at resolving the sharp velocity gradients associated with the plume (see Figure 6.4). In fact the second-order solution on Grid B is almost as good as the first-order solutions in Grid C.

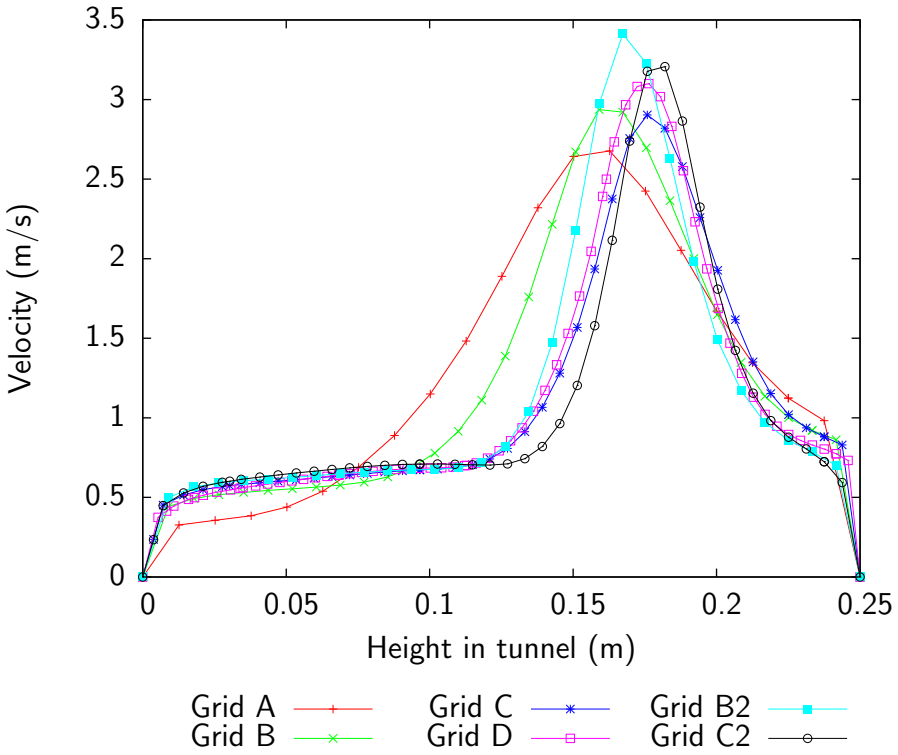

Figure 6.4: Centreline velocities 200 mm downstream of heat source for four grids (A, B, C & D) and second order solutions (B2 & C2)

6.1.2.4 Heat source

The CFD models presented by Wu and Bakar (2000) use a combustion model to represent the propane burner. Whilst this is obviously the *correct* approach it adds a large amount of complexity to the model, and increases the computational cost of the solution. As the aim of this study was to verify the modelling of thermally driven flows, it was decided to investigate the use of an energy source model to represent the burner. This approach is quite common, particularly as it eliminates a level of complexity (Hara and Kato, 2004). Combustion modelling will be considered in Section 6.2 where it is applied to full-scale tunnel fires.

This source term should be applied to the volume where combustion is taking place (i.e. the 'flame'), but as there is no simple way to determine this a variety of volumes were tried.

The most flexible way of implementing the heat source was to use a *user defined function* (UDF) to extend the standard solver (see Section 6.1.2.9).

6.1.2.5 Buoyancy

The presence of a localised heat-source means that the density of air will vary throughout the tunnel. This tends to induce a flow as the force of gravity acts on the density variations. The importance of buoyancy forces in a case that contains both convective and forced flows is given by the ratio of the Grashof to the Reynolds number (which is a form of the Richardson number):

$$\frac{\mathrm{Gr}}{\mathrm{Re}^2} = \frac{\Delta\rho g h}{\rho v^2} \tag{6.1}$$

ρ and $\Delta\rho$ are the ambient density and difference in density between the hot and cold region ($\mathrm{kg/m^3}$),

g is the acceleration due to gravity ($\mathrm{m/s^2}$),

h is the height of the space (m), and

v is the forced ventilation velocity (m/s)

For the case in question, this is approximately 8 ($\rho = 1.2\,\mathrm{kg/m^3}$, $\Delta\rho = 1\,\mathrm{kg/m^3}$, $g = 10\,\mathrm{m/s^2}$, $h = 0.25\,\mathrm{m}$, and $v = 0.5\,\mathrm{m/s}$).

In order to model buoyancy in a CFD package, an equation of state that allows for density variation must be selected[2] (Fluent, 2002). Typically this would be based on the ideal gas law.

$$\rho = \frac{p_{\mathrm{op}} + p}{\frac{R}{M_w}T} \tag{6.2}$$

where

$p_{op} + p$ is the pressure consisting of a reference pressure p_{op} usually taken as atmospheric and a deviation p (Pa),

T is the temperature (K),

M_w is the mean molecular weight of the gas (g/mol), and

R is the gas constant ($8.314\,\mathrm{J/K/mol}$)

[2]In some cases a *Boussinesq* approximation is used, which treats density as constant, except when solving the momentum equation. This is inappropriate when large temperature variations exist, and in any case cannot be used for multi-phase or reacting flows

If the flow is considered to be incompressible, then the density can be calculated from the temperature and a fixed reference pressure.

$$\rho = \frac{p_{\text{op}}}{\frac{R}{M_w}T} \tag{6.3}$$

This is potentially easier to solve and should provide better convergence.

6.1.2.6 Effect of buoyancy on turbulence

In addition to promoting a convective flow, buoyancy has an effect on the generation of turbulence within the flow that depends on the stability of the temperature gradients. When there is warmer fluid beneath a colder fluid, the flow is unstable and there will be an increased amount of turbulence. When the warmer fluid is *above* the colder fluid, the flow is stable, and there will be a decreased amount of turbulence.

When using the k-ε turbulence model, the generation of k due to buoyancy is given by Equation 6.4.

$$G_b = -g_i \frac{\mu_t}{\rho \text{Pr}_t} \frac{\partial \rho}{\partial x_i} \tag{6.4}$$

where

μ_t is the turbulent viscosity (Pa s),

Pr_t is the turbulent Prandtl number (dimensionless),

ρ is the density (kg/m^3),

g_i it the gravitational vector (m/s^2), and

$\frac{\partial \rho}{\partial x_i}$ is the density gradient (kg/m^3/m)

As g_i is the gravitational vector, and $\frac{\partial \rho}{\partial x_i}$ is the density gradient, it is clear that this is positive for an unstable flow, and negative for a stable flow.

The effect of buoyancy on the turbulent dissipation rate, ε, is less well understood, so G_b is multiplied by a constant $C_{3\varepsilon}$ (which is often taken to be zero). Wu and Bakar, however, report that $C_{3\varepsilon} = 0.25$ produced optimal results, and Henkes et al. (1991) suggest:

$$C_{3\epsilon} = \tanh \left| \frac{v}{u} \right| \tag{6.5}$$

where v is the component of flow velocity parallel to the gravity, and u is the component perpendicular to gravity.

Sinai (2000) showed that the predicted fluctuation frequency of a flame can depend on the value of $C_{3\epsilon}$. Sinai states that this dependences is most critical for fire plumes in otherwise stagnant air, as the buoyancy is the only source of turbulence. This implies that it *may* be less important in cases such as this where strong ventilation flows are present.

Despite the uncertainty, *Fluent* only allows for $C_{3\varepsilon}$ to be zero or calculated from Equation 6.5. In this study the above relationship was used.

6.1.2.7 Solution controls and Under-relaxation

Table 6.2: *Fluent*'s default under-relaxation values, and values used in this study

Variable	Default	Modified
Pressure	0.3	
Density	1	**0.5**
Body Forces	1	
Momentum	0.7	
Turbulence Kinetic Energy	0.8	
Turbulence Dissipation Rate	0.8	
Turbulent Viscosity	1	
Energy	1	**0.7**

Table 6.2 shows the under-relaxation factors, which were found to produce reliable convergence for this problem.

In the cases that showed artificially high temperatures (i.e. above 5000 K – see Section 6.1.2.10 and Figure 6.7) it was not possible to converge the energy equation to the desired level. This does not seem to be related to the under-relaxation factor.

6.1.2.8 Unsteady solution

Although this study is primarily interested in the fully-developed thermal flow, and not in any time-dependent behaviour, an *unsteady* solution is employed.

This is usually recommended for high-Rayleigh-number flows (Ra $> 10^8$). This is because there may not actually be a steady-state solution. Additionally, due to the large variation of density, the mass of fluid in the domain is unknown, so continuity can be hard to achieve.

The Rayleigh number for this problem[3] is in the region of 3×10^9.

The suggested time-step for the unsteady calculation is $\Delta t \approx \frac{\tau}{4}$ (Fluent, 2002), where

$$\tau = \frac{L}{U} \sim \frac{L^2}{\kappa}(\mathrm{PrRa})^{-\frac{1}{2}} = \frac{L}{\sqrt{g\beta\Delta T L}} \tag{6.6}$$

where

L is a length scale (m),

g is the acceleration due to gravity (m/s^2),

β is the coefficient of thermal expansion (K^{-1}), and

ΔT is the temperature range (K),

This gives a time step of 0.015 s. By comparison, the time taken for air to flow through the domain is around 16 s, which means a large number (> 1000) of time steps may be required.

In order to assess the sensitivity of the solution to the size of the time-step, runs were carried out with $\Delta t = 0.01$, 0.1, and 1 s. The results of this showed that the angle of the plume was particularly sensitive to the time step, tending to be much shallower for the larger time steps.

6.1.2.9 User defined function (UDF)

A *user defined function* (UDF) written in the C language was used to implement the heat source model within the *Fluent* solver (see listing in Appendix B).

[3] $g = 10\,\mathrm{m/s^2}$, $\beta = 3.5 \times 10^{-3}\,/\mathrm{K}$, $\kappa = 2.39 \times 10^{-5}$, $\mu = 1.8 \times 10^{-5}\,\mathrm{kg/ms}$, $\Delta T = 2000\,\mathrm{K}$, $\rho = 1.2\,\mathrm{kg/m^3}$

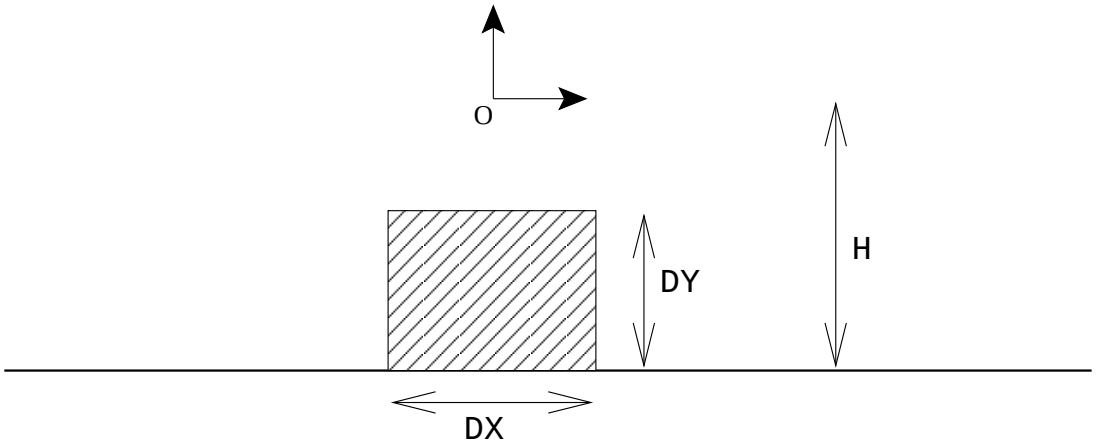

Figure 6.5: Location of volumetric heat source defined by UDF

The function is executed once per time step for every single cell in the domain. If the centroid of the cell is located within the volume defined, then the heat release rate for that cell is set to the specified value, otherwise it is set to zero.

The function implicitly assumes that the tunnel is centred on the origin with the tunnel floor a distance `H` below the origin. The heat source is applied over a volume of `DX`×`DY`×`DZ` (see Figure 6.5).

The values of `Q`, `DX`, `DY`, etc. are defined in a separate source file (see Appendix B), as these are the only parameters that should change.

The heat source is applied whenever the *centroid* of a cell is within the volume. This means that the exact value of the total heat source may vary slightly depending on the mesh geometry (see Figure 6.6). This was avoided by selecting values of `DX`, etc. that correspond to multiples of the grid size. However, as the mesh is very dense in the region of the heat-source this effect should be minimal as long as the size of the heat-source is significantly larger than the mesh size.

It would not be impossible to develop the UDF to either adjust the size of the source-term for cells that fall partially within the designated volume, or to automatically fit the volume to integer mesh coordinates, however this was felt to be unnecessary.

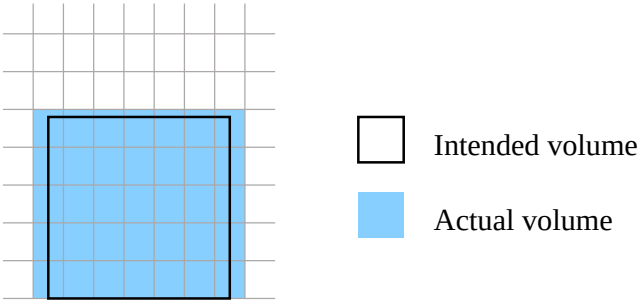

Figure 6.6: Aliasing of heat source volume

6.1.2.10 Issues with using a fixed-size heat source

Initially it was assumed that applying the heat source over a small volume directly above the position of the burner would be a reasonable way of representing the fire. However, this tended to artificially distort the shape of the plume, and gave the appearance of a burning solid object in the flow field (see Figure 6.7). As an alternative, the heat source was applied as a *heat flux* across the boundary. This produced much more reasonably shaped temperature contours, however the maximum temperature was severely over-estimated and exceeded the temperature limit of 5000 K. A detailed analysis was carried out, and a strong correlation between the maximum temperature and the volume of the heat source was observed. The case of heat-flux across the boundary is the extreme case, as the heat is applied to a single layer of cells along the boundary. This is exacerbated by the low velocities in this region.

6.1.3 Results

Figure 6.8 shows the temperature contours predicted by the CFD model overlaid on the experimentally measured values. Note however that the experimental contours shown were derived from a 3×8 array of thermocouples and so are of limited spatial resolution.

The overall angle of the plume is in very good agreement, however the CFD vastly over-predicts the temperatures, giving temperature rises in the region of 1000 K at the 500 K experimental contour.

The CFD also shows a sharper transition between plume and ambient than ap-

a) Heat release over cylinder $H = D = 0.106\,\text{m}$ (300 K – 1300 K)

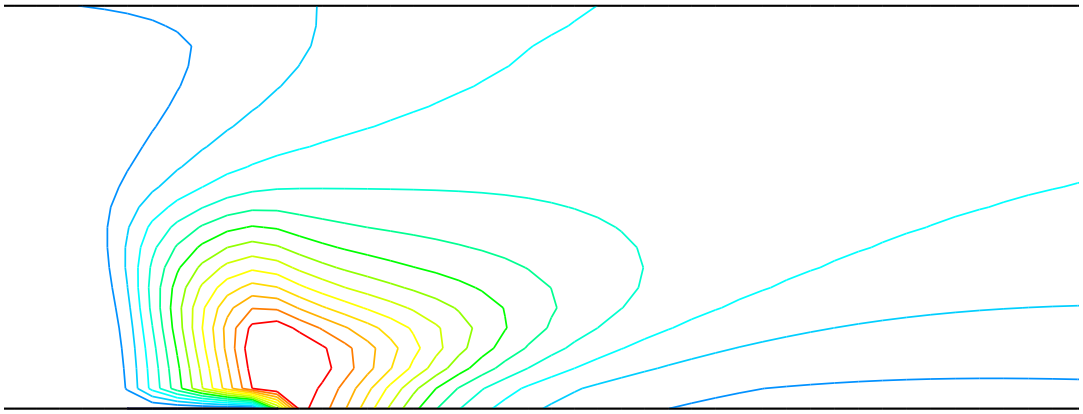

b) Heat release across circle $D = 0.106\,\text{m}$ (300 K – 5000 K)

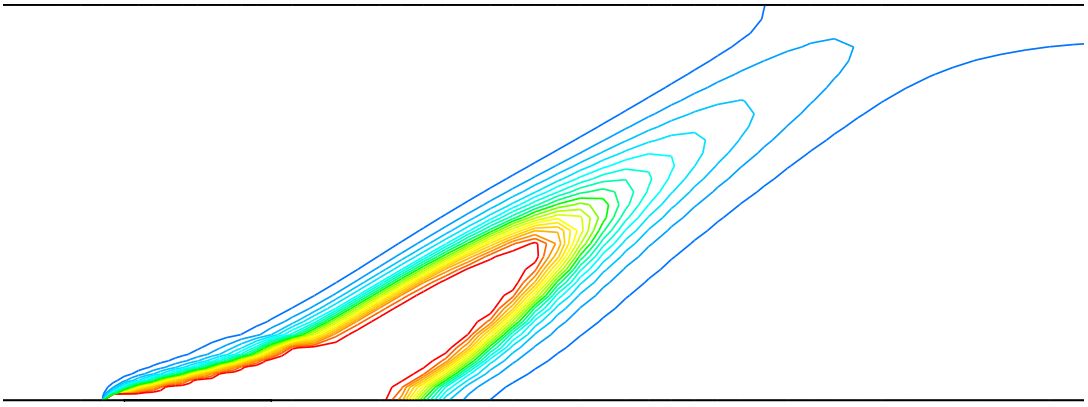

c) Heat release over cube $D = 0.05\,\text{m}$ (300 K – 5000 K)

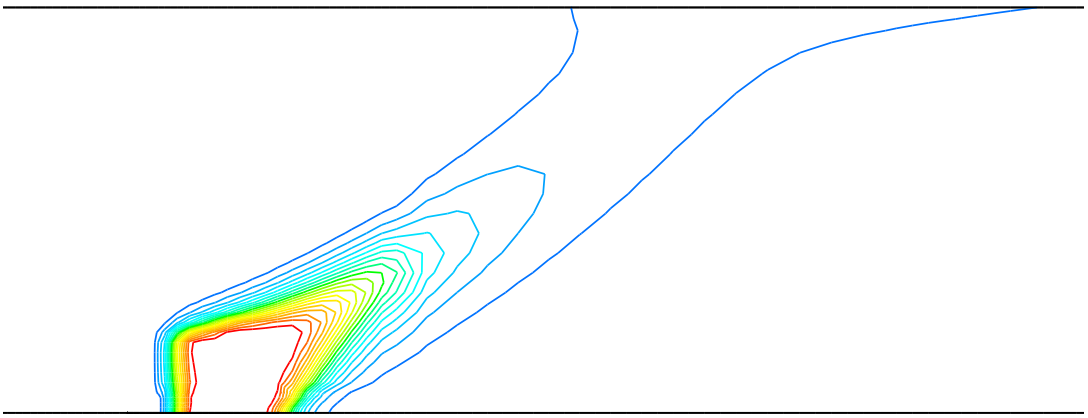

Figure 6.7: Temperature contours for different size heat sources

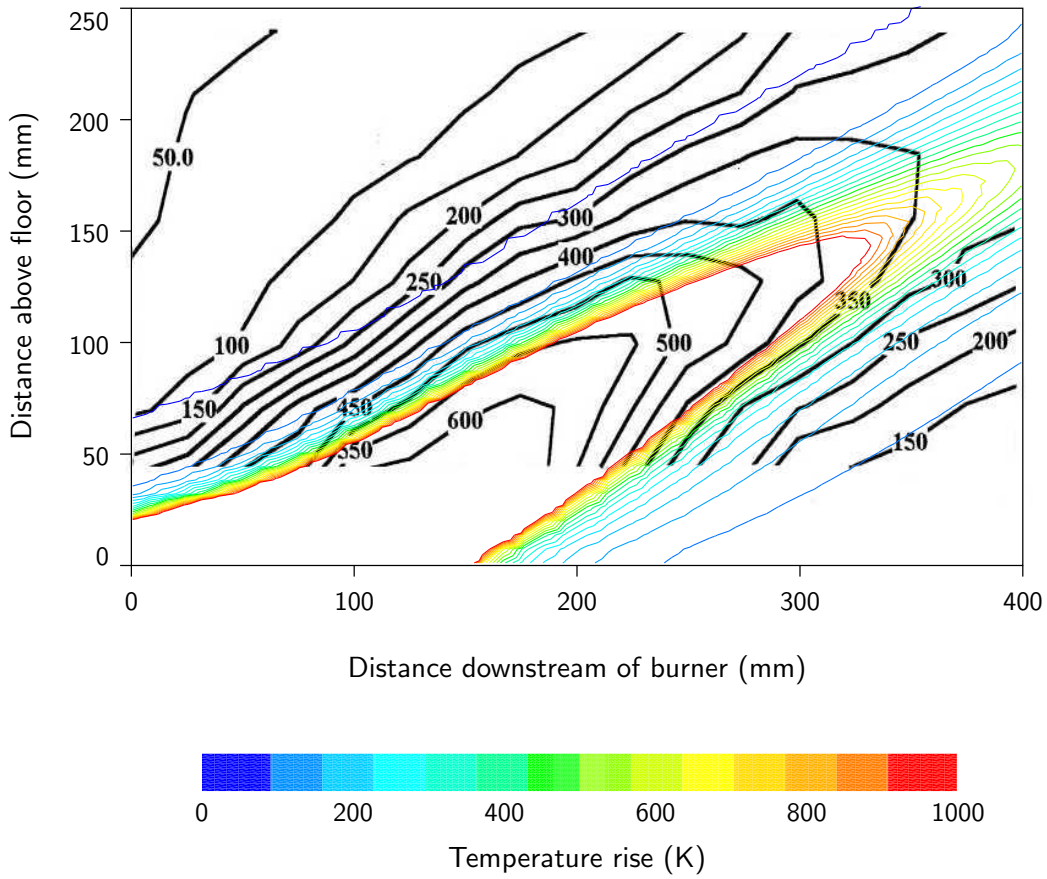

Figure 6.8: Comparison of CFD results with experimental temperatures Experiment shown as thick black contours, CFD as thin coloured contours, both in 50 K increments.

pears in the experimental data. This could merely be due to the low resolution of the thermocouple array, or an artifact of the high temperatures in the CFD model. An alternative suggestion is that unlike the simplified heat source, the volumetric heat output of a real fire varies significantly in intensity across the diameter of the burner.

6.1.4 Summary of findings

- The 400,000 cell grid was optimal. This corresponds to 40 nodes across the height of the tunnel in the region of the heat source.
- An unsteady solution is required, and care must be taken when selecting the size of the time step. A time step of $\frac{\tau}{4}$ was found to be adequate, where $\tau = \frac{L}{\sqrt{g\beta\Delta T L}}$ (see Equation 6.6.

- The volume and shape of the heat-source used must be consistent with the fire it represents, if both the maximum temperatures and the shape of the temperature field are to be correctly predicted. As a corollary of this, the use of a predetermined heat-source may not be appropriate unless the burning object has a definite shape or is very small compared to the domain or where only far-field behaviour is of interest.
- It is beneficial to reduce the under-relaxation factors for density and energy, and to choose a second-order discretisation scheme.

Table 6.3: Geometry of fire galleries

Gallery	Location	Length (m)	Cross section (m^2)	Inclination[a] (°)
1		125	$8 \cdot 2$	0
2	Tremonia	209	$14 \cdot 5$	$16 \cdot 66$
3		250	$17 \cdot 0$	0
4	Ramsbeck	620	$7 \cdot 8$	$13 \cdot 77$
5		150	10	0

[a]Inclinations recorded in DMT et al. (2004a) is given in gon (where 100 gon = 90°) to one decimal place

6.2 Modelling of flow due to a fire

In Section 6.1, a thermal flow was modelled by assuming a fixed volumetric heat source. In this section, a pool fire model similar to that used in Chapter 5 is utilised to represent a pool fire within a tunnel. The scenario modelled is based on full-scale experimental tests carried out by DMT et al. (2004a), a summary of which is given below in Section 6.2.1. Details of the CFD model are given in Section 6.2.2.

6.2.1 Details of experiment

A series of full-scale fire tests were carried out by Deutsch Montan Technologie (DMT) as part of an European Coal and Steel Community (ECSC) research program into the prediction of fire effects in mines (DMT et al., 2004a).

The experiments were designed to determine the effect of tunnel geometry (cross section and inclination) and the effect of ventilation rate on a diesel pool fire in a tunnel.

The first series of tests was carried out in fire galleries 1–4 (see Table 6.3) using a constant ventilation rate of 1.2 m/s and a *'180 l diesel pool fire'*. The pool consisted of nine square pans with a total area of 4.5 m^2 (DMT et al., 2004a). For the inclined galleries separate tests were performed for ventilation in both directions (i.e. uphill and downhill) giving a total of six tests.

The second series of tests was carried out in fire gallery 5. Four tests were

Table 6.4: Results of first series of tests (1.2 m/s)

Test	Gallery	Direction	Temperature Equalisation (m)	Temperature (°C)	Backflow (m)
1	1		170	50	30
2	3		150	80	70
3	2	Up	120	100	0
4	2	Down	50	200	85
5	4	Up	140	80	0
6	4	Down	30	300	90

Table 6.5: Results of seconds series of tests (all in gallery 5)

Test	Ventilation (m/s)	Temperature Equalisation (m)	Temperature (°C)	Backflow (m)
1	2.4	30	520	3
2	1.8		Not available[a]	
3	1.2		Not available[a]	
4	0.8	53	495	>36

[a]Although mentioned in DMT et al. (2004a) no results are given for tests at 1.2 m/s and 1.8 m/s. Communication with DMT et al. has not yet obtained this data.

performed, with ventilation at 0.8, 1.2, 1.8, and 2.4 m/s. In each case, the fire source was a *'9.3 m^2 pool of fuel oil'* located on the floor of the tunnel 41 m from the inlet. The pool consisted of three 1 m × 3.1 m pans. Initially, the pool contained 360 l of fuel, but the tests were subsequently repeated with 720 l. The test gallery was 150 m long with a cross-sectional area of approximately 10 m^2. A total heat release rate of 11 MW was recorded, which *varied little with ventilation rate* showing that the fire is oxygen rich and that the ventilation had little effect on the rate of fuel volatilisation. The 720 l pools burned for approximately 40 min.

Thermocouples were placed both up- and down-stream of the fire to record steady-state temperatures for the fully developed fire, at ceiling-, mid-, and floor-height (see Table D.1–D.8 and Figure D.1). Observations of the length of backflow from the plume were also recorded (see Table 6.4 and 6.5).

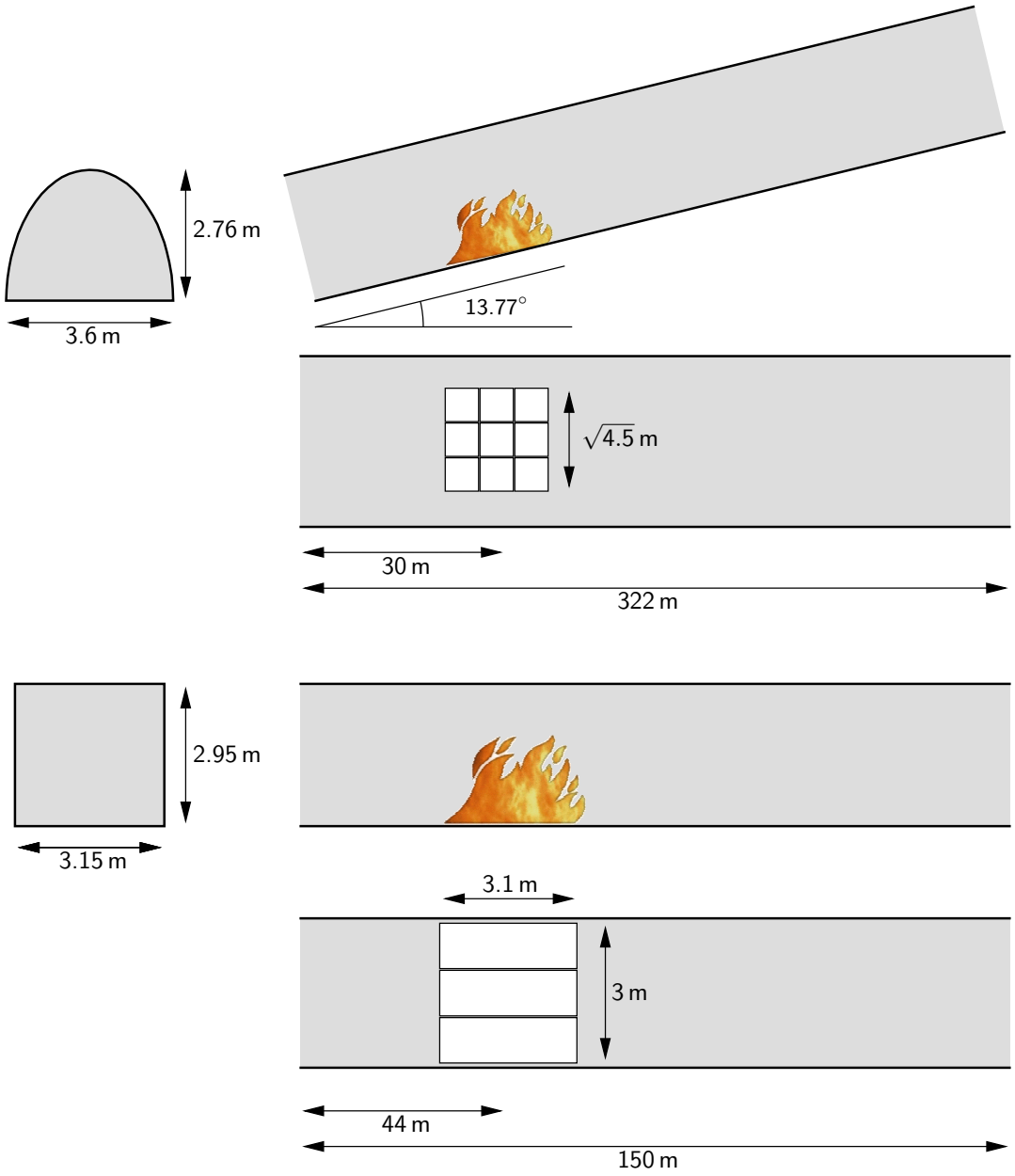

Figure 6.9: Schematic of DMT Test Gallery 4 (Ramsbeck) and Test Gallery 5

Figure 6.10: Photograph of Ramsbeck test gallery (Gallery 4) (DMT et al., 2004a)

6.2.2 Details of CFD model

6.2.2.1 Overview

The CFD model constructed to replicate the tunnel fire was very similar to the enclosure fire model of Chapter 5, using the following sub-models and settings, details of which are given below:

- structured hexahedral mesh
- standard k-ε turbulence model with buoyancy modification
- isothermal walls
- velocity inlet and pressure outlet
- eddy breakup (EBU) combustion model
- Discrete ordinance (DO) radiation model
- second order discretisation in space and time

6.2.2.2 Geometry, meshing and coordinate system

The CFD simulations documented in this chapter are based on the tests performed in fire galleries 4 and 5. Schematics of these galleries are shown in Figure 6.9. A semi-elliptical cross-section was assumed for gallery 4 with dimensions based on the 7.8 m^2 cross-sectional area stated in the report and an aspect ratio of 1.305 measured from a photograph of the tunnel (see Figure 6.10), giving a maximum width of 3.6 m and a maximum height of 2.76 m.

The depth of the fuel was calculated as 40 mm for gallery 4 and 79 mm for gallery 5 based on the stated quantity of fuel and total surface area. It was assumed that the pan walls were equal in height to the fuel (i.e. the pan was full to the brim and there was no protruding lip), and that the pool consisted of a single pan. Additionally for gallery 5, the pool width is taken as being equal to the tunnel width in order to remove any difficulties with grid resolution in the small gap. The effect of these assumption is studied in Section 6.2.5.

Initial simulations were carried out on a 44 m length of tunnel, with the fire located centrally (i.e. 22 m or approximately 8 diameters in each direction). The results of these simulations clearly showed the need for a longer section of tunnel, particularly downstream of the fire, in order to allow the flow to develop fully. For this reason in subsequent simulations an additional 44 m of tunnel was added downstream of the fire, giving over 20 tunnel diameters in which the plume could develop, and a total of 88 m length.

The geometry was created such that the tunnel was aligned with the y-axis, and the z-axis was vertical. The origin was located at the mid-height and mid-width point above the centroid of the pool. For the simulations of the inclined gallery, the slope was achieved by setting components of gravity in both the z and y directions (i.e. the tunnel was still aligned with the y-axis, but z was no longer strictly vertical)

The initial mesh (i.e. 22 m either side of the fire) contained 20 cells across the height and width of the tunnel. The cells were cubic (aspect ratio of one) close to the fire, and gradually elongated further away up to a maximum aspect ratio of 4. The mesh was refined close to the boundaries and the pool surface in order to better resolve the high gradients of temperature and species concentration expected there.

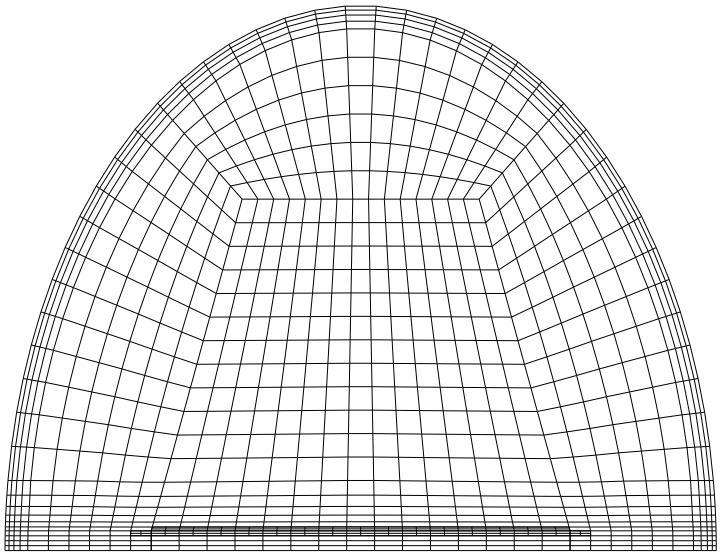

Figure 6.11: Cross-sectional slice of Gallery 4 (Ramsbeck) mesh showing mesh refinement close to boundary and pool surface

Due to restrictions on the number of cells that can be feasibly handled by the computer hardware available, a lower mesh density was used for the additional length of tunnel and a *non-conformal interface* was used to link the two meshes together in the solver. A non-conformal interface allows two grids with different geometry and/or meshing to be linked together by splitting mesh faces at the interface to create a common mesh at the boundary (see Figure 6.12).

In order to demonstrate grid independence of the results, two different meshes were generated for Fire Gallery 5, and cases at 0.8 m/s and 2.4 m/s were performed on both meshes. The coarse mesh contained 129,000 cells and the finer 280,000 cells, In comparison the arched gallery mesh contains 213,000 cells.

Figure D.2 and D.3 compares the temperature profile at steady-state for the two different grids. For the higher ventilation rate the agreement is good, with the temperatures being virtual indistinguishable everywhere except for close to the pool surface. At the lower ventilation rate, the difference is more significant, although it would be difficult to state which results are most in keeping with the experimental data. The more stringent mesh requirements of the lower ventilation rate can be attributed to the stratification that occurs in the back flow and to a lesser extent downstream of the fire. Ideally, results should be obtained from an even finer mesh, however 280,000 is essentially the limit of feasibility for the available computer resources.

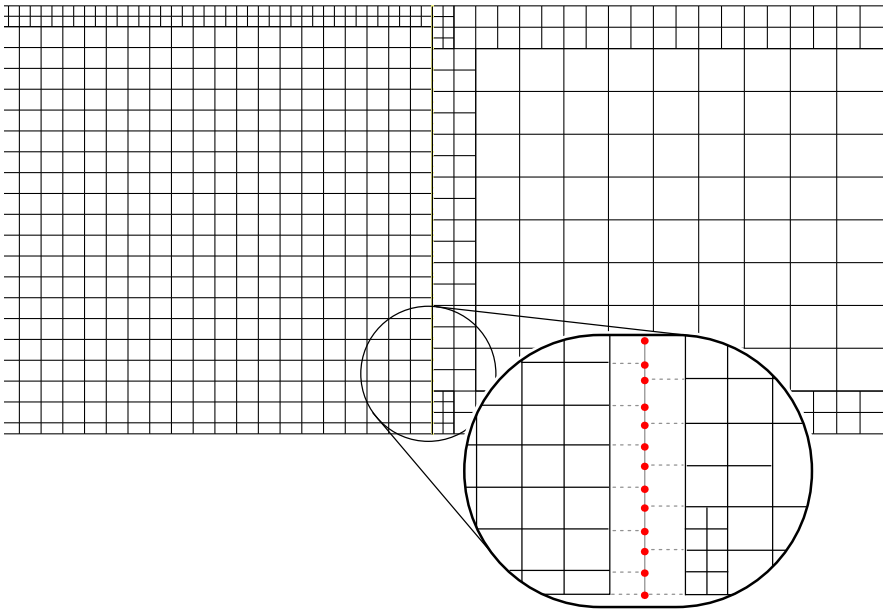

Figure 6.12: Grid interface between fine mesh and coarse mesh
(Note coarse mesh has been refined near the interface. This is not necessary, however it seems to avoid discontinuities across the interface)

In some later simulations symmetry was exploited to halve the size of the domain, and allow a corresponding increase in the mesh resolution. The total number of cells remained roughly constant.

6.2.2.3 Combustion and species

Combustion was implemented using the eddy breakup (EBU) model. In the report produced by DMT et al. (2004a) the fuel is described as *'diesel'* for some tests and *'fuel oil'* for others. Diesel and fuel oil are generic terms that refer to complex mixtures of hydrocarbons with varying composition and physical properties depending on the source and manufacturing process. For the purposes of this study, a single chemical substance, $C_{19}H_{30}$, is assumed to be representative of the fuel, as its properties such as density and molecular weight are close to typical diesels.

Table 6.6: Material properties

Species	Formula	Molecular Weight (g/mol)	Specific Heat (J/kgK)	Enthalpy (J/kgmolK)
Fuel	$C_{19}H_{30}$	258.19	2430	-6.4×10^8
Oxygen	O_2	32.0	919.3	0
Water	H_2O	18.0	2014	-2.418×10^8
Carbon Dioxide	CO_2	44.0	840.4	-3.935×10^8
Nitrogen	N_2	28.0	1040	0

Liquid Species	Density (kg/m^3)	Thermal Conductivity (W/mK)	Specific Heat (J/kgK)
Fuel	660	0.137	2512

The equation for stoichiometric combustion of $C_{19}H_{30}$ is:

$$C_{19}H_{30} + 26.5\,O_2 \xrightarrow{\text{energy}} 19\,CO_2 + 15\,H_2O \tag{6.7}$$

The enthalpy of combustion (calculated from the standard enthalpies of each species) is 1.046×10^7 kJ/kgmol. From this the rate of fuel release required to give 11 MW of heat is 0.001 kgmol/s.

The key material properties for each species are shown in Table 6.6.

6.2.2.4 Diffusion

It was established in the enclosure fire model that the rate of fuel release is dependent on the value of the diffusivity coefficient and the mesh density close to the fuel surface (see Section 5.2.4 and Figure 5.7).

As the rate of fuel release is known for the tunnel fire (based on the stated 11 MW heat release) it was used as a criterion to adjust the model diffusivity coefficient. This was achieved by using a simple negative feedback loop between the rate of reaction and the diffusivity coefficient implemented in a user defined function (UDF).

The rate of fuel release is not easily ascertainable from *Fluent* but at *equilibrium* it must be equal to the rate of reaction, which is. Tests showed that after a small adjustment in the diffusivity coefficient approximately five time steps were needed before the rate of reaction reached a new equilibrium value. The UDF was implemented to only update the diffusivity value once every five time steps, and to adjust it by no more than ±30% at once. An extract of the UDF source file is shown in Appendix B, Figure B.4.

Typically diffusivities of between 20 and 200 times greater than the default value ($2.88 \times 10^{-5}\,\mathrm{m}^2/\mathrm{s}$) were required depending on the mesh density close to the pool surface.

6.2.2.5 Boundary conditions

The inlet to the tunnel was specified as a constant velocity, with a turbulent intensity of five percent and a representative length equal to the tunnel height of 3 m. A pressure outlet was used at the outlet, in order to allow non-uniform, and non-normal, flow across the boundary.

No information was available concerning the construction or thermal properties of the gallery walls. Given the high level of heat loss apparent in the experimental data, an isothermal condition, fixed at the ambient temperature of 300 K, with an emissivity (and hence absorption) of 1.0, seemed a reasonable initial assumption.

6.2.2.6 Other model details

The standard k-ε model with buoyancy modifications and standard wall functions was used. As stated earlier, the grid was refined close to the boundary. This ensured the y^+ value was in an acceptable range even in the coarser areas of mesh. The tunnel walls were assumed to be smooth, as used, for example, by Lea et al. (1997). However photographs discovered at a later date suggest that this was nowhere near reality (see Figure 6.10).

The discrete ordinance (DO) radiation model was used. As in Chapter 5 the number of iterations between update was reduced to five, and the resolution of the angular discretisation was increased. The improved angular resolution is

considered to be particularly important for the tunnel model due to the high aspect ratio (30:1) of the overall domain.

6.2.2.7 Discretisation

The second-order upwind differencing scheme was used for all variables, with default under-relaxation factors. A second order implicit time-stepping scheme was used and the Semi-Implicit Method for Pressure-Linked Equations (SIMPLE) algorithm was used for pressure–velocity coupling.

During some simulation runs a problem was encountered with the radiation model which caused the residuals to spontaneously leap up by 15 orders of magnitude or more even though the solution had previously been both convergent and stable. This appeared to be due to a bug in the *Fluent* solver (version 6.2.16 was being used at this point). Selecting a first-order discretisation for the radiation model appeared to avoid this problem, and did not have any discernible effect on the results.

6.2.2.8 Time step

The required time step was estimated as 0.064 s using Equation 6.6 taking the tunnel height as a representative length scale ($L = 3\,\mathrm{m}$) and using the thermocouple data for the temperature range ($\Delta T = 1300\,\mathrm{K}$). Unfortunately, given the size of the mesh, and the anticipated need to run at least 200 s, the overall run time of the problem would have been prohibitive.

Trials were carried out with time steps of 0.1, 1, 2, and 5 s, and a 1 s time step was shown to give time step independent results at an acceptable computational cost.

In order to investigate the sensitivity of the model to variation in time step size, the 2.4 m/s case was run with a time step of 1.0 s until a steady state solution had been reached (after 200 s). The time step was then dropped to 0.1 s, and a further 100 time steps were solved in order to ensure any deviation from the earlier steady solution had a chance to appear.

A comparison of the temperature profiles between the two solutions shows a maximum deviation of 5.0 % at the leading edge of the fuel pan. This discrepancy was isolated to a small number of cells with the steepest temperature gradient. At all other locations the deviation was less than one percent with an RMS deviation of 0.34 %. A comparison of the solution after 100 time steps with the solutions after 20, 40, 60 and 80 time steps, showed that the deviation was stable or diminishing at all points (see Figure 6.13).

6.2.3 Results

Figures 6.14 – 6.17 show a comparison of the temperature profile predicted by the CFD model and the peak thermocouple data from the experiments.

The CFD data and the experimental data are in reasonably good agreement, except for the following discrepancies:

- over prediction of far downstream temperatures at ceiling and mid-height for 0.8 m/s case.
- under prediction of ceiling temperatures and mid-height temperatures close to the fire for 2.4 m/s case.
- over prediction of floor-level temperatures, and under prediction of mid- and ceiling-level temperatures at 0 m mark for sloping cases (in Gallery 4), both up and down.

6.2.4 Discussion of results

6.2.4.1 Heat losses

The results for the 0.8 m/s case (Figure 6.14) shows a reasonable agreement with the experimental (thermocouple) data. The obvious discrepancy is in the rate of temperature decay downstream of the fire. This can most easily be seen in the mid-height profile, where the thermocouple points seem to suggest an exponential

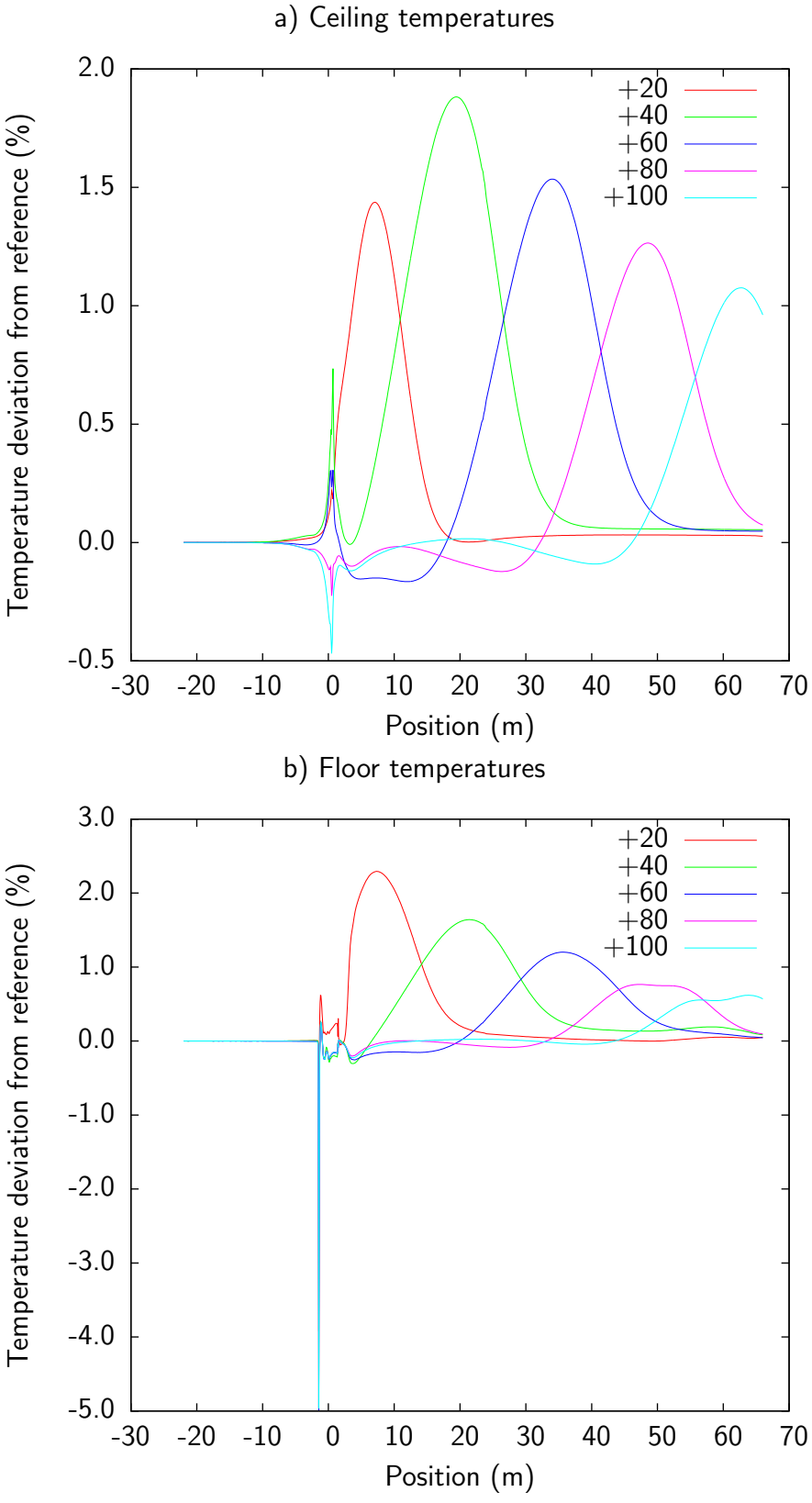

Figure 6.13: Deviation in steady-state temperatures between a solution obtained with 1 s time step and solutions obtained after 20, 40, 60, 80 and 100 further time steps of 0.1 s

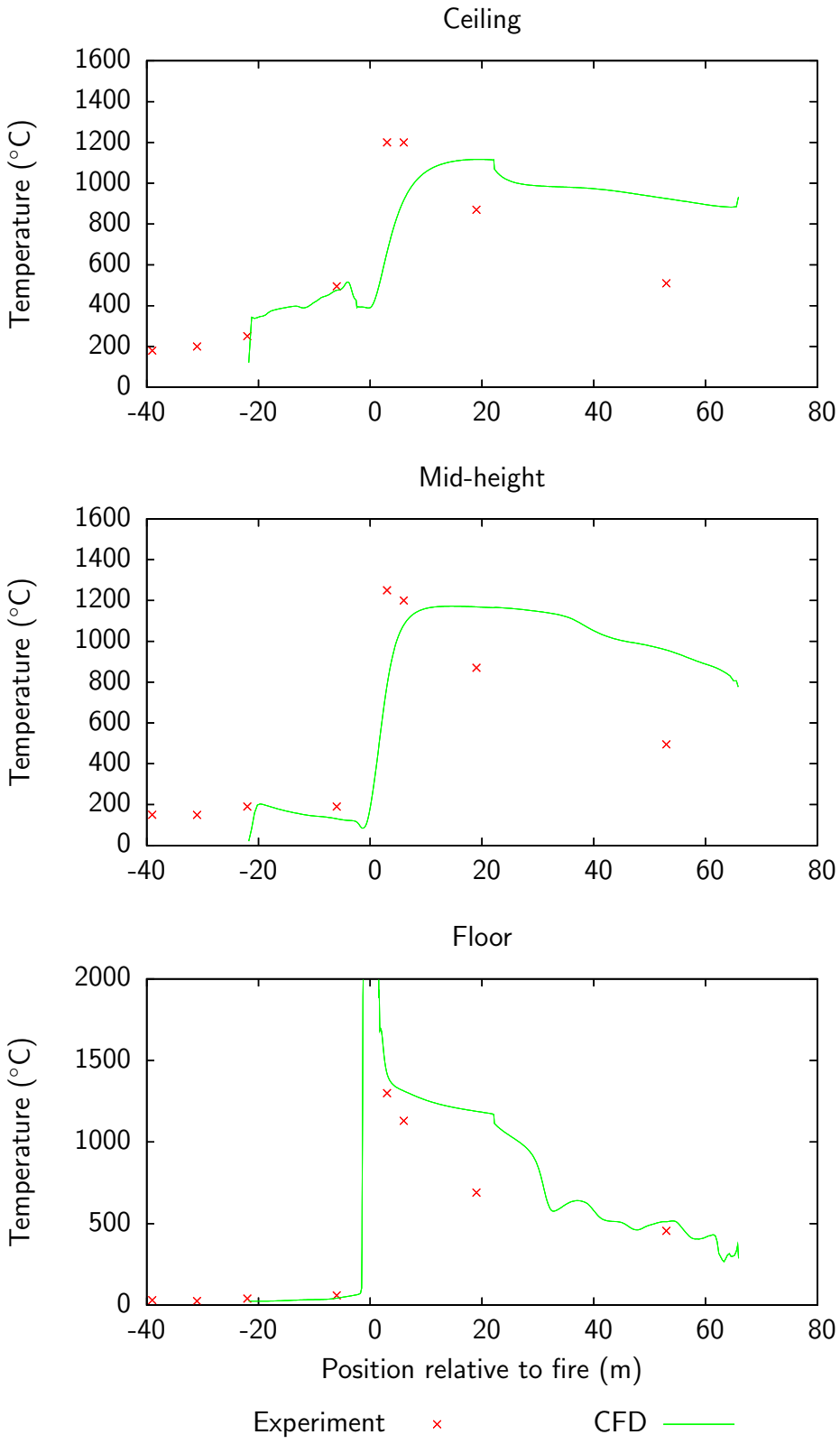

Figure 6.14: Comparison of CFD results with thermocouple data (0.8 m/s ventilation, Gallery 5)

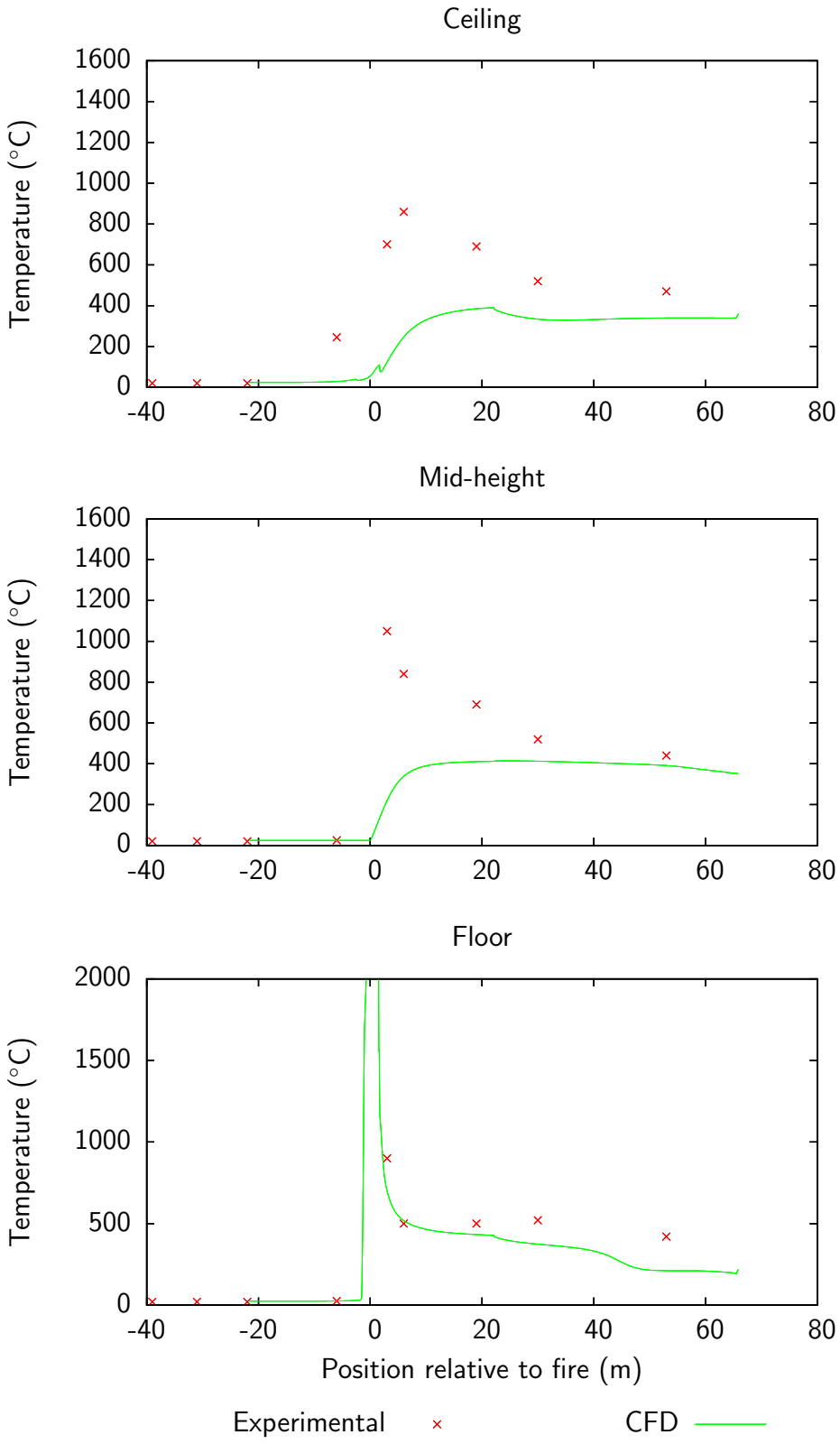

Figure 6.15: Comparison of CFD results with thermocouple data (2.4 m/s ventilation, Gallery 5)

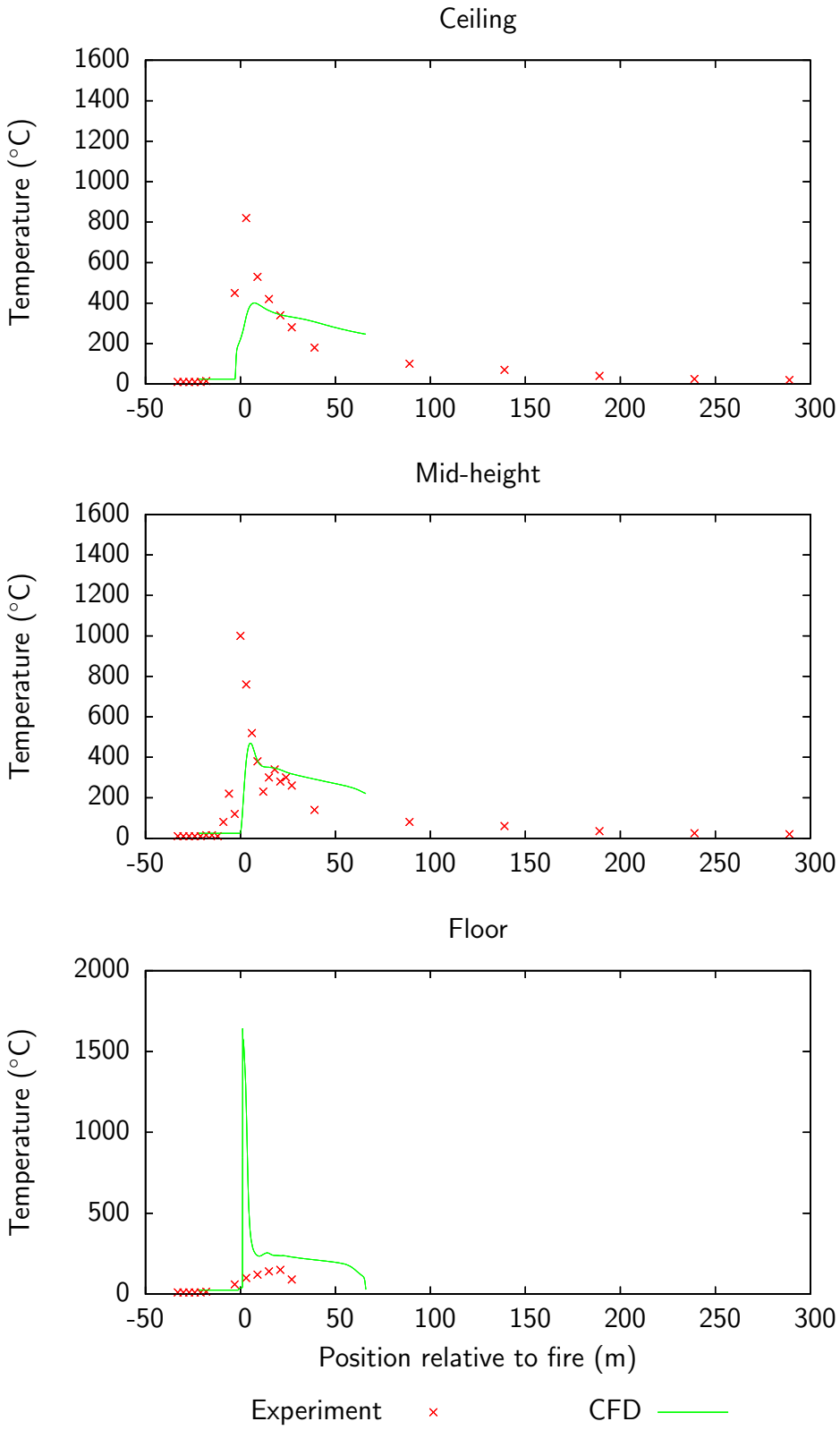

Figure 6.16: Comparison of CFD results with thermocouple data (1.2 m/s upward flow, Gallery 4)

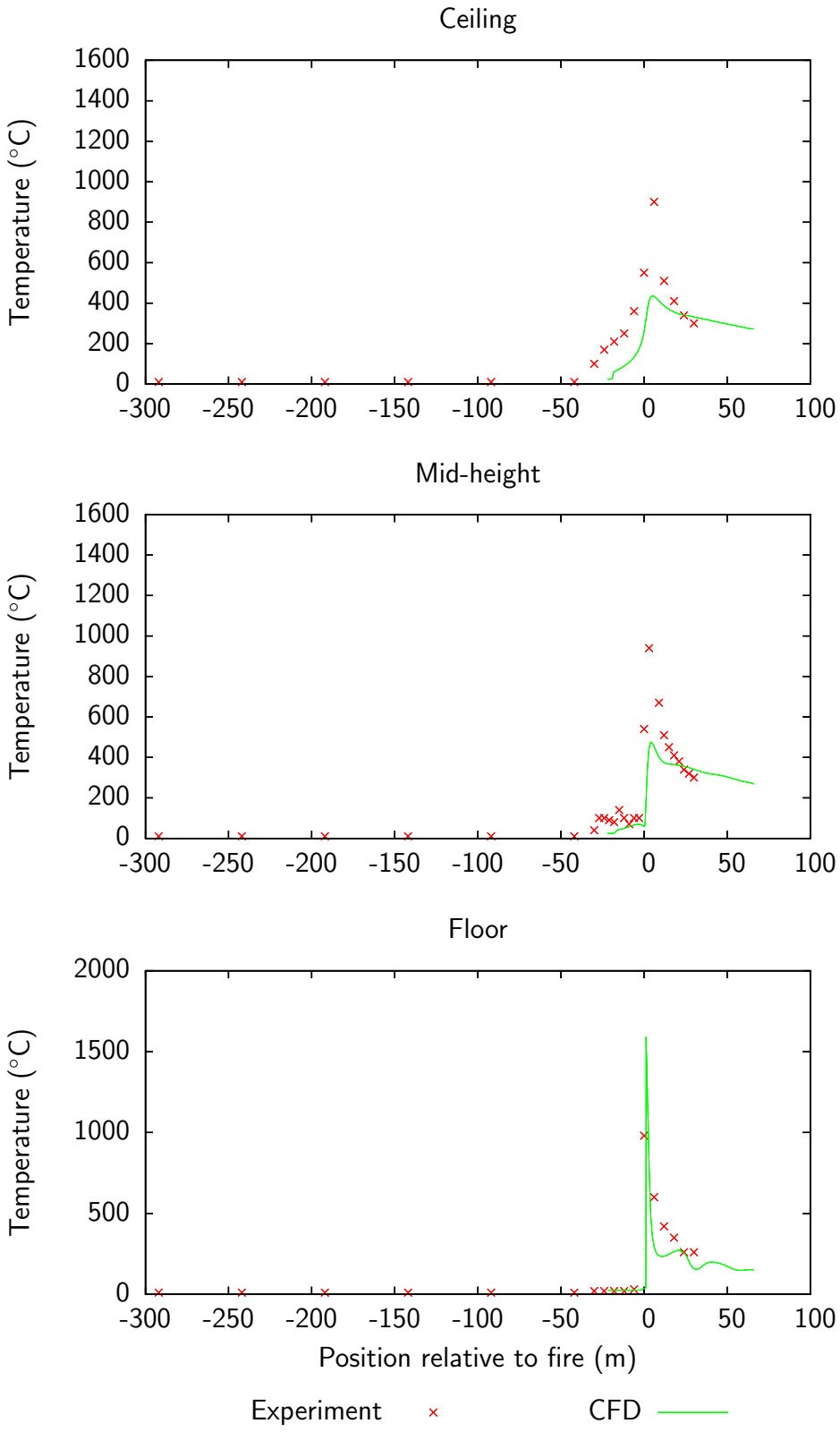

Figure 6.17: Comparison of CFD results with thermocouple data (1.2 m/s downward flow, Gallery 4)

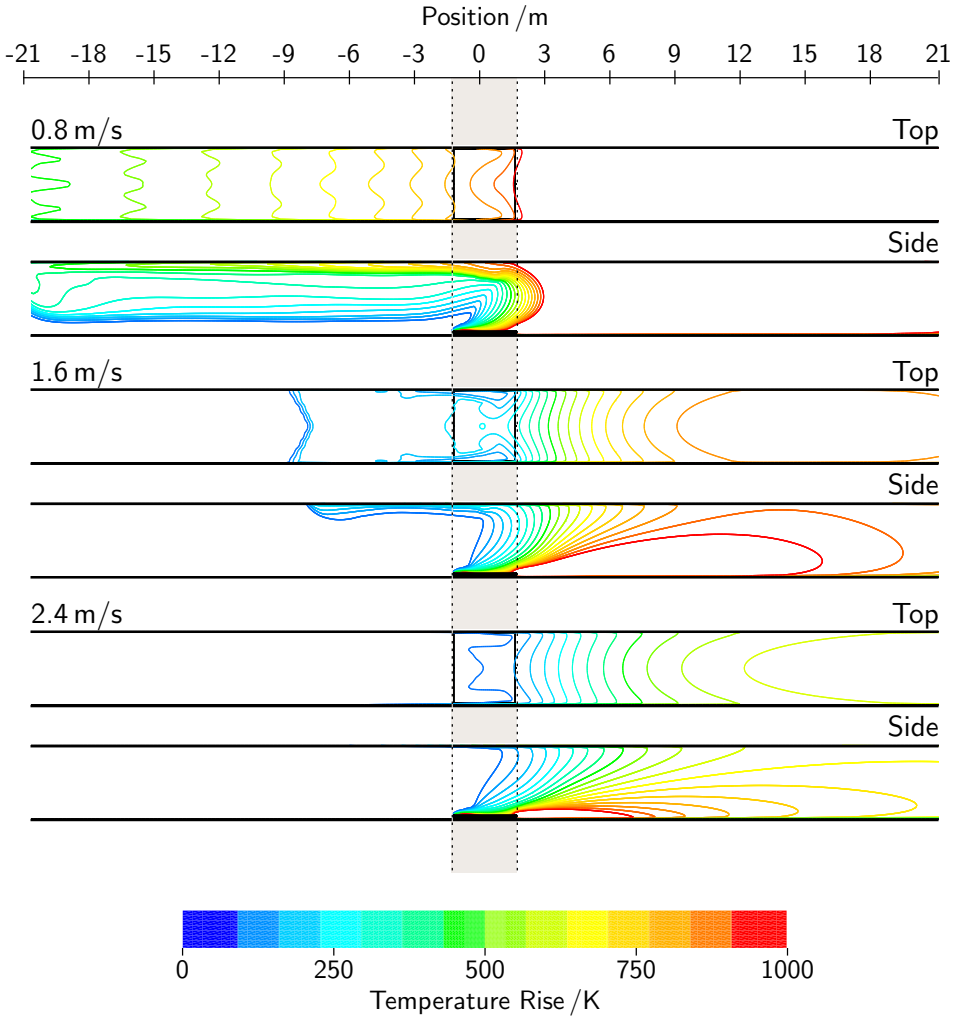

Figure 6.18: Ceiling and mid-plane temperatures in horizontal tunnel (Gallery 5) at different ventilation rates

decay. In contrast, the CFD prediction remains nearly constant for around 20 m before falling away at a near linear rate.

This implies that the CFD model under-predicts the heat lost to the boundary, due to one or more of radiation, convection or conduction. Conduction and convection are determined by the boundary conditions used for the walls, floor and ceiling, and although there is some uncertainty in the model parameters, the values used could not cause a significant underprediction of heat loss.

Radiative heat transfer to the boundaries depends on several aspect of the model, some of which are not well defined. Figures 6.19 to 6.23 show the effect of various adjustments to the radiation model on the temperature profiles.

In Figure 6.19, the soot production model included in *Fluent* is activated with default parameters. This produces an exponential decay consistent with the experimental data in the far downstream region. It does appear to show some grid dependence, as there is a discontinuity at the location of the grid interface (22 m downstream of fire).

In Figure 6.20, the weighted sum of grey gases model (WSGGM) is used to calculate the attenuation coefficient for the continuous phase, firstly using a single-band, and then using the six bands recommended by McGrattan (2005). The difference between the two is minimal and the discontinuity at the grid interface is again visible.

Figure 6.21, uses a finer grid, with less difference in cell size between the two meshes. This underpredicts temperature by 50 %, but does produce profiles that fit the shape of the experimental data.

6.2.5 Plume shape and pan geometry

Although a detailed description of the experimental flow field is not available the high temperature values recorded at the mid-height and ceiling thermocouples 3 m downstream of the fire imply a strongly buoyant plume with an angle of around 45°.

In the CFD simulation, a much larger distance is required for the plume to develop, and the peak ceiling temperature occurs around 20 m downstream of the fire source. Figure 6.24 shows the predicted temperature profile downstream of the fire for 2.4 m/s ventilation. The fire plume is virtually horizontal, and remains attached to the tunnel floor for a considerable distance. Heat transfer to ceiling level primarily occurs due to turbulent mixing and diffusion, rather than convection.

The strength of buoyancy forces in the flow can be estimated from the ratio of Grashof number to Reynolds number (see Equation 6.1 in Section 6.1.2.5). For the 0.8 m/s case this ratio is around 38, whereas for the 2.4 m/s case the ratio drops to approximately 4.2 (Based on $\rho = 1.2\,\mathrm{kg/m^3}$, $\Delta\rho = 1\,\mathrm{kg/m^3}$, $g = 10\,\mathrm{m/s^2}$, and $h = 2.95\,\mathrm{m}$). In comparison the scale-tunnel experiments had a ratio of 8.0, so the 2.4 m/s case has the weakest buoyancy by a considerable margin.

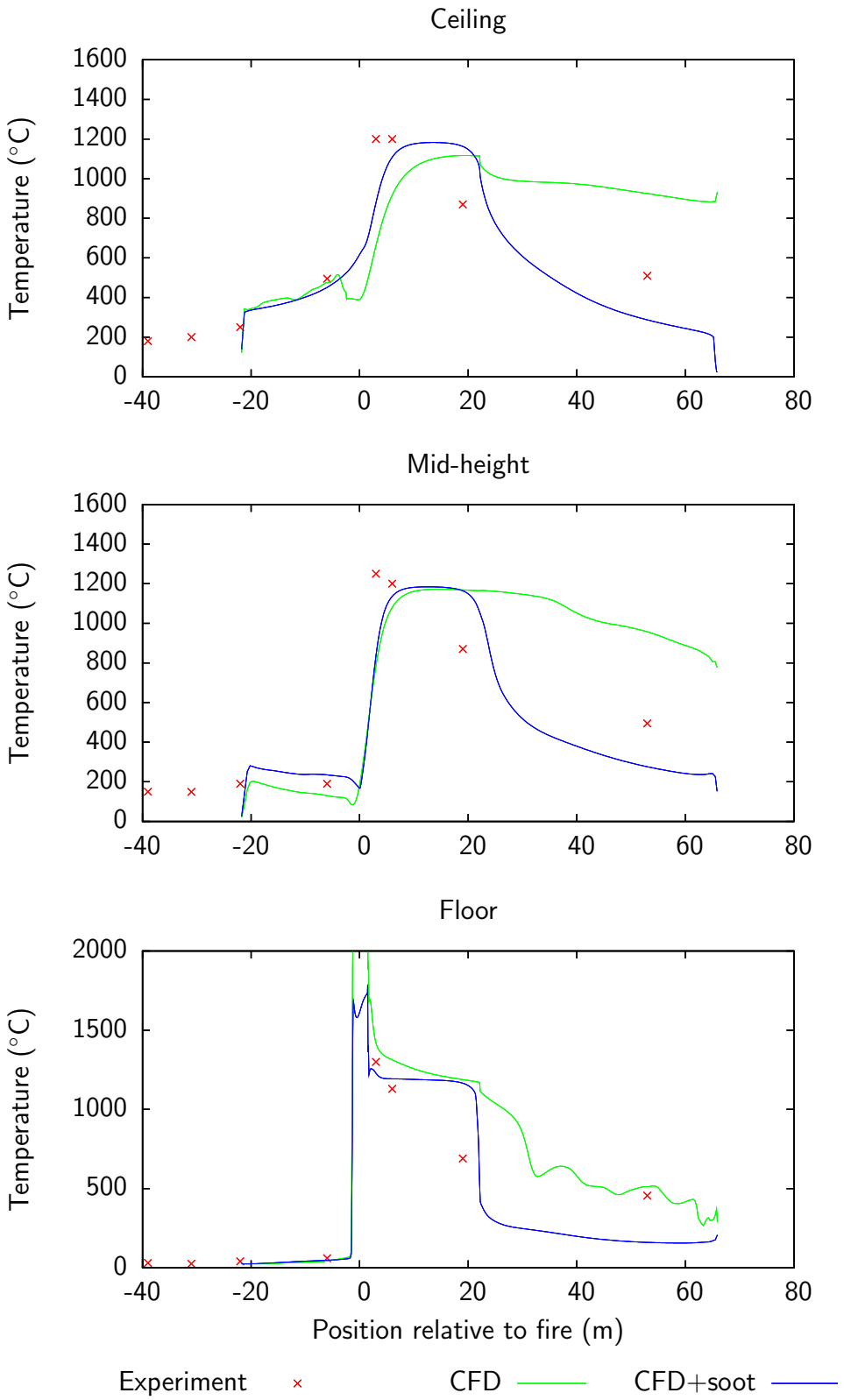

Figure 6.19: Comparison of CFD results with and without soot model and thermocouple data (0.8 m/s ventilation, Gallery 5)

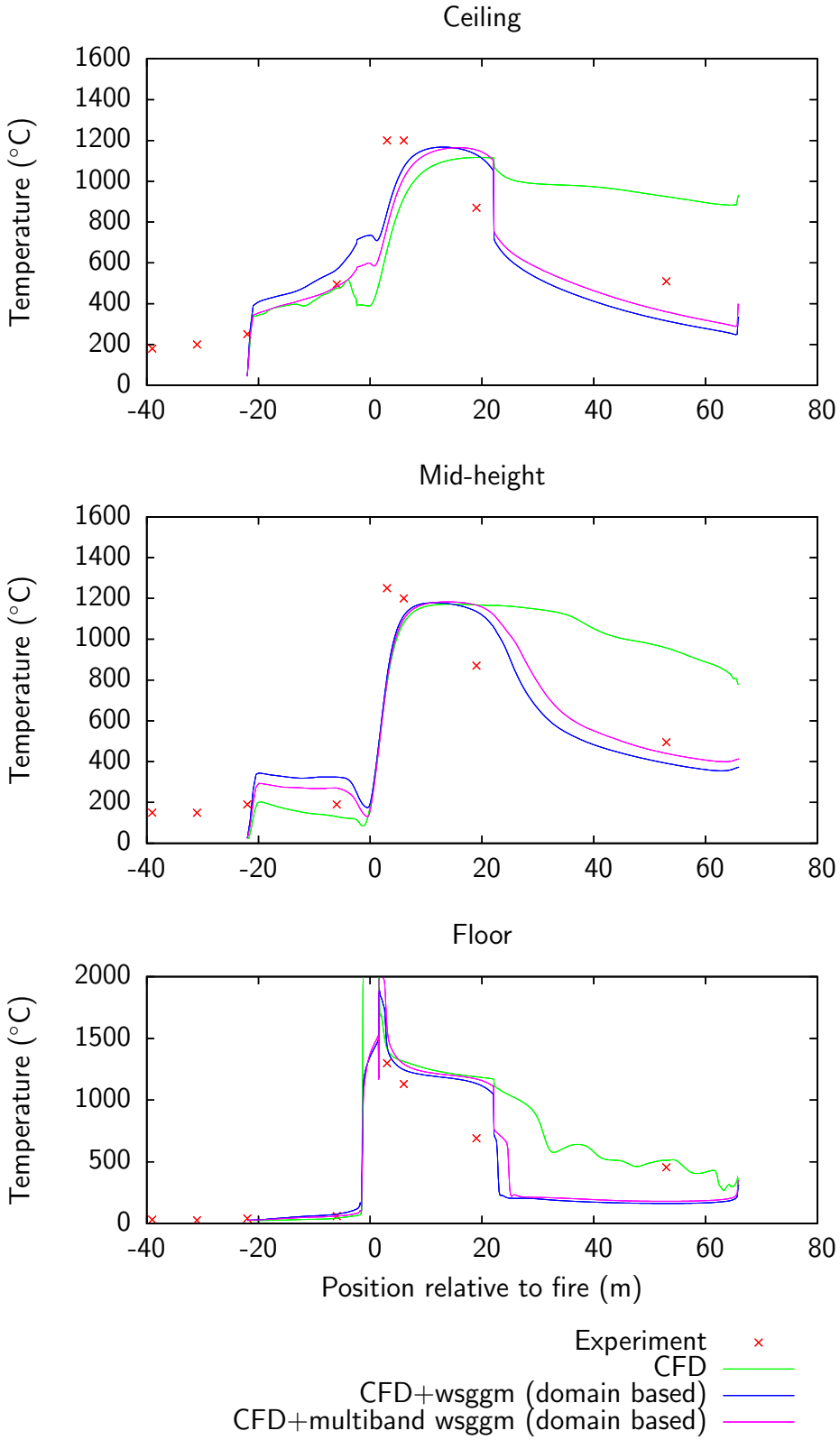

Figure 6.20: Comparison of the original CFD results with cell based WSGGM and domain based WSGGM (0.8 m/s ventilation, Gallery 5)

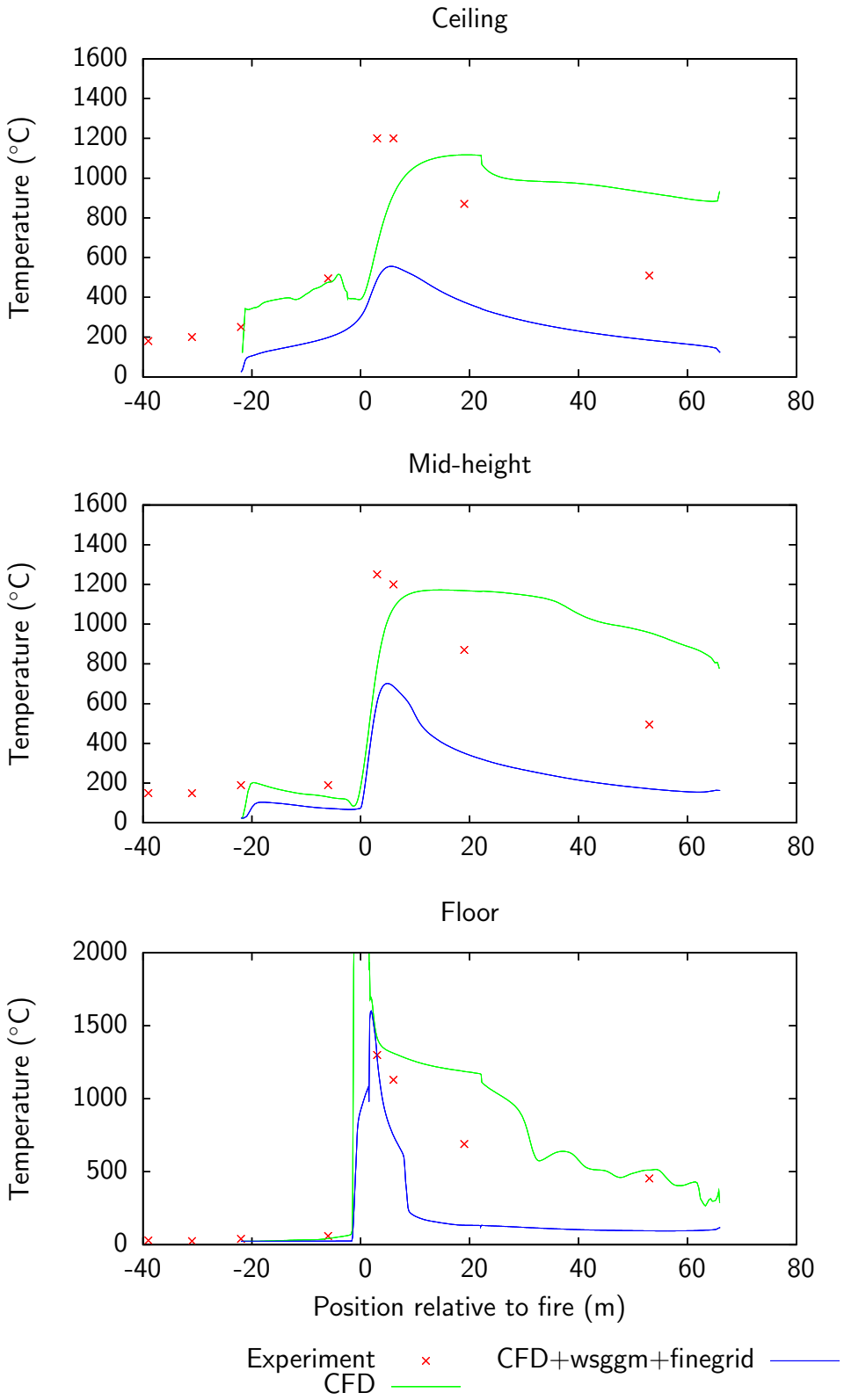

Figure 6.21: Comparison of the original CFD results with results using WSGGM for radiation absorption and a finer grid (0.8 m/s ventilation, Gallery 5)

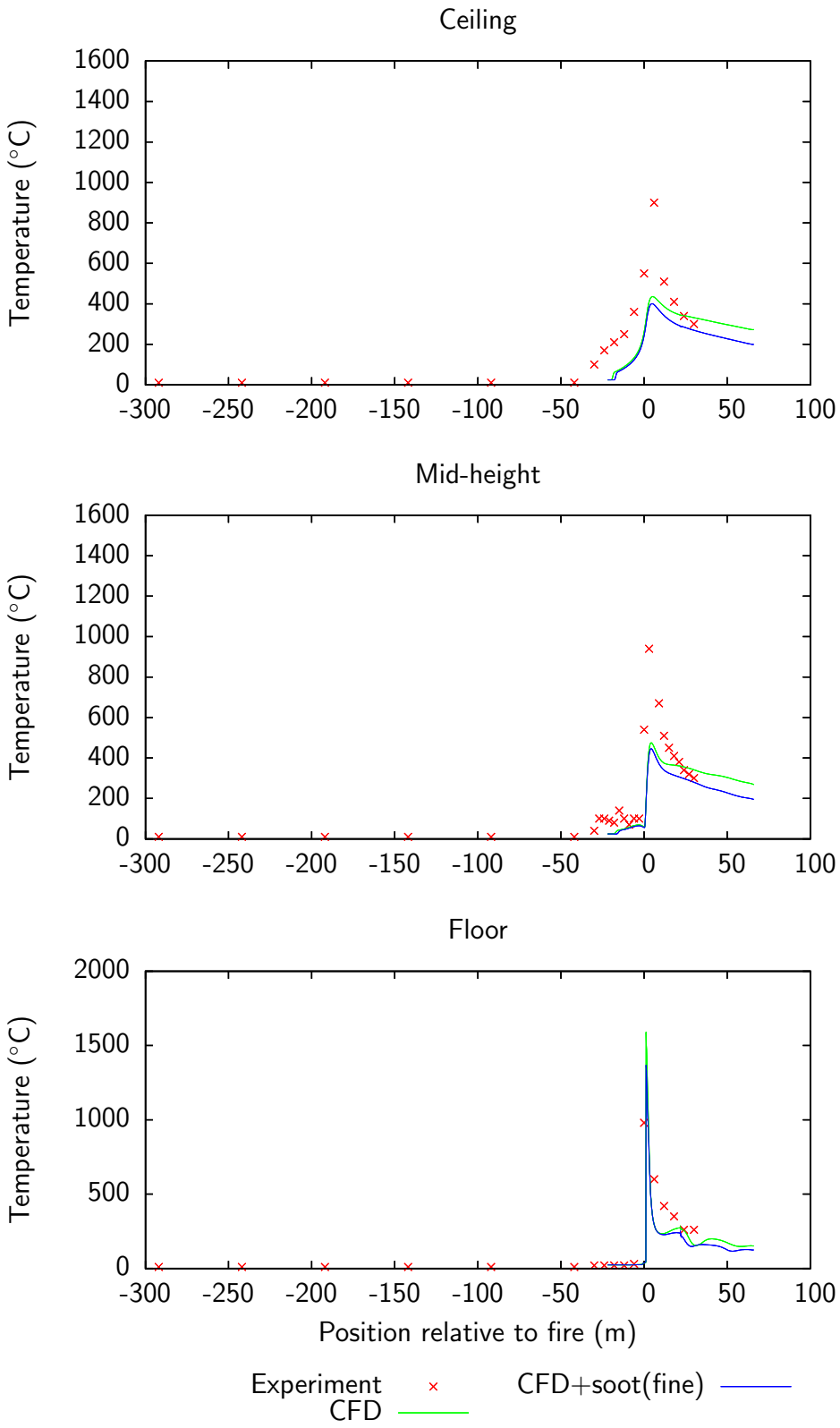

Figure 6.22: Comparison of the original CFD results with soot and domain based WSGGM for Gallery 4 (Ramsbeck) downward flow

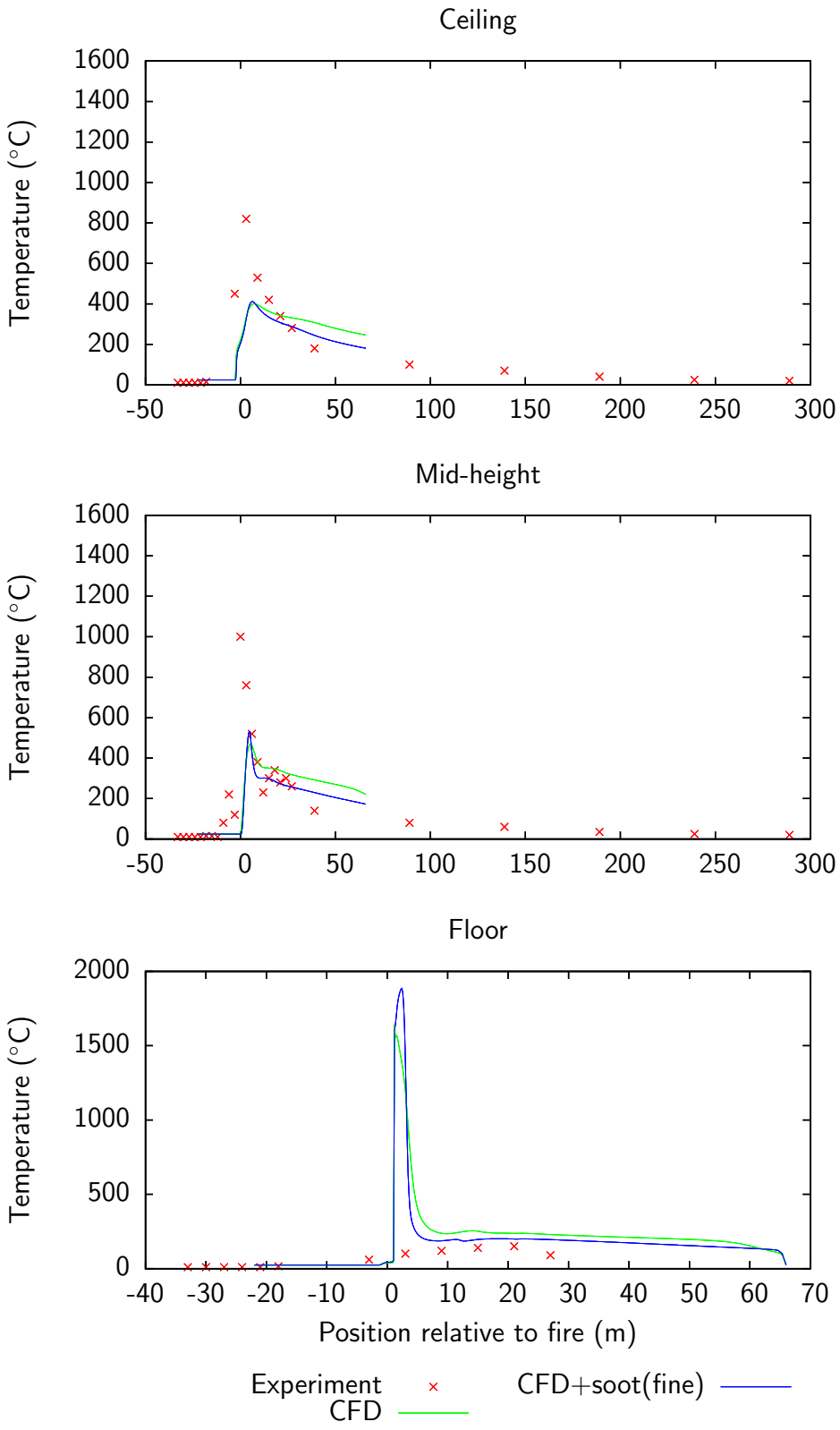

Figure 6.23: Comparison of the original CFD results with soot and domain based WSGGM for Gallery 4 (Ramsbeck) upward flow

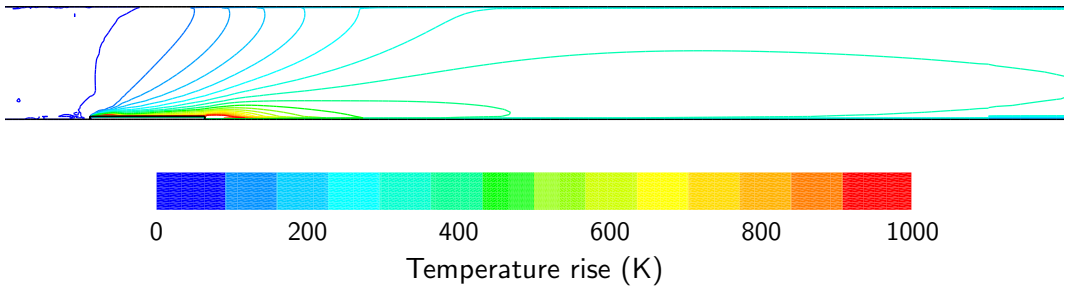

Figure 6.24: Attachment of plume to tunnel floor downstream of pool for 2.4 m/s ventilation (Gallery 5)

The attachment of a fire plume to an adjacent surface occurs when the entrainment of air to one side of the plume is restricted, and would be expected downstream of a fire with such a large cross wind. Sinai and Owens (1995) performed CFD modelling of an open-air pool fire in a cross-wind. Their initial simulation based on the k-ε turbulence model significantly over-predicted the length of attachment or *'base drag'*. An investigation of the cause of this problem showed that the results could be dramatically improved by including the protruding section of the pool wall in the mesh geometry. Additionally the model was shown to be sensitive to the surface roughness upstream of the fire.

In order to ascertain whether a similar problem exists in the tunnel fire simulation, a new mesh was created with a more detailed representation of the pan geometry. Firstly, the overall height of the pan was doubled to 16 cm (in other words the 720 l of fuel is assumed to only half fill the pan), and secondly a gap is left between the edge of the pan and the tunnel wall. As none of the previous simulations had exhibited any asymmetric flow patterns, and as the more detailed geometry required a finer mesh around the pan, and particularly between the pan and the tunnel wall, symmetry was exploited in order to allow a better mesh at no additional computational cost.

Results from this mesh are shown in Figure 6.25 and Figure 6.26. At 0.8 m/s the results are good, with the peak occurring in the correct position, and although temperatures are slightly over-predicted, the general pattern is entirely consistent with the experimental data. At 2.4 m/s the temperature predictions are not particularly improved compared to the original mesh.

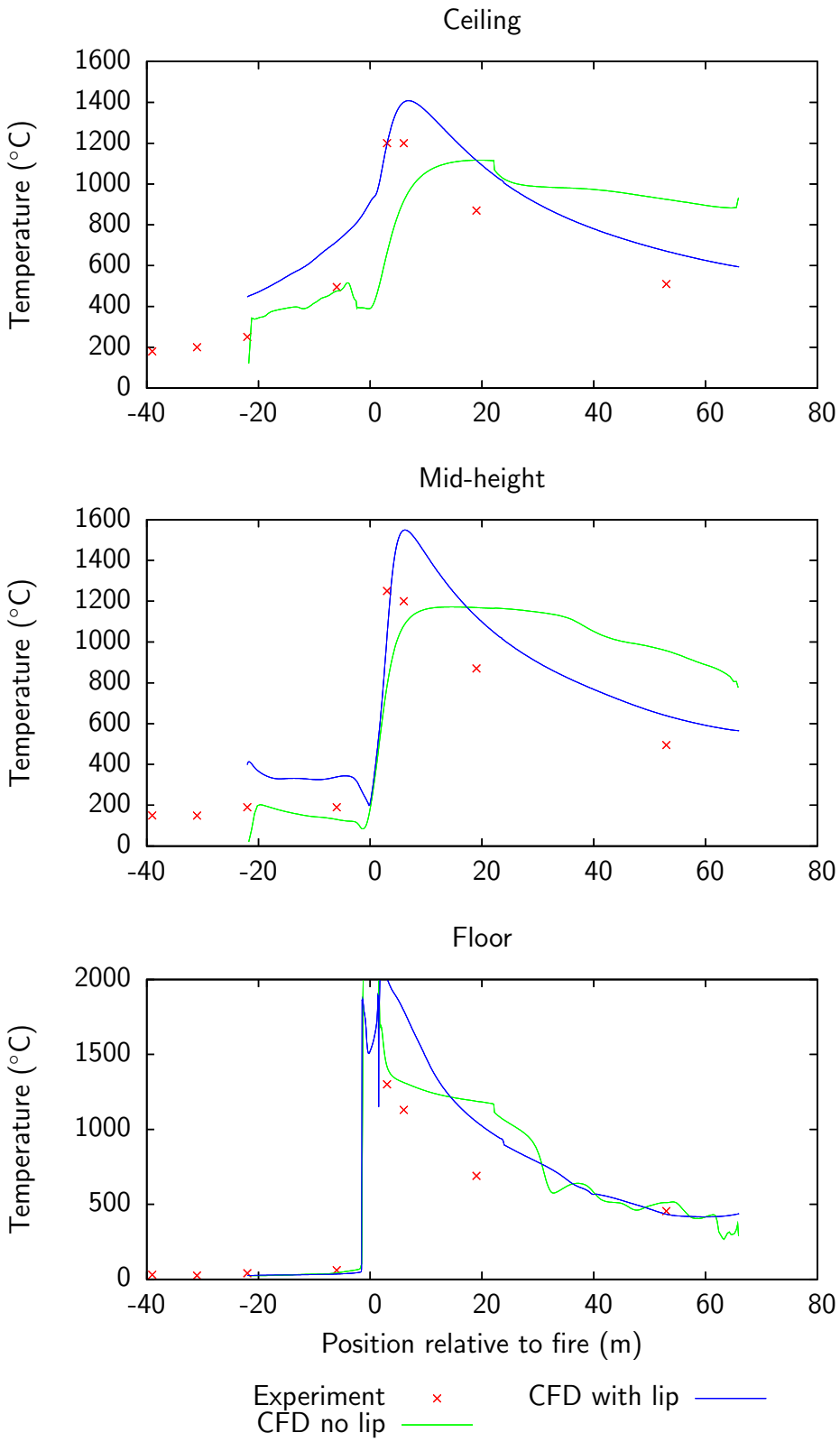

Figure 6.25: Comparison of CFD results with and without a 'lip' and the experimental data (0.8 m/s ventilation, Gallery 5)

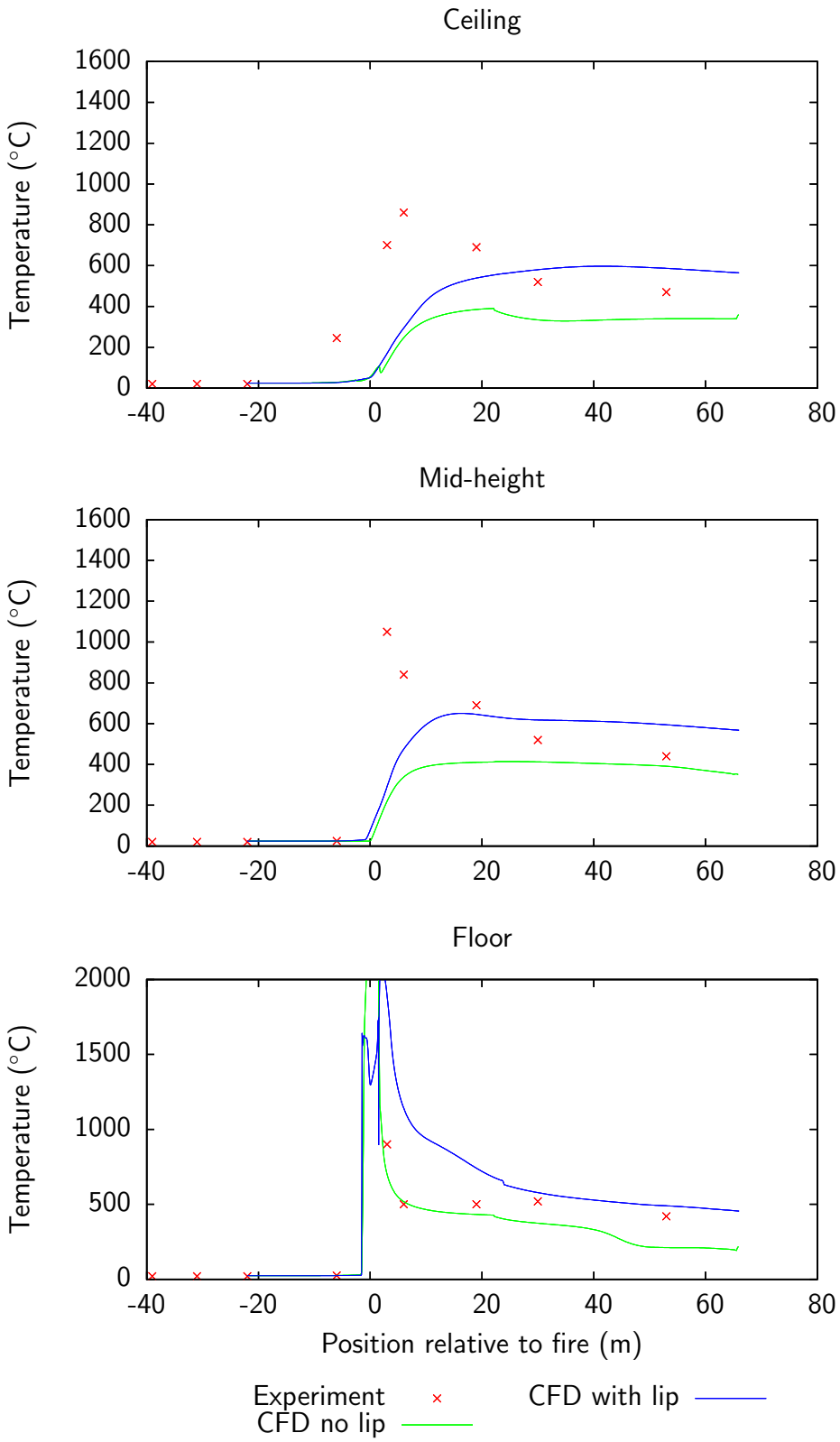

Figure 6.26: Comparison of CFD results with and without a 'lip' and the experimental data (2.4 m/s ventilation, Gallery 5)

6.2.5.1 Hybrid combustion model

Once a steady solution had been reached based on the EBU combustion model, the hybrid Arrhenius/EBU model was activated. This is a prerequisite for the modelling of fire suppression that is covered in Section 7.2, but is also useful in testing the mixed-is-burned assumption of the plain EBU model.

For the enclosure fire, a slight discrepancy in the flame location was evident at the transition between models that quickly stabilised over the next five or six time steps. A similar behaviour was expected for the tunnel fire model.

Unfortunately, for the tunnel fires, the transition to the hybrid model caused a much more significant deviation, particularly at the higher ventilation rate, where the rate of reaction would quickly drop to zero. The exception to this pattern was with the cases based on the detailed representation of the pan geometry, where the presence of the protruding pan wall stabilises the leading edge of the flame. The reason for this can be clearly seen in Figure 6.27, which shows the steady state temperatures close to the pool for the two cases. Without a lip, the leading edge of the pan remains cold, which inhibits the reaction once the hybrid model is activated. This, of course, leads to a progressive retreat of the flame, until the hot recirculation zone behind the pan is reached. For the 0.8 m/s case, this is sufficient to maintain the combustion (albeit 3 m further downstream than before), but at 2.4 m/s, the flame becomes completely detached from the fuel source, and complete extinction follows shortly afterwards. The presence of a lip creates a hot recirculation zone at the leading of the pan, and therefore prevents this phenomenon. Figure 6.28 and Figure 6.29 compare the rate of reaction as predicted by the plain EBU model, and the hybrid Arrhenius/EBU model. With the exception of a small region just in front of the pan, the only effect of the hybrid model is on the far-field, where the rate of reaction is already minimal.

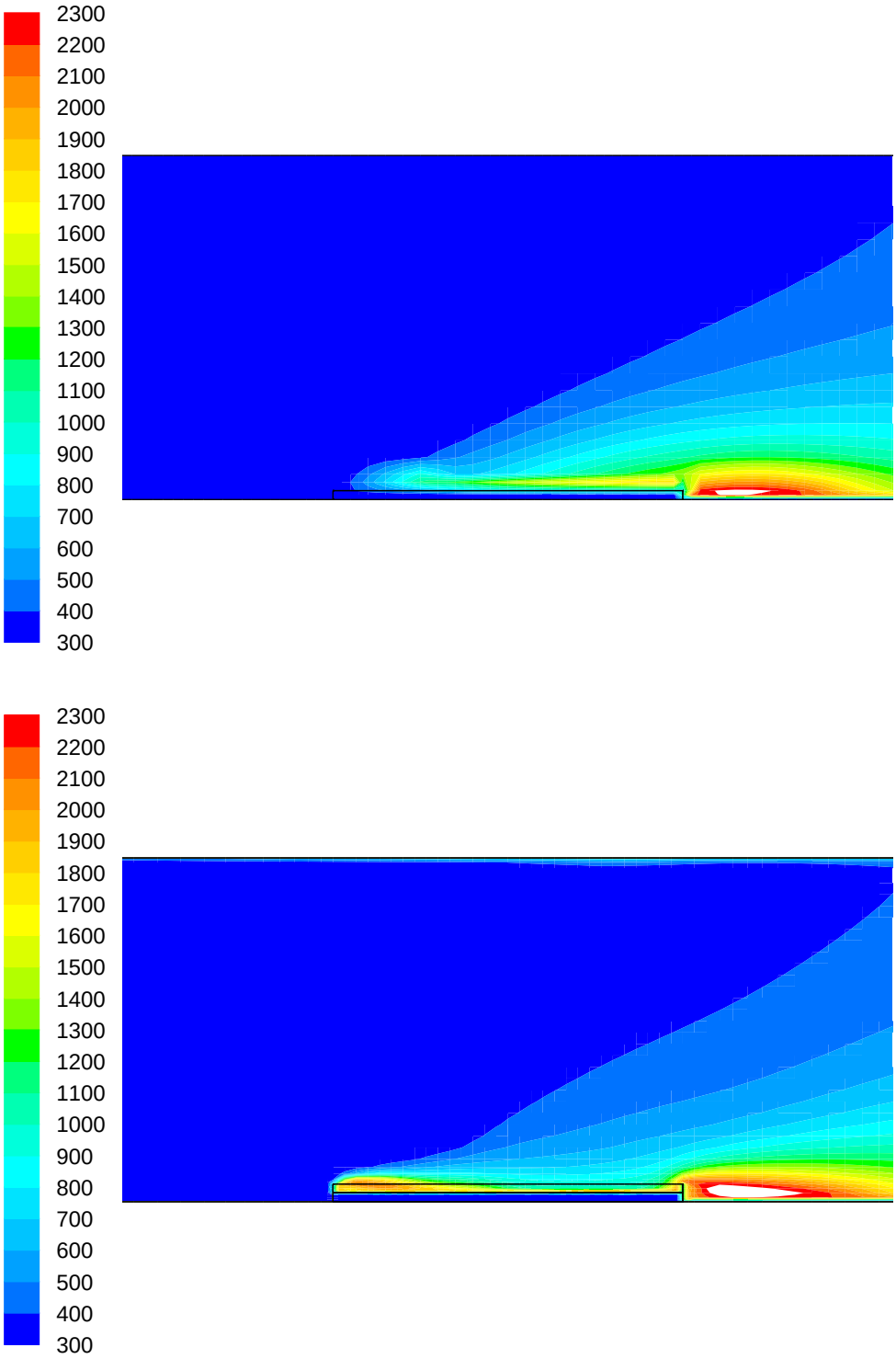

Figure 6.27: Contours of temperature plotted on mid-plane for simplified and detailed geometry
(2.4 m/s ventilation, Gallery 5)

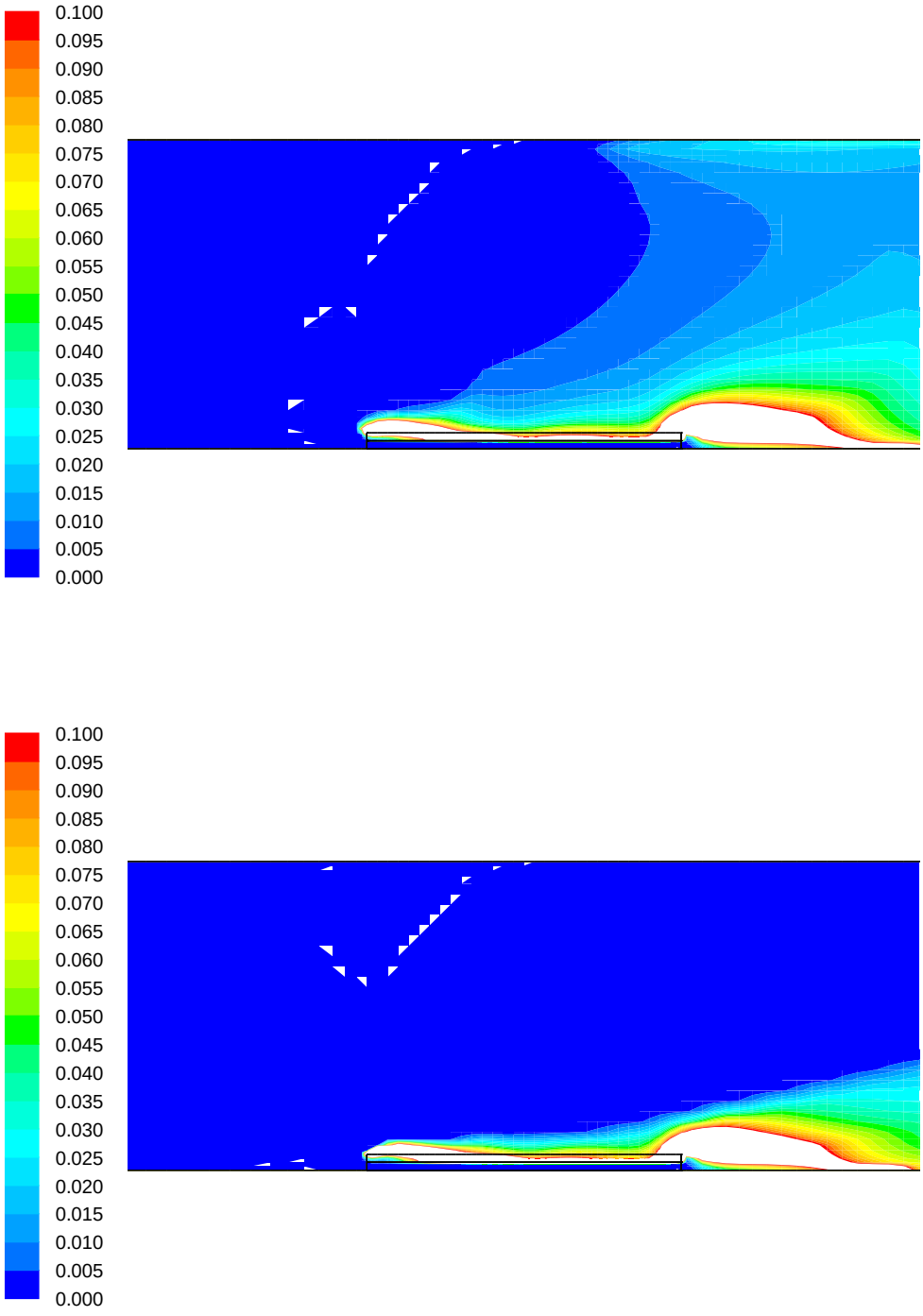

Figure 6.28: Contours of reaction rate plotted on mid-plane for plain EBU model and hybrid Arrhenius/EBU model, 0 – 0.1 mol/m^3/s (2.4 m/s ventilation, detailed pool geometry, Gallery 5)

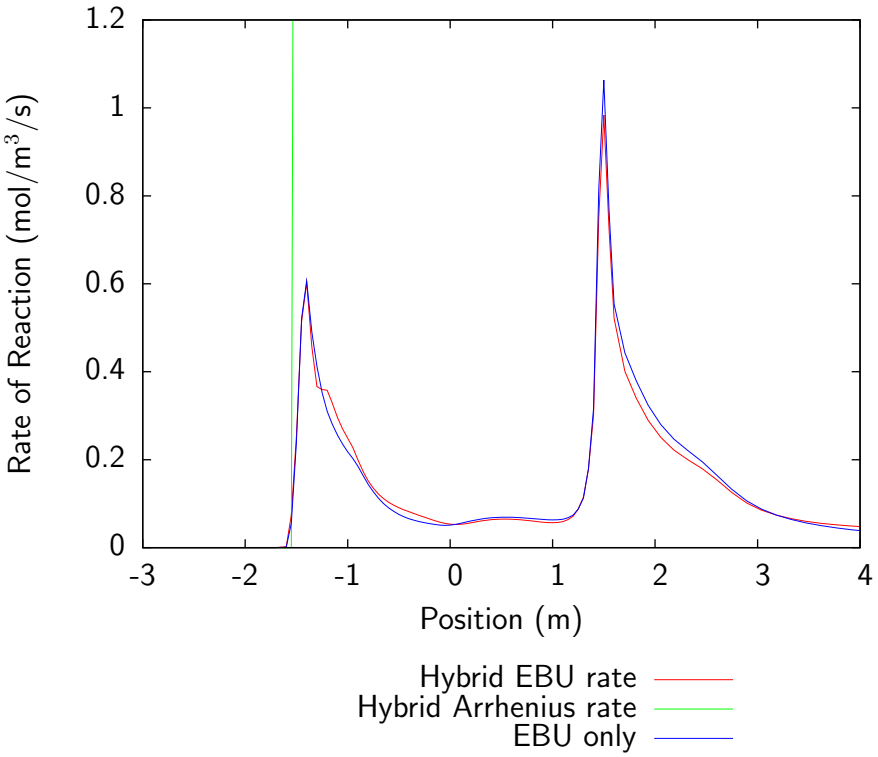

Figure 6.29: Comparison of reaction rate level at the intersection of the mid-plane and the top of the pan, for EBU only and Arrhenius and EBU from the hybrid model
(2.4 m/s ventilation, detailed pool geometry, Gallery 5)

6.2.6 Comparison with theoretical and generic empirical correlations

6.2.6.1 Plume temperature

Using Equations 2.4 and 2.5, an expression for the centreline temperature of the fire plume can be derived. This neglects the effects of forced ventilation and of the tunnel walls.

$$\Delta T_0 = 26\frac{\dot{Q}_{\text{conv}}^{\frac{2}{3}}}{(z-z_0)^{\frac{5}{3}}} \tag{6.8}$$

$$\frac{z_0}{D} = -1.02 + 0.083\frac{\dot{Q}_{\text{c}}^{\frac{2}{3}}}{D} \tag{6.9}$$

$$\tag{6.10}$$

For $\dot{Q}_c = 11\,\mathrm{MW}$ and $D = 3\,\mathrm{m}$, this gives:

$$\begin{aligned} z_0 &= -3.06\,\mathrm{m} \\ \Delta T_0 &= \frac{12,860}{(z+3.06)^{\frac{5}{3}}} \end{aligned}$$

This relationship is shown graphically in Figure 6.30, along with data from the tunnel fire model (each CFD datum corresponds to the peak temperature observed at a given height above the tunnel floor).

The peak plume temperature from the analytical free plume is around 2000 K, which is around 400 K cooler than the CFD predictions. The analytical relationship is sensitive to the value of the *virtual origin* (z_0), and only a ten percent reduction is needed to give an identical peak temperature. There are many factors which will influence the virtual origin, notably the proximity of the tunnel walls, and the shear distortion of the flames due to the forced ventilation.

For a free plume, the reduction in temperature with height is due to entrainment of cool air into the hot plume gases, and radiation losses. For the confined plume, the tunnel walls prevent almost all of this entrainment, however heat is lost across the tunnel walls and ceiling. At 0.8 m/s the temperature profile takes a similar form to the free plume, but with a much shallow curve. At 2.4 m/s however, the increased forced ventilation has two effects: i) greater temperature loss due to dilution (i.e. the steep temperature gradient immediately above the fire) and ii) prevention of stratification (i.e. the lack of variation of temperature over most of the tunnel height).

6.2.6.2 Critical velocity

According to Wu and Bakar (2000) the critical ventilation velocity for a tunnel fire (i.e. the ventilation rate above which there is no reverse flow of hot gases upstream of the fire source) is given by: $V'' = 0.4$ for $Q'' > 0.2$, where:

$$V'' = \frac{V}{\sqrt{g\bar{H}}} \tag{6.11}$$

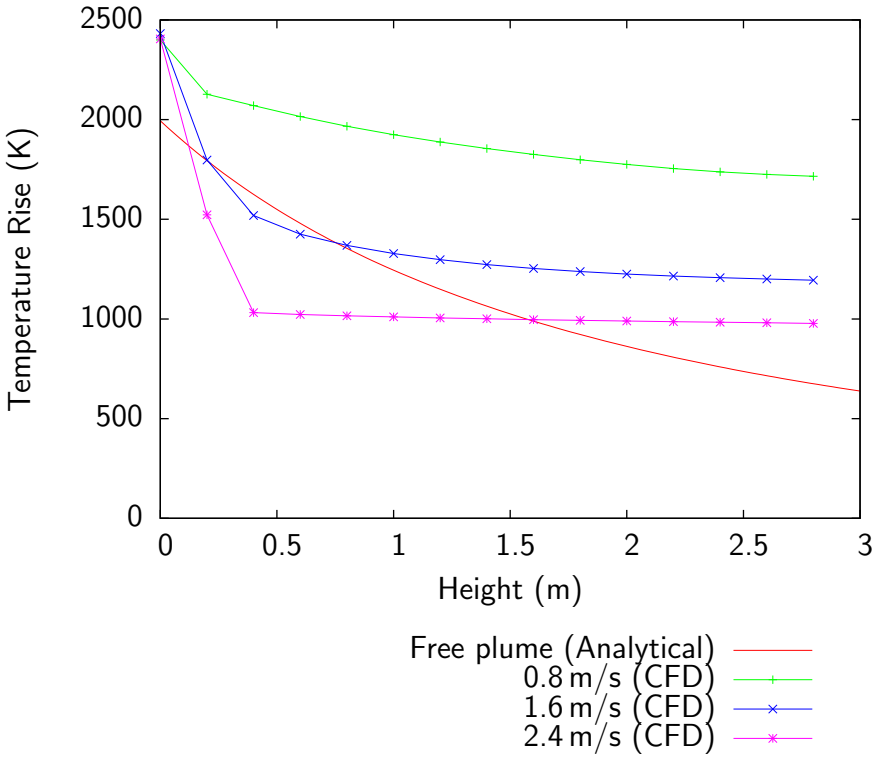

Figure 6.30: Variation of plume temperature with height in tunnel for 0.8 m/s and 2.4 m/s contrasted with an unconfined plume from an 11 MW diesel fire in Gallery 5

and

$$Q'' = \frac{Q}{\rho_0 T_0 C_p \sqrt{g \bar{H}^5}} \tag{6.12}$$

Taking

$$\begin{aligned} C_p &= 1006.43\,\mathrm{J/kg\,K}, \\ \rho_0 &= 1.225\,\mathrm{kg/m^3}, \\ T_0 &= 300\,\mathrm{K}, \text{ and} \\ \bar{H} &= 4\tfrac{\text{Area}}{\text{Perimeter}} = 3.05\,\mathrm{m}, \end{aligned}$$

gives $Q'' = 0.586$.

In other words, the fire is sufficiently large that the critical velocity is independent of fire size. The critical ventilation velocity corresponding to $V'' = 0.4$ is 2.19 m/s.

The recorded length of back flow in the experiments was 3 m for 2.4 m/s, and more than 36 m for 0.8 m/s (DMT et al., 2004a). This suggests a critical velocity

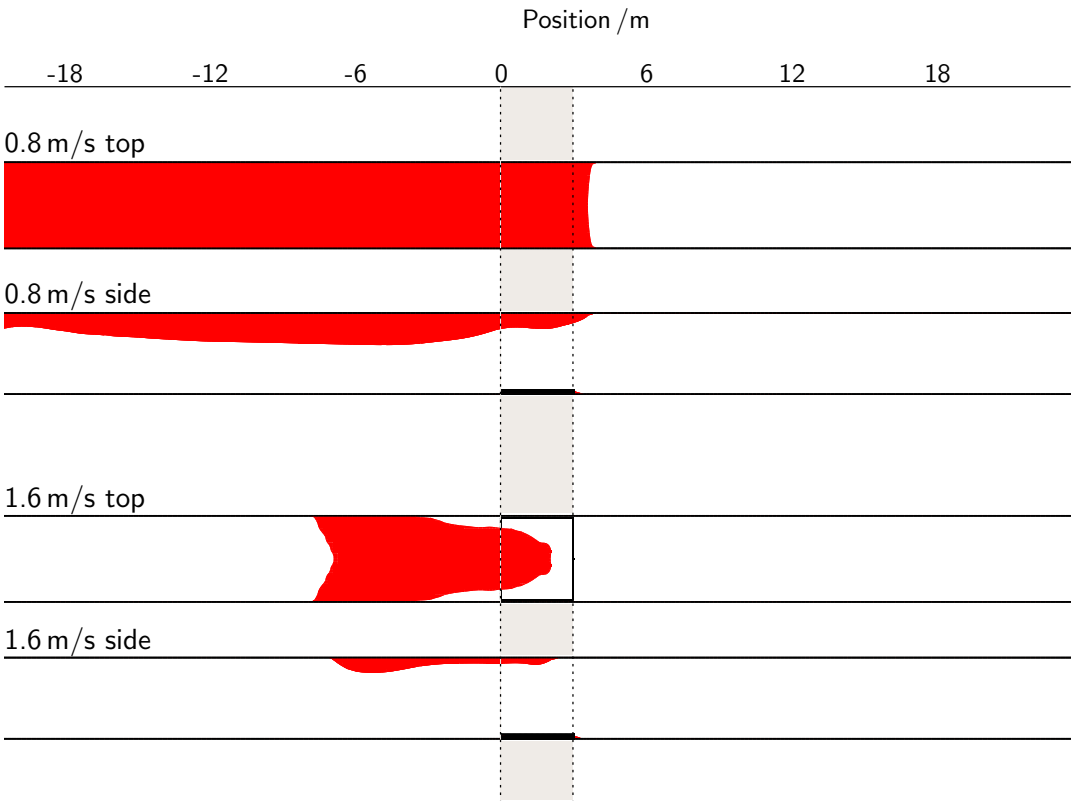

Figure 6.31: Location and extent of back flow in horizontal tunnel for 0.8 m/s and 1.6 m/s forced ventilation (Gallery 5)

slightly above 2.4 m/s.

Similarly, the CFD simulations show an extensive back flow at 0.8 m/s, but no back flow at all at 2.4 m/s. A simulation performed at an intermediate velocity of 1.6 m/s showed approximately 10 m of back flow, suggesting a critical velocity slightly below 2.4 m/s. The CFD is therefore consistent with both the empirical results and the experimental observations.

6.2.6.3 Frequency of oscillations

The frequency of oscillations can be correlated to the fire size by Equation 6.13 (Drysdale, 1998; Sinai, 2000).

$$f = (0.5 \pm 0.04)\sqrt{\frac{g}{D}} \tag{6.13}$$

Which for the size of fire considered here gives:

$$f = 0.85 \pm 0.07\,\mathrm{Hz} \tag{6.14}$$

No particular fluctuation was observed in the CFD results, however as the time step used was larger than the expected frequency this is to be expected. Oscillations (or *flickering*) of flames are due to complex turbulence–combustion interaction, and therefore may not be reproducible without advanced turbulence models such as LES and fine grids and small time steps.

6.2.6.4 Deflection of plume

For fires in the open, a plume will deflect by around 45° under a 2 m/s wind, and will hug the ground downstream of the fire by around $0.5D$ (Drysdale, 1998). CFD results show the plume attaching itself to the tunnel floor for much greater distances. It is unclear whether this is a physical phenomenon – perhaps due to the confining nature of the tunnel – or an artificial one – due to some numerical problem. The experimental data (see Table D.8) is not particularly conclusive showing slightly lower floor level temperature at a few but not all positions downstream.

Some information is available from the literature concerning plume deflection in ventilated tunnels. For example, Kurioka et al. (2003) used non-dimensionalised plots of small scale experimental data to construct empirical relationships for the plume tilt in ventilated tunnel fires. They found:

$$\cos\theta_1 = \alpha \left[A_f^{1/2} \frac{b^{1/2}}{H^{3/2}} Q^{*(1-2\eta)/5} \mathrm{Fr}^{-1/2} \right]^{\beta} \tag{6.15}$$

where: $\alpha = 0.80, \beta = 1$ for $0.15 \leq A_f^{1/2} \frac{b^{1/2}}{H^{3/2}} Q^{*(1-2\eta)/5} \mathrm{Fr}^{-1/2} < 1.25$ and $\alpha = 1.0, \beta = 0$ for $1.25 \leq A_f^{1/2} \frac{b^{1/2}}{H^{3/2}} Q^{*(1-2\eta)/5} \mathrm{Fr}^{-1/2}$ (see Table 6.7 for nomenclature).

For this scenario, the Froude number, $\mathrm{Fr} = U_{wind}^2/(gH_d) = 0.0221$ for $U_{wind} = 0.8\,\mathrm{m/s}$, and 0.199 for $U_{wind} = 2.4\,\mathrm{m/s}$.

The dimensionless heat release rate is:

$$Q^* = \frac{Q}{\rho_a C_p T_a g^{1/2} H_d^{5/2}} = 0.636 \tag{6.16}$$

This gives a value of $\cos\theta_1$ of 1.0 for all cases, and therefore predicts a vertical plume. However, they assume that:

- *moderate forced ventilation is operating, namely not becoming one well-mixed layer, but upper hot and lower cold layers are formed.*
- *extension of the flame base by forced ventilation is negligible.*

neither of which is apparent in the CFD model or experimental data for this scenario.

Additionally, the fire data that Kurioka et al. used all came from fires with a diameter less than one third of the tunnel. For this case the fire is nearly 95% of the tunnel width, and so is outside of the range of validity of Equation 6.15.

6.2.7 Summary of findings

- the aerodynamic effects of the fuel pan can be important and need to be represented.
- at sub-critical velocities, agreement between the CFD simulations and experimental temperatures is good.
- at super-critical velocities, the CFD simulations and experimental temperatures do not agree, as the CFD model does not exhibit the expected buoyant plume.
- the variation of backflow length with velocity and the critical velocity predicted by the CFD model are consistent with the experimental observations and empirical data from the literature.
- the thermal boundary conditions (both convective and radiative) are very important to the accuracy of the model.

Table 6.7: Empirical relationship of Kurioka et al. (2003) applied to DMT scenario

Parameter	units	Description	Value
b	m	width of tunnel	$3 \cdot 15$
H	m	height of tunnel	$2 \cdot 95$
A_s	m^2	Cross sectional area of tunnel	$9 \cdot 2925$
A_p		Aspect ratio of tunnel height/width	$0 \cdot 937$
A_f	m^2	area of fire-source	$9 \cdot 3$
D	m	Representative length of fire source	$3 \cdot 05$
H_d	m	height from the surface of fire source to tunnel ceiling	$2 \cdot 95$
Q	kW	heat release	$11,000$
T_a	K	Temperature of ventilation	300
ρ_a	kg/m^3	density of ventilation air	$1 \cdot 225$
C_p	kJ/kg/K	Specific heat capacity	$1 \cdot 005$
g	m/s/s	gravity	$9 \cdot 81$
U_{wind}	m/s	representative ventilation velocity	2.4 or 0.8
ΔT_{max}	K	maximum rise in temperature above ambient	$2,000$
η		*coefficient of plume zone*	$-0 \cdot 333$

6.3 Conclusions

The modelling of a tunnel fire was successfully achieved. Two different approaches were taken for the representation of the fire itself, and an understanding of the relative advantages and disadvantages of each was reached.

Whilst the predetermined volumetric heat source approach avoids many of the unknowns and complexities of a realistic fire model, it is unduly sensitive to the shape and size of the heat source used. This is especially problematic if the physical size of the fire is similar to that of the tunnel itself.

On the other hand, the use of a combustion model is by no means fool proof, and a number of potential pitfalls exist. The fixed mass fraction boundary condition was chosen because it seemed the most appropriate way to handle the aerodynamic processes. However, the need to calibrate the laminar diffusion constant to the experimentally determined fuel release rate is a significant limitation, and it may be that alternative ways of modelling the liquid surface need to be investigated.

The CFD model also required a significant amount of computational resources to solve, due to the need for an unsteady solution and the requirement for a mesh fine enough to capture the stratification of the flow, as well as the fuel vapourisation and combustion close to the pan in the full model. This would limit the scope of any parametric study based on this model.

In the next chapter, the CFD model is extended to include a water mist fire suppression system.

Chapter 7

CFD modelling of water mist fire suppression

In this chapter, a CFD model of a water mist fire suppression system is developed. The discrete phase model (DPM) of *Fluent* is used to represent the water mist. The model is applied to the enclosure and tunnel fire scenarios that were modelled in Chapters 5 and 6 respectively. For the enclosure, experimental data are available (Kim and Ryou, 2003), allowing the model to be validated. For the tunnel, the modelled system is hypothetical because no adequate source of experimental data is available. In both cases, the sensitivity of the water mist system to variation in key parameters – such as water flow rate, droplet diameter, spray angle and nozzle velocity – is explored.

7.1 Application of water mist to an enclosure fire

The aims of this study are to demonstrate that the suppression of a pool fire by water mist can be modelled and that the DPM behaves correctly when used to represent water mist.

An enclosure fire scenario was selected for the initial development of the fire suppression model for three reasons:

1. published experimental data was available to validated the model;

2. enclosures provide a well controlled and defined environment that is easily replicated;

3. existing research and current applications focus almost entirely on enclosures. A qualitative understanding exists of various potential mechanisms of action;

4. the limited domain of the problem limits the size of the mesh and allows symmetry to be exploited in order to further minimise the computational resources required.

An understanding of the various parameters of the model, both numerical (such as under-relaxation factors, time-step size, etc.) and physical (such as water flow rate, droplet diameter, spray angle, etc.) will be reached.

7.1.1 Background

Kim and Ryou (2003) investigated the extinction of methanol and n-hexane pool fires in an enclosure using water mist. A CFD model of the enclosed pool fire was developed and validated in Chapter 5, and will be used as the basis for a model of the fire suppression process.

Details of the enclosure and fire used in the experimental study are given in Section 5.1.

7.1.1.1 Water mist

Water mist was injected from five points near the roof of the enclosure (see Figure 7.1). The key specifications of the water mist system are shown in Table 7.1. The droplet diameter distribution of the mist, as presented in the paper, can be fitted to a Rosin-Rammler distribution of the form:

$$Y_d = e^{-(d/\bar{d})^n} \tag{7.1}$$

where $\bar{d} = 107\,\mu\text{m}$ and $n = 1.563$. This differs slightly from the fit shown by Kim and Ryou (2003) which appears closer to $\bar{d} = 113\,\mu\text{m}$ and $n = 2.383$ (see

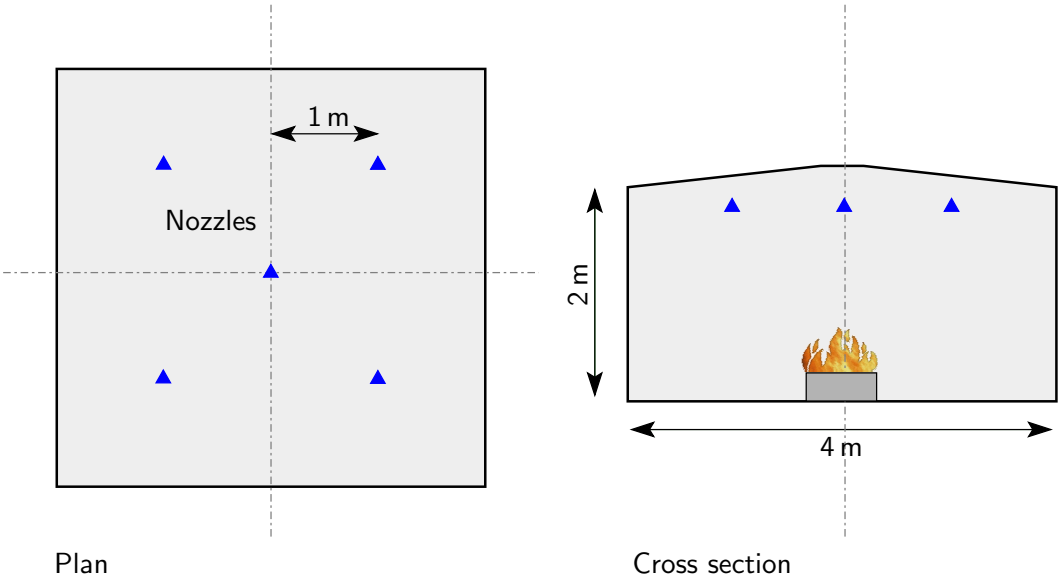

Figure 7.1: Schematic view of experimental setup (Kim and Ryou, 2003)

Table 7.1: Specification of water mist (Kim and Ryou, 2003)

Sauter mean diameter (SMD)	121 µm
Orifice diameter	3 mm
Operating pressure	13 bar
Flow-rate	6 l/min
K-factor	1.66
Spray pattern	Hollow cone
Spray angle	70-90 °
Spray velocity	14.1 m/s

Figure 7.2). As discussed in Section 3.2.7, substantial variation in the value of distribution parameters can be observed depending on how a distribution is fitted to measured data.

7.1.1.2 Results

Kim and Ryou (2003) are more interested in the cooling of the smoke layer than fire extinction, and the published data is primarily concerned with the evolution of mean ceiling temperature after mist activation.

This pertains to the interruption of the plume, disruption of stratification, and cooling of the space by conduction through the walls and ceiling.

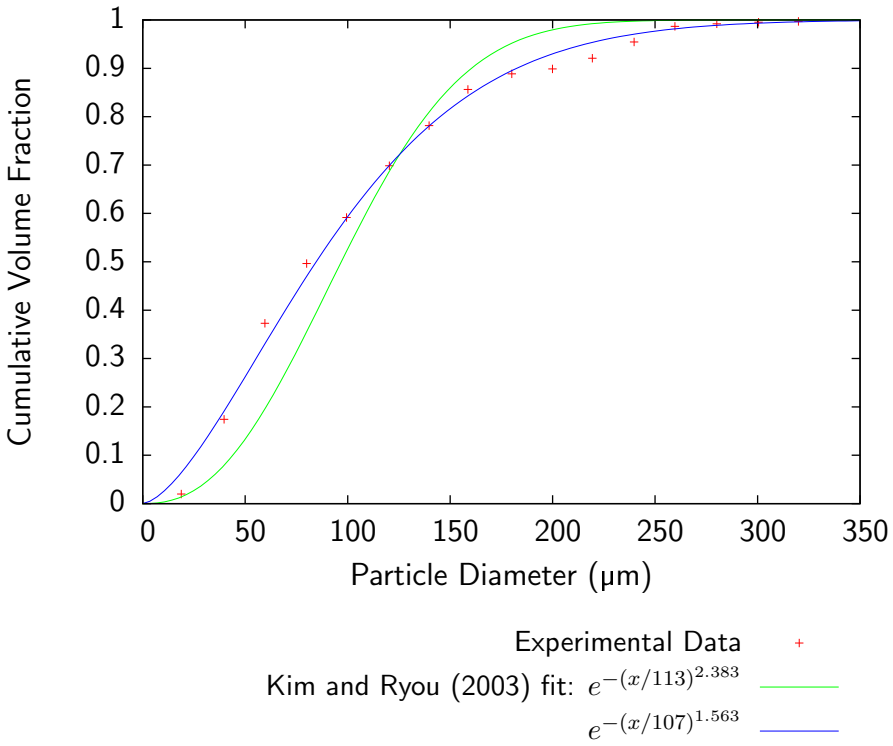

Figure 7.2: Droplet diameter distribution

The use of an average over the entire ceiling combined with uncertainties in the response of the water-mist system and thermocouples make it difficult to determine a clear datum for validation of the CFD model.

They do not record flame or plume temperatures, or any other data that relates directly to the fire itself.

7.1.2 CFD model

7.1.2.1 Meshing, combustion, initial conditions

Full details of the enclosure fire CFD model are given in Section 5.2 and except where explicitly stated were not modified. The hybrid Arrhenius/EBU combustion model was used, and initial conditions were taken from the corresponding fire case at the time of mist activation.

7.1.2.2 Discrete phase model

In order to investigate the feasibility of using the discrete phase model (DPM) to represent water mist, it was initially applied to a 2D axisymmetric case based on the enclosure fire experiments. This allowed a complete investigation of the large number of parameters associated with the DPM without the cost of running a full 3D case.

For this study, a single nozzle located in the centre of the room at a height of 1.8 m was considered. The four other nozzles could not have been included in an axisymmetric simulation, but given the location of the fire and fire plume would not have had a significant effect.

A fixed droplet diameter of 121 µm was used, corresponding to the SMD of the experimental data. The initial velocity was 14 m/s with an angle in the range 35 °–45 ° from the vertical. The flow rate was 0.1 kg/s.

The following factors are important to the numerics of the DPM:

number of streams This is the number of tracking particles released from a nozzle (or *'injection'*) in each time step. This is analogous to the mesh size – the number needs to be sufficient to accurately represent the physics, but the larger the number the greater the computation cost.

time step size The particle tracking algorithm is not limited by the time step used to solve the continuous phase, however this is of significance when the discrete phase and the continuous phase are coupled.

continuous phase iterations per DPM iteration The interval between updates of the discrete phase sources during the solution of the continuous phase.

other factors: mesh size; underrelaxation factors; radiation interaction; and stochastic tracking.

These factors are often interrelated, for example the number of particles in the model is a function of the number of streams per injection and the time step size.

The single injection point was offset by 0.001 m from the central axis to ensure

it definitely lay within the domain and to avoid any numerical issues concerning the axis of symmetry.

As the action of mist is known to be rapid, the time step was reduced to 0.0025 s, and a maximum of 60 iterations per time step was used. This time step was based on limiting particle motion to around one cell per time step based on the maximum velocity of 14 m/s and a typical cell size of 0.035 m. Six streams were used to represent the range of angles of the hollow cone. This was shown to be adequate to achieve convergence from the activation of the mist system up to the point the mist began to reach the combustion region.

Beyond this point the solution became unstable, indicating that heat transfer to (or possibly mass transfer from) the discrete phase rather than particle motion should be used to establish the required time-step size.

In order to maintain stability, a further reduction in time step to 0.0005 s and an increase in the number of particles injected per time step from 6 to 20 was required. This has the effect of reducing the number of droplets represented by each tracking particles (to approximately 17,000) preventing unduly concentrated source terms in the continuous phase.

The final model therefore required a total of 40,000 particles per second, or a maximum of 400,000 particles for ten seconds, which was the longest period of time considered. The *Fluent* solver easily coped with this number, with the CPU and RAM usage increasing linearly with the number or particles. The post-processor (in *Fluent* version 6.1) was not so efficient, needing increasingly long times (roughly increasing with the square of the number of particles) to produce plots and animations as the number of particles increased, giving a practical limit in the region 100,000 particles if post-processing of droplet temperature, velocity or mass is required. Contour plots of DPM source terms in the continuous phase and droplet concentration were not affected. The latest version of *Fluent* (6.2) does not suffer from this problem.

7.1.3 Results

Table 7.2 summarises all the cases run, showing the extinction time for each case (or the time the run was terminated if extinction did not occur during

the simulation). Graphs of the total rate of reaction and the mid-height plume velocity against time for each case are show in Appendix C.2.1.

A parameter sensitivity study was carried out in order to assess the importance of the various input values to the effectiveness of the water mist system and to the numerical model.

In the base case, water mist is activated at $T = 300\,\mathrm{s}$. It quickly overwhelms the buoyant plume, and causes extinction roughly 1.65 s later (The base case is shown in each of Figure C.4–C.8). The extinction process is virtually instantaneous once the mist has reached the fuel pan.

Figure C.4 shows the effect of the injection cone angle on the plume velocities and rate of reaction. The base case (full range of 35°-45°) is compared with three separate cases using only the minimum, maximum and average angle respectively.[1] It is observed that decreasing the cone angle increases the effectiveness of the mist. At lower cone angles, the penetration of the mist from the nozzle is improved because the mist has a greater momentum relative to the vertically moving plume and because it is spread over a smaller horizontal area. There is little observable difference between using a range of values, and simply taking an average.

Similarly, Figure C.5 shows the effect of varying the initial droplet diameter.[2] In three cases, a single initial diameter is used (the base case of 121 µm, and 100 µm and 200 µm). The fourth case uses a Rosin-Rammler distribution with a characteristic diameter of 113 µm. Droplet diameter has a strong effect on extinction time, with smaller diameters giving faster extinction. The Rosin-Rammler distribution, despite having a characteristic diameter greater than 100 µm is the most effective (the Sauter Mean Diameter of this distribution is approximately 73 µm). The behaviour of a polydisperse mist is more complex than the monodisperse cases. Figure 7.3 shows the distribution of droplet size throughout the enclosure after extinction. The larger droplets do not disperse well, and are clearly not directly involved in extinguishing the fire, and it is only droplets of 75 µm or less that reach the fire in quantity. As the larger droplets have a higher momentum, they end up at the outside of the spray pattern, and it may be that although

[1] The total water flow rate is constant.

[2] Again water flow rate is constant, there is therefore a corresponding change in the number of droplets in each particle.

Table 7.2: Summary of results from parametric study

Parameter	Value	Extinction Time[a] s	Plume Collapse[b] s
Water flow rate	0.002 kg/s	$> 9 \cdot 55$	$> 9 \cdot 56$
	0.005 kg/s	$6 \cdot 70$	$> 8 \cdot 51$
	0.01 kg/s	$4 \cdot 12$	$> 4 \cdot 98$
	0.05 kg/s	$2 \cdot 72$	$1 \cdot 17$
	0.1 kg/s	$1 \cdot 65$	$0 \cdot 655$
	0.2 kg/s	$1 \cdot 17$	$0 \cdot 517$
Velocity	1.0 m/s	$1 \cdot 76$	$0 \cdot 983$
	5.0 m/s	$2 \cdot 44$	$1 \cdot 30$
	10.0 m/s	$2 \cdot 20$	$1 \cdot 04$
	14.1 m/s	$1 \cdot 65$	$0 \cdot 655$
	20.0 m/s	$1 \cdot 27$	$0 \cdot 481$
Angle	35 °	$1 \cdot 33$	$0 \cdot 539$
	35-45 °	$1 \cdot 65$	$0 \cdot 655$
	40 °	$1 \cdot 68$	$0 \cdot 685$
	45 °	$2 \cdot 45$	$1 \cdot 00$
Diameter	Rossin-Rammler[c]	$1 \cdot 20$	$0 \cdot 457$
	100 µm	$1 \cdot 35$	$0 \cdot 558$
	121 µm	$1 \cdot 65$	$0 \cdot 655$
	200 µm	$2 \cdot 32$	$1 \cdot 18$
Hexane			
Water flow rate	0.01 kg/s	$> 6 \cdot 12$	$> 6 \cdot 12$
	0.02 kg/s	$4 \cdot 46$	$> 6 \cdot 21$
	0.03 kg/s	$3 \cdot 82$	$4 \cdot 55$
	0.05 kg/s	$3 \cdot 62$	$2 \cdot 16$
	0.1 kg/s	$1 \cdot 66$	$0 \cdot 851$
	0.2 kg/s	$1 \cdot 03$	$0 \cdot 547$
Hexane-diameter	Rossin-Rammler[d]	$1 \cdot 17$	$0 \cdot 519$
	25 µm	$1 \cdot 07$	$0 \cdot 320$
	50 µm	$1 \cdot 04$	$0 \cdot 351$
	121 µm	$1 \cdot 66$	$0 \cdot 851$
	160 µm	$2 \cdot 37$	$1 \cdot 29$
	200 µm	$> 7 \cdot 71$	$1 \cdot 93$

[a] a time shown with '>' is the termination time for cases where extinction/plume collapse did not occur

[b] time taken for plume velocity at mid-height to reach zero

[c] $\bar{d} = 113\,\mu\text{m}$, $n = 2.383$

[d] $\bar{d} = 113\,\mu\text{m}$, $n = 2.383$

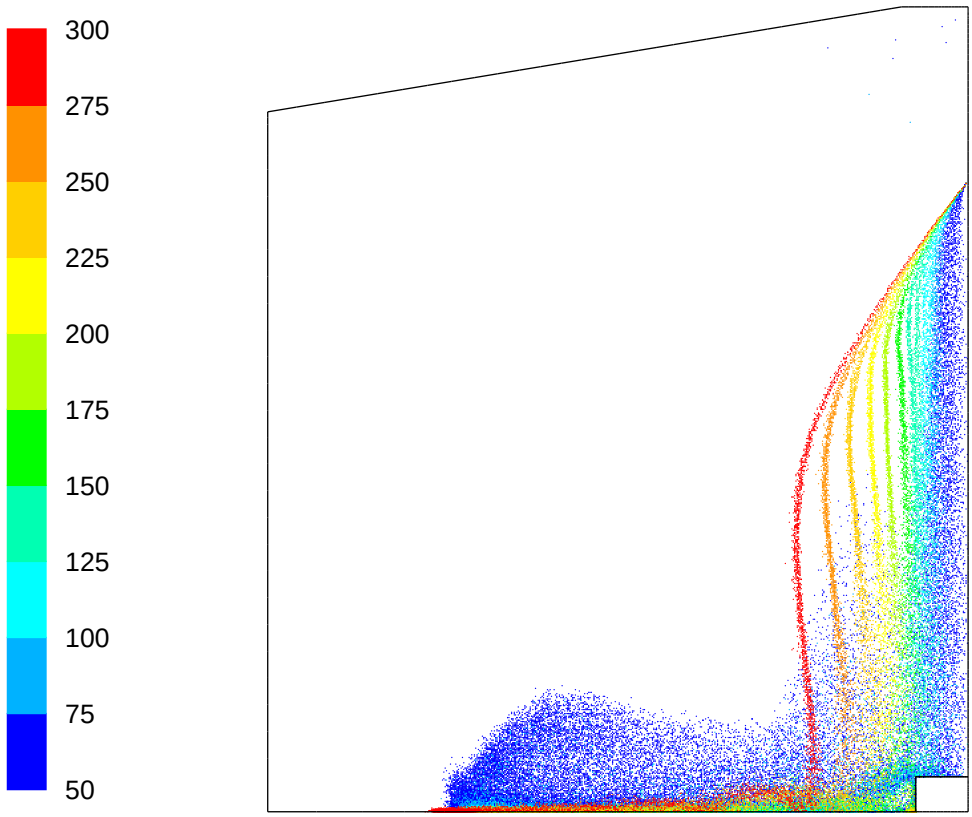

Figure 7.3: Penetration of polydisperse mist into an enclosure (50–300 µm)

they are not directly active, they form a 'sheath' around the smaller droplets improving their penetration into the enclosure.

Figure C.6 shows the effect of initial velocity. In general, higher initial velocities gave more rapid extinction, however, the *lowest* velocity (1 m/s) was more rapid than both 5 m/s and 10 m/s. Figure A.2 (and Animation A.2) shows the evolution of mist concentration over time for these different cases. For the high initial velocities, the mist was effective due to its high momentum which overwhelmed the momentum of the fire plume. There was also however, a great deal of horizontal spread, which means that the concentration of mist close to the plume axis is relatively low. For the low velocity cases, the momentum of the plume initially overwhelms the momentum of the mist and the mist is transported upwards. There was little horizontal spread, giving a high local mist concentration, and, due to the downward force of gravity, and the cooling effect, the plume momentum is soon overcome.

The effectiveness of the mist at low nozzle velocities is due to the *position of the*

nozzle within the plume. This would *not* apply where the mist is not applied coaxially with the fire plume.

Increasing total flow rate increases effectiveness (see Figure C.7). At low water flow rates, the mode of extinction was different from the earlier cases. In the earlier cases, the injected water mist was able to overcome the momentum of the buoyant plume, leading to *negative plume velocities* before *extinction occurred*. In the low flow cases, the plume velocity remained unchanged until *after* extinction had occurred. Once the heat source had been removed, the plume velocity gradually fell away. Figure A.3 and Animation A.3 show the evolution of mist concentration with time. At low mass flow, the mist is transported upwards, but unlike the low velocity cases, the mist concentration remains low.

For each fire, there is a minimum mass flow rate below which extinction does not occur. The minimum flow that achieved extinction was 0.005 kg/s for the methanol fire, and 0.02 kg/s for the hexane. A simple energy balance between the water flow rates and the heat release of the fires (26.6 kW and 114.5 kW respectively) implies the mist is absorbing over 5000 kJ/kg, which is far beyond what is possible given the temperatures in the domain. This can be explained by two phenomena:

1. Even before the mist is activated, the fire is in a state of equilibrium, the heat it releases is lost to the liquid fuel, the cold air that is entrained into the flame, and by radiation to the enclosure boundaries. Any heat loss to the mist will therefore cause a drop in temperature.

2. Although the mist enters the domain at a constant flow rate, the entrainment of air causes the relative velocity to reduce over time, leading to a 'concertina effect'. The initial rate that mist arrives at the fire is thus higher than the net mass flow rate. This explains why cyclical application of mist may be more effective (see Section 3.2.9).

Figure 7.4 plots the extinction time against water mist momentum for a range of cases. This shows a strong correlation between momentum and extinction time. The single outlier corresponds to the minimum (1 m/s) velocity case which shows atypical behaviour as discussed above. In Figure 7.5 the same data is plotted with error bars to indicate extinction times calculated by more and less stringent criteria.

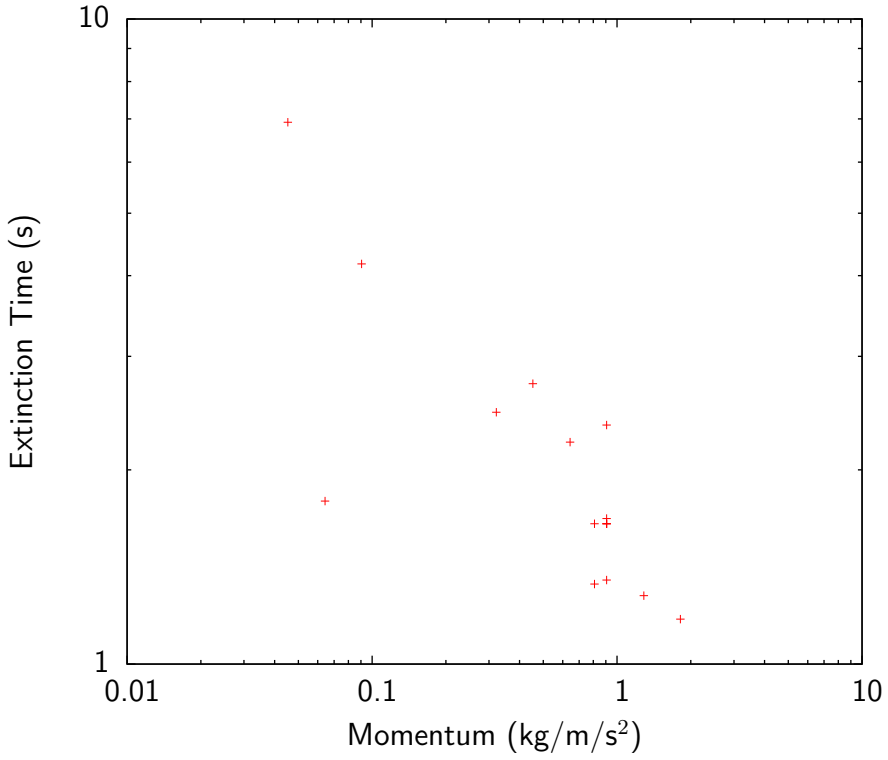

Figure 7.4: Comparison of extinction time with water mist momentum for CFD model

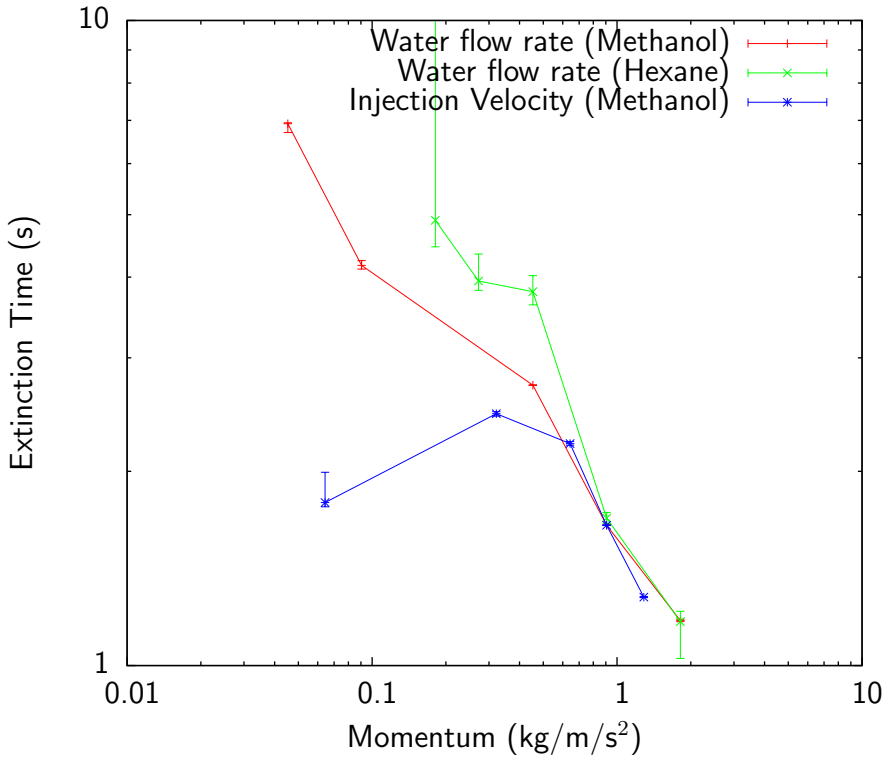

Figure 7.5: Comparison of extinction time with water mist momentum for CFD model

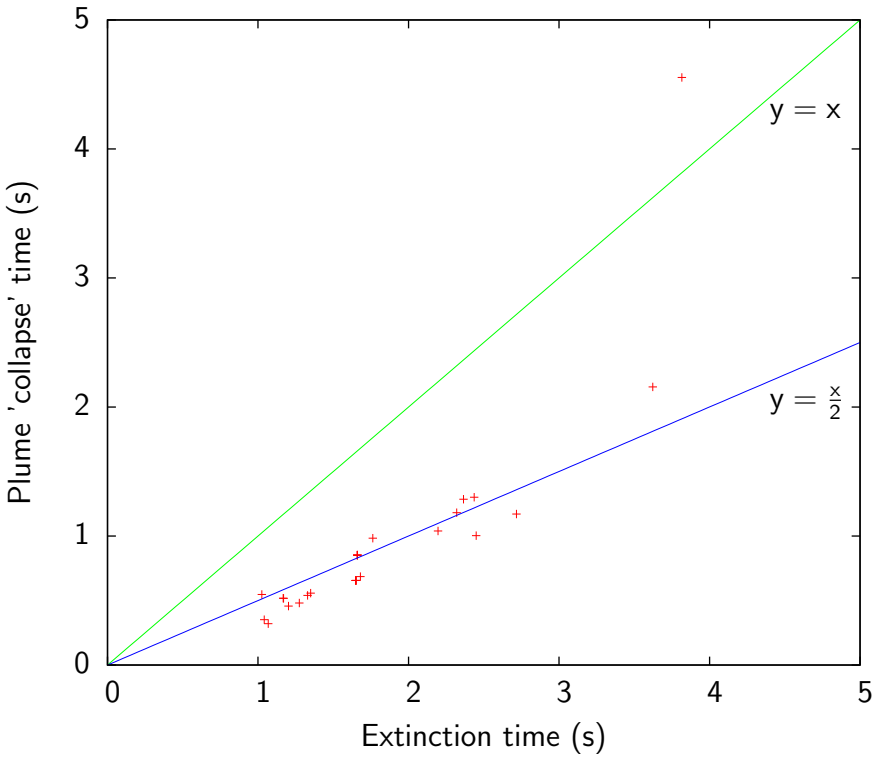

Figure 7.6: Comparison of extinction time with 'collapse' of plume for CFD model
(time taken for axial velocity at mid-height to reach zero)

Finally, Figure 7.6 plots the plume collapse time against extinction time. Plume 'collapse' is defined as the upward velocity become less than or equal to zero at a point midway between the pool surface and the mist source. Most points fall on the line $y = \frac{x}{2}$, showing that all these cases show the same basic behaviour. The single outlier in this case corresponds to a water flow rate of 0.03 kg/s (for the hexane fire). There are also three other cases with low water flow rates where extinction occurred but have not been plotted because plume velocity did not drop to zero during the simulation that would also lie above the $y = x$ line.

This would suggest that although total spray momentum is indicative of mist effectiveness if extinction time is used as a measure of performance, it is not indicative of the limit of mist performance.

7.1.3.1 Analysis of extinction mechanism

In Section 3.2.2 six potential mechanisms of action for a water-mist fire suppression system were identified based on a review of the academic literature. These were compared with the results of the CFD simulation in order to reach a conclusion about how water mist causes extinction for this scenario.

Oxygen dilution Figure 7.7 shows the oxygen concentration close to the pool 1.5 s after mist activation and shortly before extinction occurs (at 1.65 s). The majority of the domain is within one percent of atmospheric (23 %), with any reduction below this being due to the fire itself. This can be verified by noting that the mist droplets are largely at 100 % of their original mass. *Oxygen depletion is not significant.* The mist-induced air flow is however pushing oxygen depleted air back towards the fire, which would result in a slight dip in oxygen concentration as the mist reaches the fire, but this would not be sufficient to extinguish the fire.

Gas phase cooling Figure 7.8 shows a break-down of the energy absorption of the mist (which obviously equates to the gas phase cooling) compared to the heat output of the fire. At the point extinction occurs, around 75 % of the heat absorbed is due to inert heating (i.e. it has simply raised the temperature of the liquid droplets), the remaining 25 % being due to latent heating (evaporation). Compared to its potential (see Figure 3.1) very little of the thermal capacity of the water has been utilised, few droplets reach their boiling point (see Figure 7.9) and fewer still completely evaporate. *The thermal energy absorbed by the mist is significant and* exceeds *the energy output of the fire.*

Fuel cooling No cooling of the solid region is observed until after the fire has been extinguished.

Attenuation of radiation The fuel source was already fully involved before the mist was activated, so this mechanism of action is not applicable to this scenario. In any case, by the time the mist reaches the line-of-sight between the flame and the fuel surface the fire has already been extinguished.

Disruption of air flow A significant disruption to the air flow was observed in almost all the cases modelled. In most of these, the momentum of the water was sufficient to induce a counterflow directly, however at low velocities, the

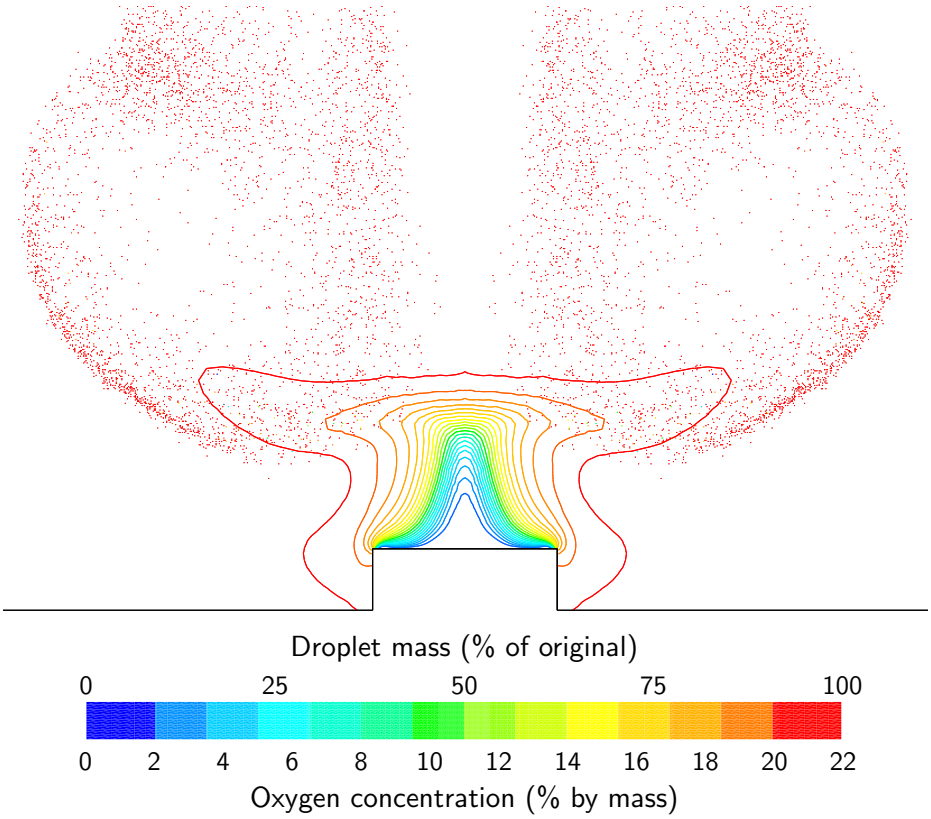

Figure 7.7: Contour plot of oxygen concentration (1 % by mass increments) overlaid with particle locations coloured by mass relative to injection mass at 1.5 s and shortly before extinction occurs

counteraction of buoyancy due to the cooling became significant. Reducing mass-flow rate (and hence both momentum and counter-buoyancy) reduced or eliminated the disruption, leading to longer extinction times. It is plausible to suggest that the fire-induced convection currents would eventually bring the mist to the fire in the other direction, however this would take substantially longer, and much of the mist may be lost due to evaporation in the hot ceiling layer or to the walls and floor of the enclosure. *Disruption to air flow, whilst not responsible for extinction, is a significant part of the action of water mist in this scenario.*

Modification to combustion mechanism The combustion reaction is represented as a single step, and no attempt is made to model the formation or action of reaction intermediates. *The CFD model is therefore incapable of representing this effect.*

As a result, the following conclusion can be drawn:

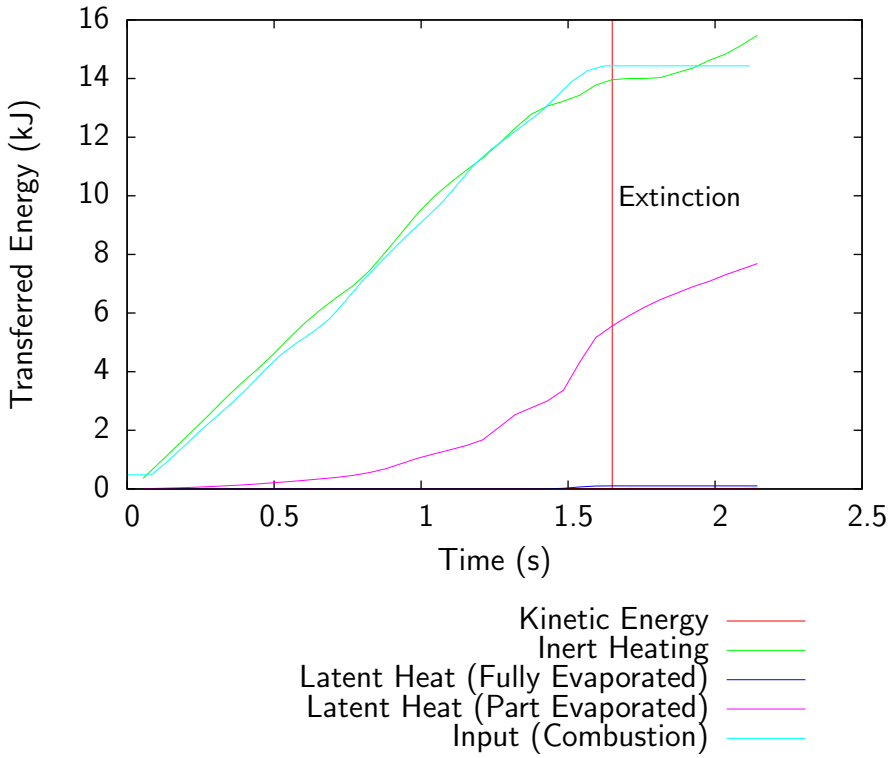

Figure 7.8: Transfer of energy to water mist

The primary mechanism of action of the water-mist system on these enclosure fires is heat removal. This is facilitated by a disruption to the fire-induced air flow.

It should be noted however, that whilst the full potential of the mist was not realised, that in this scenario, the placement of the nozzle directly above the fire, was significant, and the water mist may have behaved differently, and perhaps been less effective if the nozzle was offset from the plume axis.

The relatively small size of the fire is also significant. For the methanol fire, the mean temperature rise in the enclosure was a mere 20 K and temperatures only exceeded 100°C in the core of the plume. Low temperature prevents significant evaporation, and the limited saturation pressure of water vapour would always prevent oxygen dilution regardless of the design of the water mist system.

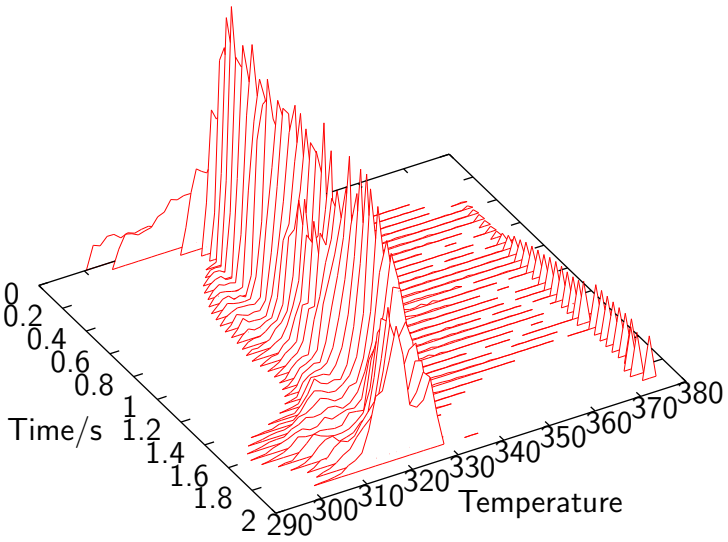

Figure 7.9: Evolution of droplet temperature for initial 0.1s of mist over time

7.1.4 Comparison of CFD model with experimental results

Kim and Ryou (2003) includes plots of the variation of 'ceiling mean temperature' with temperature after mist injection. For the 0.3 m methanol pool a piecewise linear fit is provided (see Equation 7.2).

$$\bar{T} = \begin{cases} -1.48t + 82 & t < \Delta t_{th}, \\ -0.019t + 35.3 & t > \Delta t_{th} \end{cases} \tag{7.2}$$

Where

t is the time since mist activation (s)

$\bar{T}$ is the smoke layer/ceiling mean temperature (°C)

Δt_{th} is the time of transition between two cooling regimes ($\sim$ 31.96 s)

In order to directly compare the CFD model with the experimental results, an equivalent temperature was calculated. It was assumed that this was an area-weighted average of the ceiling level thermocouples (see Figure 7.10 and Equa-

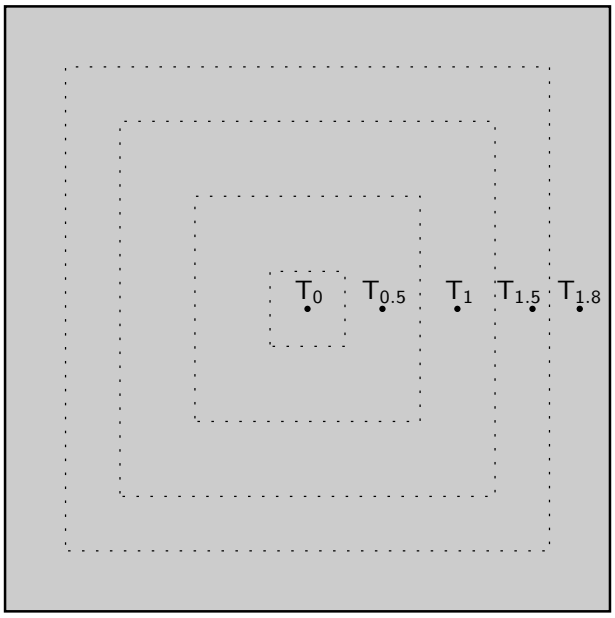

Figure 7.10: Area-weighted average of thermocouple temperatures to give mean ceiling temperature

tion 7.3).

$$\bar{T} = 0.1406T_{0.5} + 0.25T_1 + 0.29T_{1.5} + 0.319T_{1.8} \quad (7.3)$$

$$\bar{T} = 0.0156T_0 + 0.125T_{0.5} + 0.25T_1 + 0.29T_{1.5} + 0.319T_{1.8} \quad (7.4)$$

Where

T_x is the temperature at a point x m from the central axis, and

$\bar{T}$ is the mean smoke layer temperature.

The CFD model included a monitoring point at the central axis, T_0, and if this is included in the average (as in Equation 7.4) then temperature are initially much higher but fall more rapidly, as the point is within the fire plume and coincident with the nozzle location. As there is no corresponding thermocouple in the experiment Equation 7.3 was used to compute the mean temperature ($\bar{T}$), and the axis temperature (T_0) has been plotted separately.

Figures 7.11 and 7.12 show a direct comparison of the CFD prediction with the experimental data for the two fires.

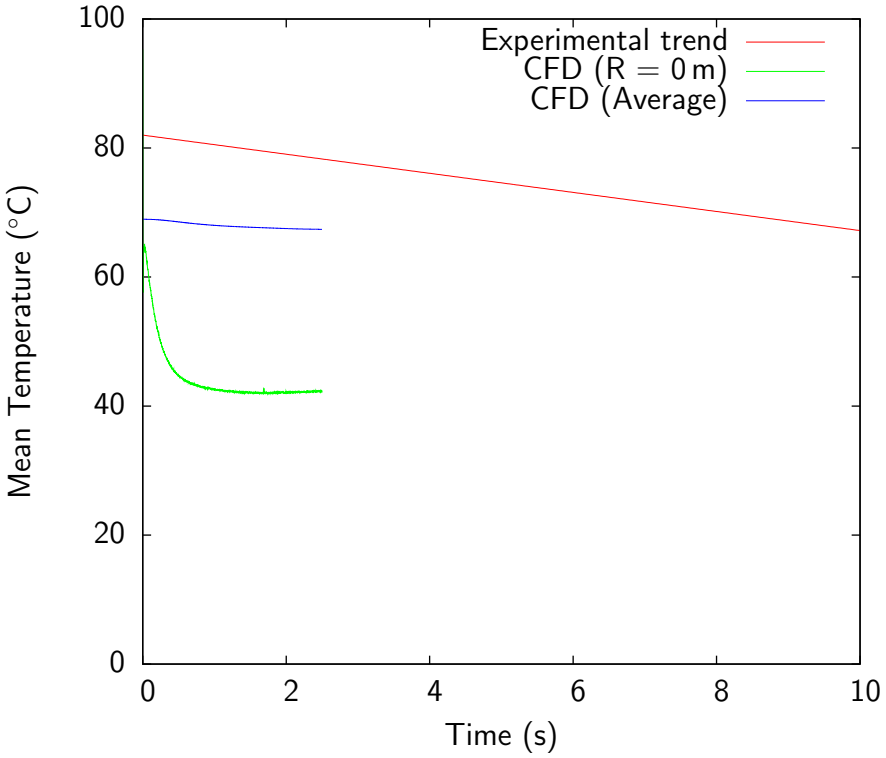

Figure 7.11: Comparison of measured ceiling temperature with CFD prediction for methanol fire

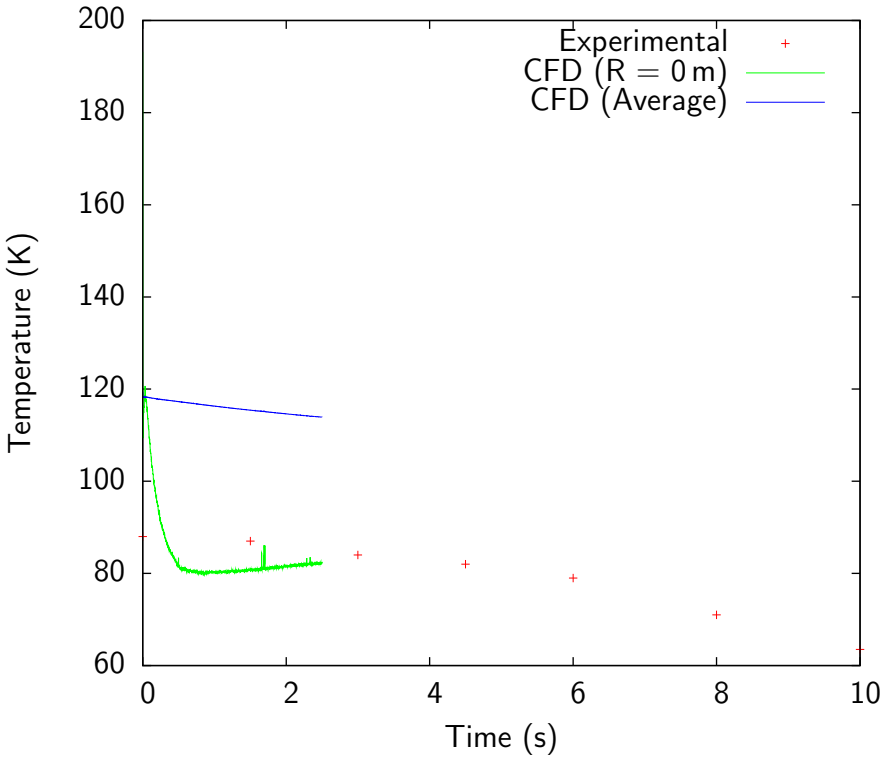

Figure 7.12: Comparison of measured ceiling temperature with CFD prediction for hexane fire

In each case, the initial temperature (at $t = 0\,\mathrm{s}$) is determined by initial conditions taken from the enclosure fire model (see Chapter 5). As discussed in Section 5.2.5 this is sensitive to the thermal boundary conditions at the wall and ceiling. After the activation of the mist, temperature falls rapidly in the plume, and falls more gradually elsewhere. In the case of the methanol fire, the mean temperature fell by 0.6 K/s in the CFD model and 1.48 K/s in the experiment. For the hexane fire, the CFD predicts 1.8 K/s compared to 1.3–2.5 K/s measured in the experiment.

Cooling of the hot layer occurs due to direct cooling by the mist and indirectly because the mist disrupts the fire plume. This upsets the thermal equilibrium and the temperature falls back towards ambient, for example due to conduction through the ceiling.

The CFD model included only one nozzle at the centre of enclosure, whereas the experiments included four additional nozzles towards each corner (see Figure 5.1). These are some distance (1 m) from any of the thermocouples and may not contribute significantly to the cooling measured in the first few seconds after mist activation. The heat loss to ambient is likely to be sensitive to the value of the heat transfer coefficient as before.

As Figures 7.11 and 7.12 show, the cooling observed close to the nozzle is much more rapid, suggesting a different behaviour in this region. It seems unreasonable therefore to suggest that validity of the smoke layer cooling can be used as a *complete validation* of the mist-fire interaction. Unfortunately, there is no experimental data available that could be used to further validate the model.

7.1.5 Summary of findings

- Heat transfer to the discrete phase determines the required time-step size, which was 0.0005 s for this scenario, corresponding to 1/400 of the combustion-only time step.
- Tracking particles could represent approximately 17,000 droplets (equivalent to 15 mg of water)
- Extinction occurs due to gas phase cooling by the mist.
- Significant disruption to the air flow occurs, but this is not necessary for extinction to occur.

- Many factors affect the performance of water mist:
  - Smaller droplets are more effective.
  - Mist penetration and therefore extinction time is mainly determined by overall spray momentum. However other factors such as spray angle, and counter-buoyancy can be significant.
- Results for cooling of the hot gas layer beneath the ceiling are in line with experimental measurements. However the short period of time simulated and the distance between the seat of the fire and the hot layer prevents this serving as a complete validation of the mist-fire interaction.

7.2 Application of water mist to a tunnel fire

In this section, CFD modelling techniques developed and validated in Sections 6.2 and 7.1 are applied to the water mist fire suppression of a tunnel fire.

The only known physical testing of water mist in tunnels was carried out in Germany by DMT as part of the same European Coal and Steel Community (ECSC) project that funded this PhD research. This work is outlined in Section 3.3.1. Unfortunately those tests have a few drawbacks that make them less than ideal for validation of the CFD model.

1. Limited data - The only recorded data was whether the mist caused extinction of the fire. There is not even a record of how long this took.
2. Complex fire - The experimental fire consisted of two conveyor belts – arranged one above the other – ignited by a large wooden crib fire. This is more difficult to model than diesel pools because the burning area changes with time due to flame spread and burn-through.
3. Clutter - the conveyor belt was supported by a large number of incombustible trestles. These present an obstruction both to the air-flow and the mist droplets, and would have to be explicitly modelled, potentially leading to a larger and more complex mesh.

It was therefore decided to model a simpler scenario by adding a plausible water mist system to the same tunnel fire and ventilation parameters used in Section 6.2. The parameters of this hypothetical system are considered in Section 7.2.1 below.

7.2.1 Details of hypothetical mist system

The design of the hypothetical mist system is based on the mist system used by Kim and Ryou (2003), and successfully modelled in Section 7.1. Details of this are given in Table 7.1. Given the practical constraints in altering these properties, these will initially be left unchanged, leaving only the number and location of nozzles as design parameters.

7.2.1.1 Energy balance

The required water mist supply rate can be inferred by assuming an energy balance between the heat of evaporation and the rate of combustion.

$$\dot{m}_w = f \frac{\dot{Q}}{\Delta H_{\text{Evap}}} \tag{7.5}$$

where:

$\dot{m}_w$ is the water supply rate /kg/s

f is a factor to account for the water mist effectiveness and any uncertainty in the fire size.

$\dot{Q}$ is the heat release of the fire /kW, and

ΔH_{Evap} is the specific heat of evaporation of water /kJ/kg

Taking $f = 1.0$, $\dot{Q} = 11,000\,\text{kW}$ and $\Delta H_{\text{Evap}} = 2270\,\text{kJ/kg}$ gives a required water flow rate of $4.85\,\text{kg/s}$.

However, for the enclosure fire, the mist was shown to be much more effective than this. Furthermore, much higher temperatures exist in the tunnel fire, and so the high specific heat capacity of water vapour could also be taken into account – a potential absorption $5380\,\text{kJ/kg}$ (evaporation + heating to $1000\,^\circ\text{C}$) – giving a water requirement of $2.04\,\text{kg/s}$.

This is an upper-bound estimate on the water requirement of the water mist system because:

- the assumed fire is a pool fire that *fills the width of the tunnel*. It seems reasonable to assume that this is the worst case scenario, and that most real fires would be substantially smaller than this.
- 11 MW is the fully-developed heat release rate of the fire. A well designed fire detection system should be able to activate the water-mist system before a fire has reached this stage.

  Obviously if a real water mist fire system were to be designed a design fire size should be determined from a full risk assessment/HAZOP exercise or by reference to an appropriate standard.

7.2.1.2 Nozzle placement

It is unknown what proportion of the mist produced by a nozzle will reach the fire, and how this varies with the nozzle location relative to the fire. It could be assumed that the closer a nozzle is to the fire, the more mist will reach the fire, and that there is a maximum distance beyond which a nozzle is completely ineffective, depending on factors such as droplet size, initial droplet velocity, nozzle spacing, and most importantly ventilation rate.

In order to provide protection an arrangement of nozzles must be determined that allows water droplets to reach any feasible fire location.

In order to assess the effect of forced ventilation on the transport of water mist in a tunnel, a series of simple steady-state CFD simulations were performed. This was based purely on the ventilation airflow and no fire, heat source, or plume was included.

Single nozzle

For a single nozzle, water mist will reach a volume that is determined by the droplets' size and velocity, the nozzle's total flow rate, and the free-stream velocity of the air.

At *low* water flow rates and small droplet sizes, the transfer of momentum from the spray to the air can be neglected and the drag force dominates the droplet trajectory. Each droplet will fall at its terminal velocity (relative to any air flow).

If a significant cross flow exists the mist will reach the floor at a distance downstream from the nozzle equal to the average air flow velocity multiplied by the residence time of the droplets. The residence time is the tunnel height divided by the terminal velocity. Close to the nozzle the initial *relative* velocity of the droplets will vary around the cone, and the spray pattern will be slightly elongated into an ellipse-like shape. This could also have an impact on the droplet size distribution, but this will not be considered further here.

Chaotic variations in the air flow (i.e. turbulence) will cause each droplet to take a slightly different path, and by the time the mist reaches the floor the mist will

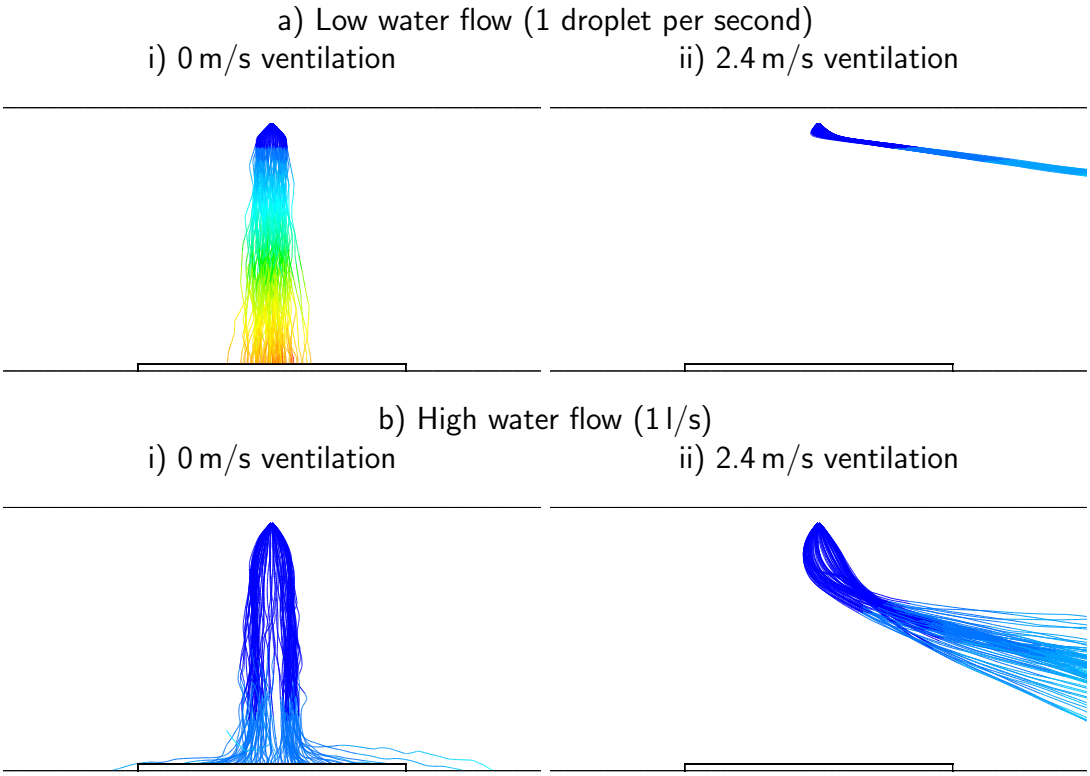

Figure 7.13: Distribution of mist from single nozzle for 0 m/s and 2.4 m/s air flow and low and high water flow rate
Coloured by residence time (0–8 s)

be dispersed over a larger area. This dispersion is a diffusion-like process, and will be most noticeably at low air velocities.

For example, for droplets of 121 µm diameter with an initial velocity of 14.1 m/s (as used in Section 7.1), the high initial velocity is sufficient to carry the droplets a few centimetres from the nozzle, by this time the velocity will have fallen to the terminal velocity (0.34 m/s).

At *high* flow rates, the transfer of momentum from the mist to the air will induce a co-flow in the region of the nozzle (see Figures 7.13 and 7.14). This co-flow has three effects:

1. The relative injection velocity, and therefore the drag force, will be reduced so the spread of the mist due to its initial velocity will increase.

2. The co-flow increases the droplet velocity, reducing residence time. At low or zero ventilation residence time is reduced from 8 s to less than 1 s. At higher ventilation rates, the co-flow is less significant, and residence time is

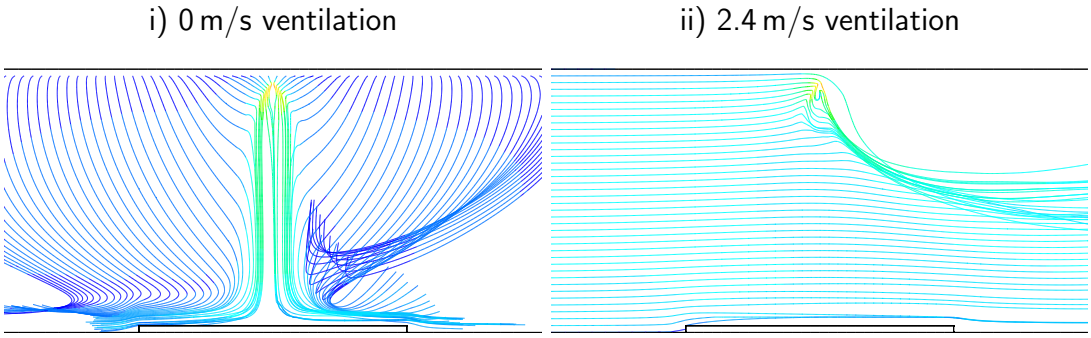

Figure 7.14: Streamlines for flow induced by water mist nozzle in 0 m/s and 2.4 m/s air flow (1 l/s water flow rate)
Coloured by velocity (0–10 m/s)

only reduced by 20% or so.

3. If the co-flow impinges on a surface such as the tunnel floor, it will be deflected, and this can improve the mist distribution close to the surface. This effect is also most significant at low ventilation rates where the co-flow is the dominant flow feature.

As the terminal velocity of a droplet decreases with its diameter, smaller droplets will travel further downstream. The droplet size distribution could therefore vary significantly throughout the tunnel. Figure 7.15 shows the spray pattern for a mist with a range of diameters (approx. 60-600 µm). The larger droplets quickly fall out of the flow whereas the smallest droplets are carried up to 12 m (or four tunnel heights) downstream. Figure 7.16 shows the droplet counts (relative to the nozzle value) against distance downstream.

Multiple nozzles

More realistically a water mist system will contain multiple active nozzles, and the air flow associated with a particular nozzle will have an influence on adjacent nozzles (particularly downstream). Figure 7.17 shows the spray pattern from a line of seven nozzles spaced at 3 m intervals along a tunnel with a net 2.4 m/s air flow. The total water flow rate is 1 l/s with an initial velocity of 14.1 m/s. The momentum transfer from the first nozzle establishes a rotational flow consisting of two counter rotating cells (see Figure 7.18). At subsequent nozzles this reduces the relative mist velocity thereby increasing the rate of penetration but decreasing the mist dispersion.

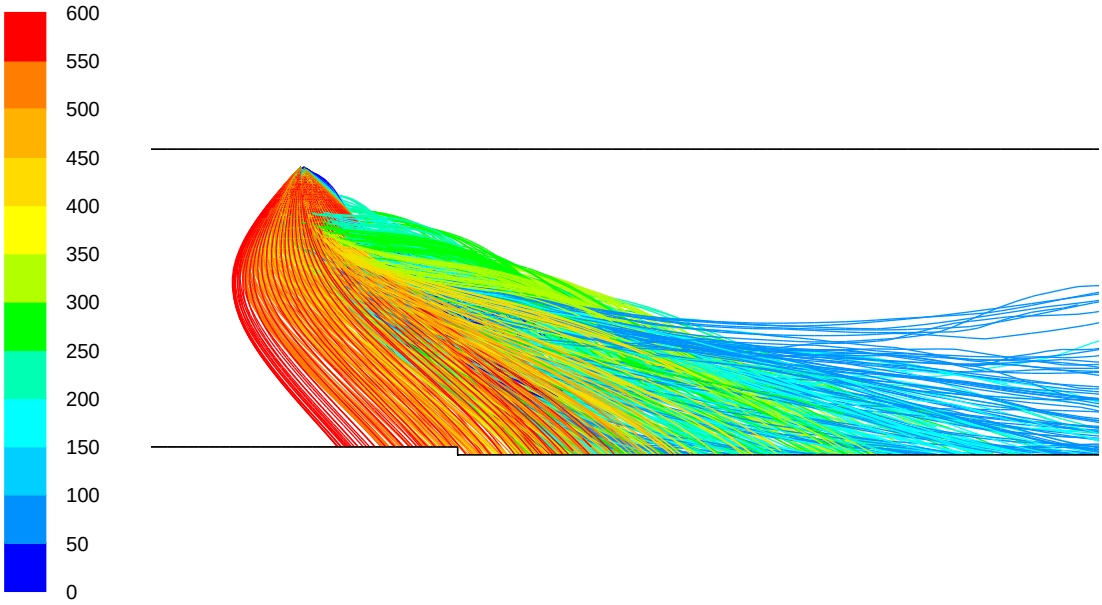

Figure 7.15: Spray pattern for mist with a range of diameters
Ventilation = 2.4 m/s, Water flow = 1 kg/s, Drop diameter in range 60-600 µm
(using Rossin-Rammler distribution)

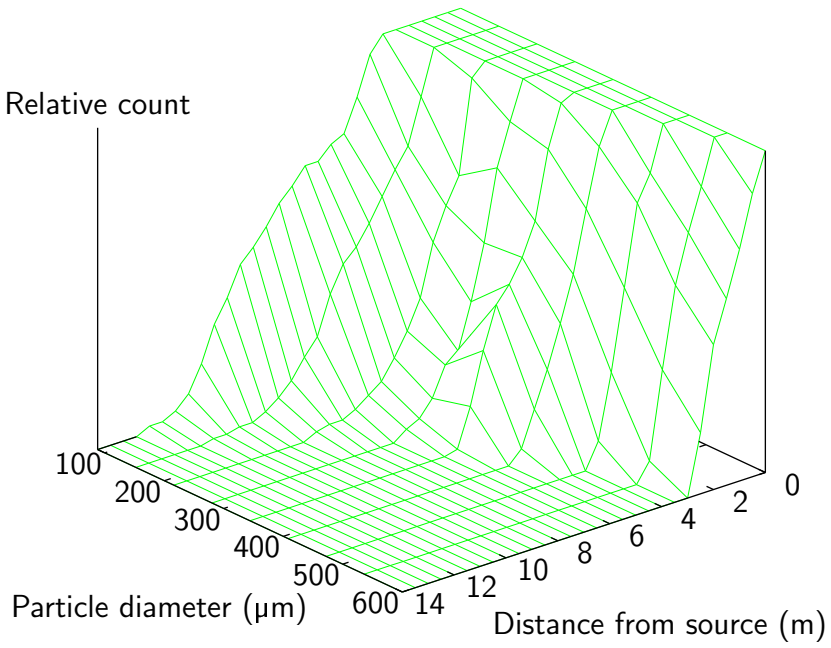

Figure 7.16: Relative droplet diameter distribution with distance downstream from the nozzle
See Figure 7.15

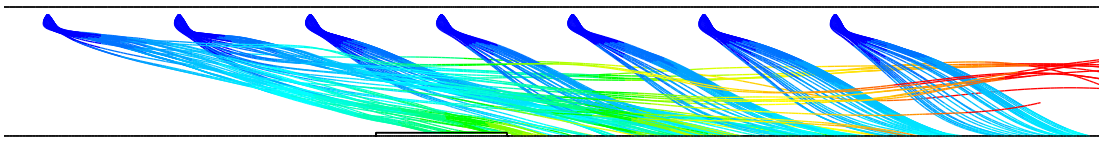

Figure 7.17: Spray pattern from a single line of seven nozzles at 3 m spacings
Air flow = 2.4 m/s, Total water flow = 1 kg/s, Initial droplet velocity = 14.1 m/s
Note how the apparent angle of spray alters downstream

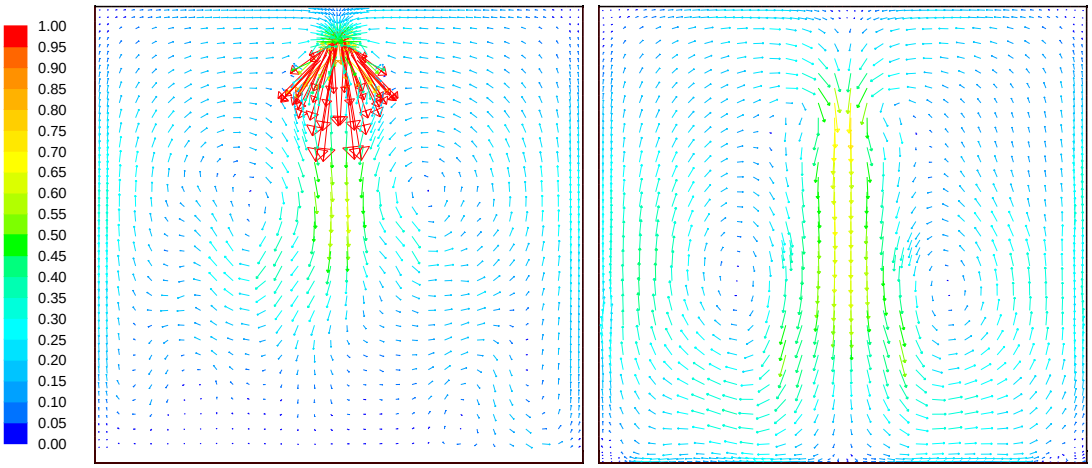

Figure 7.18: Cross section of rotational flow set up by single line of seven nozzles
a) central nozzle b) 1 m downstream of last nozzle
Scale relative to mean air flow. Air flow = 2.4 m/s, Total water flow = 1 kg/s,
Initial droplet velocity = 14.1 m/s

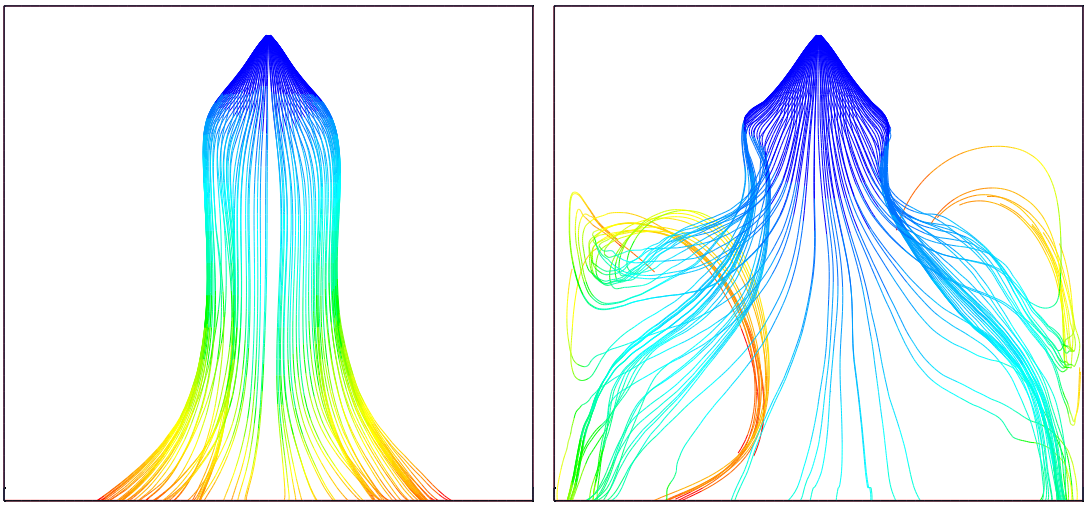

Figure 7.19: Cross section of mist distribution due to a single line of seven nozzles
a) first nozzle b) last nozzle
Scale relative to mean air flow. Air flow = 2.4 m/s, Total water flow = 1 kg/s,
Initial droplet velocity = 14.1 m/s

7.2.1.3 Summary

The distribution of mist from a nozzle depends on many factors, particularly: droplet size, total mist momentum and air flow velocity.

Steady state simulations showed that a single line of nozzles at 3 m spacings (i.e. a spacing equal to the tunnel height and width) produced a reasonable but not perfect distribution of mist (in the absence of a fire).

A spacing of 1.5 m was therefore deemed necessary for the proposed water mist system.

It was not clear whether a single row of nozzles would be sufficient for mist to reach the full width of the tunnel, so simulations with both a single and double row of nozzles were performed.

7.2.2 CFD model

The CFD model was based on the cases reported in Section 6.2.5.1 that contain a detailed representation of the pan geometry, and specifically contains an exposed lip above the fuel surface. This is required because it stabilises combustion when the hybrid Arrhenius/eddy breakup model is used.

Two different ventilation rates were used (0.8 m/s, and 2.4 m/s) in order to study the behaviour of both sub-critical and super-critical ventilation.

7.2.2.1 Combustion

As in Section 7.1, the hybrid Arrhenius/eddy breakup model was used to model combustion as it allows for a temperature dependent rate of reaction in areas that are not hot enough for the reaction to be mixing controlled.

As a start point data was taken from the end (i.e. $t = 300$ s) of the combustion only calculations performed in Section 6.2. The hybrid model had been activate for 100 s (since $t = 200$ s) to ensure that the rate of reaction had stabilised and any artificial fluctuation due to the transition to the hybrid model had propagated

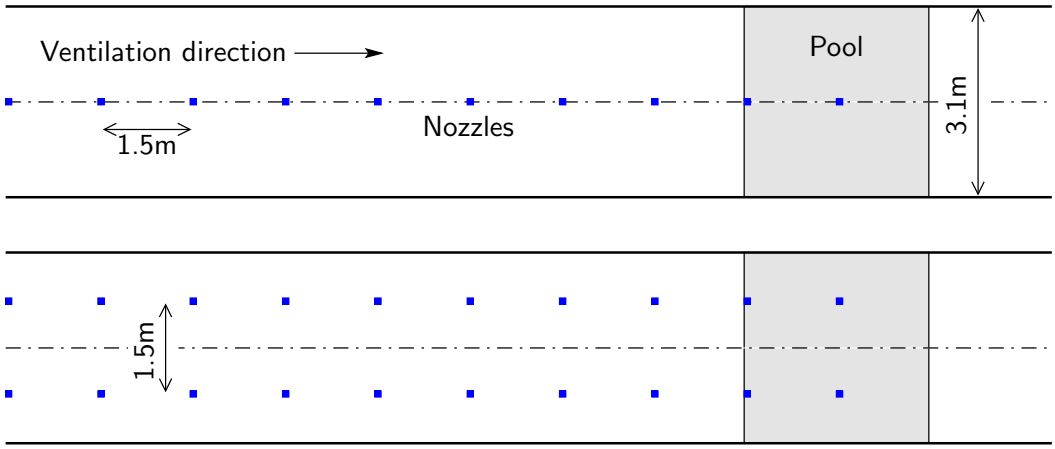

Figure 7.20: Schematic of nozzle locations for single and double rows

through the domain.

7.2.2.2 Discrete Phase Model

Each nozzle was represented by a 'cone' injection consisting of 100 streams. A single cone angle of 45° was used, and the nozzles were activated simultaneously at $t = 300.1$s. All other properties were the same as the enclosure scenario (Table 7.1). This number of streams was chosen to give a number of droplets per particle less than 17,000, which was determined to be necessary for the enclosure scenario. Using a time step of 0.01 s (see Section 7.2.2.3), this gives approximately 10,000 droplets per particle. A relatively high number of streams is also required because in the cross flow, particle trajectory varies considerably with initial direction.

Two nozzle layouts were tested (see Figure 7.20). In the first, a single line of ten nozzles at 1.5 m spacings was located at the centre of the tunnel 17.5 cm below the tunnel roof. The first nozzle was directly above the centre of the fuel pan, and the last 13.5 m upstream. As only half the tunnel is modelled, only 50 particle streams per nozzle are actually active.

The second layout consisted of two lines of nozzles 1.5 m apart, giving a total of 20 nozzles. Due to symmetry only 10 injections points were needed, but the full 100 particle streams were active.

In early model runs, problems were found obtaining convergence in the volume

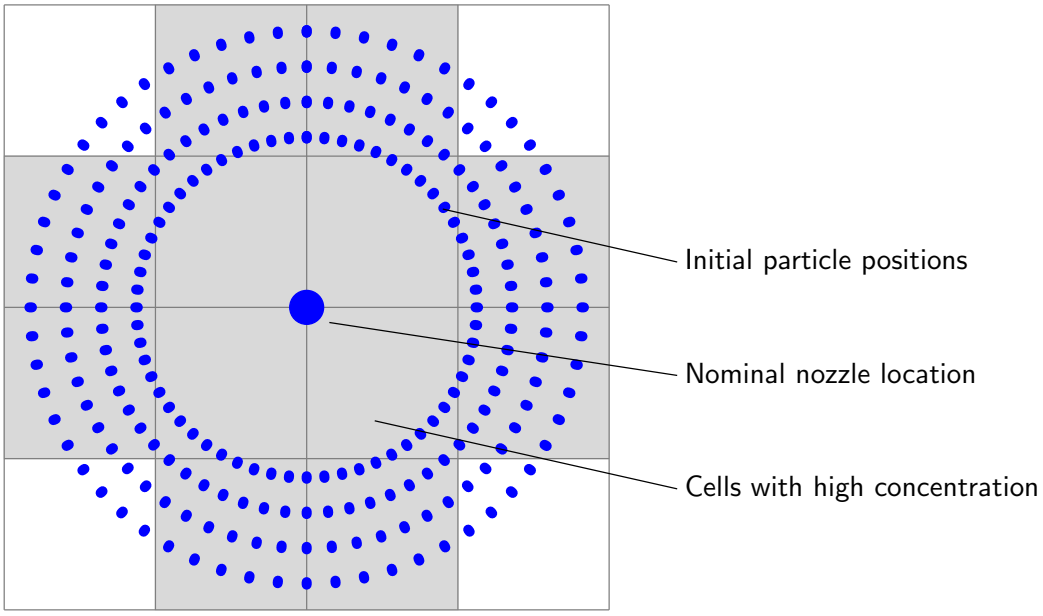

Figure 7.21: Use of non-physical cone radius to prevent numerical difficulties associated with a point source

surrounding each nozzle. In this region, small cells were required in order to resolve the sharp gradients of velocity caused by the entraining of air by the spray, and a very high droplet concentration exists at the injection point leads to large source terms. To avoid this problem, the cone injection was given a small radius of 1 cm in order to spread the particles over a number of cells (see Figure 7.21). Although this radius was larger than the physical size of a nozzle, it made no difference to the overall solution, and the slight discrepancies close to the injection point are insignificant given that the CFD model neglects the physical presence of the nozzle and associated pipe-work as well as a detailed representation of the droplet formation process that occurs outside the nozzle.

The current version of *Fluent* (6.2.16) offers a number of schemes to integrate the equations of motion: analytical; implicit; trapezoidal; and Runge-Kutta. The Runge-Kutta method was used because it is best able to cope with the effect of the rapidly changing particle mass caused by evaporation.

A reflect boundary condition was chosen for the walls and ceiling; the pool surface and pan walls were set to 'trap' (i.e. particles vapourise on contact) and the floor and tunnel inlet and outlet to escape.

Table 7.3: Estimated run time and particle numbers for different time step sizes

Time step (s)	Number of steps[a]	Droplets per particle[b]	Maximum number of particles[c]	Total run time (days)[d]
0.01	1500	10780	1,500,000	30
0.00333	4500	3589	4,500,000	90
0.0025	6000	2695	6,000,000	120

[a]based on 15 s simulation
[b]based on 100 streams per nozzle
[c]assuming no particles evaporate or escape - in practice the maximum was 25% of this figure
[d]running on a single 2 GHz Pentium III CPU

7.2.2.3 Time step

A time step of 0.01 s was selected based on one hundredth of the combustion-only time step of 1 s. Experience with the enclosure fire suggested 1/400th could be necessary, however this would not only require a prohibitively long run time, but very large numbers of tracking particles.

Table 7.3 shows the estimated run time and particle requirement for different time step size. With smaller time steps there would be potential to reduce the number of streams per nozzle, however this would be limited by the needs of angular-discretisation, and (in future work) diameter-discretisation of polydisperse sprays.

In order to establish time-step independence, one of the cases at each ventilation rate was repeated at 0.00333 s, and produced similar results for the monitored variables (see Appendix D.3) over the period of time considered (but see also Section 7.2.3.5).

7.2.2.4 Parallel solution

In order to reduce overall runtime, the parallel version of *Fluent* was used on a dual processor computer. The shape of the tunnel makes parallel solution of the continuous phase very efficient, as little information needs to be passed across the partition interface. The discrete phase was not so efficient, as for much of the simulation over 90% of the particles were located in the same partition.

The memory usage of the serial solver was around 550 MB (it slowly rose as the number of particles increased), and for the parallel solver it was generally around the same, although split between two processes (275 MB each). However when data was written to disk (or when particle plots were generated) a large quantity of memory was allocated by one of the two processes, presumably to hold a temporary copy of the particle data from both partitions. Once the number of particles reached around 155,000, the size of this spike exceeded 900 MB, which appears to be the limit for a single process under Windows on 32-bit hardware, as the solver would then crash.

The case was then resumed on a single serial solver. It seems likely that memory usage will become an issue at some point even with the serial solver, potentially with around 500,000 particles.

A long term solution would be to migrate to the GNU/Linux operating system, and ideally 64-bit hardware. The need for such a large amount of memory would appear to be avoidable, and may be fixed in a future version of *Fluent*.

7.2.3 Results

Four scenarios were modelled based on two different nozzle layouts and two different ventilation rates. The main difference between the nozzle layouts is the number of nozzles, and therefore the mass flow rate of the mist. The total flow rate is 1 kg/s for the single row, and 2 kg/s in the double row.

The behaviour of the fire plume is strongly dependent on ventilation rate, and this leads to significantly different behaviour once the mist has been activated.

At the lower ventilation rate (0.8 m/s), the fire develops a strong backflow containing gaseous products of combustion with temperatures in the region of 500°C. It is into this hot backflow that the water mist is injected. The mist is rapidly heated, and initially most of the mist evaporates within a fraction of a second of leaving the nozzle. Consequently, cooling of the backflow is also rapid, with the rate of cooling being dependent on the water flow rate (see Figure 7.22). The negative velocity in the backflow results in the mist being transported away from the fire (see Figure A.12).

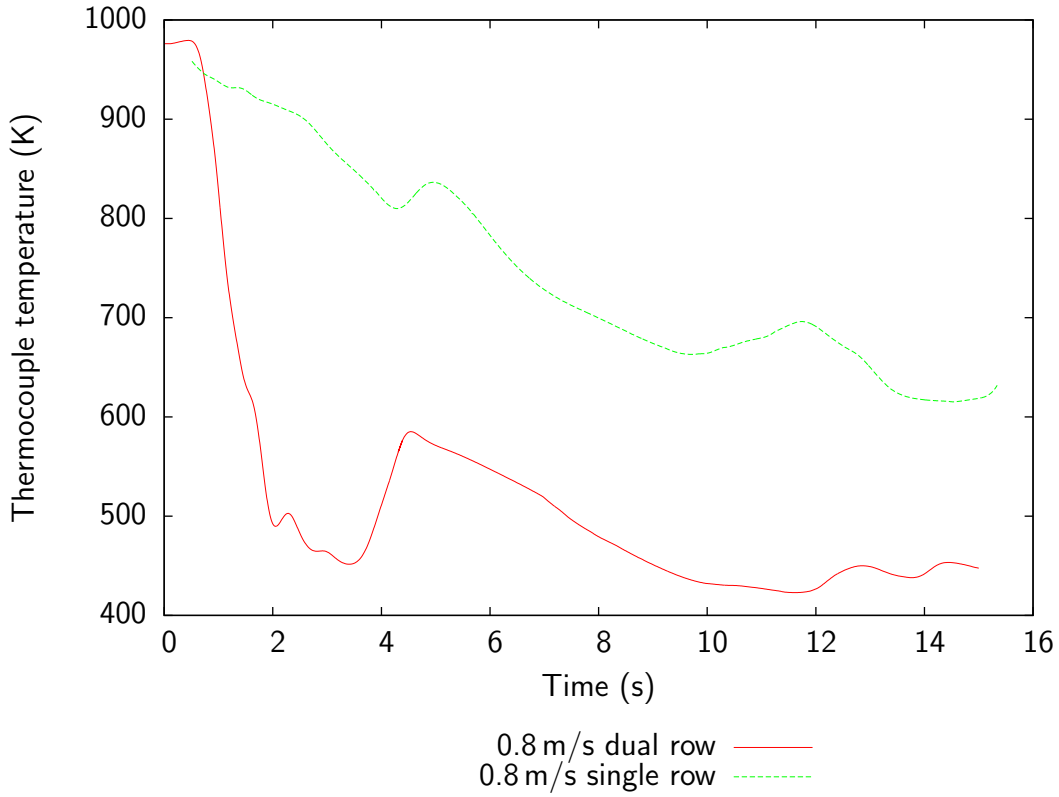

Figure 7.22: Ceiling temperature in the backflow 6 m upstream of the fire after mist activation

Close to the fire, temperatures remain high, and mist from the two nozzles closest to the fire does not reach the fire in the duration of the simulation.

Further upstream, mist *is* able to penetrate through the backflow into the cold, fresh air, where it is carried back towards the seat of the fire. Air flow velocity in the lower part of the tunnel is much higher than the nominal ventilation rate (3.5 m/s compared to 0.8 m/s), and mist reaches the fire after approximately eight seconds.

The cooling and entrainment of air by the mist causes a destratification of the backflow, and hot oxygen-depleted air falls into the lower region of the tunnel, where it is pushed towards the fire. Oxygen levels at the fire start to drop around six seconds after the mist is activated (see Figure A.13 and Animation A.13).

At the higher ventilation rate (2.4 m/s), there is no backflow, and the behaviour is much simpler. Nozzles close to the fire are ineffective as the mist is transported a significant distance downstream by the ventilation. Mist reaches the fire 4.5 s after activation (see Figure A.22). At this point the solution becomes unstable,

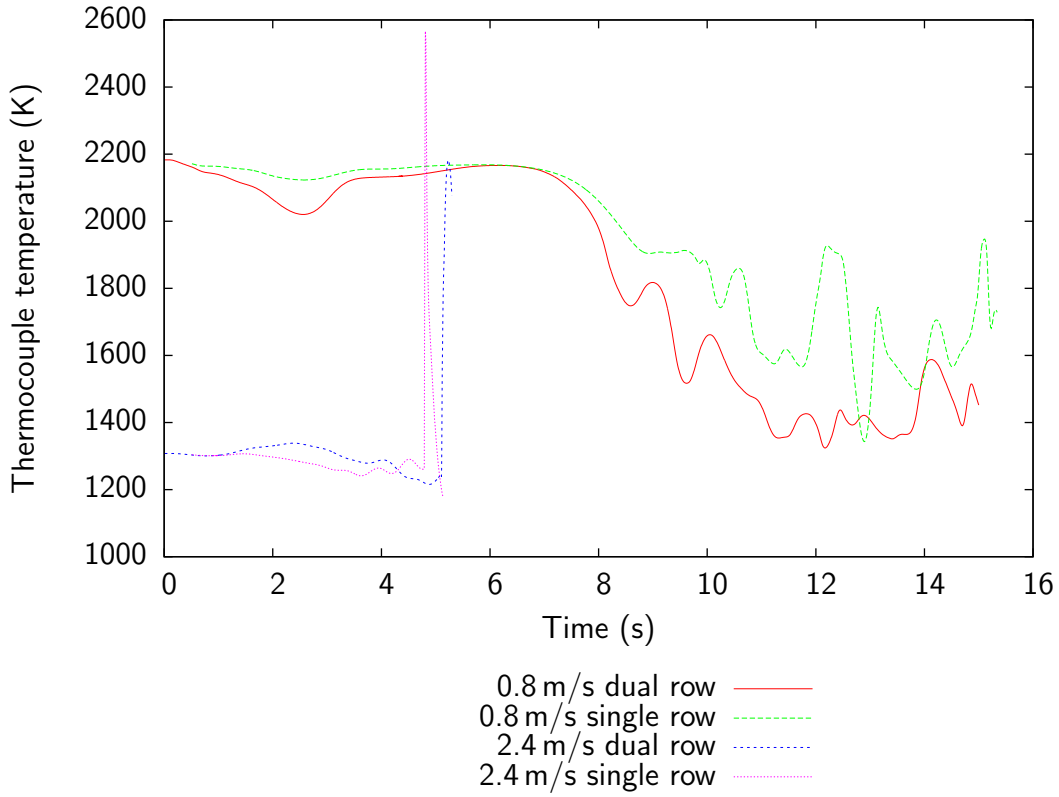

Figure 7.23: Floor level temperatures 3 m downstream of the fire after mist activation

with a very large spike in reaction rate, and consequently temperature, velocity, etc. (see Figure 7.23) and the model is terminated. This is discussed further in Section 7.2.3.5 below.

7.2.3.1 Temperatures

Figures 7.24 and 7.25 show the temperature profiles within the tunnel at 0, 5, and 10 s after the mist activation for the sub-critical (0.8 m/s) ventilation cases.

After 5 s, the temperature in the backflow region has been reduced by around 100 K at both mid-height and ceiling level. The location of the peak ceiling temperature has moved slightly upstream, possibly due to an increase in air flow due to entrainment by the mist, but temperatures downstream of the fire are unaffected. After 10 s, temperatures in the backflow have further decreased at ceiling and mid-height, and floor level temperatures have increased (due to destratification of the backflow). Temperatures in the fire have dropped to 1500°C, and peak mid-height and ceiling level temperatures are also falling.

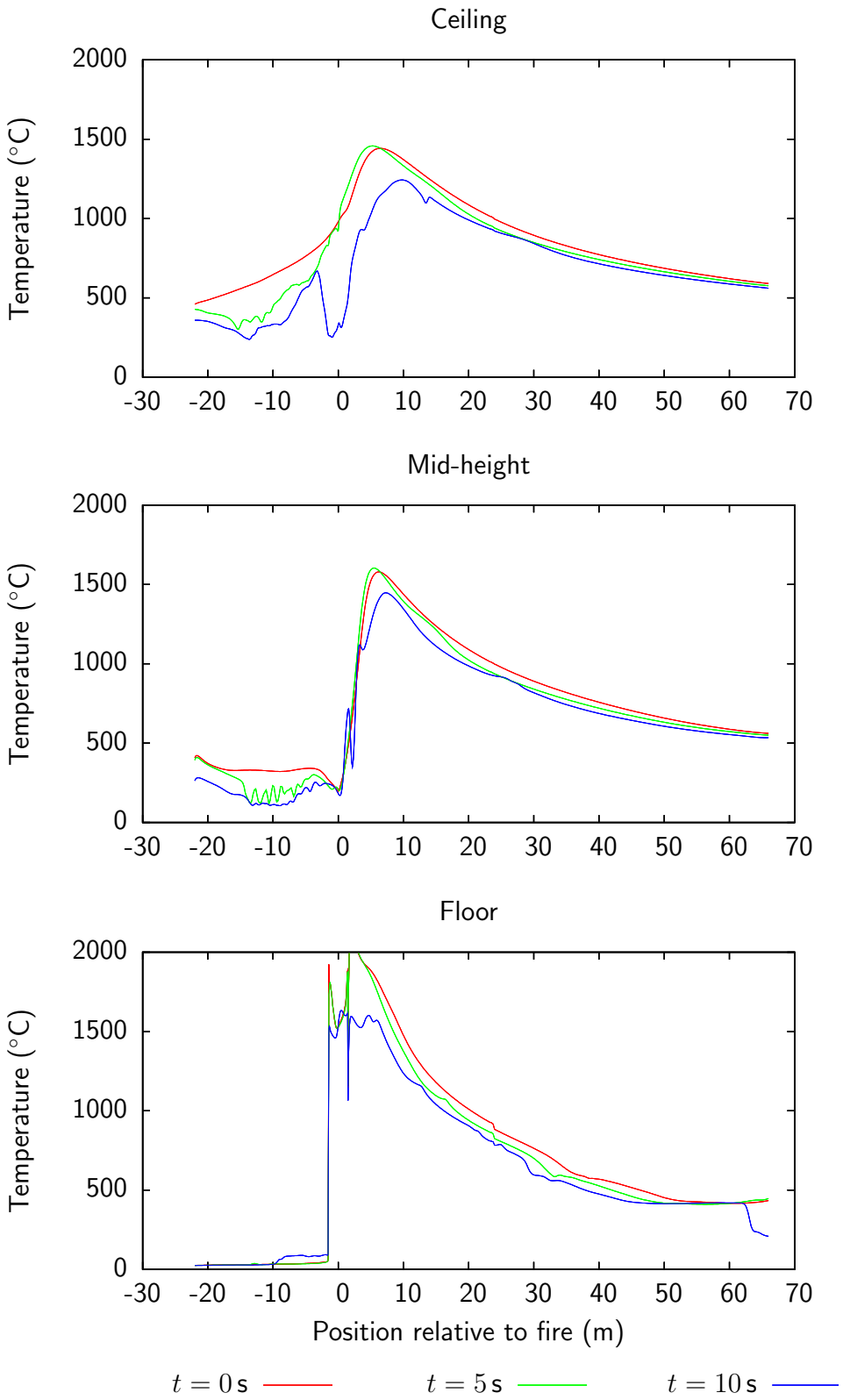

Figure 7.24: Reduction in temperature with time since mist activation for 0.8 m/s ventilation and single row of nozzles at 1.5 m spacings

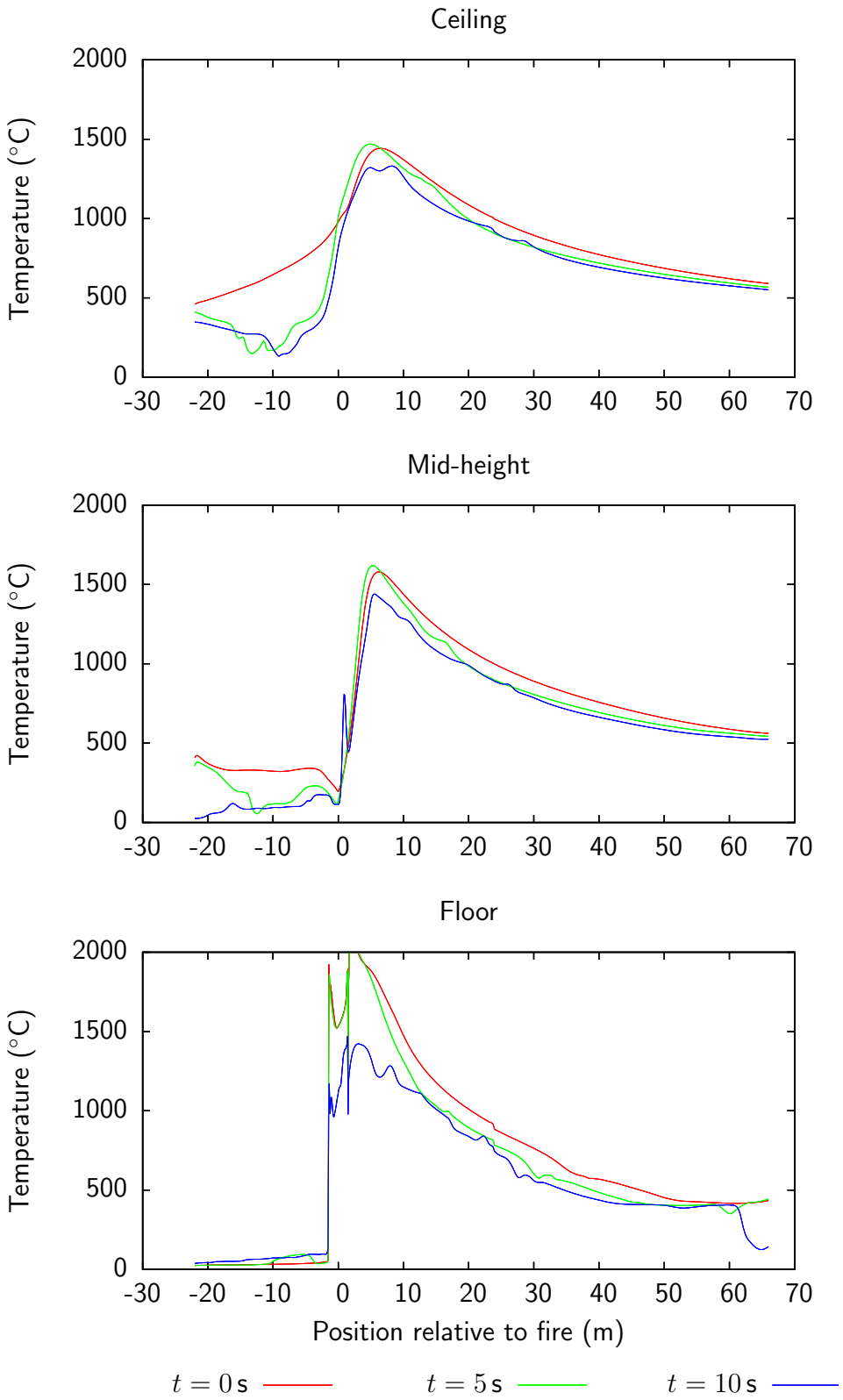

Figure 7.25: Reduction in temperature with time since mist activation for 0.8 m/s ventilation and dual rows of nozzles at 1.5 m spacings

With a double row of nozzles, the increase in mass-flow rate causes a corresponding increase in temperature drop.

Figure 7.26 and 7.27 show the temperature profiles in the tunnel at 0, 2, and 4 s after mist activation for the 2.4 m/s ventilation cases. The mist has a minimal effect on the temperatures over this period, mainly because temperatures upstream of the fire are close to ambient, and so there is little potential for heat transfer. For the single row of nozzles, there are noticeable peaks in ceiling level temperature. These occur because air close to the ceiling is heated by the radiative transfer from the fire to the ceiling. The entrained air flow brings this air down to the sampling line used to record the temperatures (see Figure 7.28).

7.2.3.2 Rate of reaction

Figure 7.29 shows the variation of the total rate of reaction with time for the four cases.

For the 2.4 m/s cases, the reaction rate stays virtually constant until the mist first reaches the fire when there is a large spike in the reaction rate. At this point, the solution became divergent, and was terminated. It is not clear, what causes this problem, but it assumed that the peak in reaction rate is non-physical.

For the 0.8 m/s cases, the variation in reaction rate can be split into three phases.

1. shallow fluctuation ($0 < t < 6$ s): this begins immediately after the mist is activated, and is due to variation in the air-flow at the fire as a result of the effects of the mist on the air-flow elsewhere in the tunnel. The fluctuation has a period of around 1 s, and an amplitude of no more than 10% of the mean reaction rate.

2. steady decline (7 s $< t < 9$ s): this occurs before the mist has reached the fire, and is due to a drop in oxygen concentration in the vicinity of the fire as a result of the destratification of the backflow layer.

3. random sharp variation ($t < 9$ s): this begins once the mist reaches the fire and is directly interacting with the flame. This destabilises the leading edge of the flame resulting in an extinction-reignition behaviour. The fluctuation occurs over very short time periods, and is of a significant magnitude. It is

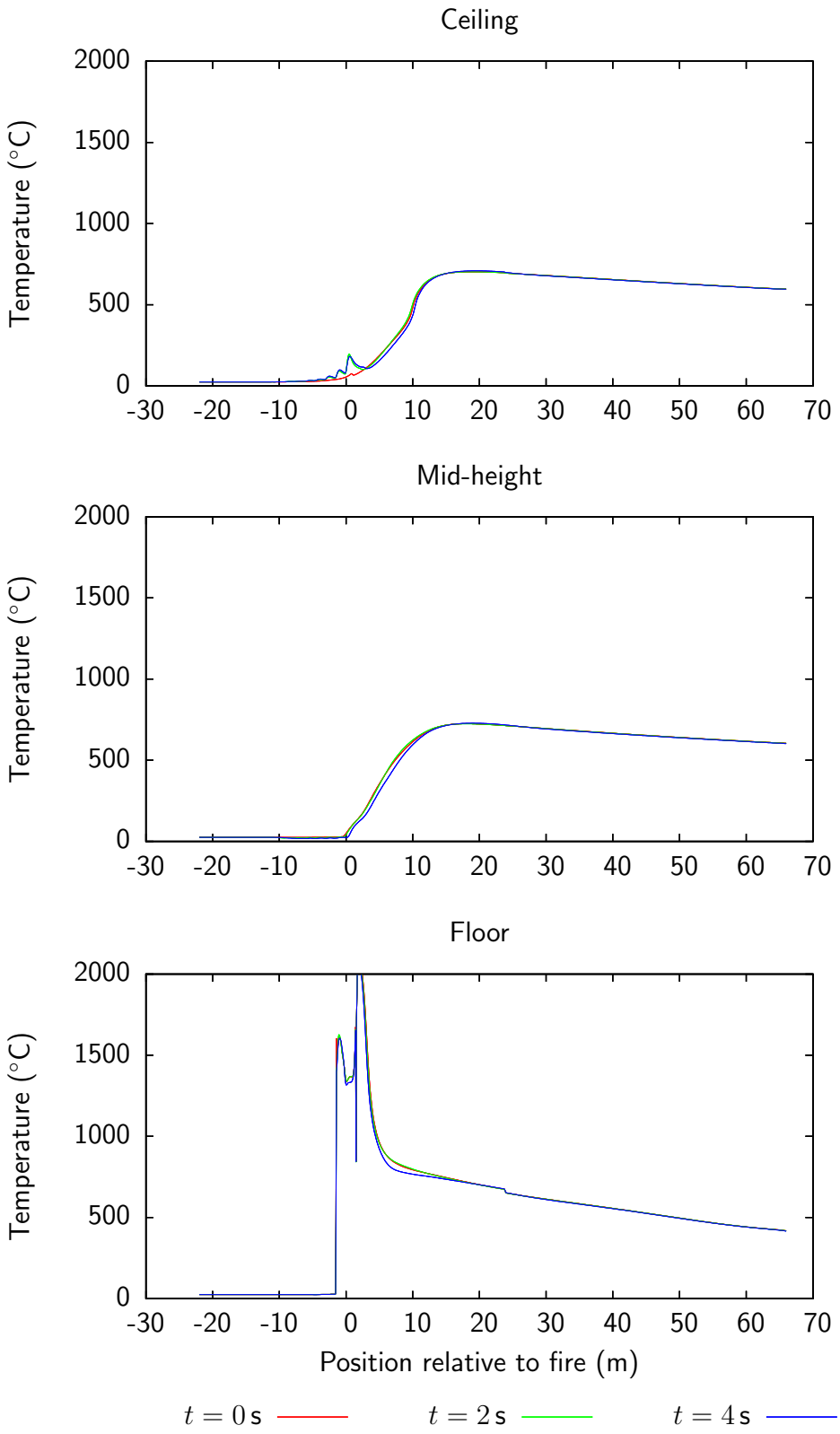

Figure 7.26: Reduction in temperature with time since mist activation for 2.4 m/s ventilation and single row of nozzles at 1.5 m spacings

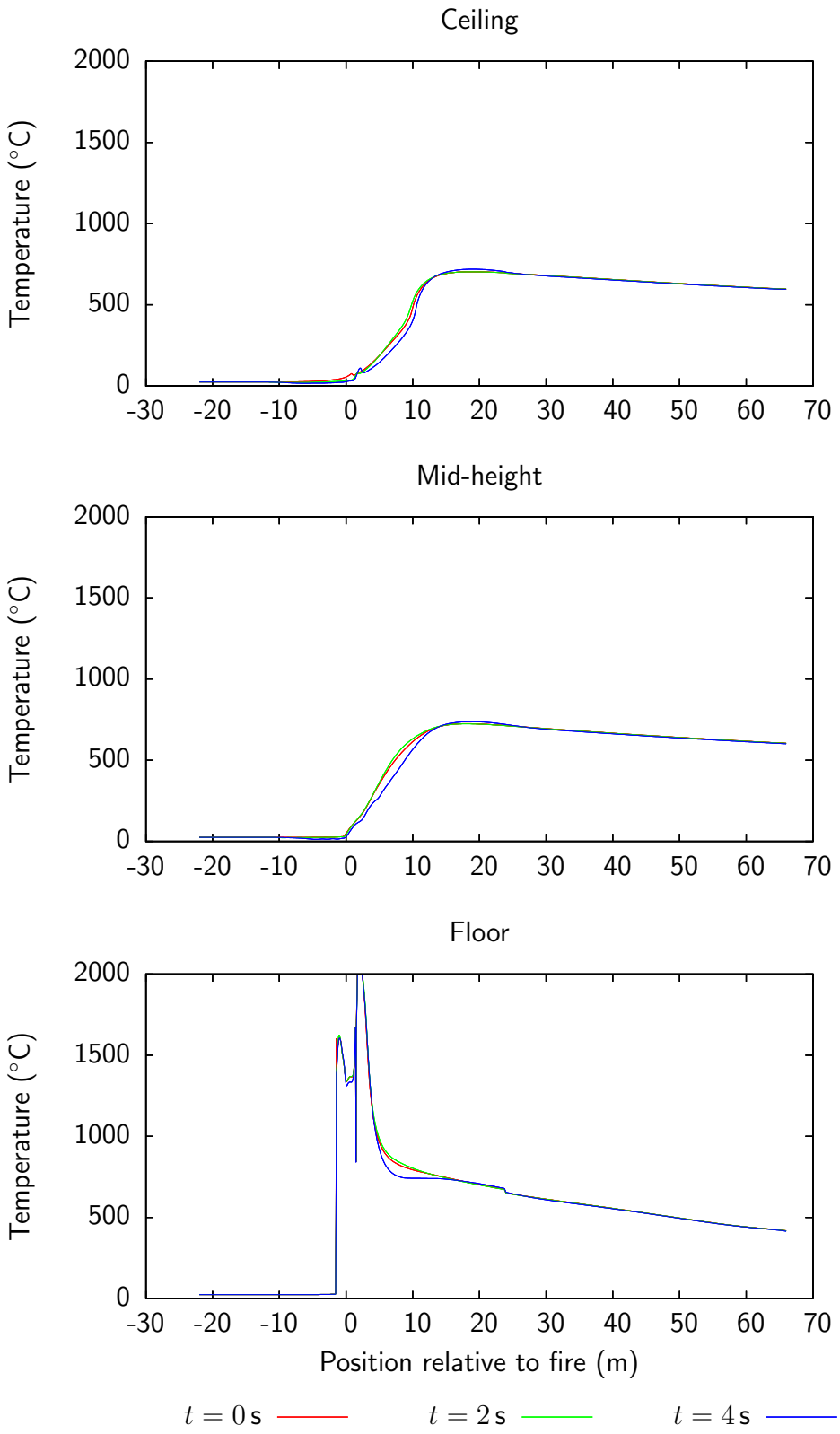

Figure 7.27: Reduction in temperature with time since mist activation for 2.4 m/s ventilation and dual rows of nozzles at 1.5 m spacings

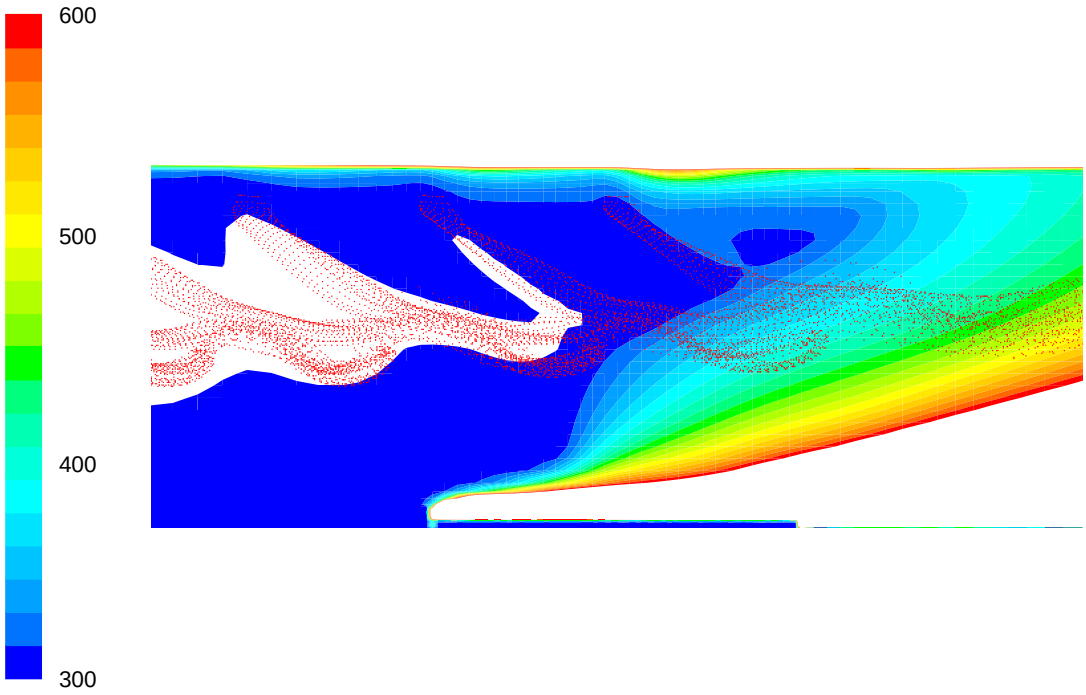

Figure 7.28: Mid plane temperatures overlaid with particle locations from a single row of nozzles with 2.4 m/s ventilation

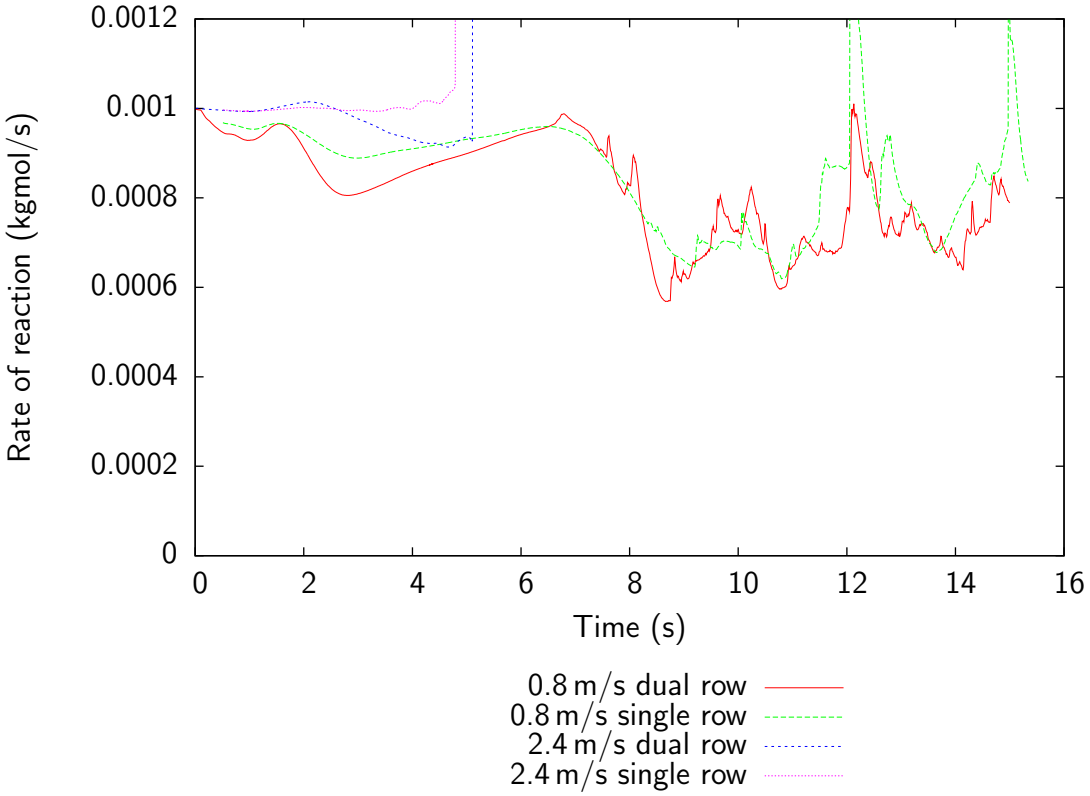

Figure 7.29: Effect of water mist on overall rate of reaction

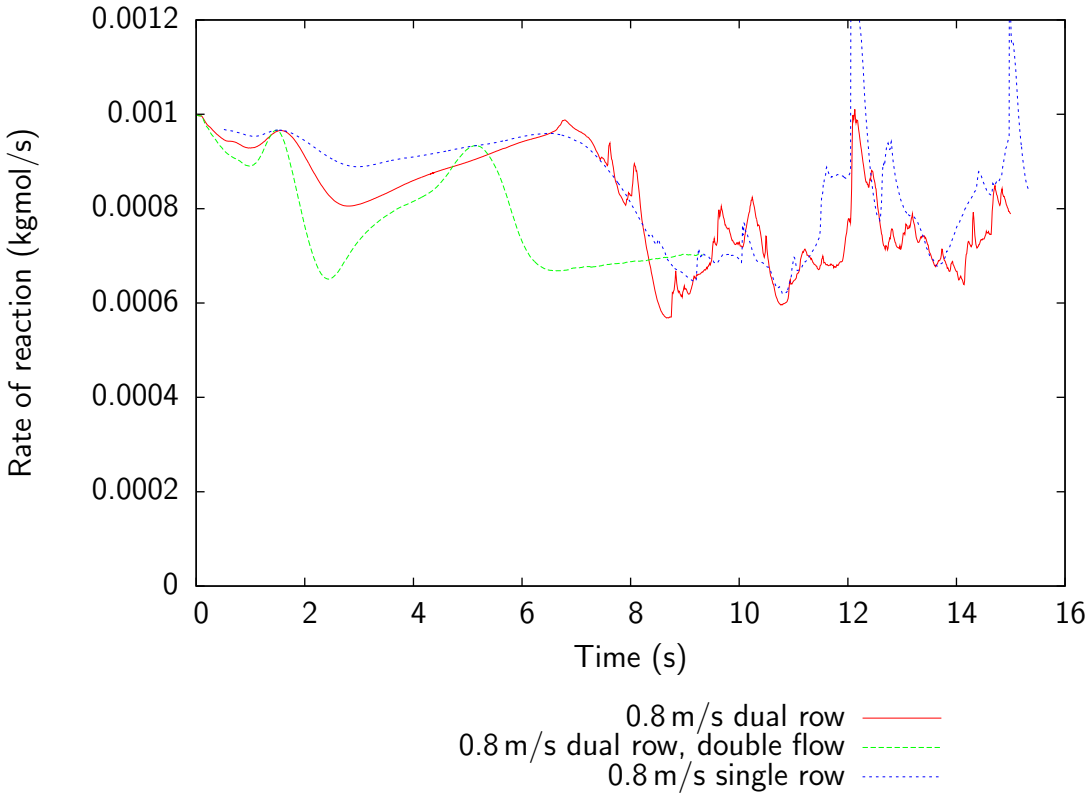

Figure 7.30: Effect of doubling water mist flow rate on suppression performance

therefore likely that a significant grid and time step dependence would be present in the results.

Doubling the water flow rate has a minimal affect on the effectiveness of the mist. The minimum observed reaction rate is 61.9 % and 56.9 % of the pre-mist levels for the single- and double-row cases respectively. A further case was modelled also using a double-row of nozzles, but with the flow rate from each nozzle doubled to 0.2 kg/s. Again, this gave similar levels of suppression as the earlier cases, however there was much less fluctuation in the rate of reaction, suggesting a more uniform mist concentration (see Figure 7.30).

7.2.3.3 Water vapour concentration

The evaporation of the droplets increases the concentration of water vapour in the air, reduces temperatures, dilutes oxygen, and increases the specific heat capacity of the air. The concentration of water vapour is a useful indicator of where the

mist is most effective.

There are two sources of water vapour in the model: the water that is a product of combustion; and the water that is released by evaporating droplets. There is also a small quantity (0.01 mass fraction) of water vapour introduced at initialisation and the flow inlet in order to ensure the EBU model gives a non-zero rate of reaction.

To find the water concentration due to the mist, the contribution of the other sources must be subtracted from the total water concentration. As the EBU model and the hybrid Arrhenius/EBU model are based on the same single step reaction (Equation 7.6), the quantity of water vapour coming from combustion can be determined with reference to the carbon dioxide concentration.

$$C_{19}H_{30} + 26.5\,O_2 \rightarrow 19\,CO_2 + 15\,H_2O \tag{7.6}$$

$$Y_{H_2O_{mist}} = Y_{H_2O_{total}} - Y_{H_2O_{inlet}} - \frac{Y_{CO_{2total}} - Y_{CO_{2inlet}}}{\alpha} \tag{7.7}$$

where

Y_{i_j} is the mass fraction of species i due to j, the $Y_{i_{total}}$ correspond to the CFD mass fractions and $Y_{i_{inlet}} = 0.01$, and

α is the ratio of carbon dioxide to water vapour by mass produced by the combustion reaction. For $C_{19}H_{30}$, $\alpha = \frac{19\times44.009}{15\times18.019} = 3.0943$

This relies on carbon dioxide and water vapour having equal diffusivities. If this were not the case, or if more complex combustion chemistry were used, then an additional scalar would need to be included (and solved) by the model in order to differentiate each source of water vapour.

Figure A.15 and Figure A.25 show the mist-originated water vapour for the two ventilation rates. At 0.8 m/s, there is significant evaporation close to the nozzles (due to the hot backflow) and the concentration rises to over 4 %. The water vapour is transported along with the mist towards the fire, and by 8 s, the mist-related water vapour concentration at the fire is 1.4 % average (3.5 % maximum) for the single row, and 13 % average (35 % maximum) for the double row. At 2.4 m/s, there is minimal evaporation close to the nozzles, and in this region the water vapour concentration remains below one percent. After 3 s, mist begins to reach the leading edge of the plume and starts to evaporate. This vapour is transported away from the fire, and has no influence on the rate of combustion. As time passes, the vertical penetration of the mist increases (see Figure A.22) and the mist reaches further down the plume. At around 5.5 s mist reaches the top of the fuel pan, and a sharp localised peak in mist-vapour is observed.

7.2.3.4 Mist distribution

Figure 7.31 shows the distribution of mist in the tunnel 5 s after mist activation. The particles are coloured by depth to indicate the vertical distribution. A single row of nozzles produces an inferior mist distribution when compared to a double row.

The influence of the air flow on the mist distribution is strong. Figure 7.32 shows the distribution of mist from a single nozzle. At 0.8 m/s an L-shape pattern is formed due to the combination of negative velocity in the backflow and high positive velocity in the fresh air beneath, and varies from nozzle to nozzle with the backflow depth and velocity. At 2.4 m/s the flow in the tunnel is virtually constant, leading to a uniform mist distribution that varies little over time and from nozzle to nozzle. The sinusoidal pattern seen in the downstream region of the mist cloud is due to interaction with the air flow from other nozzles.

7.2.3.5 Stability

There is an instability that occurs at the point in time mist reaches the fuel source in the 2.4 m/s ventilation cases, and does not occur in the 0.8 m/s cases at a comparable point. There are a few differences between these cases that could account for this:

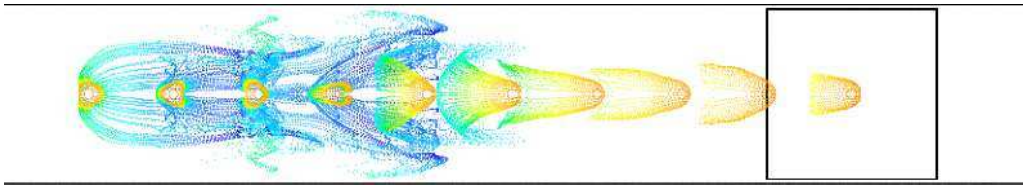

0.8 m/s ventilation single row nozzles

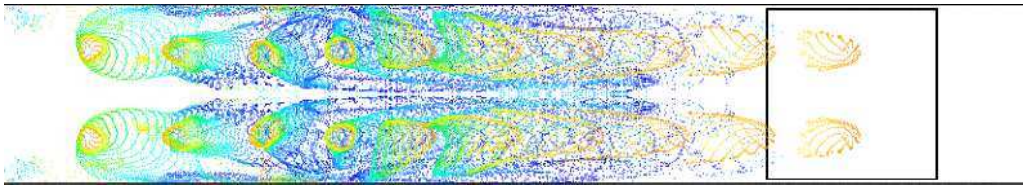

0.8 m/s ventilation double row nozzles

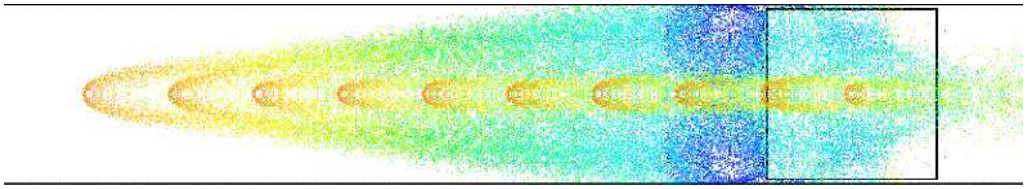

2.4 m/s ventilation single row nozzles

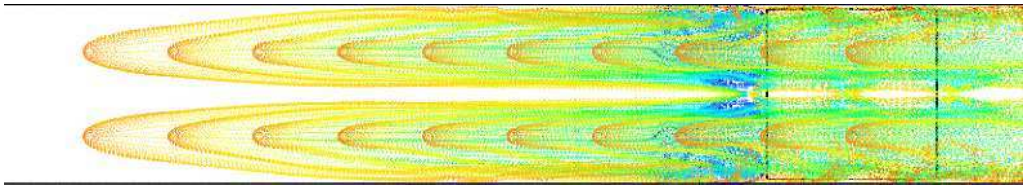

2.4 m/s ventilation double row nozzles

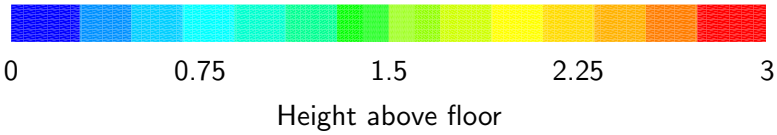

Figure 7.31: Distribution of mist in tunnel 5 s after mist activation for each of the four cases

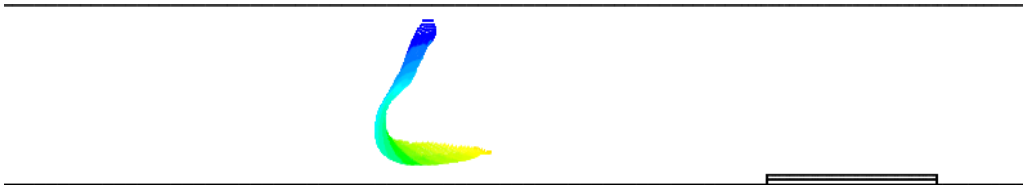

0.8 m/s ventilation single row nozzles

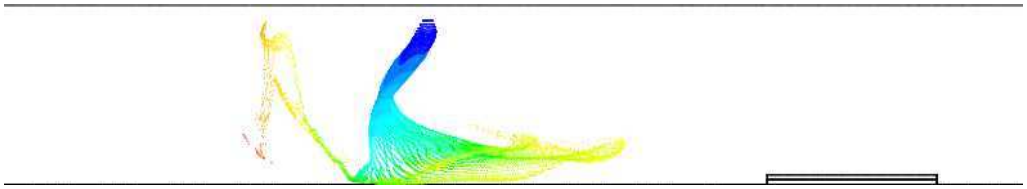

0.8 m/s ventilation double row nozzles

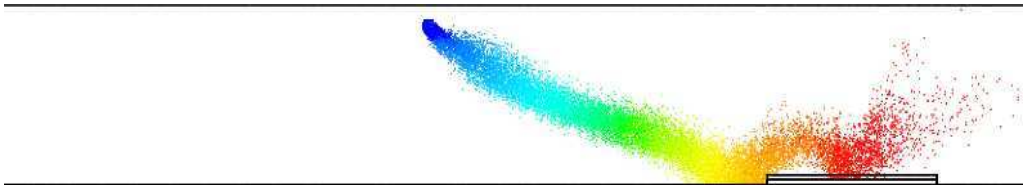

2.4 m/s ventilation single row nozzles

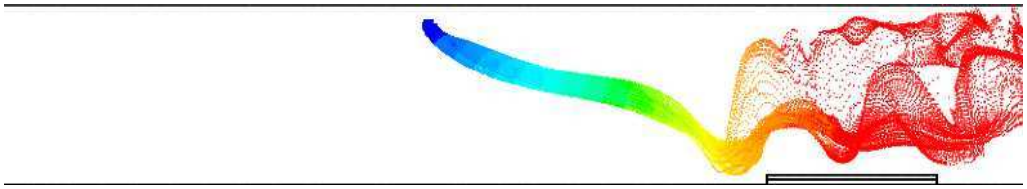

2.4 m/s ventilation double row nozzles

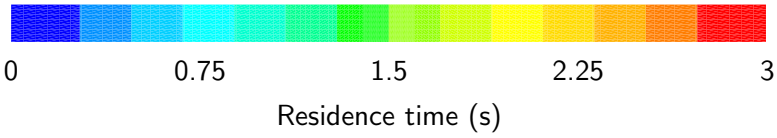

Figure 7.32: Distribution of mist from a single nozzle 6 m upstream of the fire 5 s after mist activation for each of the four cases

1. the mist in the 0.8 m/s cases has been pre-heated and partly evaporated by the backflow. The DPM source terms are much lower than for 2.4 m/s because there is less mass.

2. there is a larger thermal gradient in the 2.4 m/s cases, because there is less diffusion of heat from the plume. The mist droplets are therefore evaporating more rapidly, again leading to larger source terms.

3. the finite-rate limit of the hybrid model has a greater effect in the 2.4 m/s cases, and there is a higher concentration of unburnt fuel in the region around the flame. Disruption to the flow caused by rapidly evaporating mist could cause a spontaneous ignition.

For the first two causes, use of a smaller time step and a greater number of tracking particles (so that each particle represents less mist) should improve the stability of the solution.

In the 0.8 m/s cases, an extinction-reignition behaviour is seen, with a rapidly fluctuating reaction rate. This could be a physical phenomenon, or it could be due to a numerical instability in the CFD model. In either case, it could be of benefit to reduce the time step size and refine the grid in this region in order to better resolve the fluctuations or eliminate the instability.

Unfortunately it was not feasible to run the entire scenario with a significantly smaller time step on the available hardware. Restarting the problematic cases from a point shortly before the instability, with a 0.0025 s time step, did not avoid the issue, however a complete rerun with a 0.00333 s did appear to be stable (see Appendix D.3), suggesting that the number of droplets per tracking particle is of importance. For the reduced time-step case, a lower number of streams was used for nozzles that did not directly influence the fire, in order to limit the number of active particles, without affecting the particles that actually reach the fire.

7.2.4 Summary of findings

- The action of mist on a tunnel fire varies significantly with ventilation velocity, and entirely distinct behaviours are seen for sub-critical and super-critical flow.

- For sub-critical flow, there is a strong interaction between the mist and the hot backflow. This can be beneficially as it caused a significant reduction in oxygen levels at the fire, however it also resulted in a reduction in the concentration of mist reaching the fire.
- For super-critical flow, the smooth flow regime upstream of the fire leads to a well distributed descending layer of mist, that eventually reaches the seat of the fire. Downstream of the fire, there is significant evaporation within the fire plume, slightly reducing temperatures, but not otherwise influencing the fire.
- Complete extinction of the fire is not observed in any case considered. A reduction in the rate of reaction of around 40 % is observed.
- Use of two parallel rows of nozzles gives a better distribution of mist in the tunnel than a single central row.
- Doubling the mist flow rate, increases the overall cooling due to the mist, but has only a minimal effect on the fire itself.
- At the lower ventilation rate, a time step of 0.01 s (or 1/100th of the time step needed for the tunnel fire model) was satisfactory, although a smaller time step may provide better resolution of the mist–flame interaction.
- At the higher ventilation rate, the model was not stable with a time step of 0.01 s once the mist had reached the pool.
- Using a larger than physical nozzle radius can improve convergence without significantly altering behaviour.

7.3 Conclusions

A CFD model of water mist suppression was successfully applied to an enclosure fire. To achieve a stable solution, the use of 20 tracking particles per time step and a time step size of 0.0005 s was required. The model predicted a rapid extinction, which is consistent with the experimental data. Extinction is due to gas phase cooling facilitated by a disruption to the fire-induced air-flow. Other possible mechanisms – such as oxygen dilution, attenuation of radiation, and fuel cooling – were shown to be insignificant.

A parametric study into water mist behaviour showed that the performance of WMFSS varies considerably with mass flow rate, injection velocity, cone angle, and droplet size. Except in borderline cases, extinction time is determined by the time it takes mist to reach the fire, and the following trends were observed:

- increasing water flow rate increases effectiveness.
- there is a minimum water flow rate that can achieve extinction. This was 0.005 kg/s for a 27 kW and 0.02 kg/s for 115 kW. This implies that it is possible to extinguish a fire with *less water* than suggested by a simple *energy balance*.
- Smaller droplets are more effective.
- Increasing momentum improves penetration, and hence effectiveness,

but

- Low velocity gives a high (local) droplet concentration which can be beneficially in certain circumstances.

The model was validated against experimental data for the cooling of the hot gaseous layer beneath the ceiling.

The CFD model of water mist suppression was also applied to a tunnel fire. At sub-critical velocity, a time step of 0.01 s and 100 particles per nozzle per time step was sufficient to achieve convergence. At super-critical velocity, using the same discretisation, the solution becomes unstable as the mist reaches the fuel surface.

The behaviour of the mist was shown to be intimately linked with both the ventilation air flow and the fire induced flow. With sub-critical ventilation, the high temperature backflow causes substantial heating and evaporation of the mist. The negative velocity transports mist away from the fire. Beneath the backflow, cold fresh air transports the mist at high speed back towards the fire. The mist also disrupts the stratification of the air flow, and this – combined with the evaporation of the mist – causes a significant reduction in oxygen levels at the fire.

With super-critical ventilation, there is no backflow layer, and so little evaporation occurs until the mist reaches the fire. The ventilation flow transports the mist a significant distance downstream. Most of the observed evaporation occurs in the thermal plume downstream of the fire, and so has little effect other than to reduce temperatures. It is not known what effect mist directly reaching the pool had on the fire as the solution became unstable at this point.

Chapter 8

Conclusions and further work

This chapter brings together the findings of this thesis and highlights the original contributions to knowledge. Some areas requiring further research are also identified.

8.1 Summary of thesis

The main aim of this thesis was to develop a computational model of a water mist fire suppression system (WMFSS) and apply it to a typical tunnel fire. This task was achieved along with a number of interrelated sub-tasks.

Chapter 2 presented a review of current knowledge pertaining to fires and particularly to tunnel fires. General statistics were combined with more specific case studies in order to depict the nature of the hazard.

Chapter 3 reviewed fire fighting methods, such as water sprinkler, carbon dioxide and halon based systems, before focussing on the nascent water mist technology, its emerging uses and describing current understanding of its behaviour.

Chapter 4 outlined the theory and practice of Computational Fluid Dynamics (CFD), much of which is very well established and is detailed in respected text-books and implemented in a wide variety of software packages. CFD has been used as the basis for many fire safety studies published in the academic litera-

ture. The use of a Lagrangian particle-based model for the water mist system was proposed, and the need for the mist to interact with combustion and radiation imposes restrictions on how those phenomena can be approached. The commercial CFD code *Fluent* was selected, as at the time it had the most mature particle model.

A CFD model of an enclosure fire was developed in Chapter 5, based on experiments performed by Kim and Ryou (2003). The pool fire was represented by using a fixed mass-fraction with an otherwise unmodified wall boundary condition. Some issues were encountered with the process of diffusion in the laminar region close to the fuel surface. Overall, the model performed well, and the sensitivity of the model to the thermal boundary condition was established. As an unsteady solution is required, a three-dimensional CFD model takes several days to run.

CFD modelling was then applied to tunnel fire scenarios. Initially a simply heat source was used to replicate small scale experiments, before the pool fire model was applied to a set of full-scale tests. The required mesh size and time step were established, and the capabilities of CFD to predict backflow and thermal stratification were demonstrated. Detailed representation of the pan geometry was shown to be of particular importance. Agreement between CFD and experiment was better at low velocities.

Finally, water mist suppression was applied to both the enclosure fire and the tunnel fire scenarios. For the enclosure fire this was again based on the experiments of Kim and Ryou (2003), although the rapidity of the mist suppression and the limitations in the experimental data places some caveats on the validation of the model. For this particular case, gas phase cooling was shown to be primary mechanism of suppression, with the disruption of air flow due to both transfer of momentum and negative buoyancy also being significant.

For the tunnel fire, no experimental data were available, so the water mist system was merely hypothetical. Nonetheless, the CFD model provided valuable insight in to how such a system might behave in a tunnel: markedly different behaviours were seen depending on whether the ventilation flow was sub- or super-critical. Additionally the model was able to differentiate the performance of systems with different nozzle layouts.

8.2 Original contributions to knowledge

- An extensive literature review in relation to the use of water mist as a fire suppression system was performed. This identified a range of possible mechanisms for the suppression and extinction of fire by mist.
- A CFD model of the effect of water mist on a fire was developed and tested, and the values for important parameters such as time step size, number of tracking particles and so forth, that affect stability and accuracy were identified.
- This model was used to perform a parametric study of mist performance in an enclosure, showing the effect of varying droplet diameter, water flow rate, and injection velocity. This also showed that the model was able to distinguish between extinguishing and non-extinguishing mist systems, and a different behaviour close to the limit of effectiveness.
- The model was also used to investigate the behaviour of water mist in a well ventilated tunnel fire, and again, values for the time step size and number of particles needed for accuracy and stability were identified.
- The model showed entirely different behaviours depending on whether the ventilation rate in the tunnel was above or below the critical value needed to prevent a hot backflow, with the mist being substantially less effective at the higher velocities. This could imply that small fires will be harder to extinguish, as ventilation is more likely to be at or above the corresponding critical rate.
- The required run time of the model (given the size of mesh, and time step) was very long, and this means that numerical modelling of this type is not yet practical for routine design of water mist systems. However, 'cold tests' to investigate the distribution of mist in the absence of a fire, can be run in a few hours, and so could provide a useful tool for an experience fire engineer.

8.3 Further work

During the course of this project a number of areas were identified that fell outside the scope of this project, but which warrant further research.

The most important of these is clearly the lack of the experimental data needed for a direct validation of the tunnel water mist fire suppression model. Whilst every effort was made to use robust modelling techniques that had been validated against other data sources, the value of this work would be greatly increased if a corresponding full-scale experiment could be performed. More detailed experimental results for the enclosure fire would also be beneficial.

This study looks at a single class of fire – specifically a large diesel pool fire – but does not attempt to address the many other kinds of fire hazard that occur in mining environment. Other fuels, such as conveyor belting, present different problems, both from the point of view of fire suppression, and from a CFD modelling point of view. Additional, tests on enclosure fires have highlighted a difficulty in suppressing small and/or obstructed fires, so these clearly warrant special attention.

The pool fire model developed in Chapter 5 and used as the basis for the subsequent fire suppression model in Chapter 7, performed adequately in the cases modelled. It is not however without limitations, for example the difficulty of determining the actually fuel release rate, and the need to adjust the laminar diffusivity, and other approaches may have advantages. Whatever approach is taken, development of the fire model will be required to handle processes such as charring, burn-through, boil-over, and so forth that are associated with more complex fuels.

Finally, before water mists can be deployed in working mines reliable mist nozzles and fire detectors able to withstand the ardours of an underground environment must be developed.

Appendix A

Animations

A.1 Water mist suppression of enclosure fires

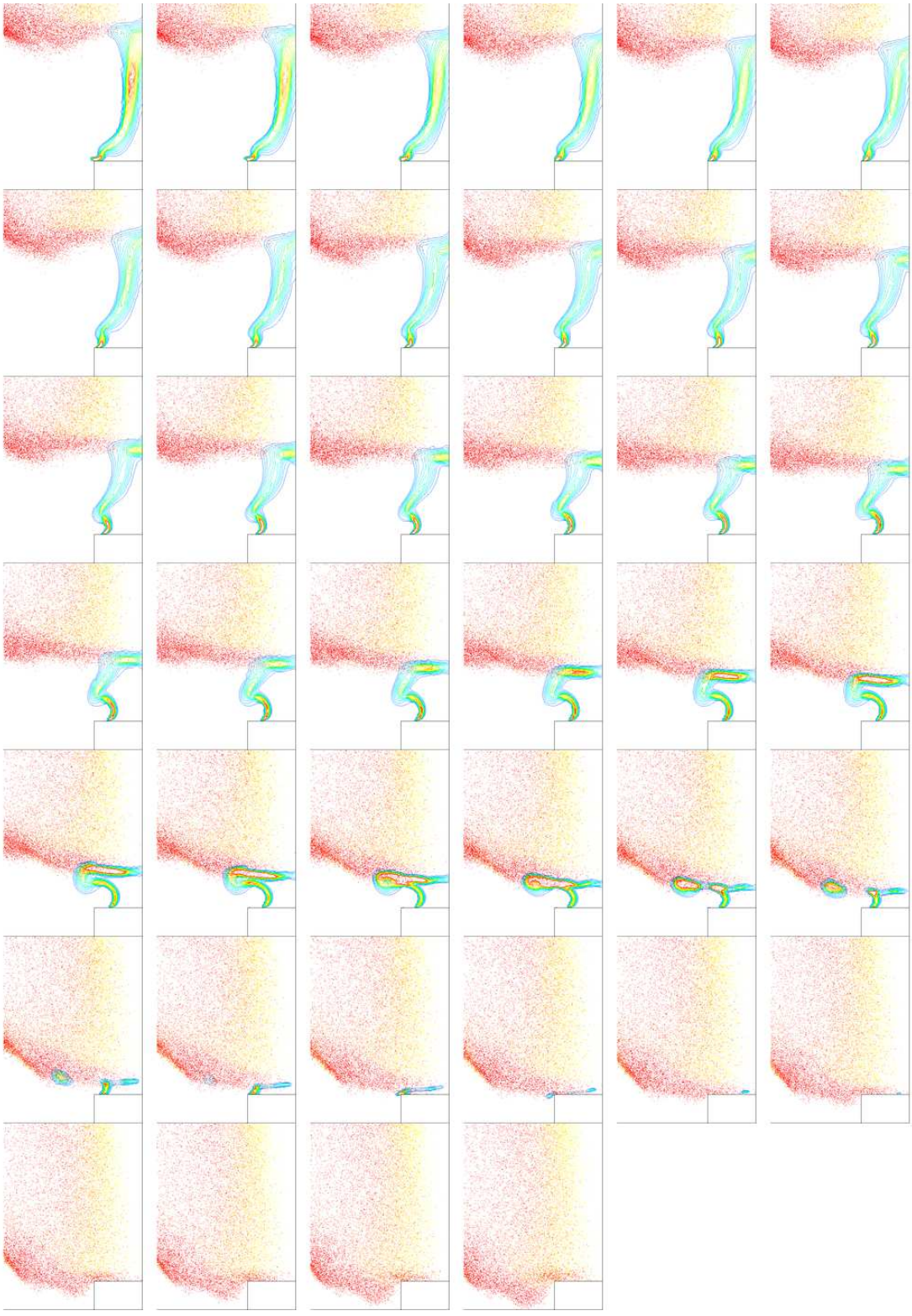

Figure A.1: Interaction of water mist with flame front
Animation A.1: Interaction of water mist with flame front (hexane fire)
kim-hexane-zoom.mpeg

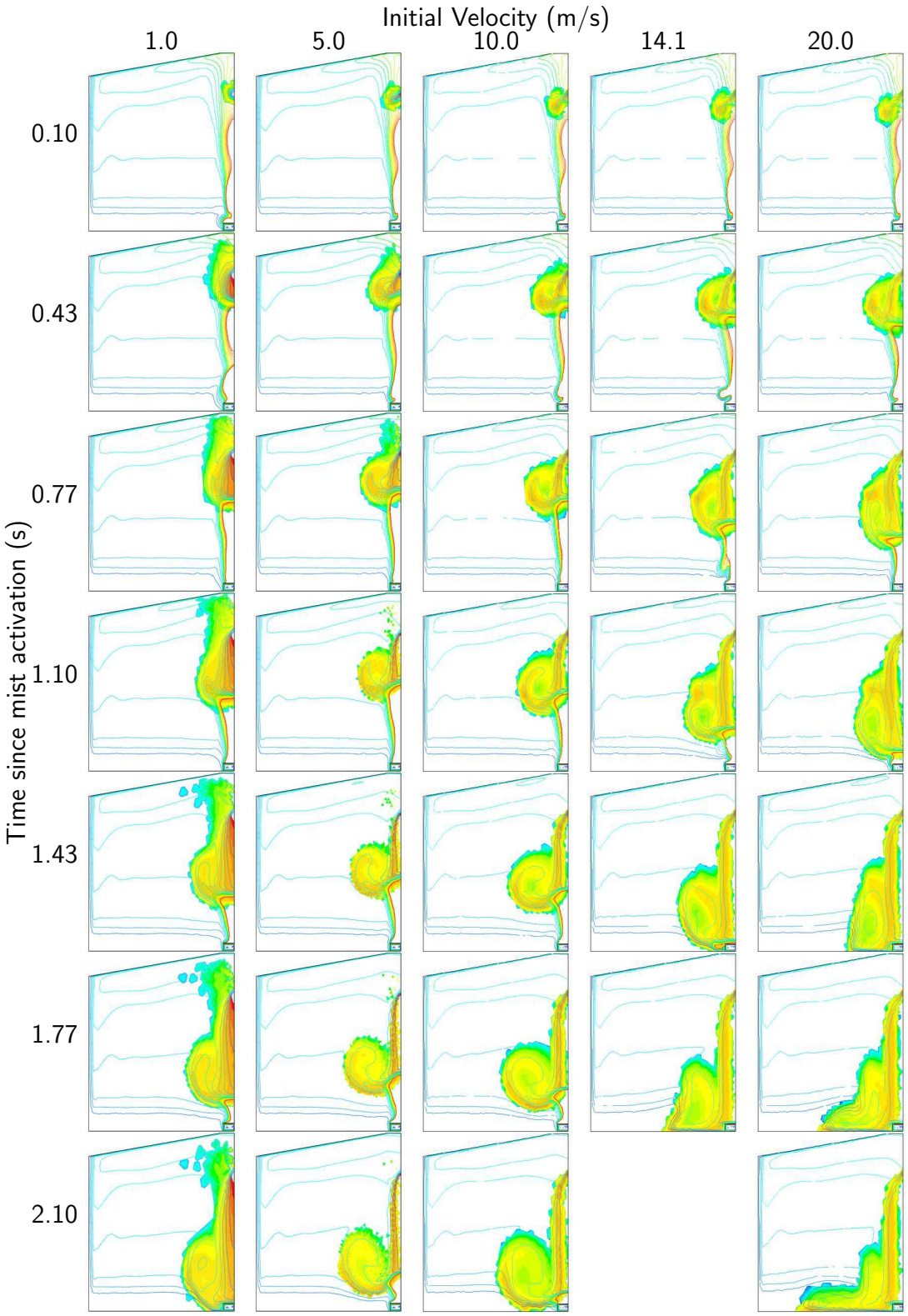

Figure A.2: Evolution of water mist concentration over time for different nozzle velocities

Animation A.2: Evolution of mist concentrations for different nozzle velocities

`kim-vel.mpeg`

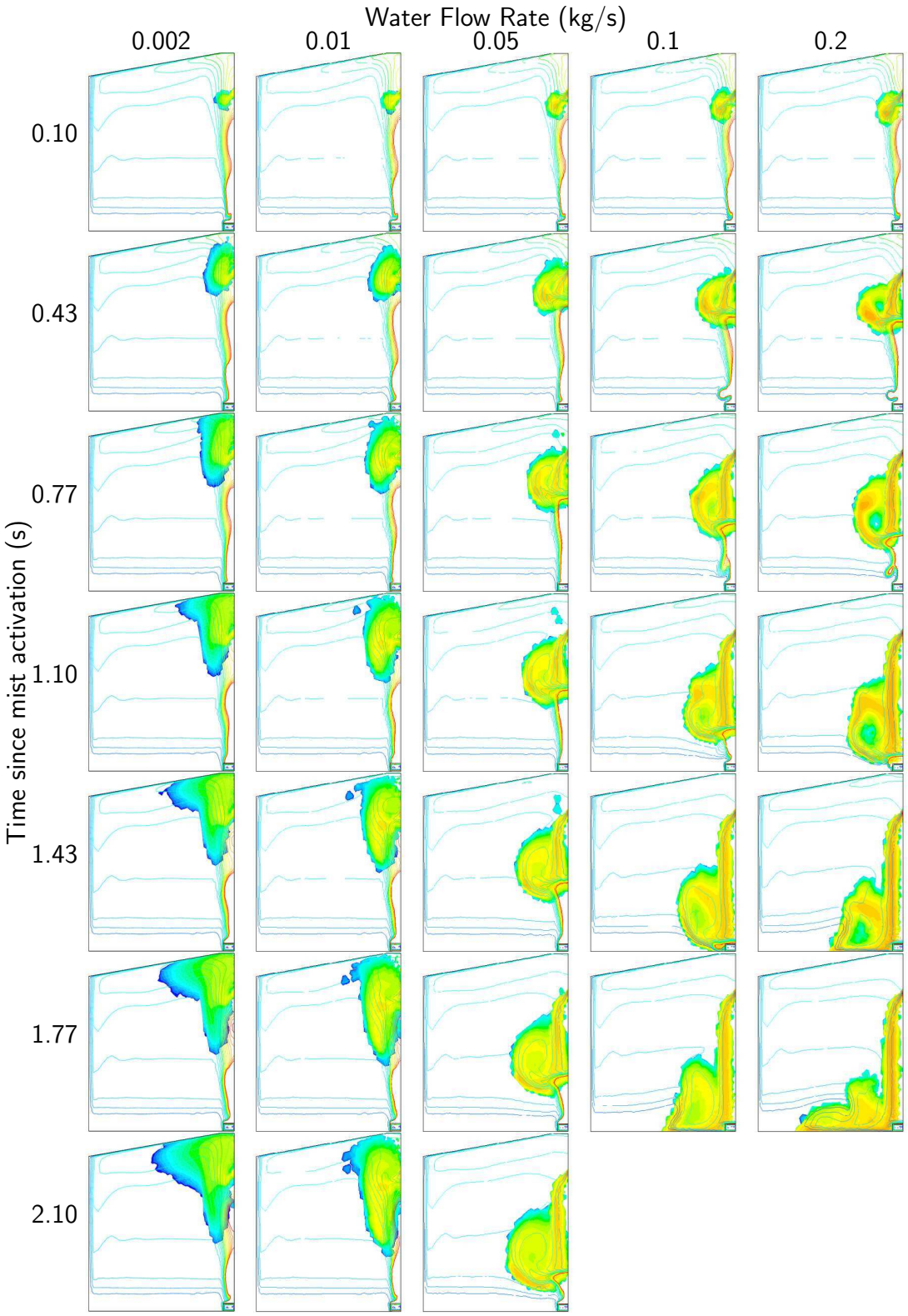

Figure A.3: Evolution of water mist concentration over time for different mass flow rates

Animation A.3: Evolution of mist concentrations for different water flow rates

kim-mflow.mpeg

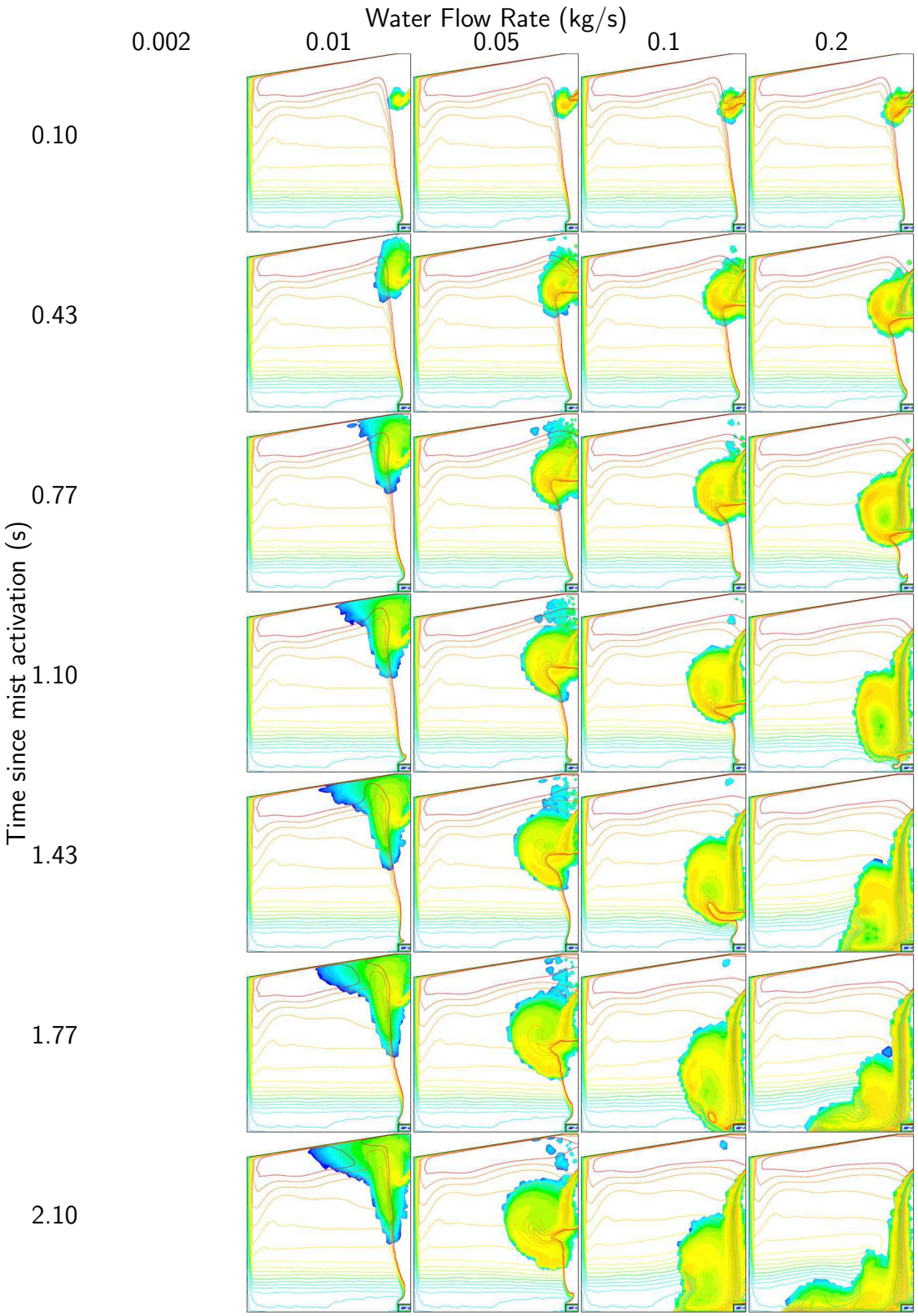

Figure A.4: Evolution of water mist concentration over time for different mass flow rates (hexane fire)

Animation A.4: Evolution of mist concentrations for different water flow rates (hexane fire) `kim-hexane-mflow.mpeg`

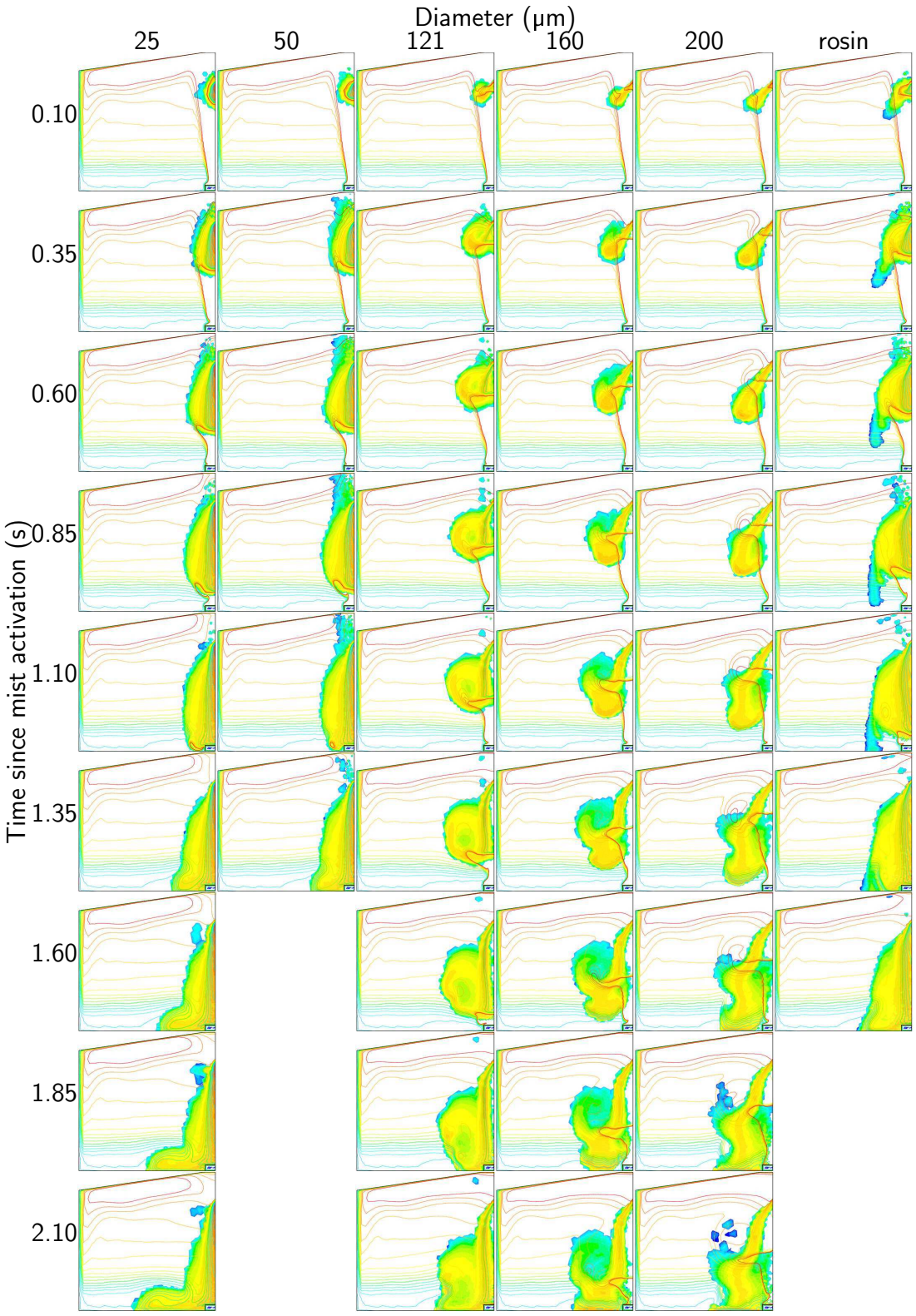

Figure A.5: Evolution of water mist concentration over time for different drop diameters (hexane fire)

Animation A.5: Evolution of mist concentrations for different diameters (hexane fire) `kim-hexane-diam.mpeg`

A.2 Water mist suppression of tunnel fires

A.2.1 0.8 m/s – single row

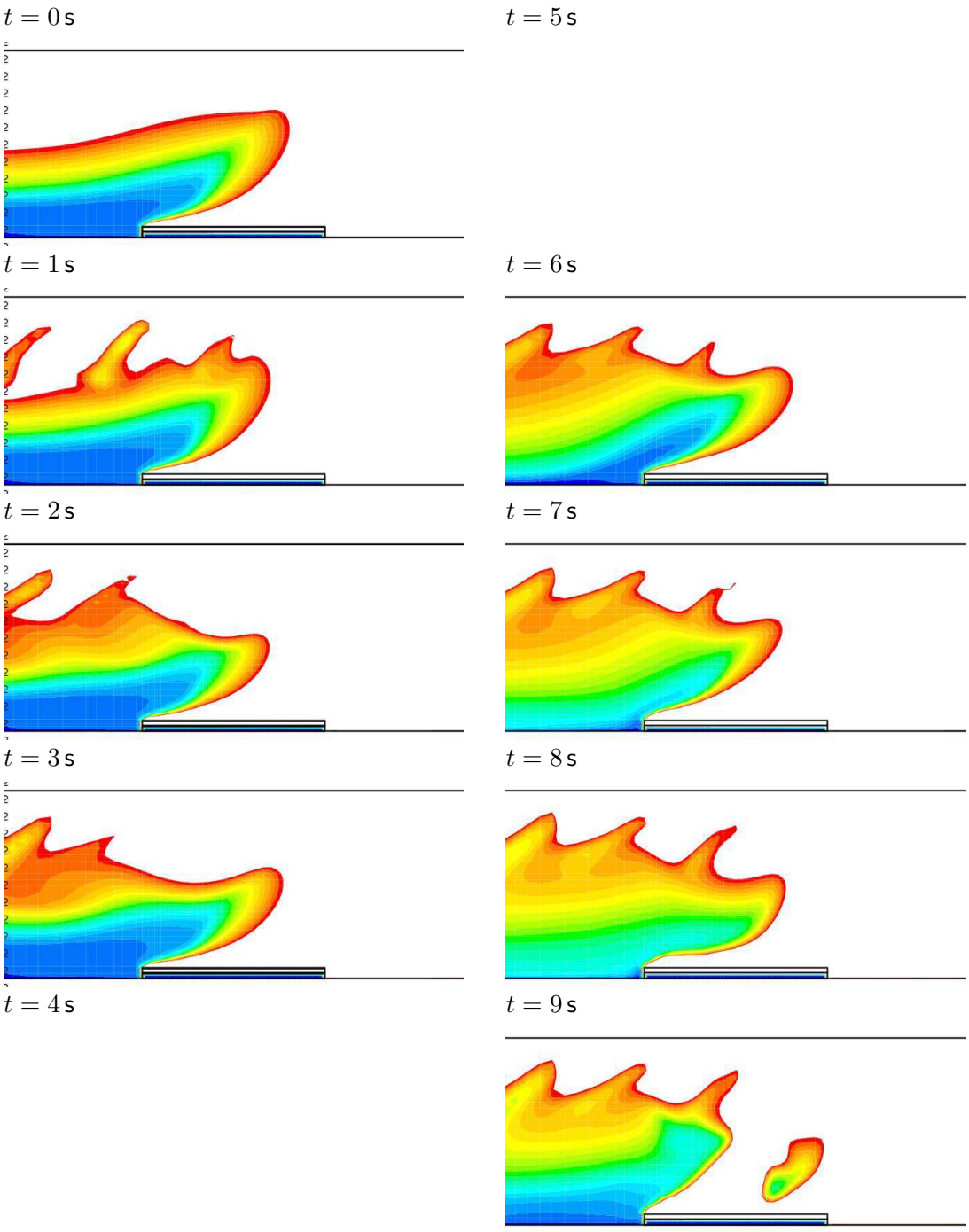

Figure A.6: Mid-plane temperatures for single row of nozzles and 0.8 m/s ventilation

Animation A.6: Mid-plane temperatures for single row of nozzles and 0.8 m/s ventilation `dmtmist-anim-08s-temp.mpeg`

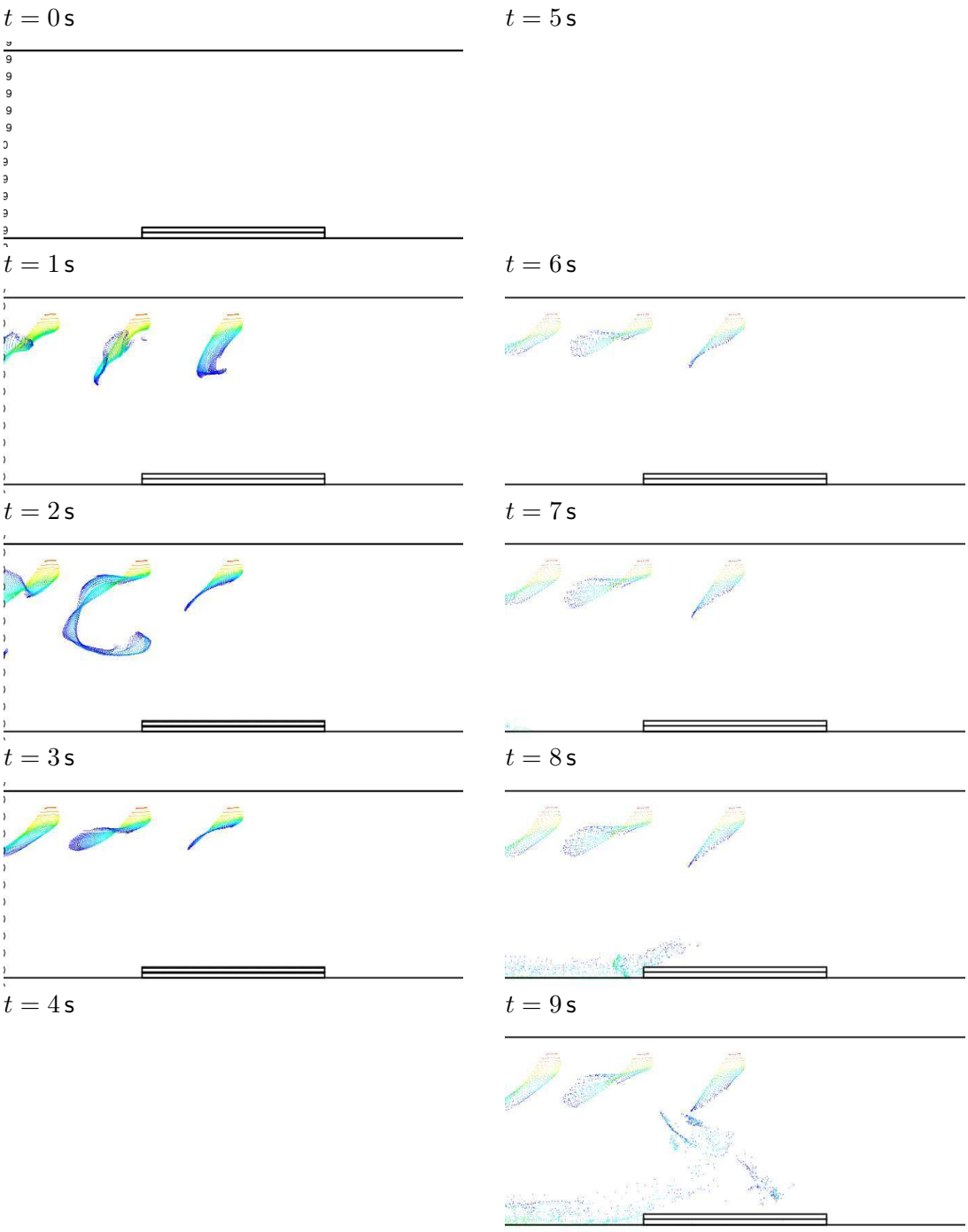

Figure A.7: Particle locations for single row of nozzles and 0.8 m/s ventilation
Animation A.7: Particle locations for single row of nozzles and 0.8 m/s ventilation
`dmtmist-anim-08s-dpm.mpeg`

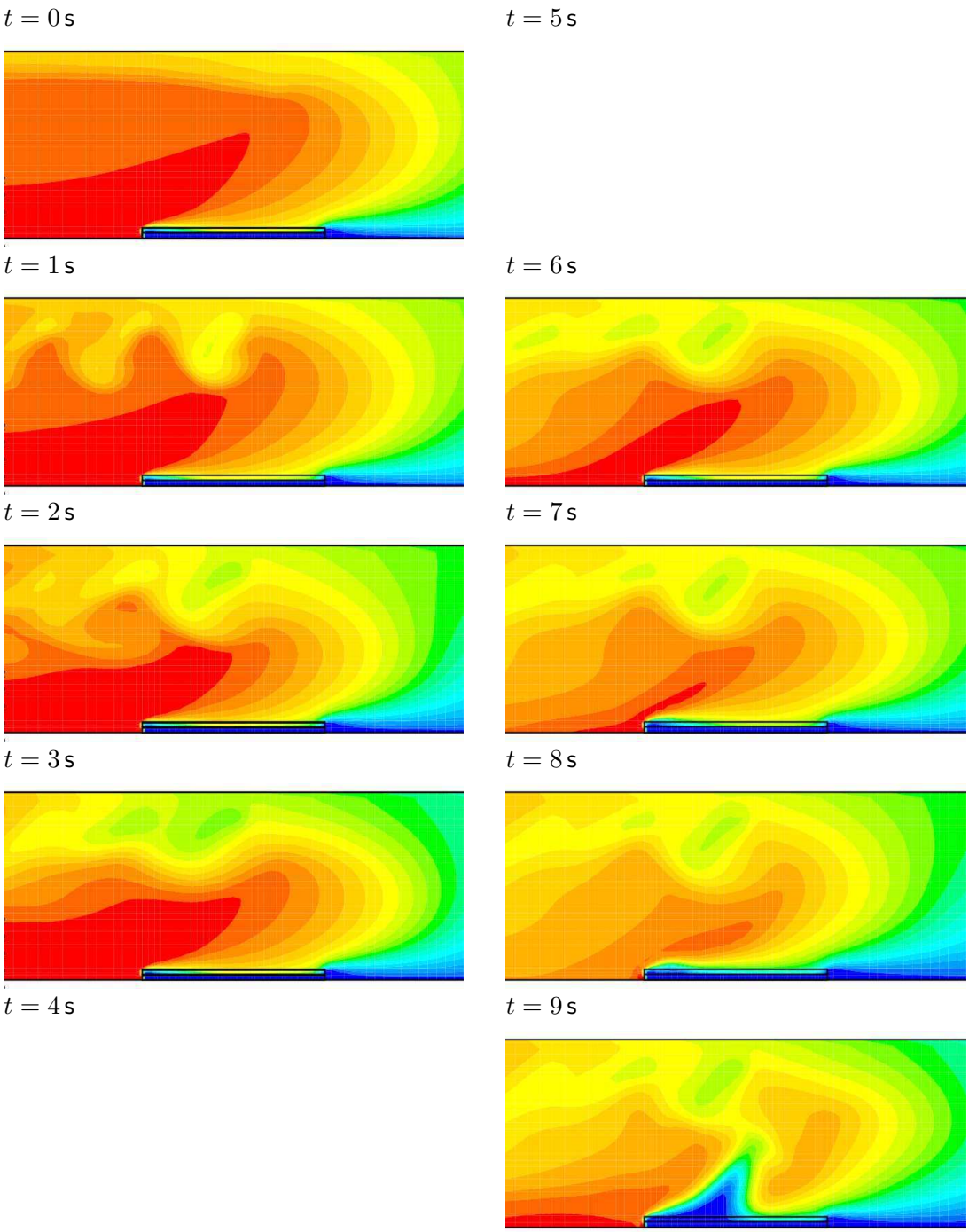

Figure A.8: Mid-pane oxygen concentration for single row of nozzles and 0.8 m/s ventilation
Animation A.8: Mid-pane oxygen concentration for single row of nozzles and 0.8 m/s ventilation `dmtmist-anim-08s-o2.mpeg`

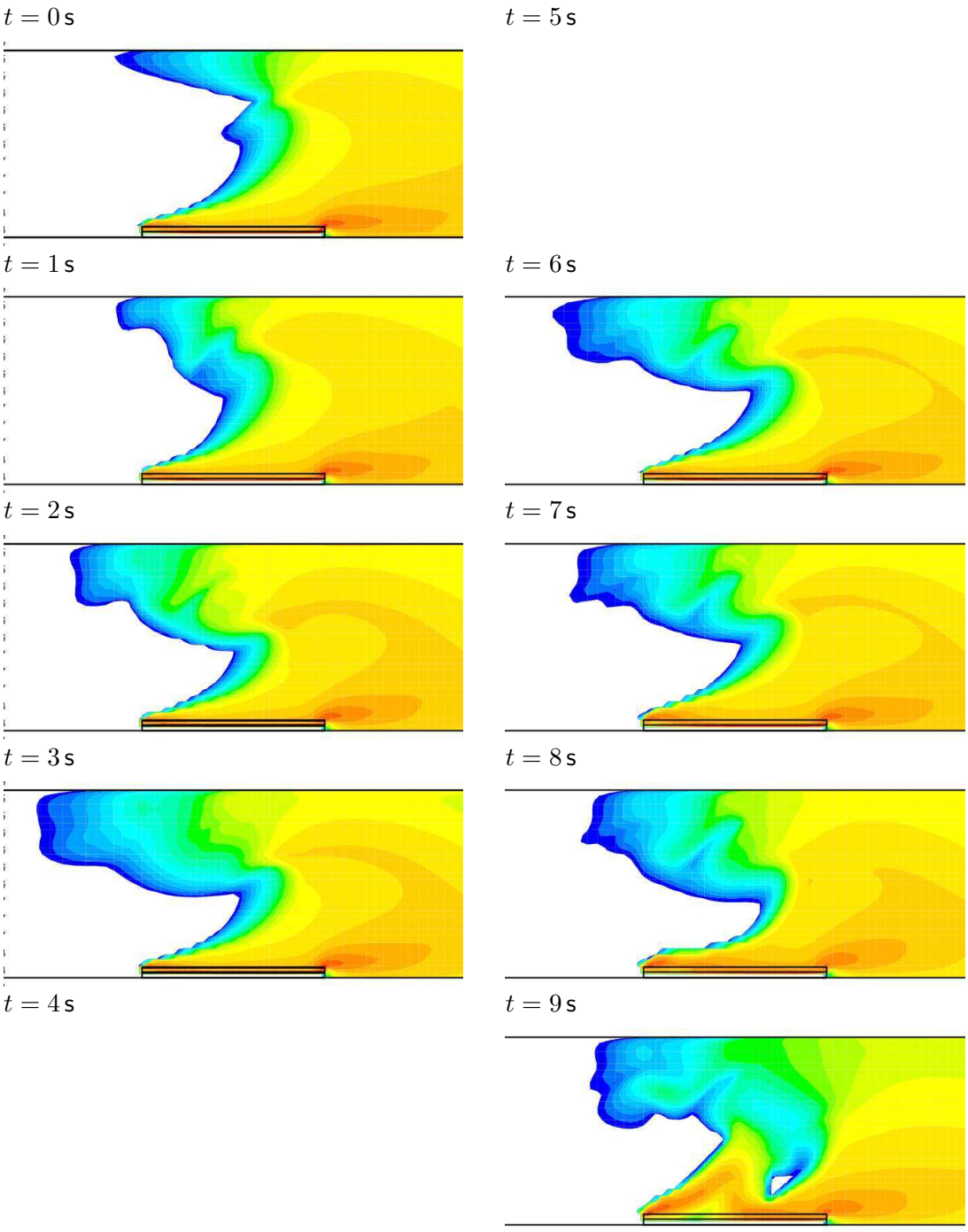

Figure A.9: Mid-plane reaction rate for single row of nozzles and 0.8 m/s ventilation

Animation A.9: Mid-plane reaction rate for single row of nozzles and 0.8 m/s ventilation `dmtmist-anim-08s-react.mpeg`

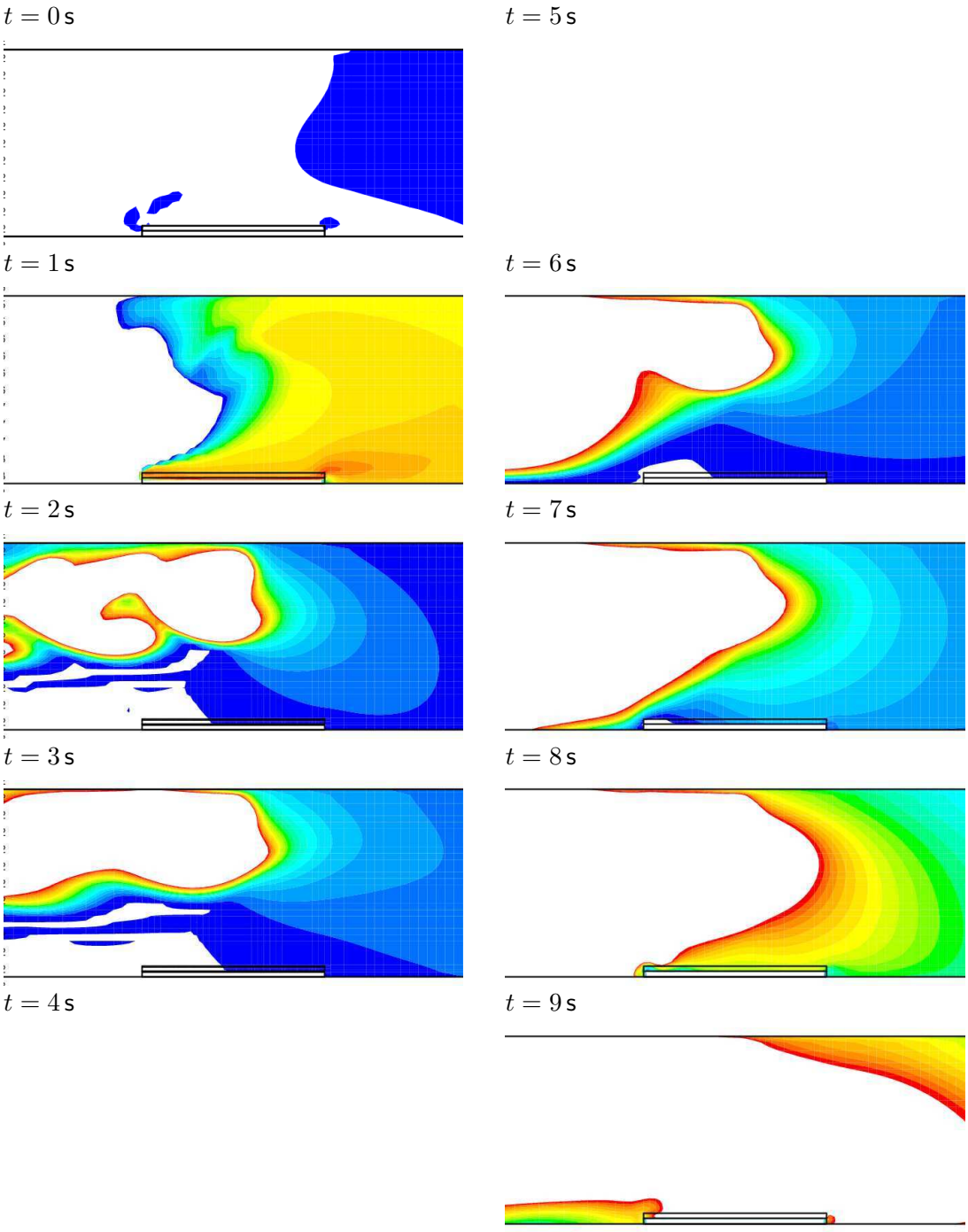

Figure A.10: Water concentration attributed to mist evaporation for single row of nozzles and 0.8 m/s ventilation
Animation A.10: Water concentration attributed to mist evaporation for single row of nozzles and 0.8 m/s ventilation `dmtmist-anim-08s-h2omist.mpeg`

A.2.2 0.8 m/s – double row

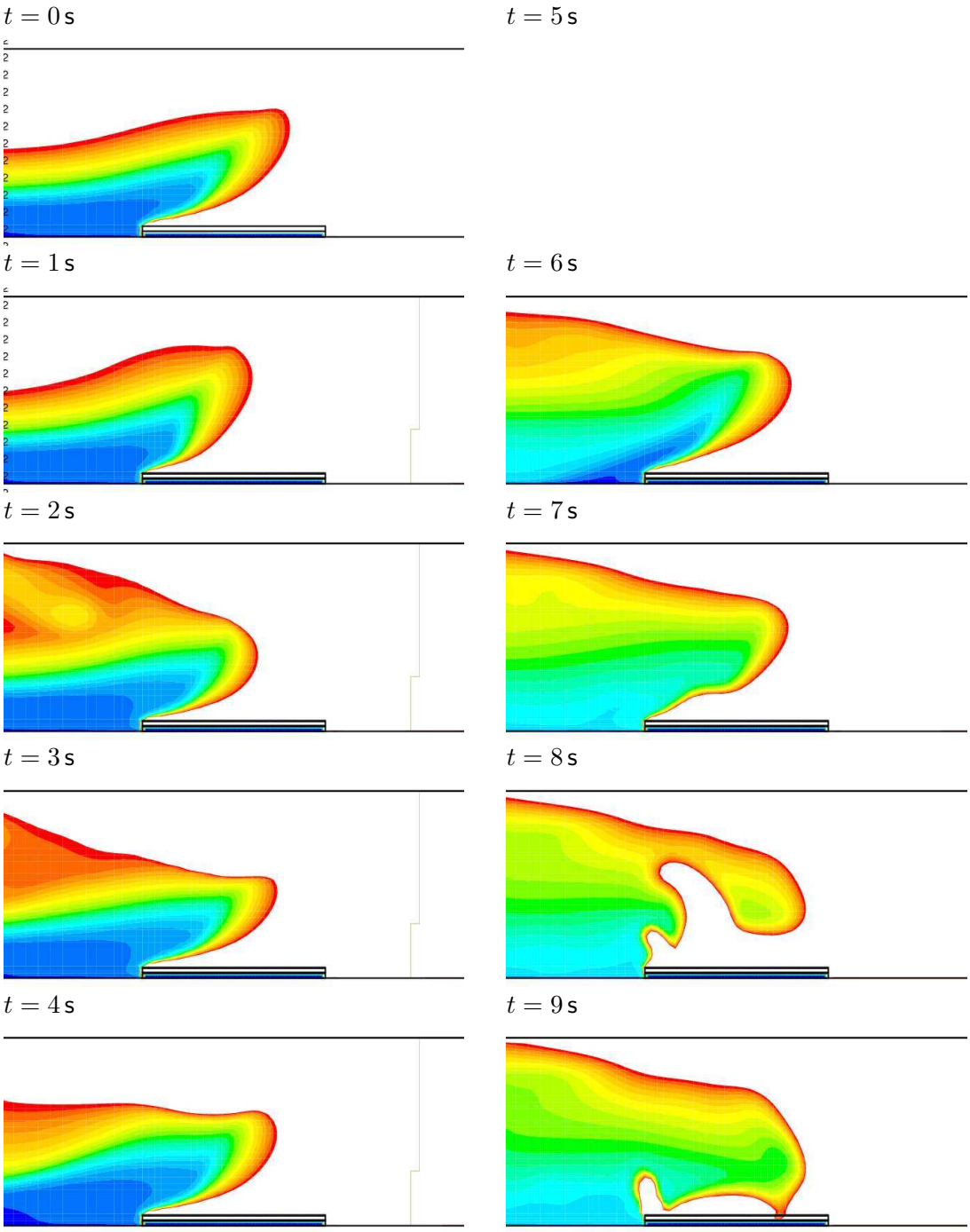

Figure A.11: Mid-plane temperatures for double row of nozzles and 0.8 m/s ventilation

Animation A.11: Mid-plane temperatures for double row of nozzles and 0.8 m/s ventilation `dmtmist-anim-08d-temp.mpeg`

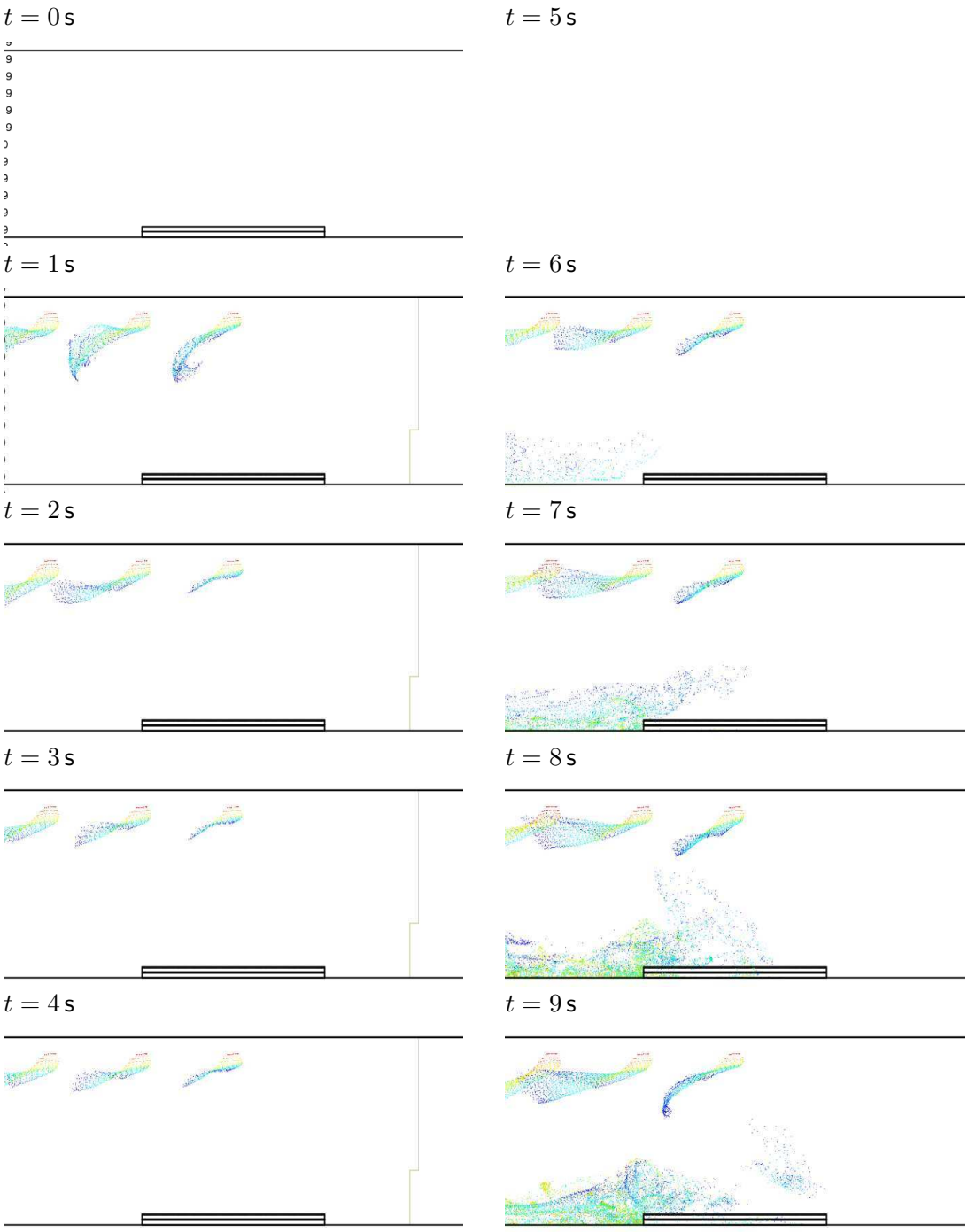

Figure A.12: Particle locations for double row of nozzles and 0.8 m/s ventilation

Animation A.12: Particle locations for double row of nozzles and 0.8 m/s ventilation
dmtmist-anim-08d-dpm.mpeg

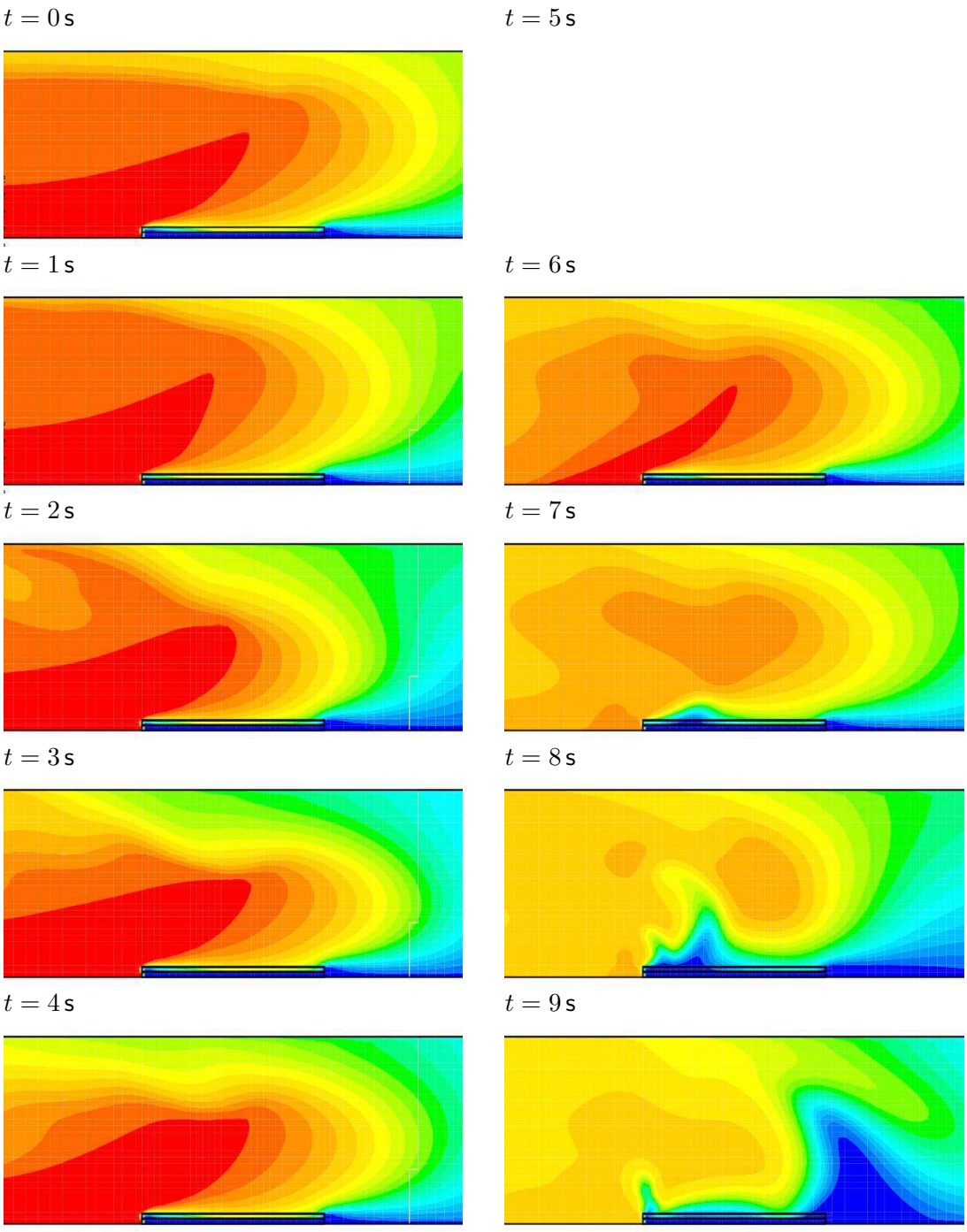

Figure A.13: Mid-pane oxygen concentration for double row of nozzles and 0.8 m/s ventilation

Animation A.13: Mid-pane oxygen concentration for double row of nozzles and 0.8 m/s ventilation `dmtmist-anim-08d-o2.mpeg`

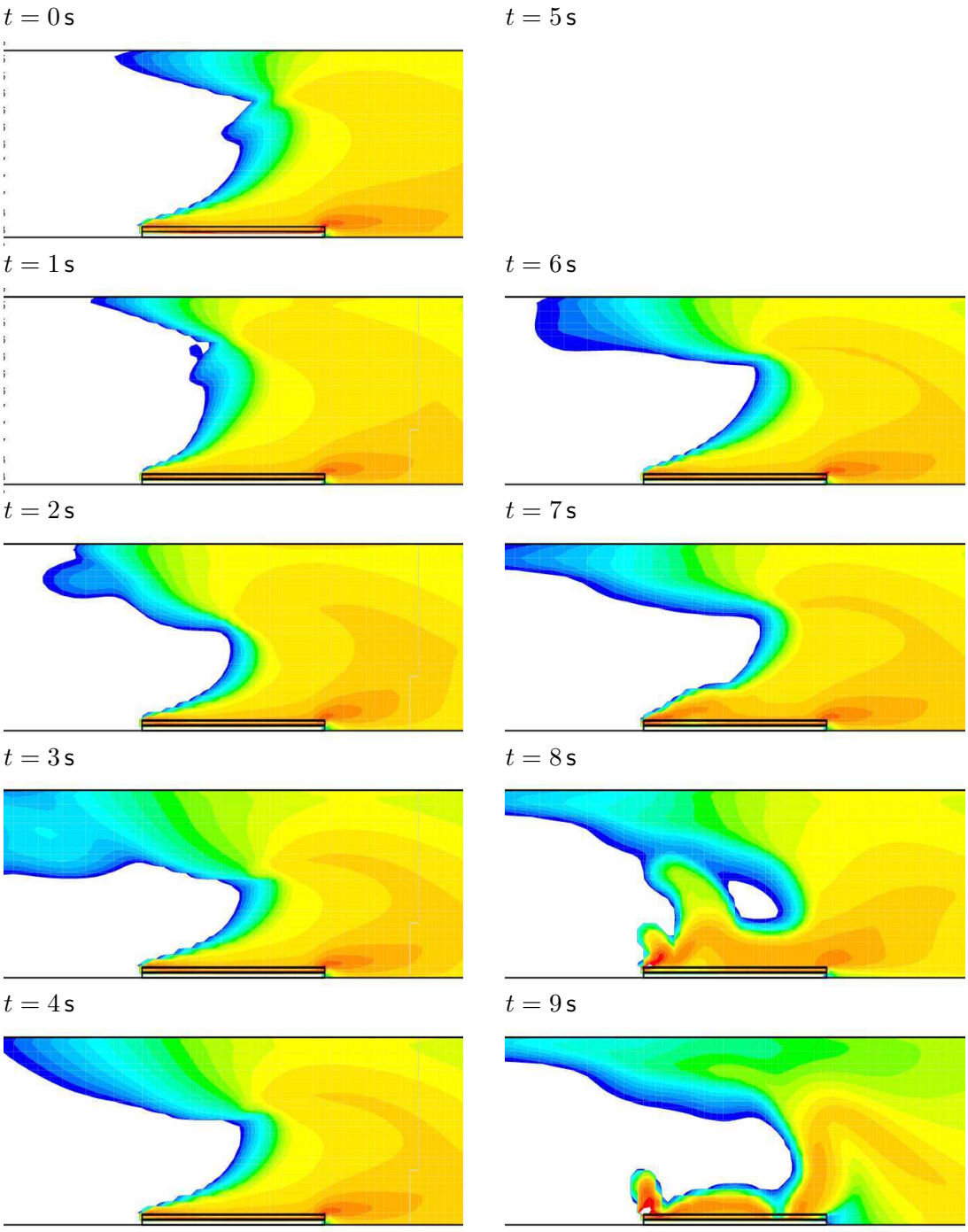

Figure A.14: Mid-plane reaction rate for double row of nozzles and 0.8 m/s ventilation

Animation A.14: Mid-plane reaction rate for double row of nozzles and 0.8 m/s ventilation `dmtmist-anim-08d-react.mpeg`

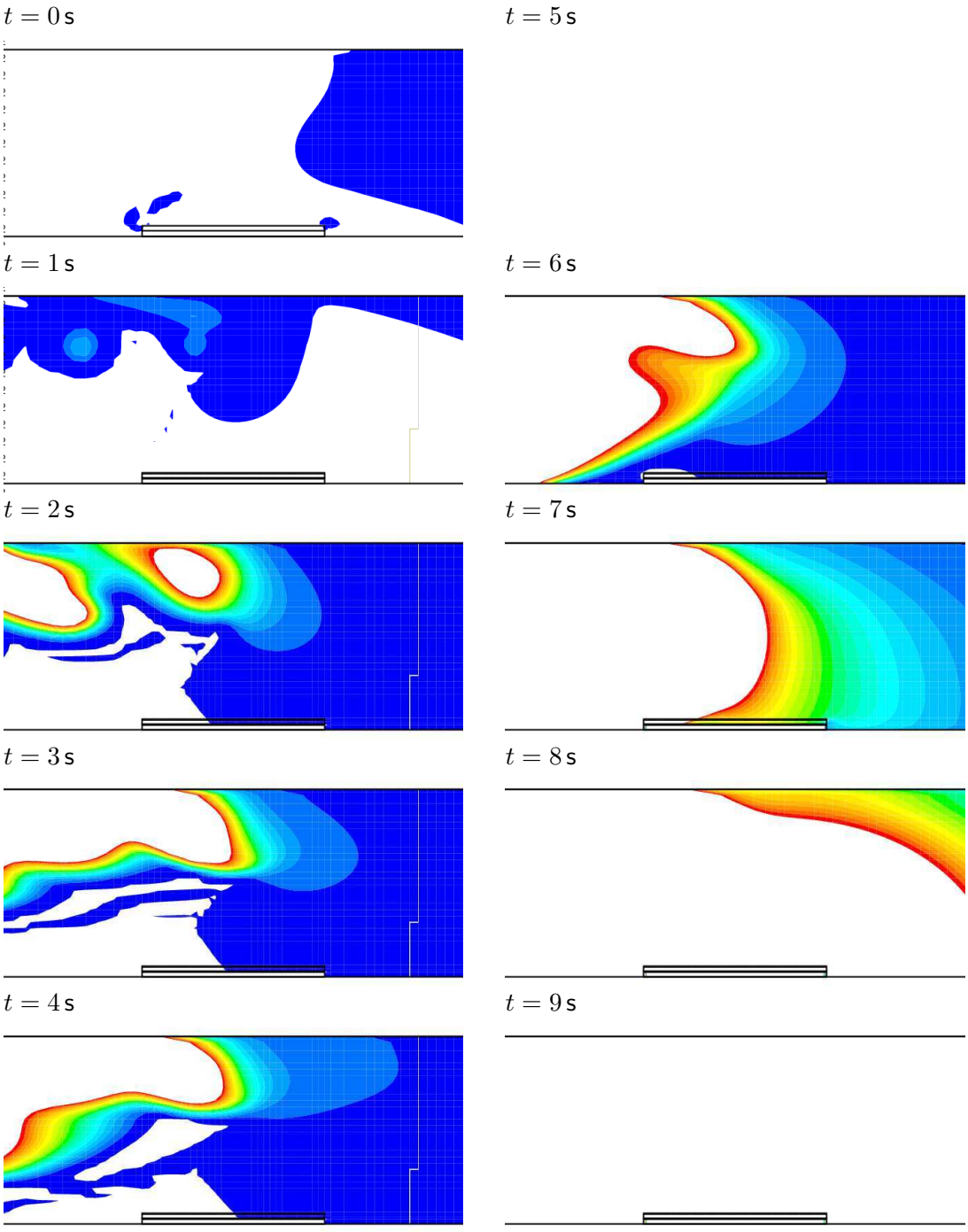

Figure A.15: Water concentration attributed to mist evaporation for double row of nozzles and 0.8 m/s ventilation

Animation A.15: Water concentration attributed to mist evaporation for double row of nozzles and 0.8 m/s ventilation `dmtmist-anim-08d-h2omist.mpeg`

A.2.3 2.4 m/s – single row

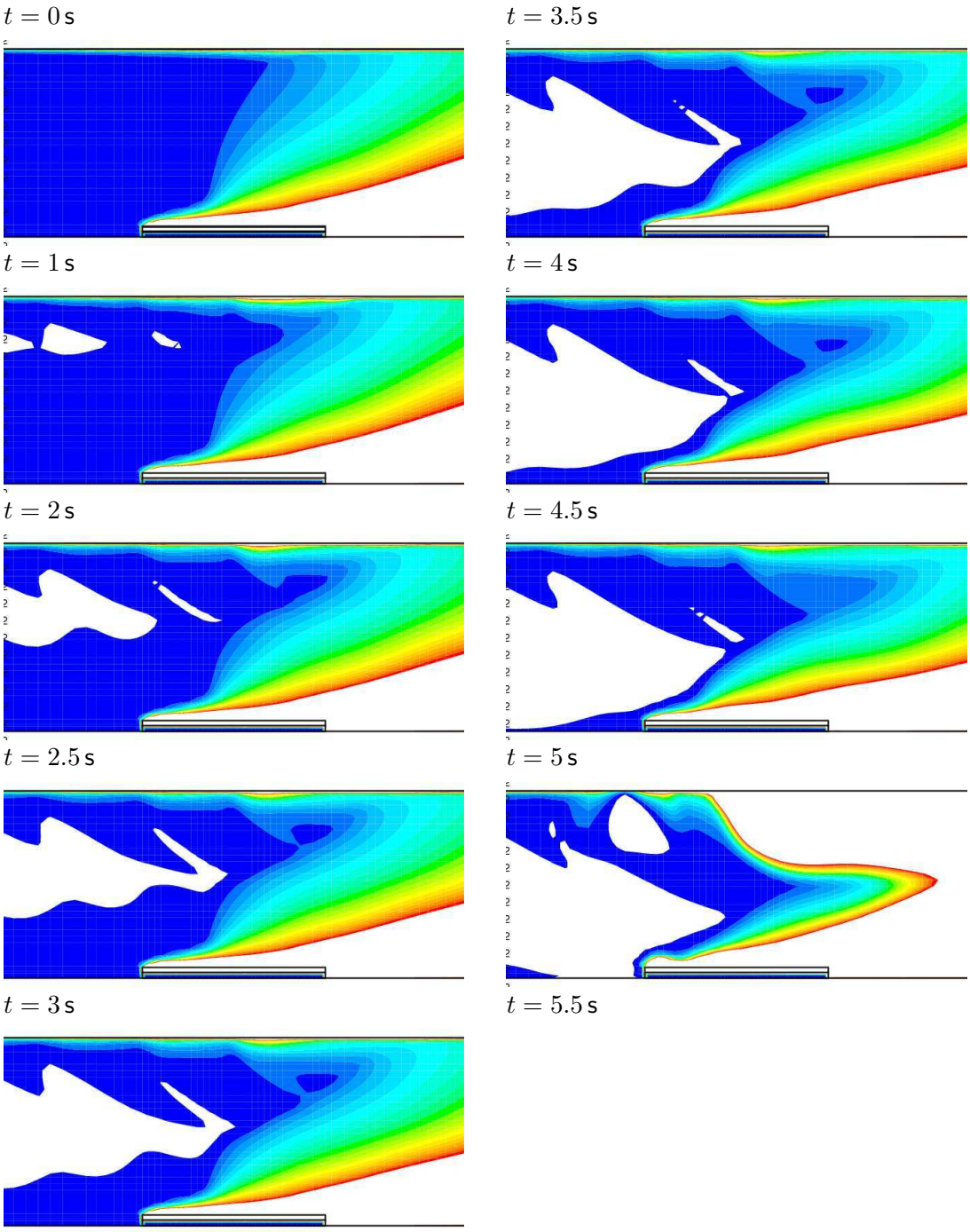

Figure A.16: Mid-plane temperatures for single row of nozzles and 2.4 m/s ventilation

Animation A.16: Mid-plane temperatures for single row of nozzles and 2.4 m/s ventilation `dmtmist-anim-24s-temp.mpeg`

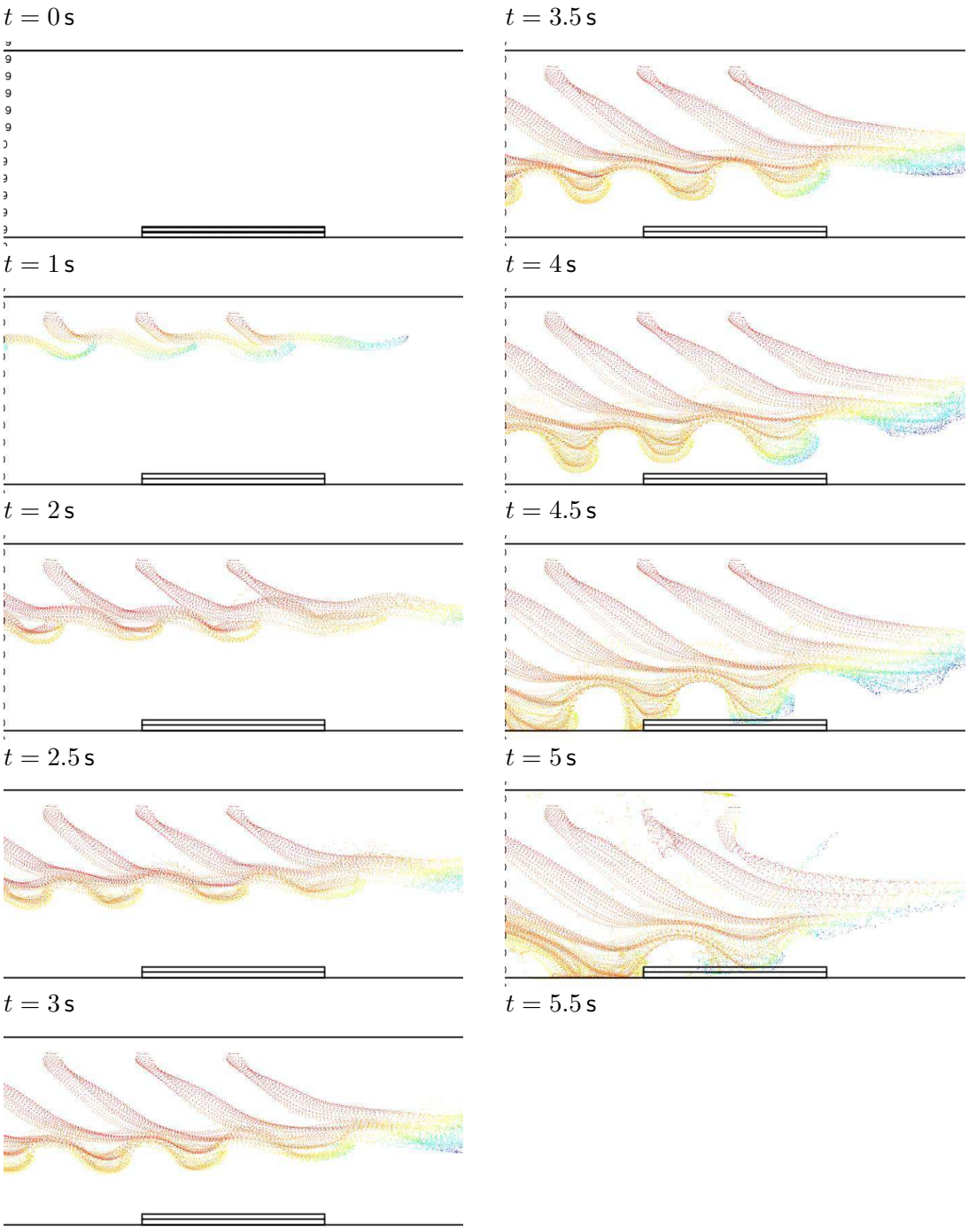

Figure A.17: Particle locations for single row of nozzles and 2.4 m/s ventilation

Animation A.17: Particle locations for single row of nozzles and 2.4 m/s ventilation
`dmtmist-anim-24s-dpm.mpeg`

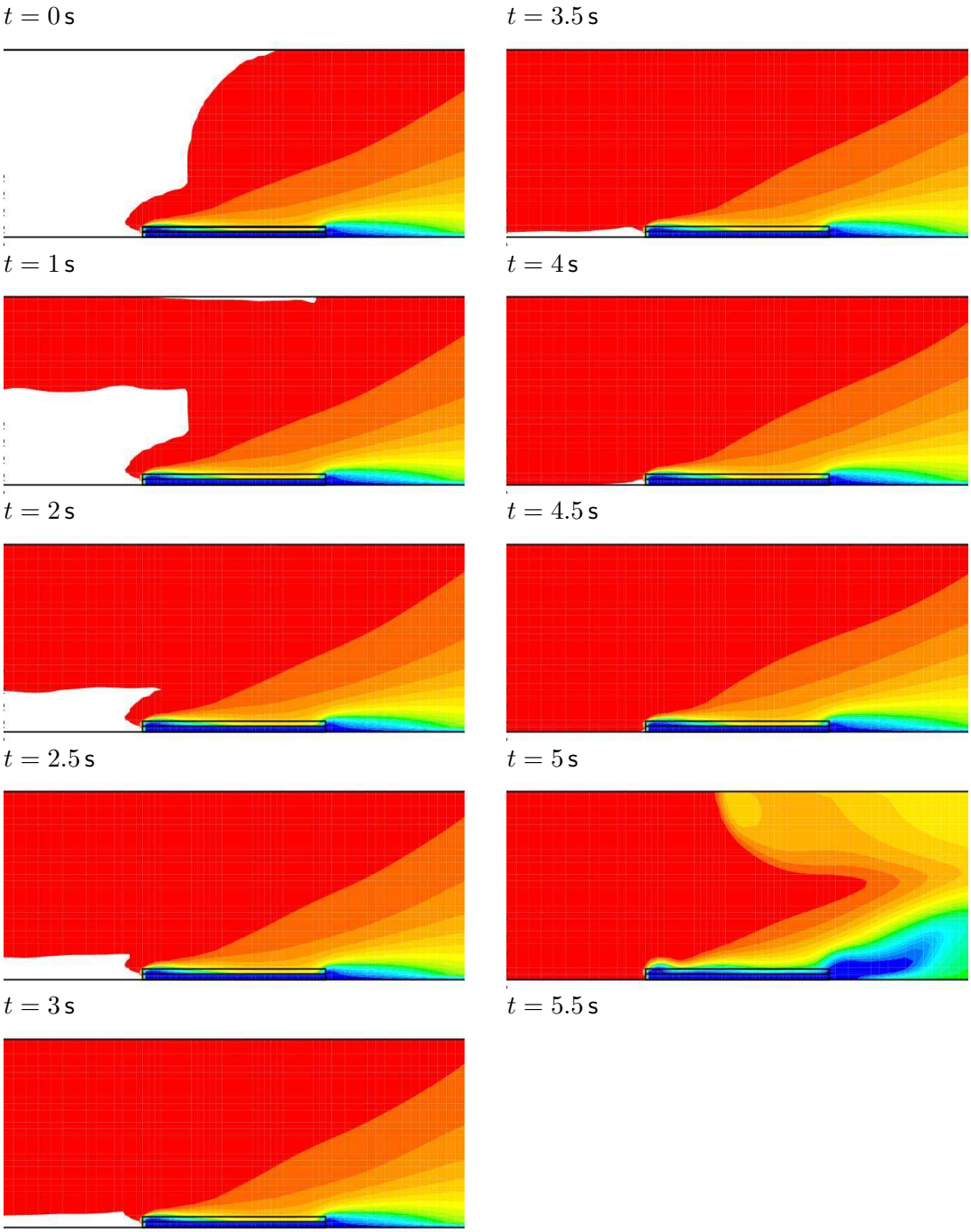

Figure A.18: Mid-pane oxygen concentration for single row of nozzles and 2.4 m/s ventilation

Animation A.18: Mid-pane oxygen concentration for single row of nozzles and 2.4 m/s ventilation `dmtmist-anim-24s-o2.mpeg`

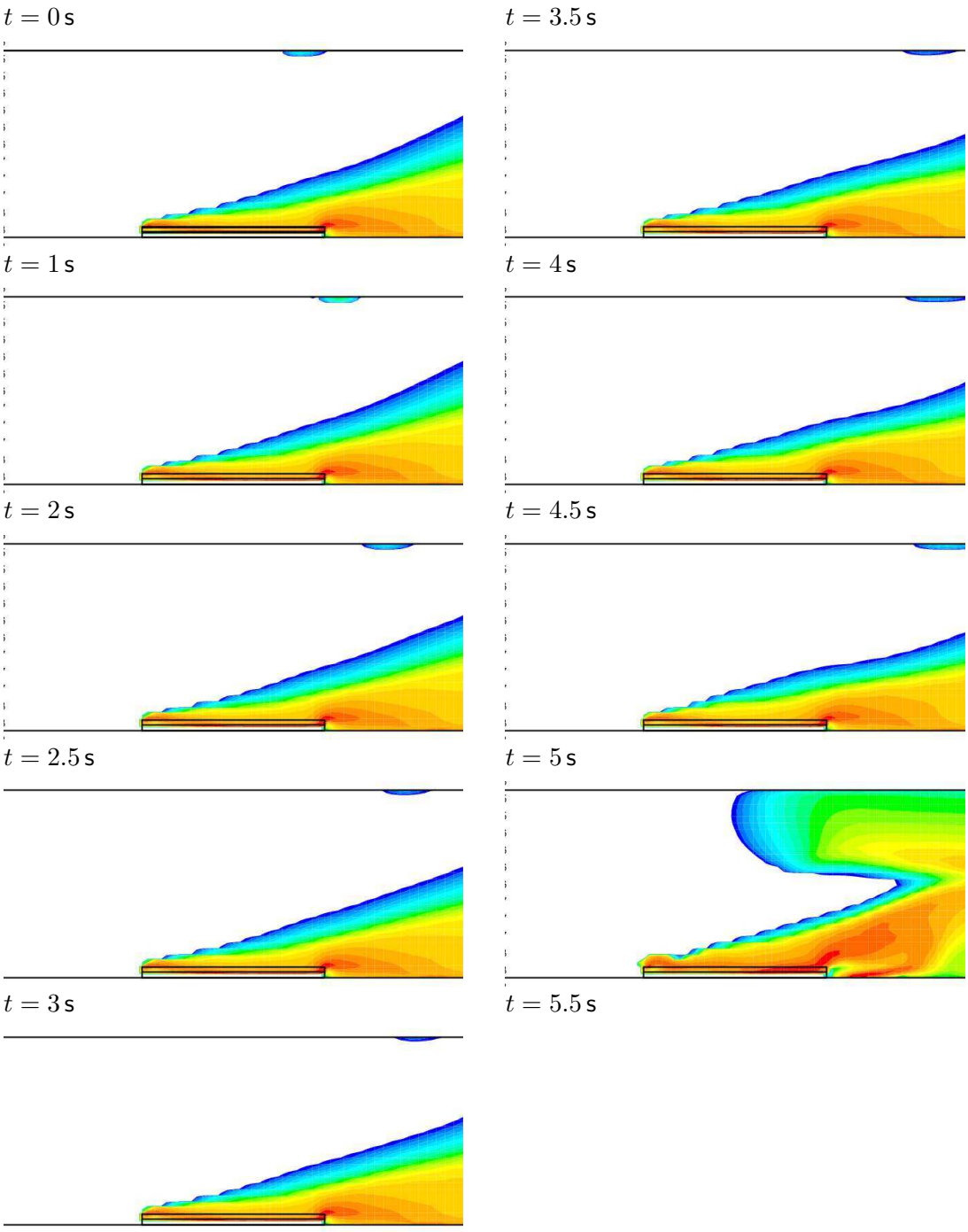

Figure A.19: Mid-plane reaction rate for single row of nozzles and 2.4 m/s ventilation

Animation A.19: Mid-plane reaction rate for single row of nozzles and 2.4 m/s ventilation `dmtmist-anim-24s-react.mpeg`

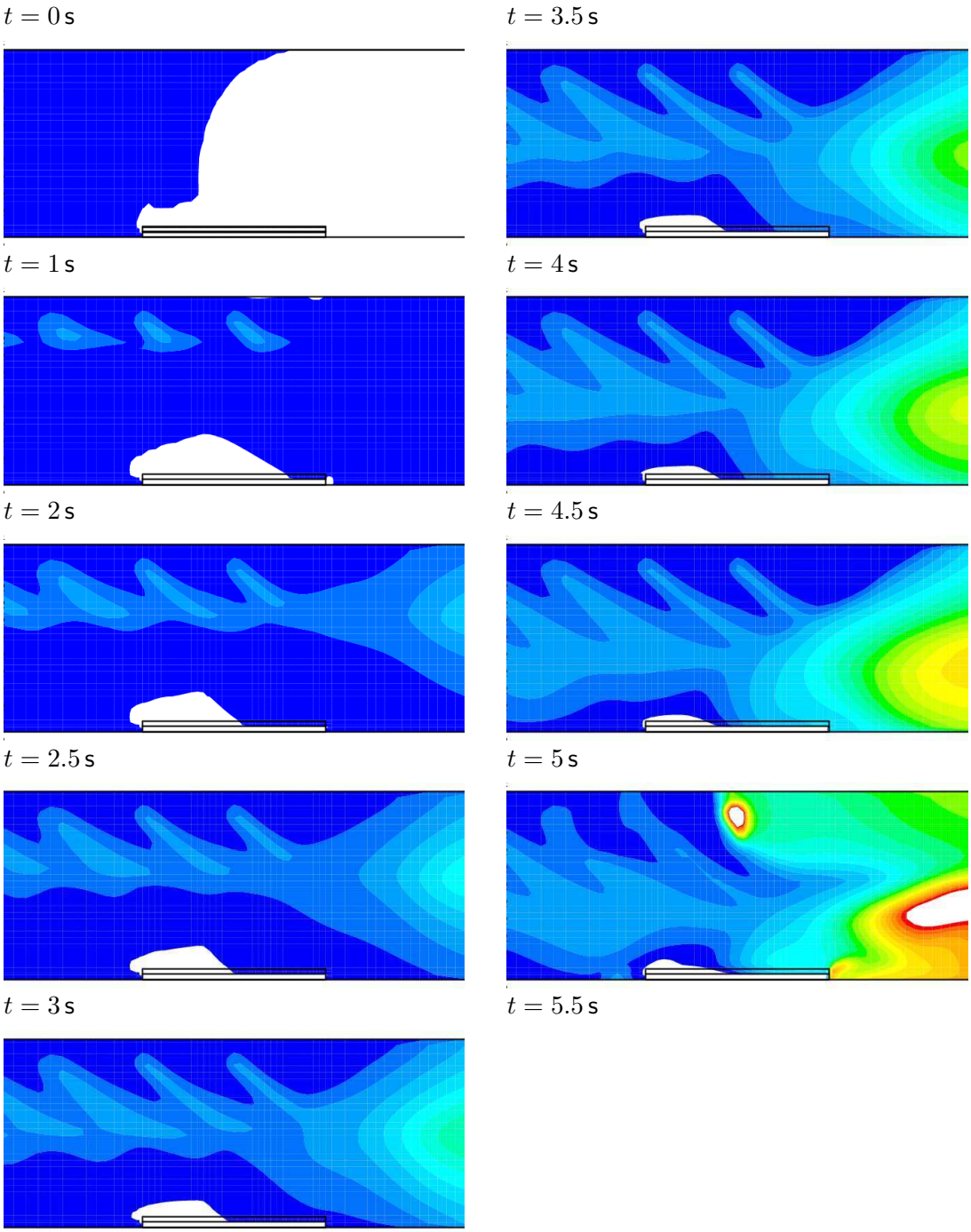

Figure A.20: Water concentration attributed to mist evaporation for single row of nozzles and 2.4 m/s ventilation
Animation A.20: Water concentration attributed to mist evaporation for single row of nozzles and 2.4 m/s ventilation `dmtmist-anim-24s-h2omist.mpeg`

A.2.4 2.4 m/s – double row

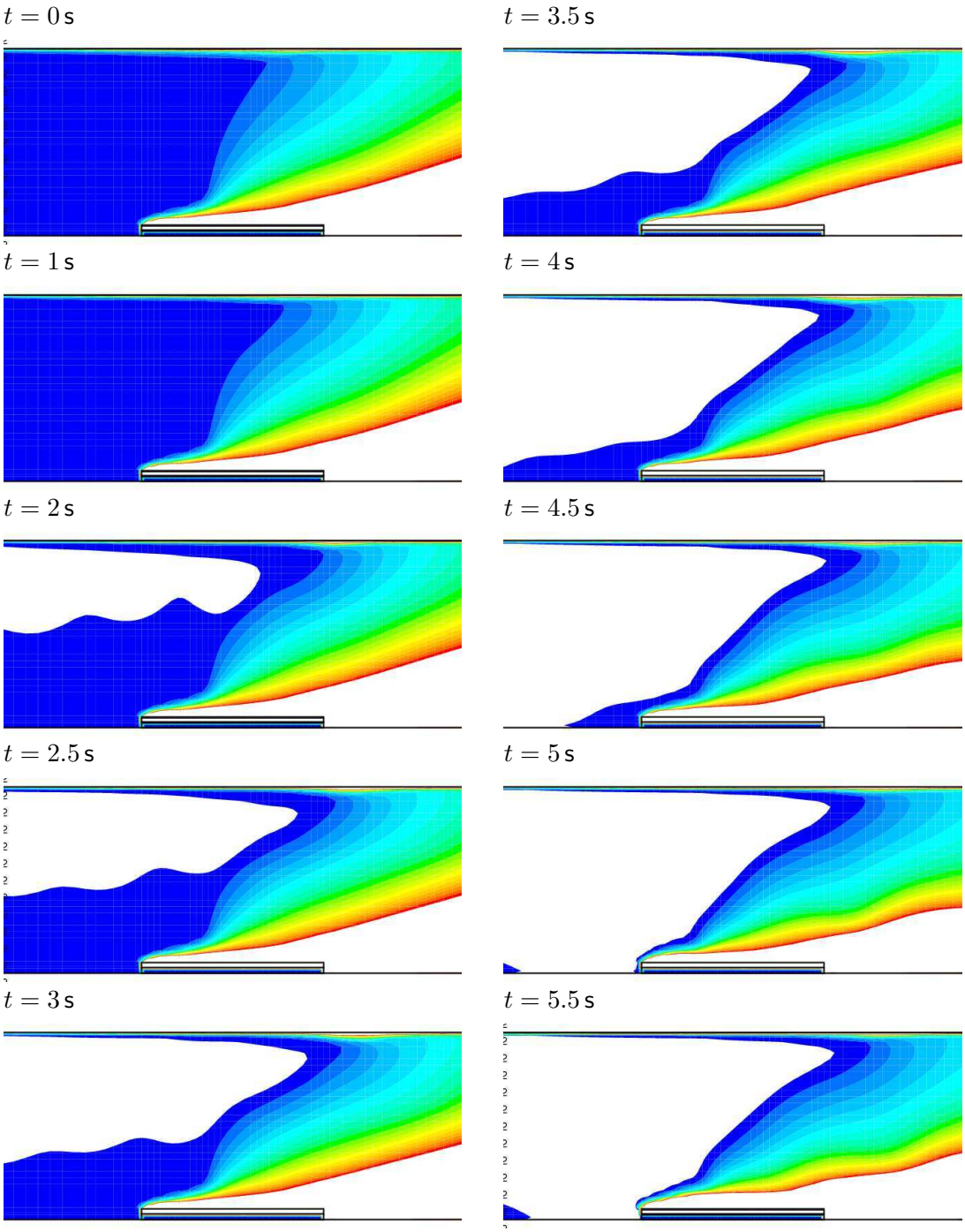

Figure A.21: Mid-plane temperatures for double row of nozzles and 2.4 m/s ventilation

Animation A.21: Mid-plane temperatures for double row of nozzles and 2.4 m/s ventilation `dmtmist-anim-24d-temp.mpeg`

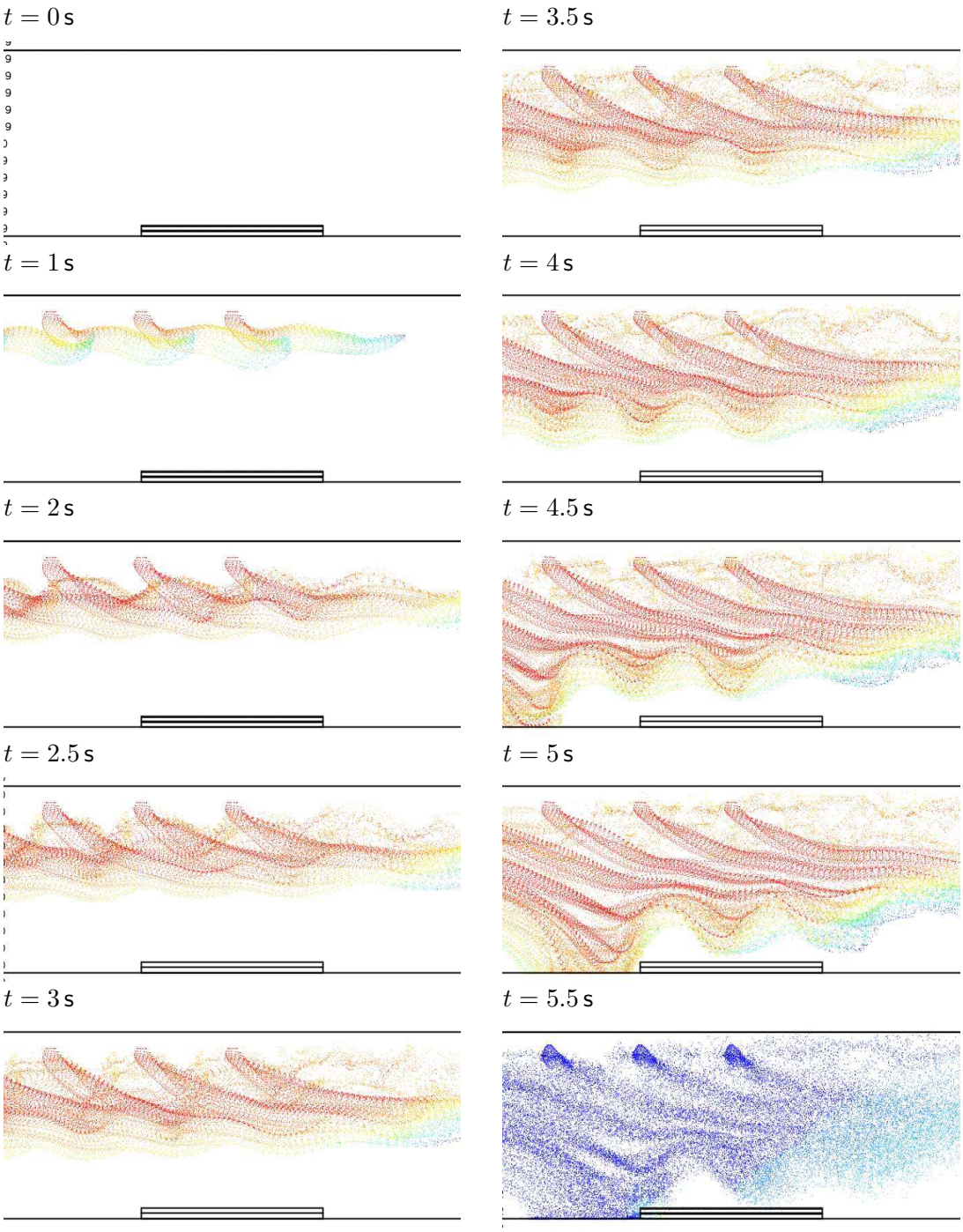

Figure A.22: Particle locations for double row of nozzles and 2.4 m/s ventilation

Animation A.22: Particle locations for double row of nozzles and 2.4 m/s ventilation

`dmtmist-anim-24d-dpm.mpeg`

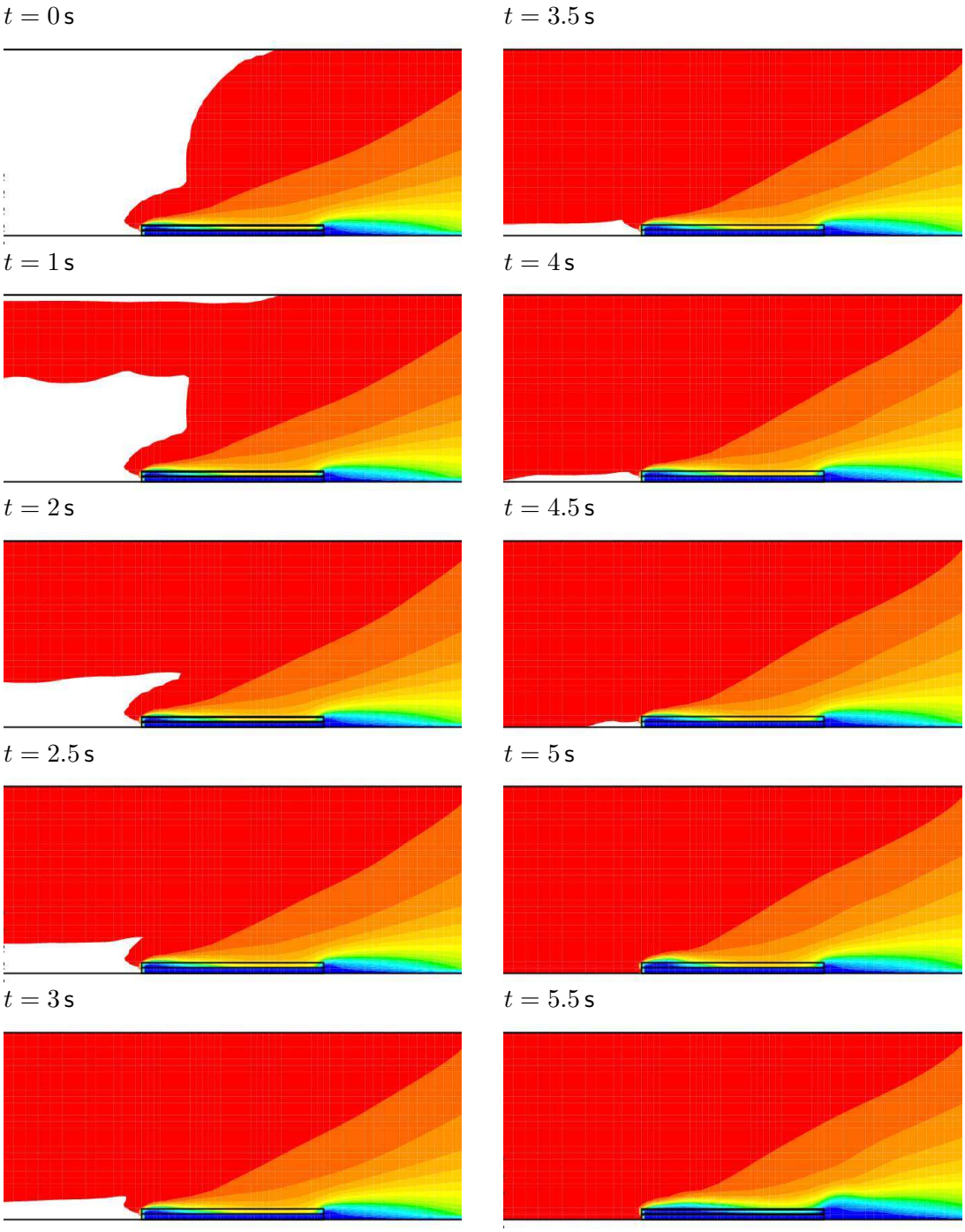

Figure A.23: Mid-pane oxygen concentration for double row of nozzles and 2.4 m/s ventilation

Animation A.23: Mid-pane oxygen concentration for double row of nozzles and 2.4 m/s ventilation `dmtmist-anim-24d-o2.mpeg`

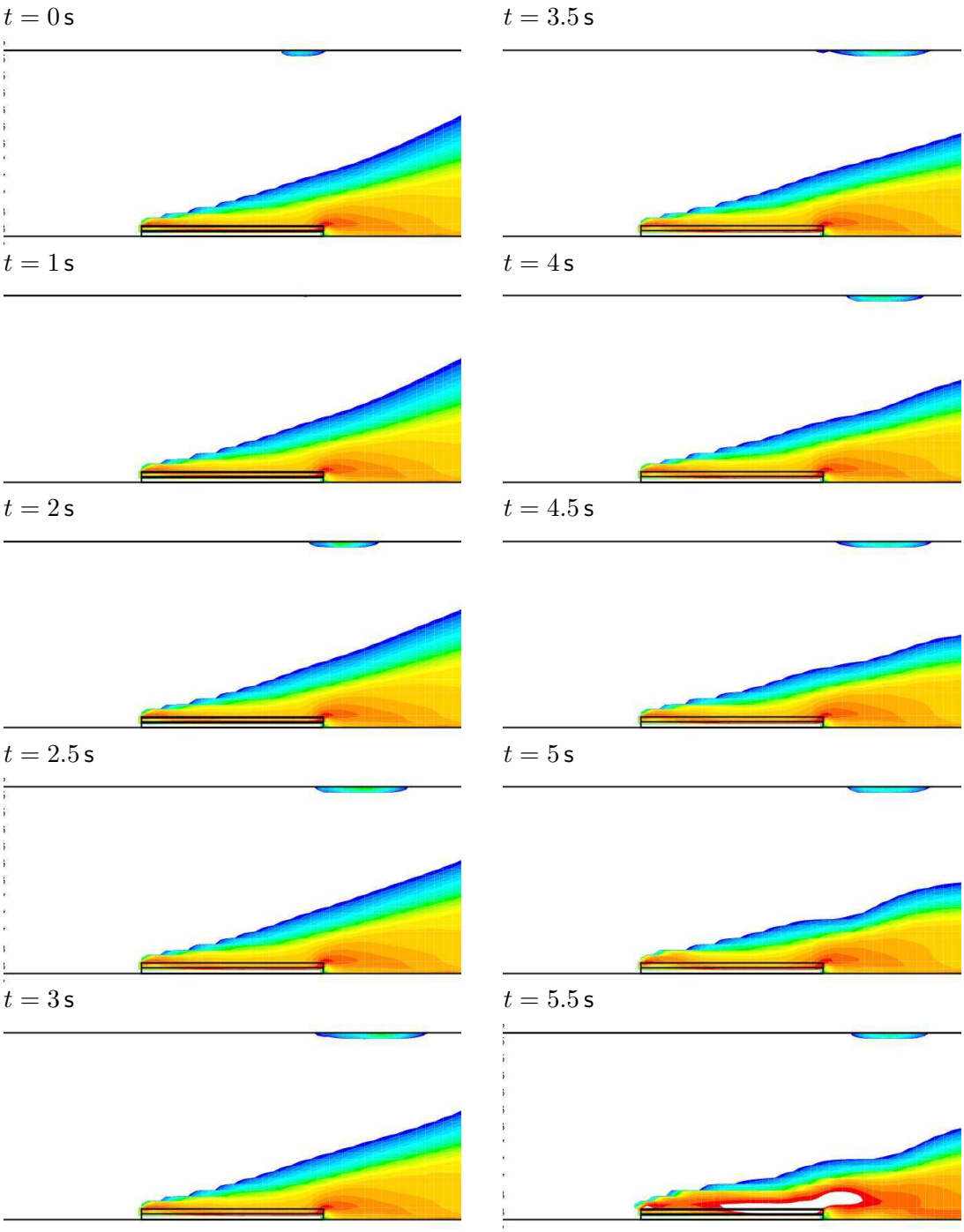

Figure A.24: Mid-plane reaction rate for double row of nozzles and 2.4 m/s ventilation

Animation A.24: Mid-plane reaction rate for double row of nozzles and 2.4 m/s ventilation `dmtmist-anim-24d-react.mpeg`

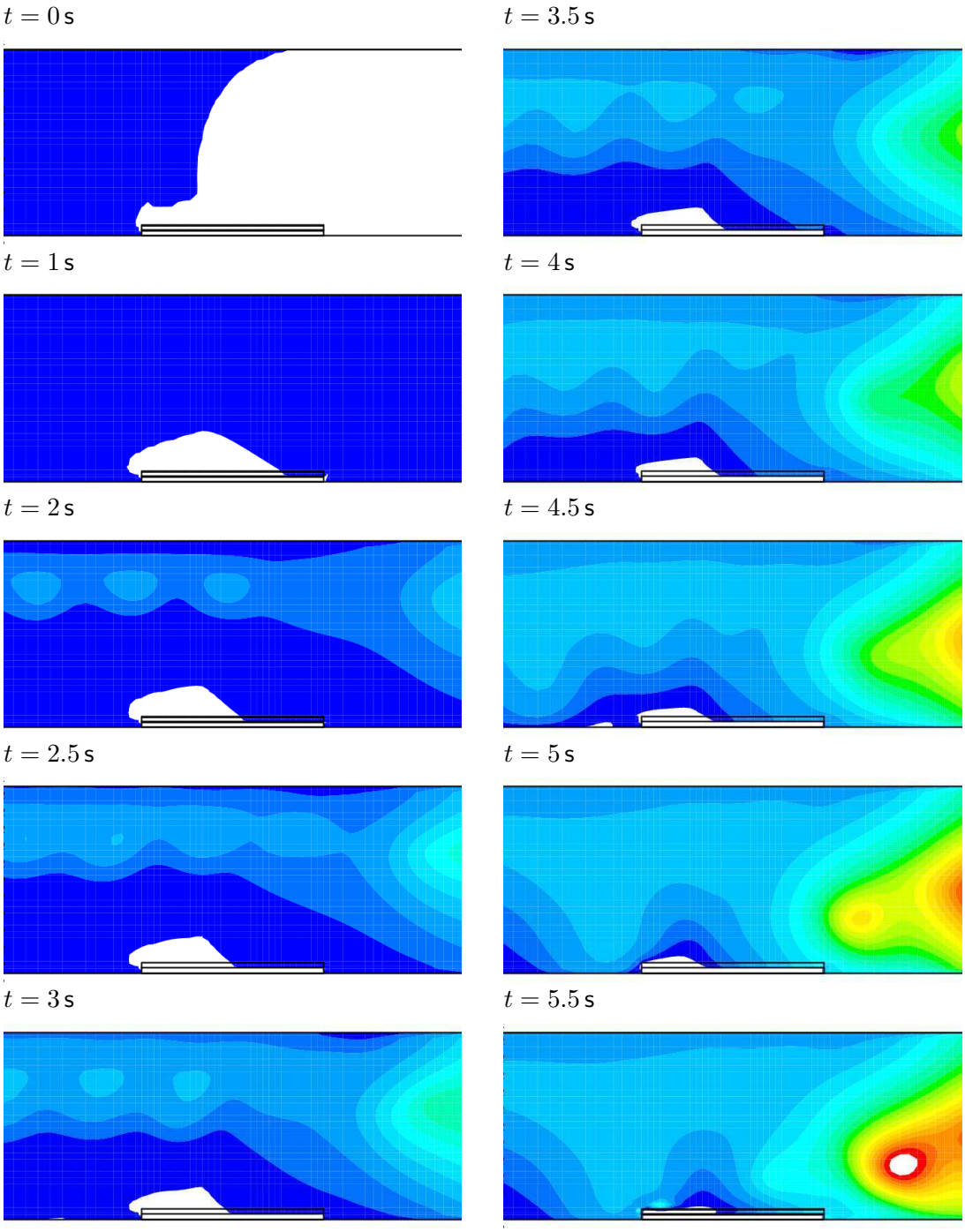

Figure A.25: Water concentration attributed to mist evaporation for double row of nozzles and 2.4 m/s ventilation

Animation A.25: Water concentration attributed to mist evaporation for double row of nozzles and 2.4 m/s ventilation `dmtmist-anim-24d-h2omist.mpeg`

Appendix B

UDF Source files

```
/************************************************************/
/* UDF for specifying a heat source term in a cuboidal zone */
/*                                                          */
/************************************************************/

#include "udf.h"
#include "defines.h"

DEFINE_SOURCE(heat_source, c, t, dS, eqn)
{
  real x[ND_ND]; /* this will hold the position vector */
  real V=DX*DY*DZ;
  C_CENTROID(x,c,t);
  if (fabs(x[0])<DX/2 && fabs(x[2])<DZ/2 && fabs(x[1]+H)<DY){
    return Q/V;
  }
  else {
    return 0.0;
  }

}
```

Figure B.1: *UDF* implementing volumetric heat source

```
#define Q 7500
#define H 0.125
#define D 0.05
#define DX D
#define DY D
#define DZ D
```

Figure B.2: Typical `defines.h` for volumetric heat source

```
#include "udf.h"

DEFINE_PROFILE (inlet_parabolic_ramp, thread, nv)
{
  face_t f;
  real t = RP_Get_Real ("flow-time");
  real tn;
  begin_f_loop (f, thread)
  {
    if (t < 0.05)
      {
        F_PROFILE (f, thread, nv) = 0.0;
      }
    else if (t < 5.0)
      {
        tn = (t / 5.0);
        F_PROFILE (f, thread, nv) = tn * tn;
      }
    else
      {
        F_PROFILE (f, thread, nv) = 1.0;
      }
  }
  end_f_loop (f, thread)
}
```

Figure B.3: *UDF* implementing parabolic boundary condition used to control fire growth

```
/* Monitor total rate of reaction and modify diffusivity value
 * periodically. reaction rate is read in from Fluent output
 * files, which must be set up in case file.
 */

DEFINE_EXECUTE_AT_END(read_greact)
{
  b = getcurrentrate();   /* get rate from solver output file */
  t = getcurrenttime();   /* get time from solver */
  k = 0.5;                /* underrelaxtion factor */

  ratio_capped = ratio = 1.0 + k * (b / TARGETRATE - 1.0);
  if (ratio>1.5)  ratio_capped = 1.5;
  if (ratio<0.66) ratio_capped = 0.66;

  /* only set value after initial "ramp" phase, and maximum of
   * once every 5 timesteps
   */

  if(lock){
    lock--;
  } else if(t>TLOCKED) {
    /* set the new value */
    myval /= ratio_capped;

    /* apply MINVAL and MAXVAL limits to value */
    if(myval>MAXVAL) myval=MAXVAL;
    if(myval<MINVAL) myval=MINVAL;

    lock=4;
  }

  /* log everything to screen and file */
  writelog(b, ratio, ration_capped, myval, lock);
}
```

Figure B.4: Extract of *UDF* implementing a negative feedback loop to reach a target rate of reaction by adjusting the diffusivity value

Appendix C

Enclosure fire model

C.1 Time step independence

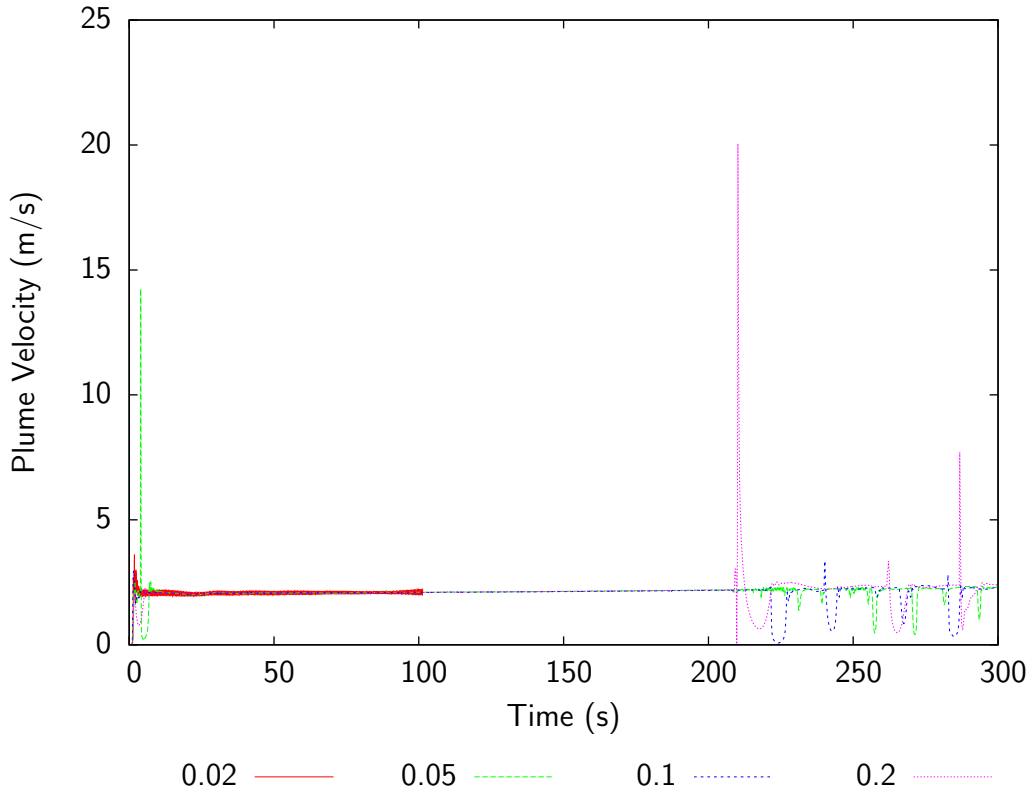

Figure C.1: Plume velocity for different time step sizes

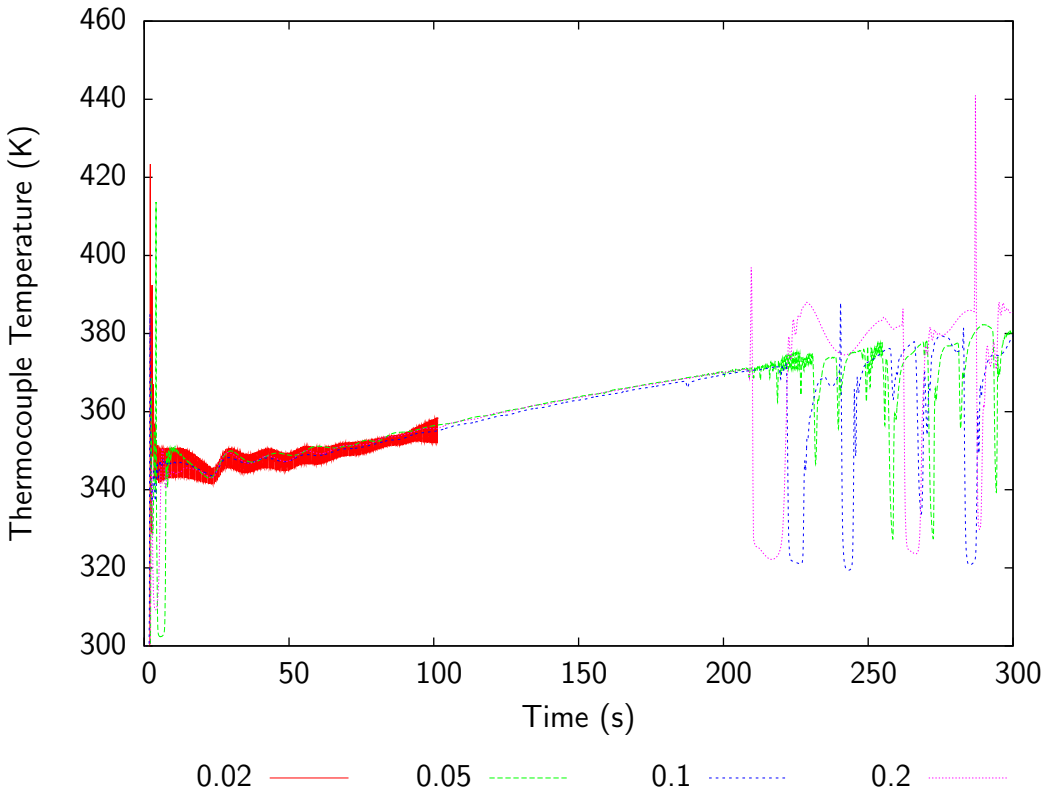

Figure C.2: Thermocouple temperature for different time step sizes

C.2 Three dimensional

C.2.1 Parameter sensitivity

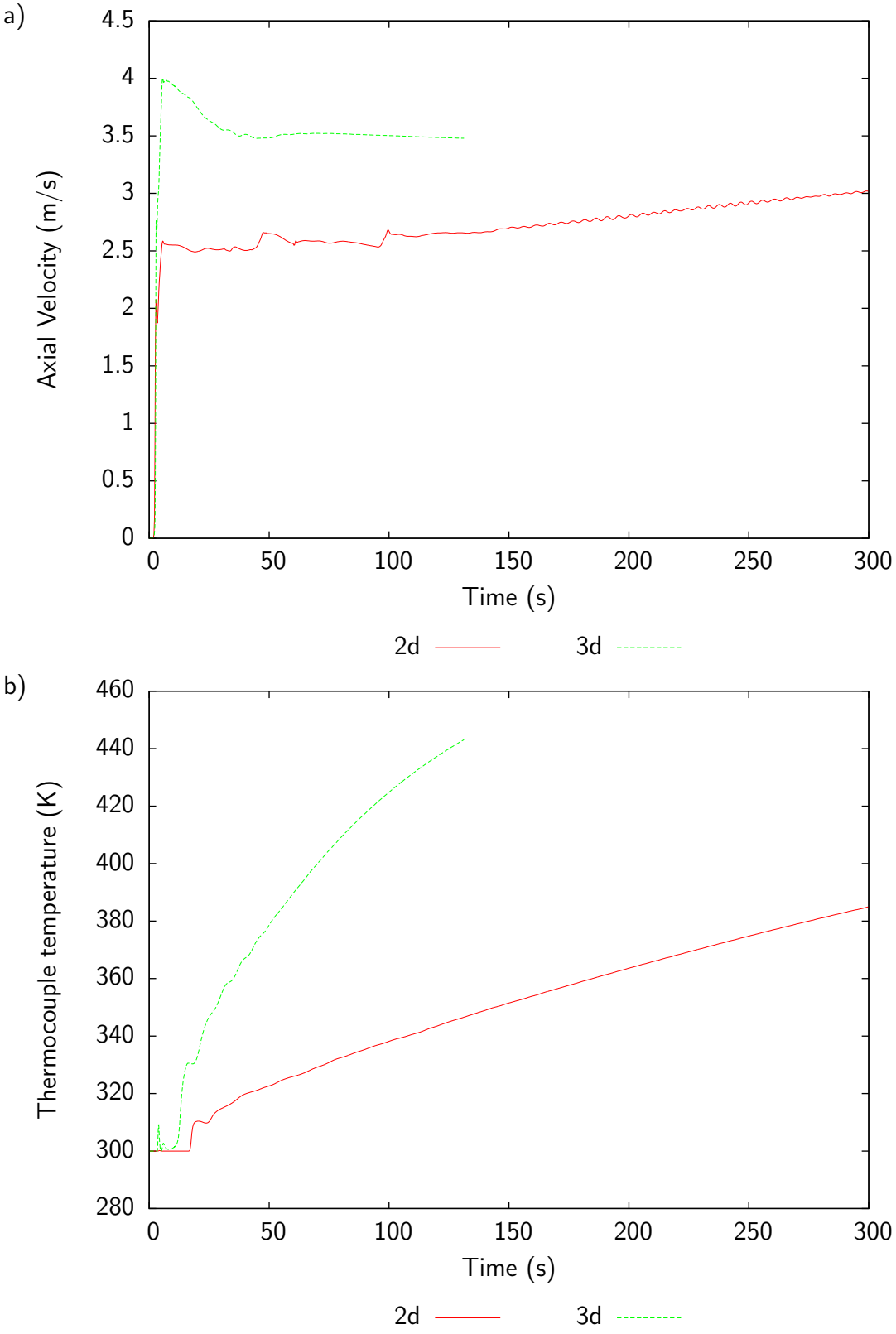

Figure C.3: Comparison of 2D and 3D model for enclosure fire
a) Plume Velocity b) Thermocouple $R = 0.5\,\mathrm{m}$ temperature

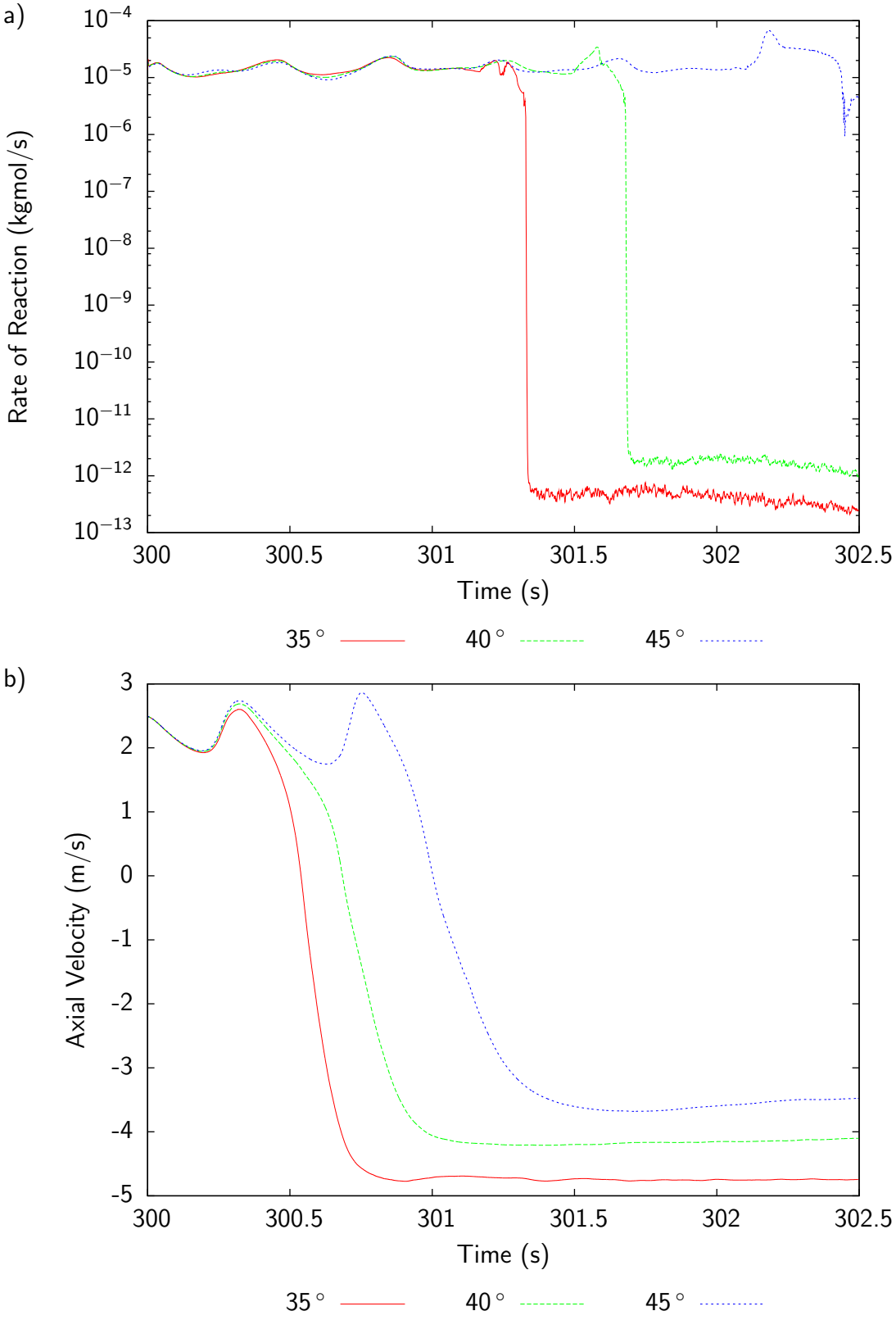

Figure C.4: Effect of variation of injection cone angle
a) Rate of reaction b) Plume velocity

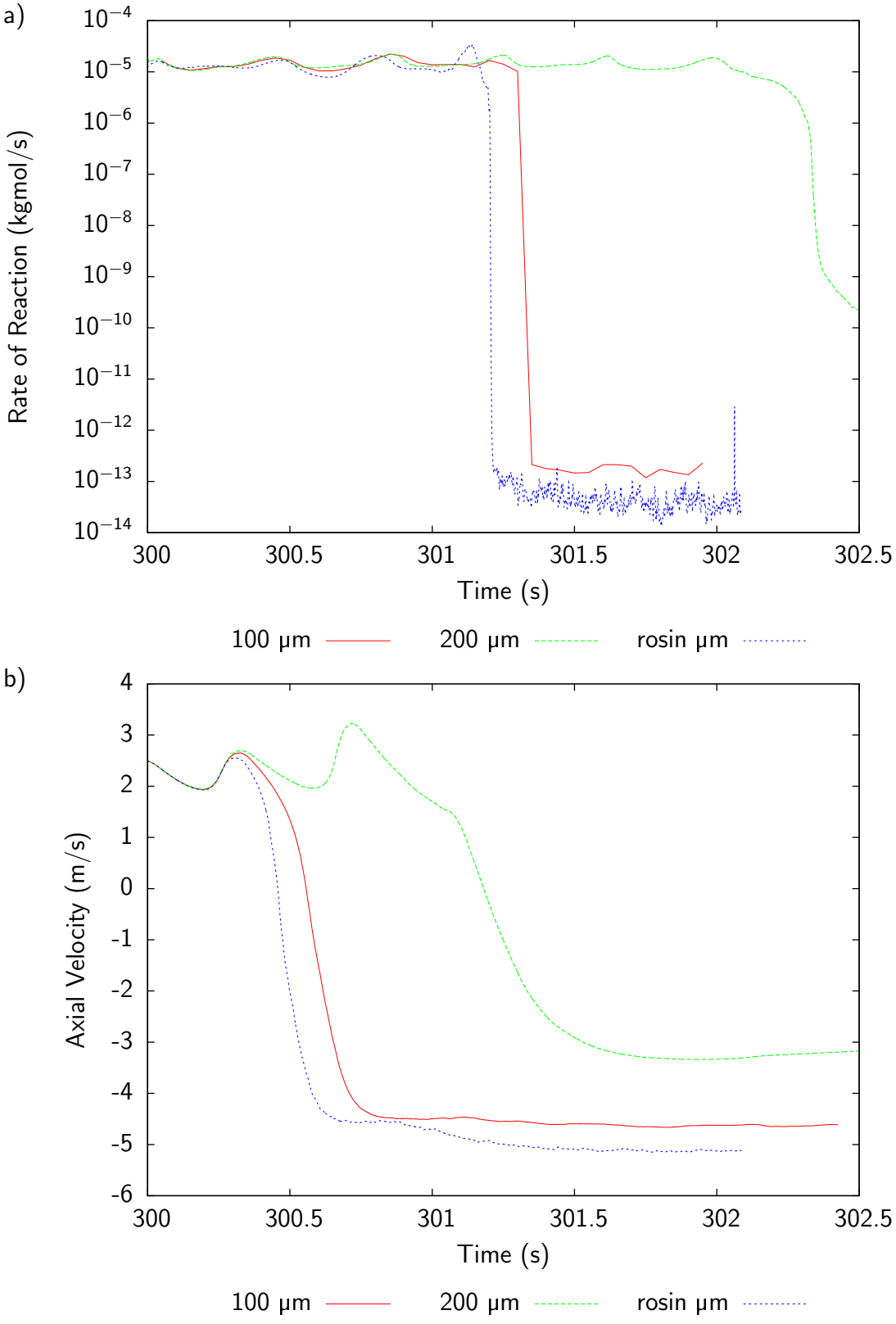

Figure C.5: Effect of variation of droplet diameter
a) Rate of reaction b) Plume velocity

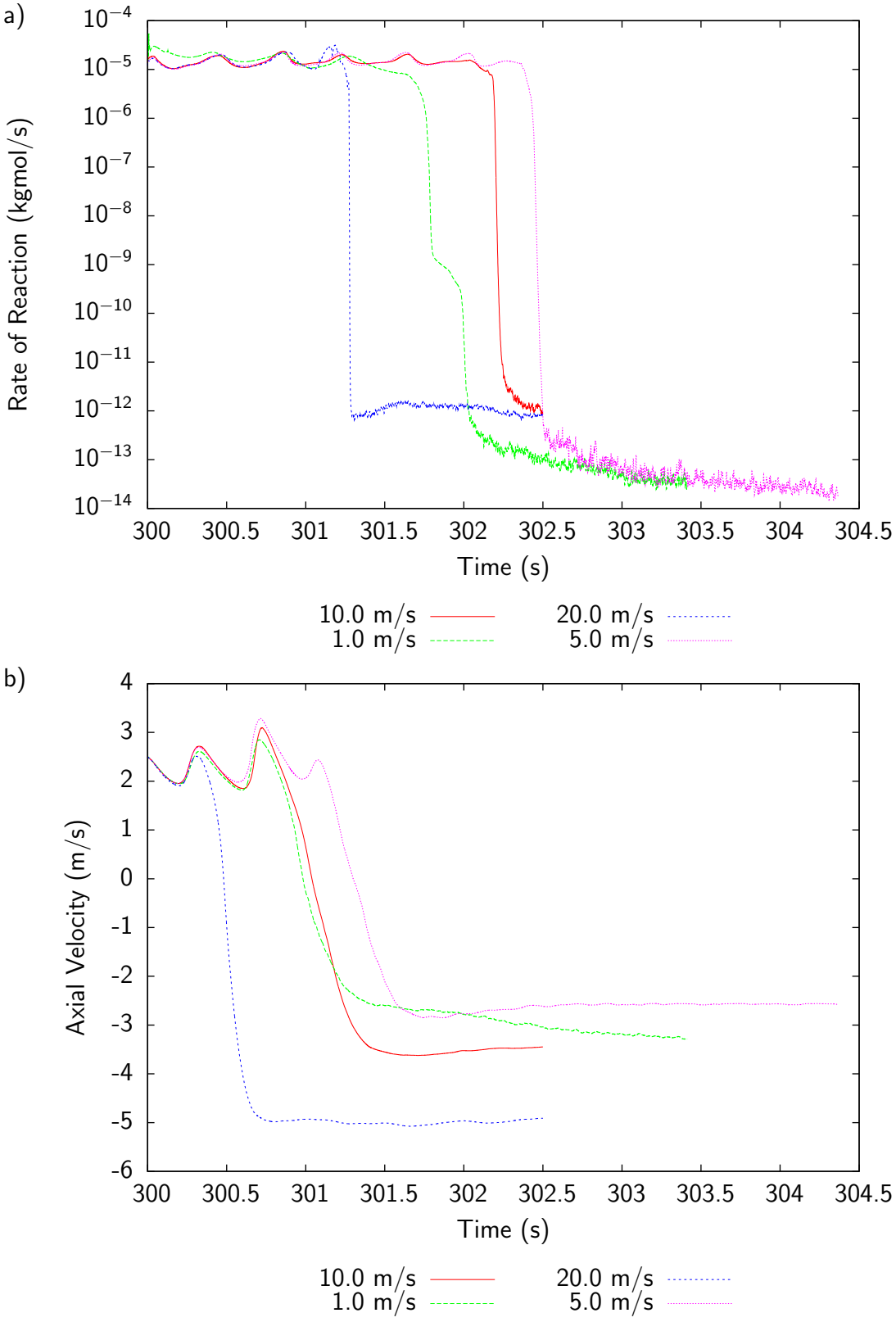

Figure C.6: Effect of variation of injection velocity
a) Rate of reaction b) Plume velocity

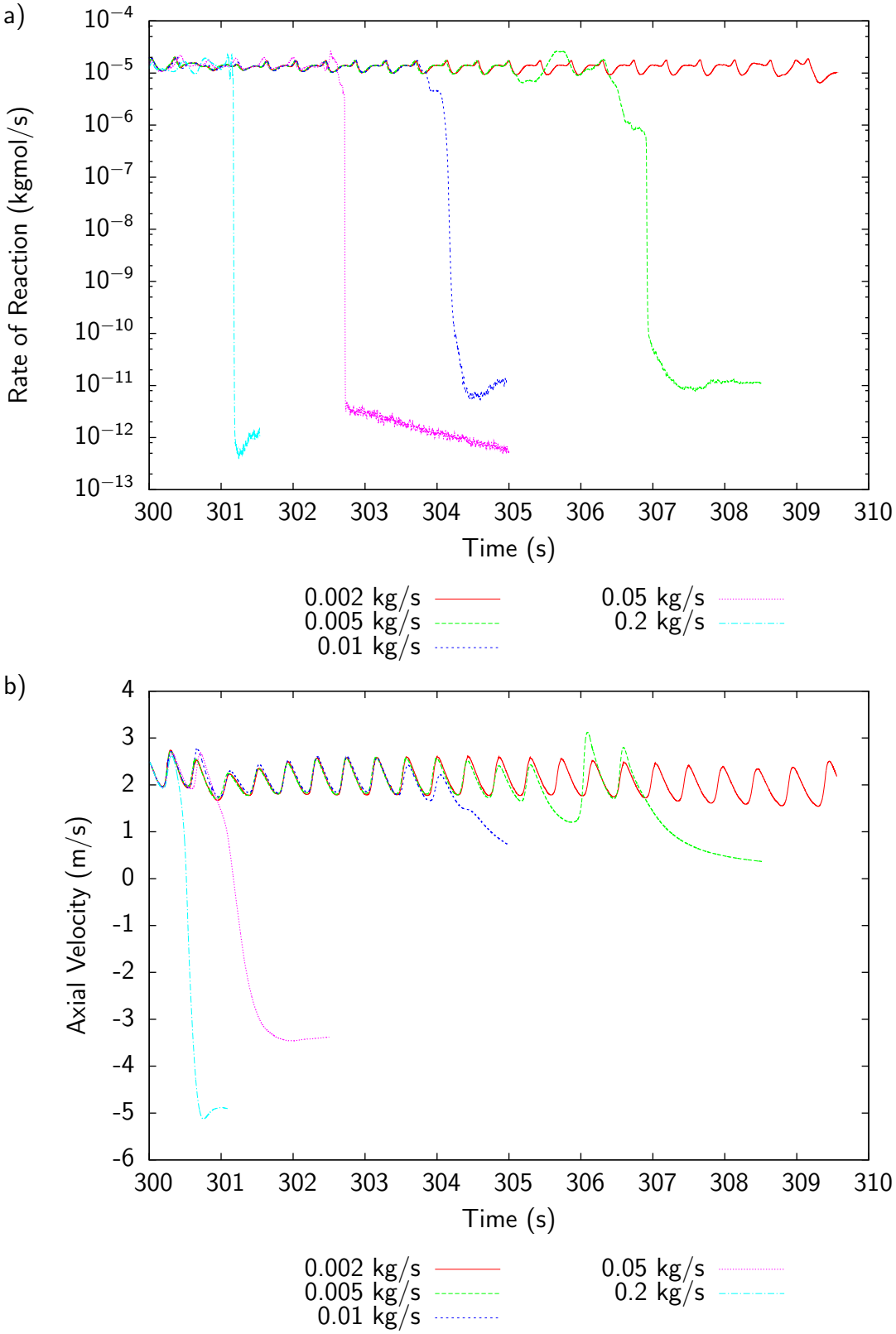

Figure C.7: Effect of variation of mist flow rate
a) Rate of reaction b) Plume velocity

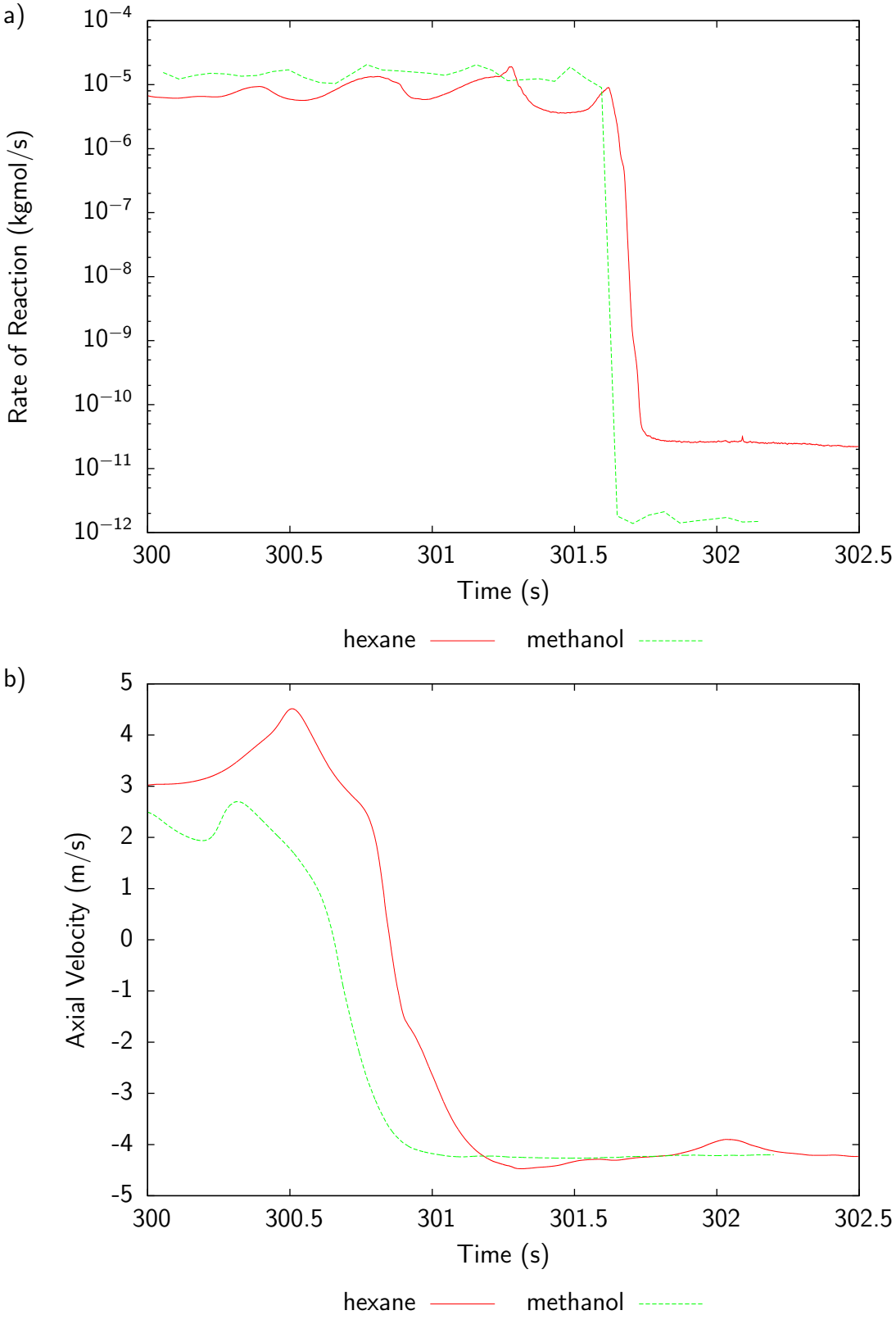

Figure C.8: Effect of fire size
a) Rate of reaction b) Plume velocity

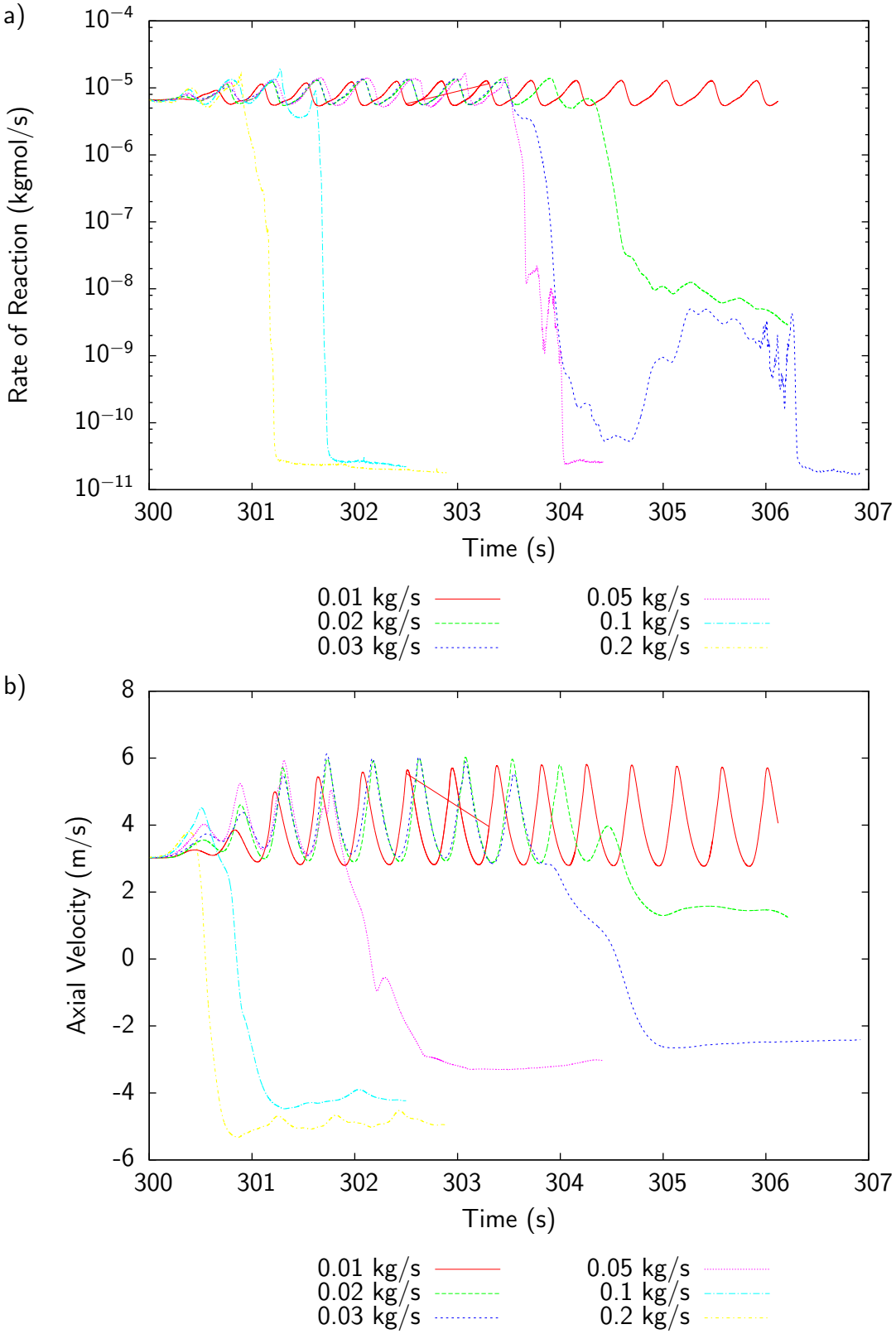

Figure C.9: Effect of variation of mist flow rate (hexane fire)
a) Rate of reaction b) Plume velocity

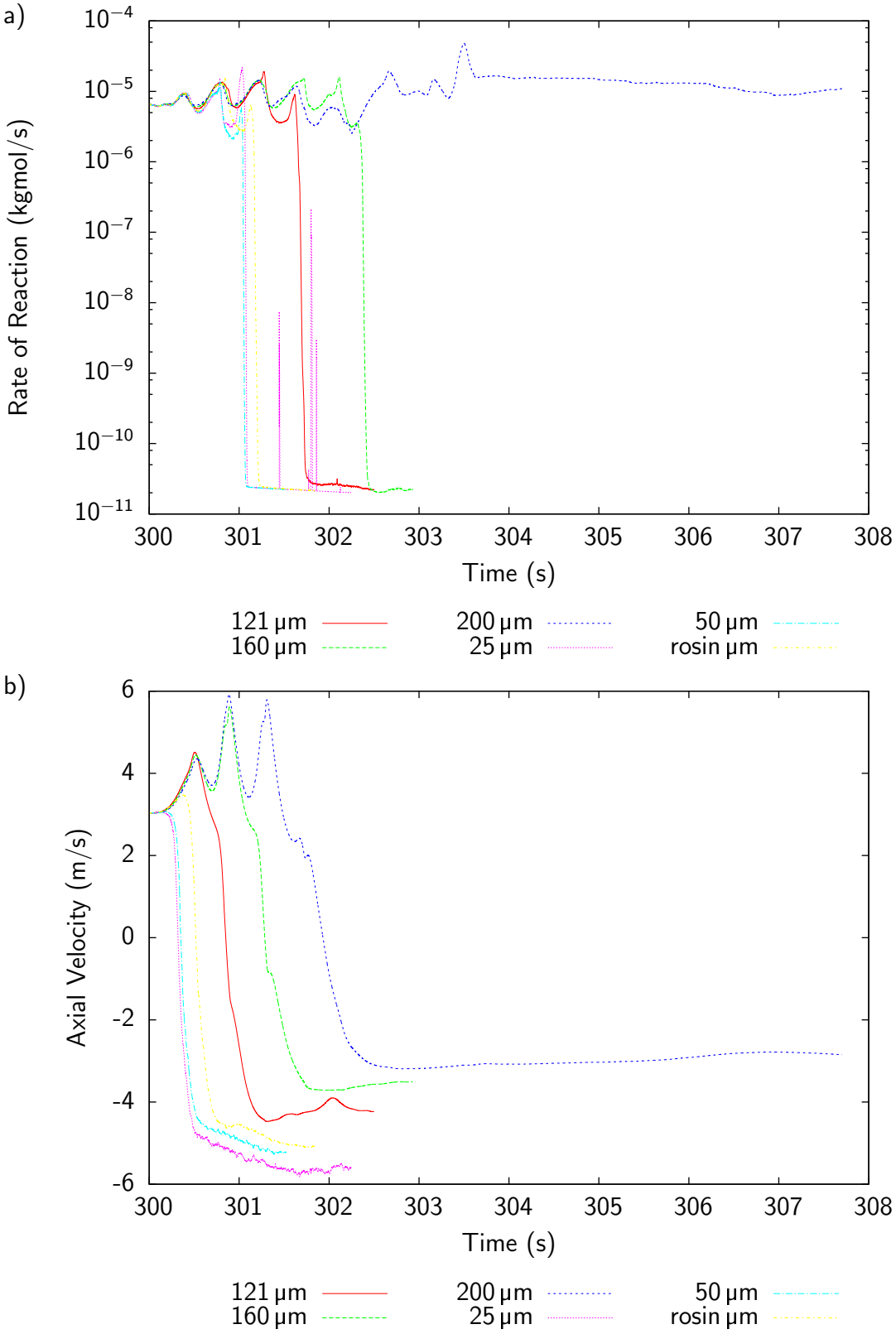

Figure C.10: Effect of variation of droplet diameter (hexane fire)
a) Rate of reaction b) Plume velocity

Appendix D

Tunnel fire

D.1 Experimental data

The data in Tables D.1– D.8 are taken from DMT et al. (2004a). The *top* and *bottom* thermocouples were located approximately 10 cm from the ceiling and floor of the galleries respectively.

Data for tests at 1.2 m/s and 1.8 m/s is not available in the original report. An attempt has been made to obtain this data from DMT et al. directly and a response is awaited.

Table D.1: Peak experimental thermocouple temperatures measured for Fire Gallery 1

Position (m)	Temperature (°C) Top	Middle	Bottom
-45	20	20	20
-25	50	20	20
-5	250	60	40
-2	800		
4	720	720	400
13	400	400	300
47	250	250	120
75	160	160	100
125	100	100	70
175	60	60	40
248	40	40	30

Table D.2: Peak experimental thermocouple temperatures measured for Fire Gallery 3

Position (m)	Temperature (°C) Top	Middle	Bottom
-89	10	10	10
-79	15	15	15
-64	100	40	35
-49	120	60	40
-34	160	90	40
-19	240	100	40
-4	380	240	40
-1	430	200	700
2	540	590	1050
5	470	300	100
8	360	220	80
11	320	200	70
14	300	260	100
17	280	240	80
20	270	230	80
23	250	220	80
26	240	200	80
29	240	200	80
56	180	160	60
86	140	140	60
116	120	120	60
146	100	100	50
176	80	80	40
201	30	30	30

Table D.3: Peak experimental thermocouple temperatures measured for Tremonia upward

Position (m)	Temperature (°C) Top	Middle	Bottom
-110	20	20	20
-85	20	20	20
-55	20	20	20
-25	20	20	20
-7	30	30	30
-4	120	50	30
-1	440	230	1050
2	500	650	900
5	480	220	60
8	400	200	40
11	370	190	40
14	340	180	40
17			
35	260	40	20
59	200	100	60
62			
65	180	140	70
68	180	140	60
71	170	150	60
74	160	140	100
77	160	140	100
80	160	140	100
83	160	110	100
86	150	140	80
95	140	140	100
110	130	130	110
125	130	130	110
139	110	110	90
145	110	110	90
155	110	110	90

Table D.4: Peak experimental thermocouple temperatures measured for Tremonia downward

Position (m)	Temperature (°C) Top	Middle	Bottom
192	50	50	30
167	60	60	30
137	70	70	70
107	100	100	90
89	110	110	100
86	120	120	110
83	120	120	110
80	130	130	120
77	130	130	120
74	130	130	120
71	140	140	130
68	150	150	140
65	160	160	150
47	200	200	180
23	320	320	280
20	340	340	290
17	390	370	330
14		400	360
11	500	460	380
8	590	570	470
5	740	700	580
2	880	880	600
-1	500	1180	1200
-4	680	140	100
-13	440	220	120
-28			
-43	260	210	100
-57			
-63	200	180	20
-73	150	40	20

Table D.5: Peak experimental thermocouple temperatures measured for Ramsbeck upward

Position (m)	Temperature (°C) Top	Middle	Bottom
-33	10	10	10
-30	10	10	10
-27	10	10	10
-24	10	10	10
-21	10	10	10
-18	15	15	15
-15		15	
-12		10	
-9		80	
-6		220	
-3	450	120	60
0		1000	
3	820	760	100
6		520	
9	530	380	120
12		230	
15	420	300	140
18		340	
21	340	280	150
24		300	
27	280	260	90
39	180	140	
89	100	80	
139	70	60	
189	40	35	
239	25	25	
289	20	20	

Table D.6: Peak experimental thermocouple temperatures measured for Ramsbeck downward

Position (m)	Temperature (°C) Top	Middle	Bottom
30	300	300	260
27		320	
24	340	340	260
21		380	
18	410	410	350
15		450	
12	510	510	420
9		670	
6	900		600
3		940	
0	550	540	980
-3		100	
-6	360	100	30
-9		70	
-12	250	100	20
-15		140	
-18	210	80	20
-21		90	
-24	170	100	20
-27		100	
-30	100	40	20
-42	10	10	10
-92	10	10	10
-142	10	10	10
-192	10	10	10
-242	10	10	10
-292	10	10	10

Table D.7: Peak experimental thermocouple temperatures measured for 0.8 m/s

Position	Temperature (°C)		
(m)	Top	Middle	Bottom
-39	180	150	30
-31	200	149	25
-22	251	190	40
-6	495	190	60
3	1200	1250	1300
6	1200	1200	1130
19	870	870	690
30	>600	>600	>600
53	510	495	455

Table D.8: Peak experimental thermocouple temperatures measured for 2.4 m/s

Position	Temperature (°C)		
(m)	Top	Middle	Bottom
-39	20	20	20
-31	20	20	20
-22	20	20	20
-6	245	25	25
3	700	1050	900
6	860	840	500
19	690	690	500
30	520	520	520
53	470	440	420

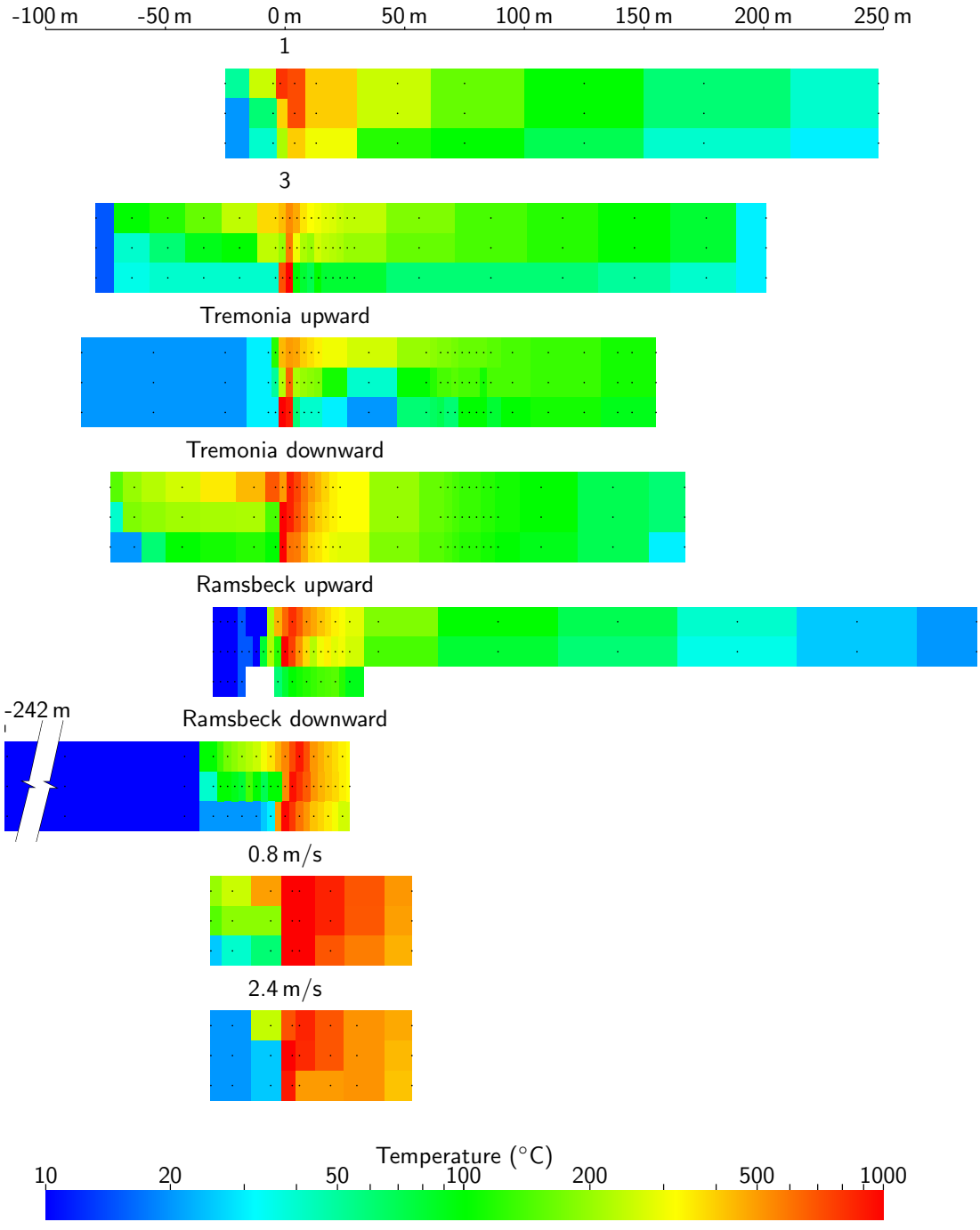

Figure D.1: Thermocouple data from DMT fire gallery tests
DMT et al. (2004b)

D.2 Grid independence for tunnel fire case

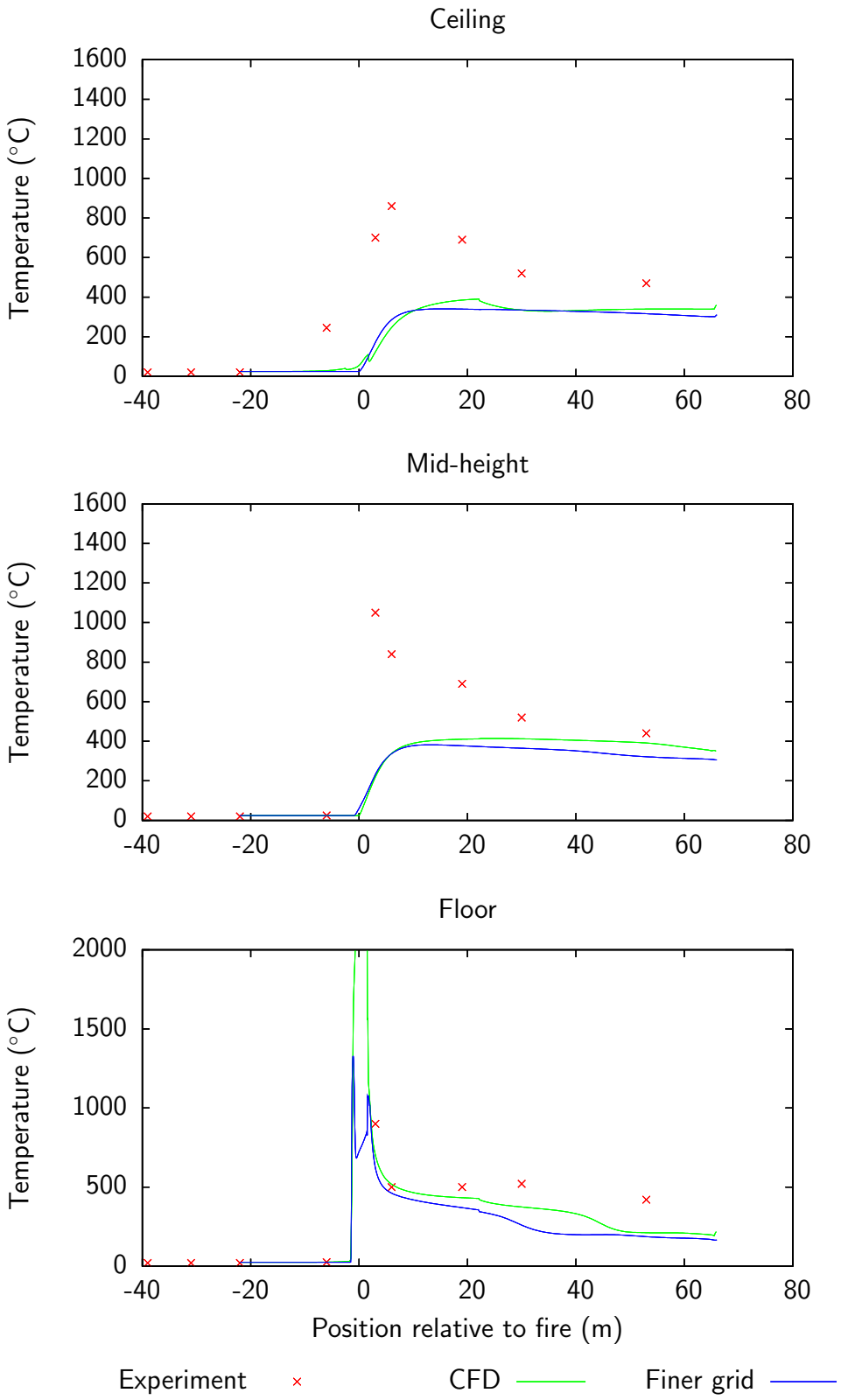

Figure D.2: Comparison of CFD results with results from a finer grid (2.4 m/s ventilation)

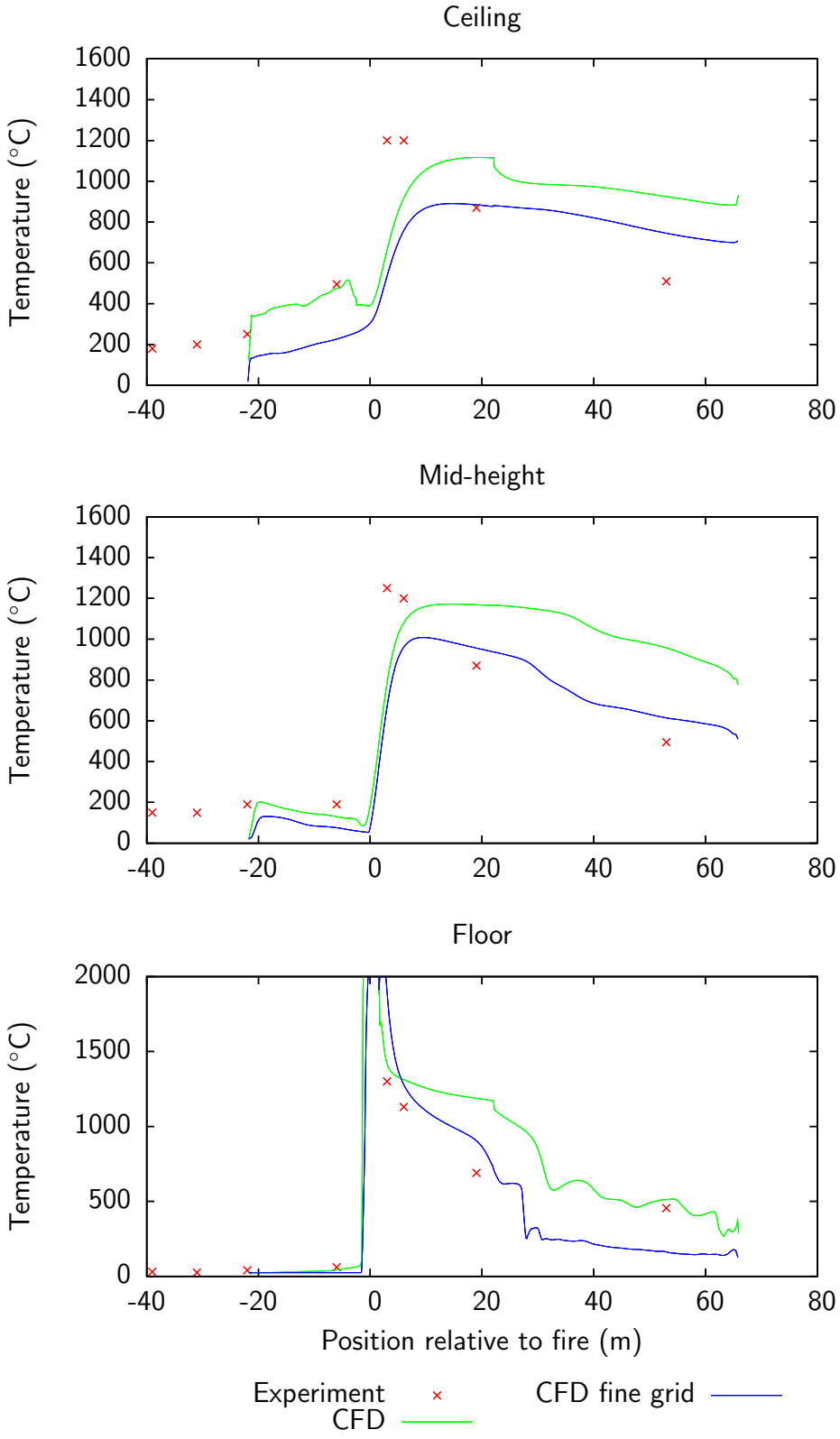

Figure D.3: Comparison of CFD results from the original mesh, and a finer mesh in the far downstream region. (0.8 m/s ventilation)

D.3 Time step independence for mist suppression of tunnel fire

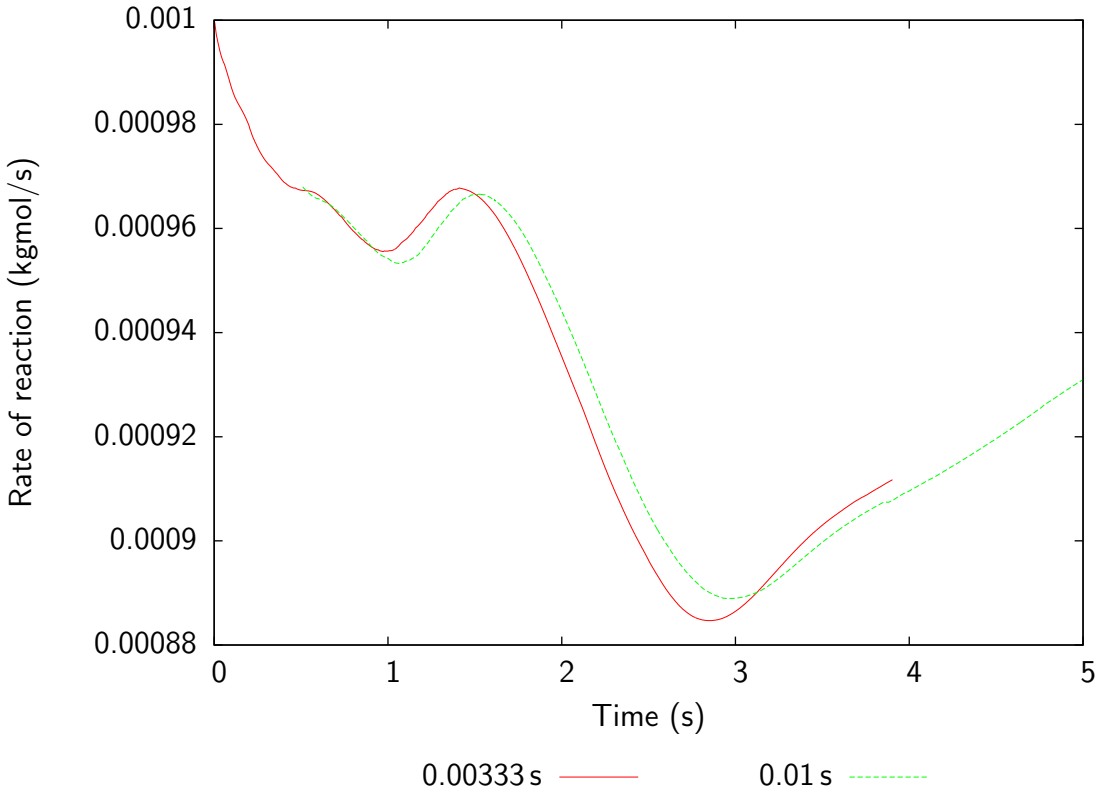

Figure D.4: Total reaction rate predicted by CFD using two different time-step sizes for 0.8 m/s ventilation and single row of nozzles

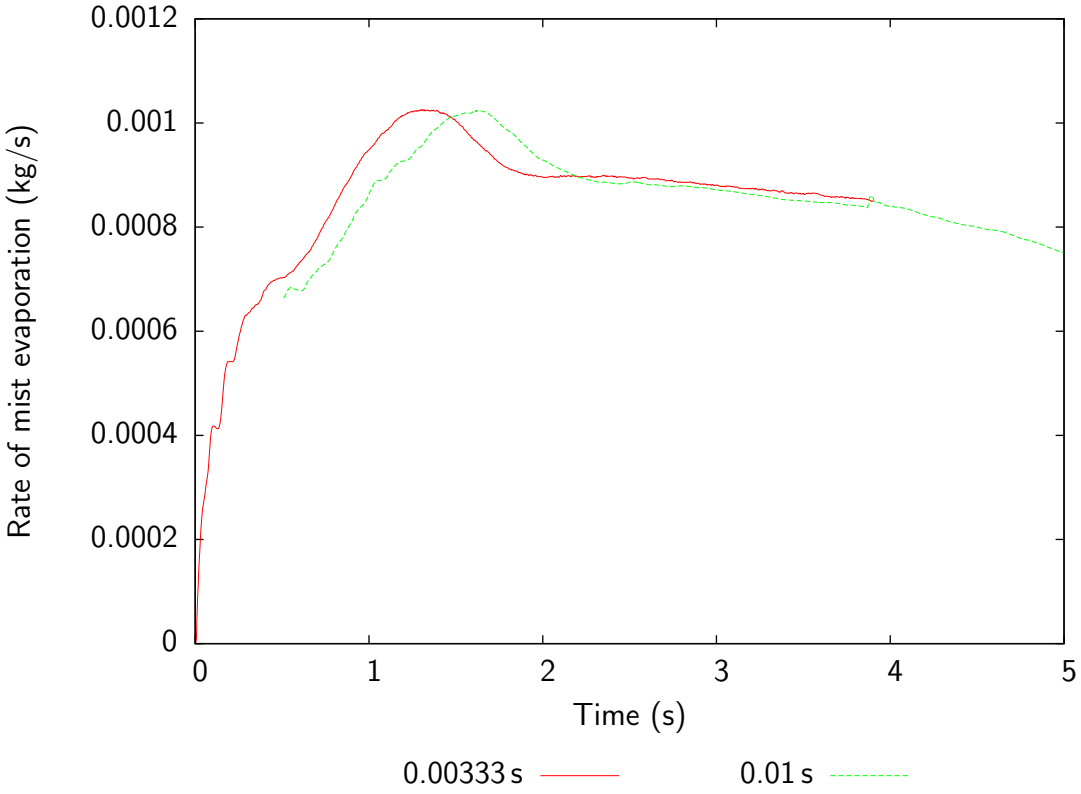

Figure D.5: Mist evaporation rate predicted by CFD using two different time-step sizes for 0.8 m/s ventilation and single row of nozzles

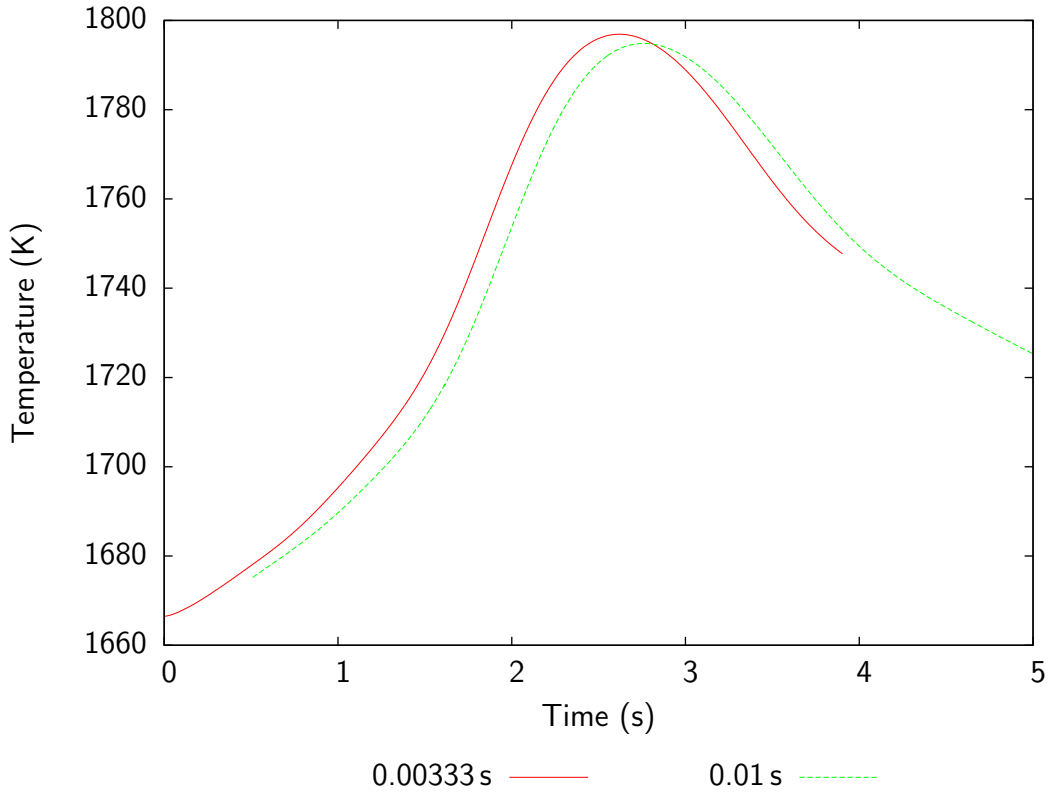

Figure D.6: Ceiling temperature 3 m downstream of fire as predicted by CFD using two different time-step sizes for 0.8 m/s ventilation and single row of nozzles

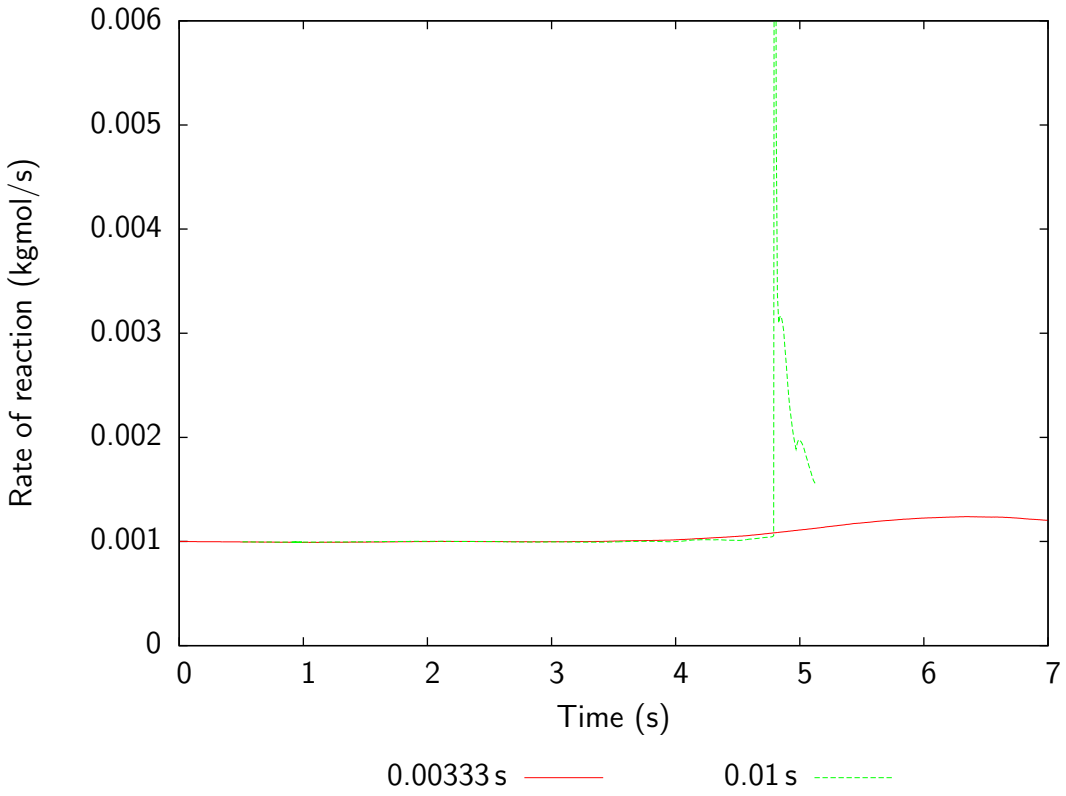

Figure D.7: Total reaction rate predicted by CFD using two different time-step sizes for 2.4 m/s ventilation and single row of nozzles

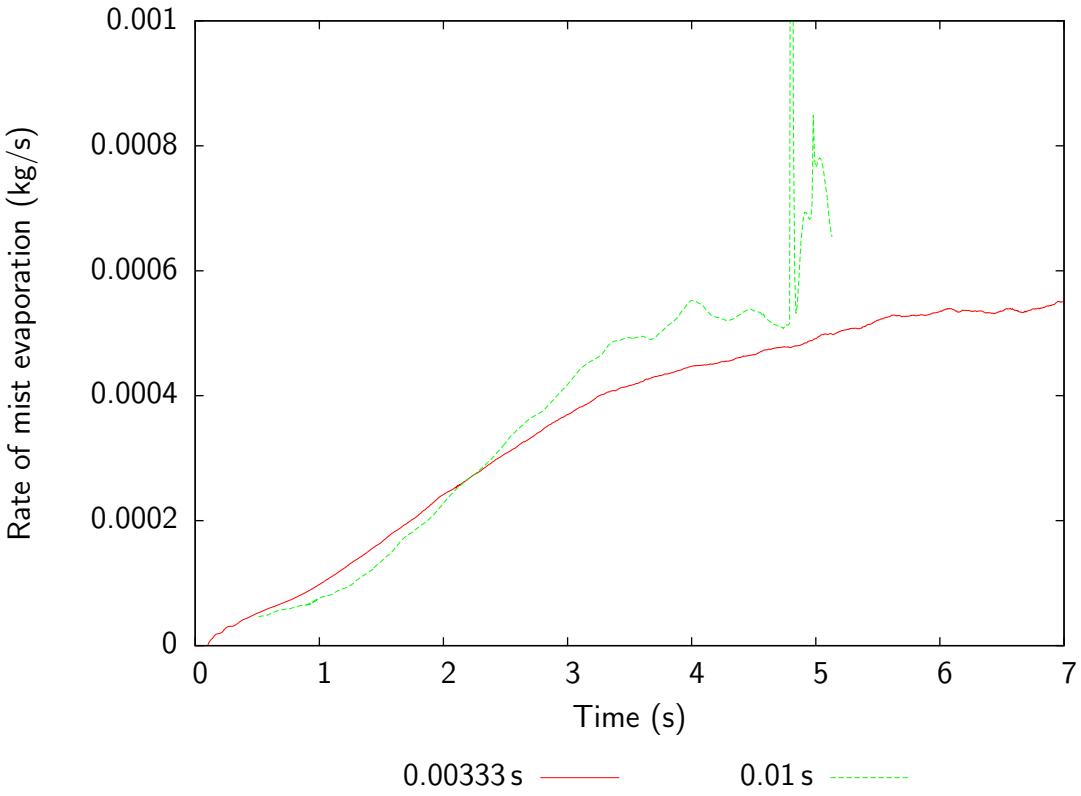

Figure D.8: Mist evaporation rate predicted by CFD using two different time-step sizes for 2.4 m/s ventilation and single row of nozzles

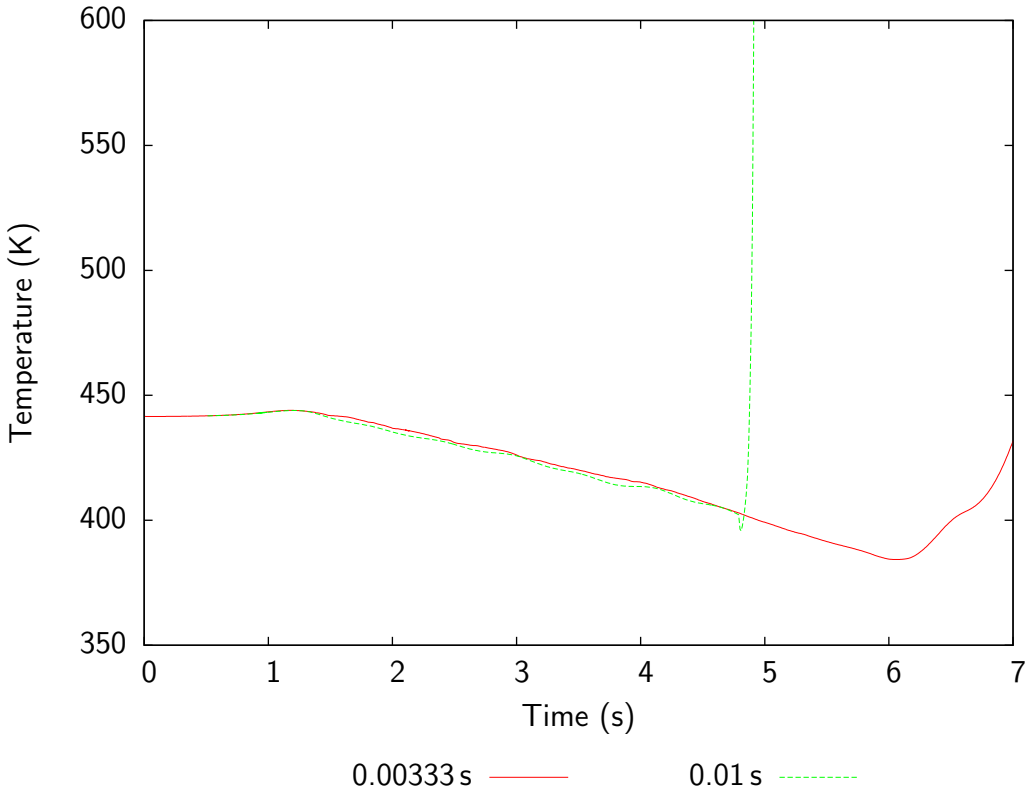

Figure D.9: Ceiling temperature 3 m downstream of fire as predicted by CFD using two different time-step sizes for 2.4 m/s ventilation and single row of nozzles

Bibliography

Abe, K. (2005). A hybrid approach using an anisotropy-resolving algebraic turbulence model. *International Journal of Heat and Fluid Flow*, 26:204–222.

Adiga, K. C. (2004). Nanomist suppresses fire. *Fluent News*, page 18.

Apte, V. B. (1998). Effect of scale and fuel type on the characteristics of pool fires for fire fighting training. *Fire Safety Journal*, 31:283–298.

Associated Press (2005). NYC Subway Gets a Computerized Facelift. *New York Times*. `http://www.nytimes.com/aponline/technology/AP-High-Tech-Subway.html` Accessed: 12/04/2005.

Autoroutes et Tunnel du Mont Blanc (2003). Rapport annuel. `http://www.atmb.net/IMG/pdf/rapport_annuel_2003/2003.pdf`. Accessed: 10/05/2005.

Babinsky, E. and Sojka, P. E. (2002). Modelling drop size distributions. *Progress in Energy and Combustion Science*, 28:303–329.

Back III, G. G., Beyler, C. L., and Hansen, R. (2000). The capabilities and limitations of total flooding, water mist fire suppression systems in machinery space applications. *Fire Technology*, 36:8–23.

Back III, G. G., Beyler, C. L., and Hansen, R. (2000). A quasi-steady-state model for predicting fire suppression in spaces protected by water mist systems. *Fire Safety Journal*, 35:327–362.

Baukal, C. E., Gershtein, V. Y., and Li, X., editors (2001). *Computational fluid dynamics in industrial combustion*. CRC Press, London.

BBC News (2000). Austria blaze fans tunnel safety fears. `http://news.bbc.co.uk/1/hi/world/europe/1018190.stm`. Accessed: 08/04/2005.

BBC News (2001a). Alps tunnels' record of danger. `http://news.bbc.co.uk/1/hi/world/europe/1617340.stm`. Accessed: 08/04/2005.

BBC News (2001b). Hope dies for Ukraine miners. `http://news.bbc.co.uk/1/hi/world/europe/1502952.stm`. Accessed: 19/04/2005.

BBC News (2005). Tunnel fire trial opens in France. `http://news.bbc.co.uk/1/hi/world/europe/4221565.stm`. Accessed: 18/04/2005.

Bettis, R. J., Jagger, S. F., and Wu, Y. (1993). Interim validation of tunnel fire consequence models: Summary of phase 2 tests. Technical Report IR/L/FR/93/11, Health and Safety Executive, Buxton, UK.

Bill, Jr., R. G., Hansen, R. L., and Richards, K. (1997). Fine-spray (water mist) protection of shipboard engine rooms. *Fire Safety Journal*, 29:317–336.

Bottom, D. A. and Denton, S. (1991). Fires in coal mines. *The Mining Engineer*, 150(354):303–311. Authored by HM Principal Inspector of Mines.

Brizuela, E. A. and Bilger, R. W. (1996). On the eddy break-up coefficient. *Combustion and Flame*, 104:208–212.

BS 5306-2:1990 (1990). *Fire extinguishing installations and equipment on premises – Part 2: Specification for sprinkler systems*. British Standard Organisation.

BS 5306-4:2001 (2001). *Fire extinguishing installations and equipment on premises – Part 4: Specification for carbon dioxide systems*. British Standard Organisation.

BS 5306-6:1988 (1988). *Fire extinguishing installations and equipment on premises – Part 6: Foam Systems*. British Standard Organisation.

BS 9251:2005 (2005). *Sprinkler systems for residential and domestic occupanies: code of practice*. British Standard Organisation.

BS ISO/TR 13387-7:1999 (1999). *Fire safety engineering – Part 7: Detection, activation and suppression*. British Standard Organisation.

Carvel, R. O., Beard, A. N., and Jowitt, P. W. (2001a). The influence of longitudinal ventilation systems on fires in tunnels. *Tunnelling and Underground Space Technology*, 16:3–21.

Carvel, R. O., Beard, A. N., and Jowitt, P. W. (2001b). Variation of heat release rate with forced longitudinal ventilation for vehicle fires in tunnels. *Fire Safety Journal*, 36:569–596.

Chan, S. (2005). Harlem Subway Tunnel Fire Forces Evacuation of 600. *New York Times*. `http://www.nytimes.com/2005/04/08/nyregion/08blast.html` Accessed: 12/04/2005.

Chen, Q. (1996). Prediction of room air motion by Reynolds-stress models. *Building and Environment*, 31:233–244.

Cheng, X., Wu, J., Yuan, X., and Zhou, H. (1999). Principles for a video fire detection system. *Fire Safety Journal*, 33:57–69.

Chow, W. K. and Yao, B. (2001). Numerical modeling for interaction of a water spray with smoke layer. *Numerical Heat Transfer, Part A (Applications)*, 39:267–283.

Clift, R., Grace, J., and Weber, M. (1978). *Bubbles, Drops and Particles*. Academic Press, New York.

Coulson, J. M. and Richardson, J. F. (1996). *Chemical Engineering*, volume 1: Fluid flow, heat transfer and mass transfer. Butterworth Heinemann, 5 edition.

Cox, G., editor (1995). *Combustion Funamentals of Fire*. Academic Press.

Crowe, C., Sommerfeld, M., and Tsuji, Y. (1998). *Multiphase Flows with Droplets and Particles*. CRC Press.

Dally, B. B., Riesmeier, E., and Peters, N. (2004). Effect of fuel mixture on moderate and intense low oxygen dilution combustion. *Combustion and Flame*, 137:418–431.

Dawson, H. F. and di Marzo, M. (1993). Multi-droplet evaporative cooling: Experimental results. In *AIChE Symposium Series. Heat Transfer*, volume 89, pages 122–131, Atlanta, GA.

Delavan (2005). *Nozzle Technology*. Delavan Spray Technologies. `http://www.delavan.co.uk/` (Accessed: 20/02/2005).

Delichatsios, M. A. (2003). Closed form approximate solutions for smoke filling in enclosures including the volume expansion term. *Fire Safety Journal*, 38:97–101.

Department of Trade and Industry (2002a). Review of the Remaining Reserves at Deep Mines within the UK. Technical Report 15104. Accessed: 15/09/05.

Department of Trade and Industry (2002b). Review of the Selby Complex. Technical Report 15087. Accessed: 15/09/2005.

Devarakonda, V. and Ray, A. K. (2003). Effect of inter-particle interactions on evaporation of droplets in a linear array. *Journal of Aerosol Science*, 34:837–857.

DiNenno, P. J., editor (2002). *SFPE handbook of fire protection engineering*. National Fire Protection Association, 3rd edition.

Disimile, P. J., Tucker, J. R., Croswell, B., and Davis, J. M. (2005). The transport of water sprays past generic clutter elements found within engine nacelles. *Fire Safety Journal*, 40:65–78.

DMT, AITEMIN, Health and Safety Executive, University of Nottingham, and IMC Technical Services (2004a). Prediction of Fire Effects in Mines – final report. Technical report, ECSC Coal RTD Programme. Contract No. 7220-PR/061.

DMT, AITEMIN, Mines Rescue Sevice Ltd, and University of Nottingham (2001). Fire fighting systems – technical report no. 2. Technical report, ECSC Coal RTD Programme. Contract No. 7220-PR/094.

DMT, AITEMIN, Mines Rescue Sevice Ltd, and University of Nottingham (2002). Fire fighting systems – technical report no. 3. Technical report, ECSC Coal RTD Programme. Contract No. 7220-PR/094.

DMT, AITEMIN, Mines Rescue Sevice Ltd, and University of Nottingham (2003a). Fire fighting systems – technical report no. 4. Technical report, ECSC Coal RTD Programme. Contract No. 7220-PR/094.

DMT, AITEMIN, Mines Rescue Sevice Ltd, and University of Nottingham (2003b). Fire fighting systems – technical report no. 6. Technical report, ECSC Coal RTD Programme. Contract No. 7220-PR/094.

DMT, AITEMIN, Mines Rescue Sevice Ltd, and University of Nottingham (2004b). Fire fighting systems – final report. Technical report, ECSC Coal RTD Programme. Contract No. 7220-PR/094.

Downie, B., Polymeropoulos, C., and Gogos, G. (1995). Interaction of a water mist with a buoyant methane diffusion flame. *Fire Safety Journal*, 24:359–381.

Drysdale, D. (1998). *An Introduction to Fire Dynamics*. Wiley, England, 2nd edition.

Durbin, P. A. and Reif, B. A. P. (2001). *Statistical Theory and Modeling for Turbulent Flows*. Wiley.

Dvorjetski, A. and Greenberg, J. B. (2004). Theoretical analysis of polydisperse water spray extinction of opposed flow diffusion flames. *Fire Safety Journal*, 39:309–326.

Dziurzyński, W., Nawrat, S., Roszkowski, J., and Trutwin, W. (1997). Computer simulation of mine ventilation disturbed by fires and the use of fire extinguishers. In Ramani, R. V., editor, *Proceedings of the 6th International Mine Ventilation Congress*, pages 389–393, Pittsburgh, Pennsylvania.

Eckert, E. and Drake Jnr, R. M. (1972). *Analysis of heat and mass transfer*. McGraw-Hill, New York.

Edwards, J. C. and Hwang, C. C. (1999). CFD analysis of mine fire smoke spread and reverse flow conditions. In *Proceedings of the 8th US mine ventilation symposium*.

Espi, E., Berne, P., and Duverneuil, P. (1998). Using CFD to understand the air circulation in a ventilated room. *Computers Chem. Engineering*, 22:S751–S754. Suppl.

Fluent (2002). *Fluent 6 User Guide*. Fluent Inc.

Fluent (2005). Fluent Inc. website. `http://www.fluent.com/`. Accessed: 18/03/2005.

Freitas, C. J. (2002). The issue of numerical uncertainty. *Applied Mathematical Modelling*, 26:237–248.

Gabay, D. (2002). Fire safety: a short history in the Paris subway. *Tunnelling and Underground Space Technology*, 17:139–143.

Gameiro, V. (2001). Water mist: A new standard in fire fighting. `http://www.energypubs.com/issues/html/f000069.html`.

Gatski, T. B., Hussaini, M. Y., and Lumley, J. L. (1996). *Simulation and Modeling of Turbulent Flows*. Oxford University Press.

Grace, J. R. and Taghipour, F. (2004). Verification and validation of models and dynamic similarity for fluidized beds. *Powder Technology*, 139:99–110.

Grant, G., Brenton, J., and Drysdale, D. (2000). Fire suppression by water sprays. *Progress in Energy and Combustion Science*, 26:79–130.

Grant, G. B., Jagger, S. F., and Lea, C. J. (1998). Fires in tunnels. *Philosophical Transactions of the Royal Society: Mathematical, Physical and Engineering Sciences*, 356(1748):2873–2906.

Gupta, A. K. (2001). Modelling the response of sprinklers in compartment fires. *Fire and Materials*, 25(3):117–121.

Haack, A. (2002). Current safety issues in traffic tunnels. *Tunnelling and Underground Space Technology*, 17:117–127.

Hara, T. and Kato, S. (2004). Numerical simulation of thermal plumes in free space using the standard k-ε model. *Fire Safety Journal*, 39:105–129.

Hawkes, E. R. and Chen, J. H. (2004). Direct numerical simulation of hydrogen-enriched lean premixed methane-air flames. *Combustion and Flame*, 138:242–258.

Health and Safety Executive (2002). Pool fires. *Fire and explosion strategy*, 1. `http://www.hse.gov.uk/offshore/strategy/pool.htm` Accessed: 15/04/2005.

Health and Safety Executive (2005). Accidents and Dangerous Occurrences in Mines. `http://www.hse.gov.uk/mining/accident/`. Accessed: 15/04/2005.

Henkes, R. A. W. M., Van Der Vlugt, F. F., and Hoogendoorn, C. J. (1991). Natural-convection flow in a square cavity calculated with low-Reynolds-number turbulence models. *Internation Journal of Heat and Mass Transfer*, 34(2):377–388.

Heskestad, G. (2002a). *Fire Plumes, Flame Height, and Air Entrainment*, chapter 2–1. In DiNenno (2002), 3rd edition.

Heskestad, G. (2002b). Scaling the interaction of water sprays and flames. *Fire Safety Journal*, 37:535–548.

Heskestad, G. (2003). Extinction of gas and liquid pool fires with water sprays. *Fire Safety Journal*, 38:301–317.

Highways Agency (1999). A303 Stonehenge (incorporating the Winterbourne Stoke bypass) preferred route annoucement. Technical report. `http://www.highways.gov.uk/roads/projects/a_roads/a303/stonehenge/a303stone/` Accessed:12/04/2005.

Holborn, P. G., Nolan, P. F., and Golt, J. (2004). An analysis of fire sizes, fire growth rates and times between events using data from fire investigations. *Fire Safety Journal*, 39:481–524.

Hua, J., Kumar, K., Khoo, B. C., and Xue, H. (2002). A numerical study of the interaction of water spray with a fire plume. *Fire Safety Journal*, 37:631–657.

Hughes, K. J., Tomlin, A. S., Hampartsoumian, E., Nimmo, W., Zsely, I. G., Ujvari, M., Turanyi, T., Clague, A. R., and Pilling, M. J. (2001). An investigation of important gas-phase reactions of nitrogenous species from the simulation of experimental measurements in combustion systems. *Combustion and Flame*, 124:573–589.

Huhtanen, R. (2002). Oil pool fire in a large turbine hall – CFD simulation. Technical Report STUK-YTO-TR 193, Säteilyturbakskus (Finnish Radiation and Nuclear Safety Authority), Helsinki, Finland.

Husted, B. P., Holmstedt, G., and Hertzberg, T. (2004). The physics behind water mist systems. In *Proceedings IWMA conference*, Rome, Italy.

Hwang, C. C. and Edwards, J. C. (2005). The critical ventilation velocity in tunnel fires–a computer simulation. *Fire Safety Journal*, 40:213–244.

ICES (2005). Institute for combustion and energy studies pool fire facility. `http://www.ices.utah.edu/capabilities/poolfire.html`. Accessed: 3/10/2005.

ISO 8421-1:1987 (1987). *Glossary of Terms associated with fire – Part 1: General terms and phenomena of fire*. Internation Standards Organisation. (BS 4422-1: 1987).

Jayaweera, T. M., Fisher, E. M., and Fleming, J. W. (2005). Flame suppression by aerosols derived from aqueous solutions containing phosphorus. *Combustion and Flame*, 141:308–321.

Jiang, Z., Chow, W. K., Tang, J., and Li, S. F. (2004). Preliminary study on the suppression chemistry of water mists on poly(methyl methacrylate) flames. *Polymer Degradation and Stability*, In Press, Corrected Proof.

Jozefowicz, R. (2004). Personal communication. E-mail 16/02/2004.

Kanury, A. M. (2002). *Ignition of Liquid Fuels*, chapter 2–8. In DiNenno (2002), 3rd edition.

Kim, M. B., Jang, Y. J., and Yoon, M. O. (1997). Extinction limit of a pool fire with a water mist. *Fire Safety Journal*, 28:295–306.

Kim, S. C. and Ryou, H. S. (2003). An experimental and numerical study on fire suppression using a water mist in an enclosure. *Building and Environment*, 38:1309–1316.

Kotchourko, A. S., Dorofeev, S. B., and Breitung, W. (1999). Test of extended eddy break up model in simulations of turbulent h_2-air combustion. In *Proceedings of the 17th International Colloquium on the Dynamics of Explosions and Reactive Systems*.

Kunsch, J. P. (1999). Critical velocity and range of a fire-gas plume in a ventilated tunnel. *Atmospheric Environment*, 33:13–24.

Kunsch, J. P. (2002). Simple model for control of fire gases in a ventilated tunnel. *Fire Safety Journal*, 37:67–81.

Kurioka, H., Oka, Y., and Satoh, H. (2003). Fire properties in near field of square fire source with longitudinal ventilation in tunnels. *Fire Safety Journal*, 38:319–340.

Laage, L. W. and Yang, H. (1995). Mine fire experiments and simulation with MFIRE. In Wala, A. M., editor, *Proceedings of the 7th US Mine Ventilation Symposium*, pages 213–220, Lexington, Kentucky.

Launder, B. E. and Spalding, D. (1974). The numerical computation of turbulent flows. *Computer Methods In Applied Mechanics and Engineering*, 3:269–289.

Lea, C. J., Owens, M., and Jones, I. P. (1997). Computational fluid dynamics modelling of fire on a one-third scale model of a channel tunnel heavy goods vehicle shuttle. In *9th International Symposium on Aerodynamics and Ventilation of Vehicle Tunnels*, Aosta Valley, Italy.

Lee, S. H. and Ryou, H. S. (2000). Development of a new spray/wall interaction model. *Internation Journal of Multiphase Flow*, 26(7):1209–1234.

Lefebvre, A. H. (1989). *Atomization and Sprays*. Combustion: An International Series. Hemisphere Publishing.

Leitner, A. (2001). The fire catastrophe in the Tauern Tunnel: experience and conclusions for the Austrian guidelines. *Tunnelling and Underground Space Technology*, 16:217–223.

Lentati, A. M. and Chelliah, H. K. (1998). Dynamics of water droplets in a counterflow field and their effect on flame extinction. *Combustion and Flame*, 115:158–179.

Lesieur, M. (1997). *Turbulence in fluids*. Dordrect: Luwer Academic, 3rd edition.

Li, J. S. M. and Chow, W. K. (2003). Numerical studies on performance evaluation of tunnel ventilation safety systems. *Tunnelling and Underground Space Technology*, 18:435–452.

Li, Y., Shing, V. C., and Chen, Z. (2003). Fine bubble modelling of smoke flows. *Fire Safety Journal*, 38:285–298.

Liu, J. F. and Hsieh, W. H. (2004). Experimental investigation of combustion in porous heating burners. *Combustion and Flame*, 138:295–303.

Liu, Z., Kim, A. K., Carpenter, D., Kanabus-Kaminska, J. M., and Yen, P.-L. (2004). Extinguishment of cooking oil fires by water mist fire suppression systems. *Fire Technology*, 40:309–333.

Liu, Z., Kim, A. K., and Su, J. Z. (1999). Examination of the extinguishment performance of a water mist system using continuous and cycling discharges. *Fire Technology*, 35:336–361.

Log, T. and Cannon-Brookes, P. (1995). 'water mist' for fire protection of historic buildings and museums. *Museum Management and Curatorship*, 14:283–298.

Loomis, I. M. and McPherson, M. J. (1995). Application of water mist for the control of fuel-rich fires in model coal mine entries. In Wala, A. M., editor, *Proceedings of the 7th US mine ventilation symposium*, pages 225–230, Litrern, Colorado.

Luo, K. (2003). New opportunities and challenges in fire dynamics modelling. In *Fire and Explosion Hazards, Proceedings of the Fourth International Seminar*, pages 39–52, Londonderry. University of Ulster.

Ma, T. G. and Quintiere, J. G. (2003). Numerical simulation of axi-symmetric fire plumes: accuracy and limitations. *Fire Safety Journal*, 38:467–492.

MacMillan, A. (1997). A Summary of Recent Mine Fire Data. Technical Report FS/PR/97/14, HSL, Buxton.

McCall, D. W., Alpert, R. L., Anderson, J. G., Dinennon, P. J., Dixon, D. A., Fernandez, R. E., Gormley, R. H., Ko, M. K., Pariser, R., Ravishankara, A. R., Rubenstein, R., Rusch, G. M., Tapscott, R. E., Wallington, T. J., Wuebbles, D. J., DeMarco, R., Sidney G. Reed, J., and Wilson, J. G. (1997). *Fire Suppression Substitutes and Alternatives to Halon for U.S. Navy Applications*. National Academy Press, Washington, D.C.

McGrattan, K. B. (2005). *Fire Dynamics Simulator (version 4) - technical reference guide*. NIST. NIST Special Publication 1018.

McGrattan, K. B., Baum, H. R., and Rehm, R. G. (1996). Numerical simulation of smoke plumes from large oil fires. *Atmospheric Environment*, 30:4125–4136.

McGrattan, K. B., Baum, H. R., Rehm, R. G., Hamins, A., Forney, G. P., Floyd, J. E., Hostikka, S., and Prasad, K. (2002). *Fire Dynamics Simulator (Version 3) - Technical Reference Guide*. NIST, 2002 edition.

McGrattan, K. B. and Forney, G. P. (2005). *Fire Dynamics Simulator (version 4) - user's guide*. NIST. NIST Special Publication 1019.

Minister of the Interior (1999). Task force for technical investigation of the 24th March 1999 fire in the Mont Blanc vehicular tunnel. Technical report, Ministry of Equipment, Transportation and Housing, France. Accessible through: `http://web.archive.org/web/20021203182040/http://www.equipement.gouv.fr/actualites/dossiers/1999/rapportuk.htm` Accessed: 14/04/2005.

Modic, J. (2003). Fire simulation in road tunnels. *Tunnelling and Underground Space Technology*, 18:525–530.

Moore, G. E. (1965). Cramming more components onto integrated circuits. *Electronics*. `http://www.intel.com/research/silicon/moorespaper.pdf`.

Morsi, S. and Alexander, A. (1972). An investigation of particle trajectories in two-phase flow systems. *Journal of Fluid Mechanics*, 55:193–208.

Mowrer, F. W. (1999). Enclosure smoke filling revisited. *Fire Safety Journal*, 33:93–114.

Nakakuki, A. (2002). Heat transfer in pool fires at a certain small lip height. *Combustion and Flame*, 131:259–272.

Nam, S. (1996). Development of a computational model simulating the interaction between a fire plume and a sprinkler spray. *Fire Safety Journal*, 26:1–33.

Nam, S. (1999). Numerical simulation of the penetration capability of sprinkler sprays. *Fire Safety Journal*, 32:307–329.

Nam, S. (2004). Actuation of sprinklers at high ceiling clearance facilities. *Fire Safety Journal*, 39:619–642.

Nam, S. and Bill, Robert G., J. (1993). Numerical simulation of thermal plumes. *Fire Safety Journal*, 21:231–256.

Ndubizu, C. C., Ananth, R., Tatem, P. A., and Motevalli, V. (1998). On water mist fire suppression mechanisms in a gaseous diffusion flame. *Fire Safety Journal*, 31:253–276.

NFPA 750 (2003). *Standard on water mist fire protection systems*. NFPA, Quincy, MA.

Notarianni, K. A. (1994). Water mist fire suppression systems. In *Proceedings of Technical Symposium on Halon Alternatives*, Knoxville, TN. Society of Fire Protection Engineers and PLC Education Foundation.

Novozhilov, V., Harvie, D. J. E., and Kent, J. H. (1997). A computational fluid dynamics study of wood fire extinguishment by water sprinkler. *Fire Safety Journal*, 29:259–282.

Novozhilov, V., Moghtaderi, B., Fletcher, D. F., and Kent, J. H. (1996). Computational fluid dynamics modelling of wood combustion. *Fire Safety Journal*, 27:69–84.

Novozhilov, V., Moghtaderi, B., Kent, J. H., and Fletcher, D. F. (1999). Solid fire extinguishment by a water spray. *Fire Safety Journal*, 32:119–135.

Oka, Y. and Atkinson, G. T. (1995). Control of smoke flow in tunnel fires. *Fire Safety Journal*, 25:305–322.

Olenick, S. M. and Carpenter, D. J. (2003). An updated international survey of computer models for fire and smoke. *Journal of Fire Protection Engineering*, 13. See also: `http://www.firemodelsurvey.com/`.

Parra, T., Castro, F., Méndez, C., Villafruela, J. M., and Rodríguez, M. A. (2004). Extinction of premixed methane-air flames by water mist. *Fire Safety Journal*, 39:581–600.

Patankar, S. V. (2002). Computational modelling of flow and heat transfer in industrial applications. *International Journal of Heat and Fluid Flow*, 23:222–231.

Peters, N. (2000). *Turbulent Combustion*. Cambridge monographs on mechanics. Cambridge University Press.

Pozrikidis, C. (1997). *Introduction to theoretical and computational fluid dynamics*. Oxford University Press.

Prasad, K., Li, C., and Kailasanath, K. (1999). Simulation of water mist suppression of small scale methanol liquid pool fires. *Fire Safety Journal*, 33:185–212.

Prasad, K., Patnaik, G., and Kailasanath, K. (2002). A numerical study of water-mist suppression of large scale compartment fires. *Fire Safety Journal*, 37:569–589.

Qin, J., Yao, B., and Chow, W. K. (2004). Experimental study of suppressing cooking oil fire with water mist using a cone calorimeter. *International Journal of Hospitality Management*, In Press, Corrected Proof.

Qu, X., Davis, E. J., and Swanson, B. D. (2001). Non-isothermal droplet evaporation and condensation in the near-continuum regime. *Journal of Aerosol Science*, 32:1315–1339.

Raithby, G. D. and Chui, E. H. (1990). A finite-volume method for predicting a radiant heat transfer in enclosures with participating media. *Journal of Heat Transfer*, 112:415–423.

Ravigururajan, T. S. and Beltran, M. R. (1989). A model for attenuation of fire radiation through water droplets. *Fire Safety Journal*, 15:171–181.

Regev, A., Hassid, S., and Poreh, M. (2004). Density jumps in smoke flow along horizontal ceilings. *Fire Safety Journal*, 39:465–479.

Richard, J., Garo, J. P., Souil, J. M., and Vantelon, J. P. (2003a). On the flame structure at the base of a pool fire interacting with a water mist. *Experimental Thermal and Fluid Science*, 27:439–448.

Richard, J., Garo, J. P., Souil, J. M., Vantelon, J. P., and Knorre, V. G. (2003b). Chemical and physical effects of water vapor addition on diffusion flames. *Fire Safety Journal*, 38:569–587.

Rogers, G. F. C. and Mayhew, Y. R. (1995). *Thermodynamic and Transport Properties of Fluids – SI Units*. Blackwell, 5 edition.

Ruffino, P. and diMarzo, M. (2004). The simulation of fire sprinklers thermal response in presence of water droplets. *Fire Safety Journal*, In Press, Corrected Proof.

Ryou, H. S. (2004). Personal communication. E-mail 25/05/2004.

Shaw, C. T. (1992). *Using computational fluid dynamics*. Prentice Hall.

Shimizu, H., Tsuzuki, M., Yamazaki, Y., and Koichi Hayashi, A. (2001). Experiments and numerical simulation on methane flame quenching by water mist. *Journal of Loss Prevention in the Process Industries*, 14:603–608.

Silvester, S. (2002). *The integration of CFD and VR methods to assist auxiliary ventilation practice*. PhD thesis, University of Nottingham.

Simcox, S., Wilkes, N. S., and Jones, I. P. (1992). Computer simulation of the flows of hot gases from the fire at King's Cross underground station. *Fire Safety Journal*, 18:49–73.

Sinai, Y. L. (1999a). Comments on the role of leakages in field modelling of under-ventilated compartment fires. *Fire Safety Journal*, 33:11–20.

Sinai, Y. L. (1999b). Pool fire modelling. `http://www-waterloo.ansys.com/cfx/PDF/PDF0264.pdf`. Accessed: 15/04/2005.

Sinai, Y. L. (2000). Exploratory modelling of pool fire instabilities without cross-wind. *Fire Safety Journal*, 35:51–61.

Sinai, Y. L. (2003). Field modelling of a Steckler experiment: An example of the relationship between level of modelling and accuracy. In *Fire and Explosion Hazards, Proceedings of the Fourth International Seminar*, pages 665–674, Londonderry. University of Ulster.

Sinai, Y. L. and Owens, M. P. (1995). Validation of modelling of unconfined pool fires with cross-wind: Flame geometry. *Fire Safety Journal*, 24:1–34.

Sinai, Y. L., Stopford, P., Edwards, M., and Watkins, S. (2003). CFD modelling of fire suppression by water spray: sensitivity and validation for a pool fire in a room. In *Eighth International IBPSA Conference*, Eindhoven, Netherlands.

Sinai, Y. L. and Stopford, P. J. (2001). CFD modelling of fire suppression by water spray: A feasibility study examining a pool fire in a simple enclosure. In *Proceedings of Interflam 2001*, volume 2, pages 1445–1451, Edinburgh.

Smolík, J., Džumbová, L., Schwarz, J., and Kulmala, M. (2001). Evaporation of ventilated water droplet: connection between heat and mass transfer. *Journal of Aerosol Science*, 32:739–748. (Erratum in 33:205).

Spalart, P. R. (2000). Strategies for turbulence modelling and simulations. *International Journal of Heat and Fluid Flow*, 21:252–263.

Sripakagorn, P., Kosaly, G., and Pitsch, H. (2000). Local extinction-reignition in turbulent non-premixed combustion. Technical report, Center for Turbulence Research.

Stachulak, J. and Scoble, M. (1992). Conveyor fires in Canadian hardrock mines: Experience with protective devices at Inco Limited. *CIM Bulletin*, pages 55–62.

Strelets, M. (2003). Turbulence modelling in convective flow of fires. In *Fire and Explosion Hazards, Proceedings of the Fourth International Seminar*, pages 53–69, Londonderry. University of Ulster.

Tan, G. L. (2002). Fire fighting in tunnels. *Tunnelling and Underground Space Technology*, 17:179–180.

Tartarini, P. and di Marzo, M. (1996). Dropwise evaporative cooling in radiative field. Technical report, National Institute of Standards and Technology, Gaithersburg, MD.

Temmerman, L., Hadžiabdić, M., Leschziner, M. A., and Hanjalić, K. (2005). A hybrid two-layer approach for large eddy simulation at high reynolds numbers. *International Journal of Heat and Fluid Flow*, 26:173–190.

Tennekes, H. (1972). *A first course in turbulence*. MIT Press.

Thomas, G. O. (2002). The quenching of laminar methane-air flames by water mists. *Combustion and Flame*, 130:147–160.

Transport for London (2005). History - Transport for London. `http://www.tfl.gov.uk/tube/company/history/`. Accessed: 07/04/2005.

Turek, S. (1999). *Efficient solvers for incompressible flow problems*. Springer.

Tyco (2005). *AquaMist® Total Compartment Deluge System – Type AM4 Open Nozzles*. Tyco. `http://www.tyco-fire.com/TD_TFP/TFP/TD1173.pdf` Accessed: 23/02/2005.

United Nations Environment Programme (2000). The Montreal protocol on substances that deplete the ozone layer. `http://www.unep.org/ozone/Montreal-Protocol/Montreal-Protocol2000.shtml` (Accessed: 22/09/2005). Original adopted September 1987, subsequently amended London 1990, Copenhagen 1992, Vienna 1995, Montreal 1997 and Beijing 1999.

US Energy Information Adminstration (2005). Ukraine country analysis brief. `http://www.eia.doe.gov/emeu/cabs/ukraine.html`. Accessed: 19/04/2005.

Vaari, J. (2002). A transient one-zone computer model for total flooding water mist fire suppression in ventilated enclosures. *Fire Safety Journal*, 37:229–257.

Vaivads, R. H., Bardon, M. F., and Battista, V. (1997). A computational study of the flammability of methanol and gasoline fuel spills on hot engine manifolds. *Fire Safety Journal*, 28:307–322.

Vauquelin, O. and Telle, D. (2005). Definition and experimental evaluation of the smoke "confinement velocity" in tunnel fires. *Fire Safety Journal*, 40:320–330.

Verakis, H. C. (1989). Fire hazard evaluation of mine conveyor belts. In *3rd International Conference "Polymers in Mining"*. University of Lancaster, United Kingdom.

Versteeg, H. K. and Malalasekera, W. (1995). *An Introduction to Computational Fluid Dynamics*. Logman.

Veynante, D. and Vervisch, L. (2002). Turbulent combustion modelling. *Progress in Energy and Combustion Science*, 28:193–266.

Vuilleumier, F., Weatherhill, A., and Crausaz, B. (2002). Safety aspects of railway and road tunnel: example of the Lötschberg railway tunnel and Mont-Blanc road tunnel. *Tunnelling and Underground Space Technology*, 17:153–158.

Walla, A. M., Dziurzyński, W., Tracz, J., and Wooton, D. (1995). Validation study of the mine fire simulation model. In Wala, A. M., editor, *Proceedings of the 7th US Mine Ventilation Symposium*, pages 199–206, Lexington, Kentucky.

Watt, A. H. (2000). *3D computer graphics*. Addison-Wesley, 3rd edition.

Wen, J. X., Huang, L. Y., and Roberts, J. (2001). The effect of microscopic and global radiative heat exchange on the field predictions of compartment fires. *Fire Safety Journal*, 36:205–223.

Wichman, I. S., Morris, S. C., and McIntosh, A. W. (2002). Experimental measurements of flow and flame spread in the development of a fire testing facility. *Experimental Thermal and Fluid Science*, 25:595–603.

Wikipedia (2004). Wikipedia. `http://www.wikipedia.org`.

Wilcox, D. C. (1994). *Turbulence Modeling for CFD*. DCW Industries, California, 1 edition.

Williams, F. (2003). Approaches to the scaling of fires and explosions through mechanistic considerations. In *Fire and Explosion Hazards, Proceedings of the Fourth International Seminar*, pages 27–38, Londonderry. University of Ulster.

Wolski, J. K. (1995). Modeling of heat exchange between flowing air and tunnel walls. In Wala, A. M., editor, *Proceedings of the 7th US Mine Ventilation Symposium*, pages 207–212, Lexington, Kentucky.

Woodburn, P. J. and Britter, R. E. (1996a). CFD simulations of a tunnel fire–part I. *Fire Safety Journal*, 26:63–90.

Woodburn, P. J. and Britter, R. E. (1996b). CFD simulations of a tunnel fire–part II. *Fire Safety Journal*, 26:35–62.

Woolfson, M. M. (1999). *An introduction to computer simulation*. Oxford University Press.

Wu, Y. and Bakar, M. Z. A. (2000). Control of smoke flow in tunnel fires using longitudinal ventilation systems - a study of the critical velocity. *Fire Safety Journal*, 35(4):363–390.

Wu, Z. and Li, H. (1993). Simulation of mine ventilation under the influence of mine fires. In Bhaskar, R., editor, *Proceedings of the 6th US Mine Ventilation Symposium*, pages 359–364, Salt Lake City, Utah.

Xia, J. and Leung, D. Y. C. (2001). A concentration correction scheme for Lagrangian particle model and its application in street canyon air dispersion modelling. *Atmospheric Environment*, 35:5779–5788.

Xishi, W., Guangxuan, L., Jun, Q., and Weicheng, F. (2002). Experimental study on the effectiveness of the extinction of a pool fire with water mist. *Journal of Fire Sciences*, 20:279–295.

Xue, H., Ho, J. C., and Cheng, Y. M. (2001). Comparison of different combustion models in enclosure fire simulation. *Fire Safety Journal*, 36:37–54.

Yang, J. C., Boyer, C. I., and Grosshandler, W. L. (1996). Minimum mass flux requirements to suppress burning surfaces with water sprays. Technical Report NISTIR 5795, National Insitute of Standards and Technology.

Yang, W. and Kee, R. J. (2002). The effect of monodispersed water mists on the structure, burning velocity, and extinction behavior of freely propagating, stoichiometric, premixed, methane-air flames. *Combustion and Flame*, 130:322–335.

Yang, W., Parker, T., Ladouceur, H. D., and Kee, R. J. (2004). The interaction of thermal radiation and water mist in fire suppression. *Fire Safety Journal*, 39:41–66.

Yin, R. and Chow, W. (2001). Studies on thermal responses of sprinkler heads in atrium buildings with fire field models. *Fire and Materials*, 25:13–19.

Zagaynov, V. A., Nuzhny, V. M., Cheusova, T. A., and Lushnikov, A. A. (2000). Evaporation of water droplet and condensation coefficient: Theory and experiment. *Journal of Aerosol Science*, 31(S1):795–796.

Zhang, W., Hamer, A., Klassen, M., Carpenter, D., and Roby, R. (2002). Turbulence statistics in a fire room model by large eddy simulation. *Fire Safety Journal*, 37:721–752.

Zukoski, E. E. (1995). *Properties of Fire Plumes*, chapter 3. In Cox (1995).